High-resolution imaging of ordering in Rydberg many-body systems

Peter Schauß

SIGILL. UNIVERSITAT. LUDOVIC. MAXIM.

München 2014

High-resolution imaging of ordering in Rydberg many-body systems

Peter Schauß

Dissertation
an der Fakultät für Physik
der Ludwig–Maximilians–Universität
München

vorgelegt von
Peter Schauß
aus Kaiserslautern

München, November 2014

Erstgutachter: Prof. Dr. Immanuel Bloch
Zweitgutachter: Prof. Dr. Stefan Kuhr
Prüfungsvorsitz: Prof. Dr. Theodor Hänsch

Tag der mündlichen Prüfung: 20.02.2015

Zusammenfassung

Rydberg Atome sind auf Grund ihrer starken und kontrollierbaren Wechselwirkungen gut geeignet zur Quantensimulation von lang-reichweitig wechelwirkenden Systemen mit ultrakalten Atomen in optischen Gittern. In dieser Arbeit wird die Präparation und hochauflösende Abbildung von Rydberg Vielteilchensystemen demonstriert und die spontane Entstehung selbst-organisierter Ordnung beobachtet. In einer ersten Reihe von Experimenten wird die Ordnung in den post-selektierten Komponenten hoher Anregungsdichte bei hoher Temperatur untersucht. Die räumliche Konfiguration der Rydberg-Atome wird mit einer neuartigen Abbildungsmethode detektiert, die es ermöglicht die Position der individuellen Rydberg-Atome im Gitter durch Fluoreszenzabbildung der ehemaligen Rydberg-Atome nach dem Umpumpen in der Grundzustand zu bestimmen. Aus den gemessenen Rydberg-Positionen werden Korrelationsfunktionen berechnet und der Blockaderadius bestimmt. Für eine zweite Experimentreihe wird die Zeitabhängigkeit der optischen Kopplung an den Rydberg-Zustand kontrolliert. Zusammen mit der genauen Modellierung des Besetzungsmusters im optischen Gitter erlaubt dies die adiabatische Präparation von Rydberg Kristallen. Das System kann auch durch einen Ising Hamiltonian mit polynomialen Wechselwirkungen beschrieben werden, das diskutierte Szenario entspricht damit der Grundzustandspräparation in einem Quantenmagnet. Es werden Eigenschaften des kristallinen Grundzustands wie seine verschwindende Suszeptibilität und lokale Magnetisierungsdichten gemessen. Diese Arbeit stellt ein neue Stufe der Kontrolle über lang-reichweitig wechselwirkende Spin-Systeme dar und ebnet den Weg zur Quantensimulation mit Rydberg Atomen.

Abstract

Rydberg atoms are well-suited for the quantum simulation of long-range interacting Hamiltonians with ultracold atoms in optical lattices due to their strong and switchable interactions. In this thesis we demonstrate the preparation and high-resolution imaging of Rydberg many-body systems and observe the spontaneous emergence of self-organized ordering. In a first series of experiments we investigate the ordering in the post-selected high-excitation-density components of high-temperature many-body states. The spatial configuration of Rydberg atoms is imaged by a novel detection technique, which allows to determine the position of individual Rydberg atoms in the lattice by fluorescence imaging of the former Rydberg atoms after depumping them to the ground state. From the measured Rydberg atom positions we calculate correlation functions and determine the blockade radius. In a second set of experiments we implement time-dependent control of the optical coupling to the Rydberg state. Combined with the precise shaping of the initial atom pattern in the lattice this allows for the adiabatic preparation of Rydberg crystals. Via a mapping to an Ising Hamiltonian with power-law interactions this scenario corresponds to the ground state preparation in a quantum magnet. We measure properties of the crystalline ground state such as its vanishing susceptibility and local magnetization densities. This work demonstrates a new level of control over long-range interacting spin systems and paves the way for Rydberg-based quantum simulation.

Contents

1. Introduction

The strong interactions between Rydberg atoms make them unique for a variety of applications in the field of quantum optics, quantum information and strongly interacting quantum many-body systems [1–4]. The investigation of ultracold Rydberg atoms in optical lattices is motivated by the wide range of proposals to implement long-range interacting many-body systems [5–7] as well as the perspectives for quantum information processing [1]. The strong interactions between Rydberg atoms can bridge the gap between neighbouring atoms in the lattice and allow for interactions on the quantum level extending over many lattice sites and thereby enable the quantum simulation of previously inaccessible Hamiltonians [8–10] . In contrast the ground state atom interactions in lattice experiments are only relevant on the same lattice site and the coupling to neighbouring lattice sites is exclusively through tunnelling. This leads to the so-called Bose-Hubbard model including on-site interactions and tunnelling to neighbouring sites. It allows to access a wide range of physics [11–16] and the related techniques [17] serve as a starting point for the quantum simulation of more complex condensed-matter systems [18].

The intensely studied superfluid-insulator quantum phase transition in the Bose-Hubbard model [11, 12, 19] opens up the possibility to initialize an optical lattice with unity filling. This is an outstanding tool for Rydberg experiments to prepare well-controlled initial atom configurations with highly sub-Poissonian on-site atom number fluctuations [20, 21]. In combination with single-site addressing techniques [22] the preparation of arbitrary atom patterns in the lattice with high fidelity is realizable. The addition of Rydberg atoms to a Bose-Hubbard system introduces strong interactions and long-range correlations. One of the main problems in this combination is the separation of timescales as the excitation dynamics of Rydberg atoms is typically a factor of thousand faster than tunnelling dynamics in the optical lattice. This leads to a decoupling of the time evolution in the electronic Rydberg sector and the motional degrees of freedom of the atoms. The mismatch of timescales can be bridged by the so-called Rydberg dressing [6, 7, 23–27], which is discussed in the outlook. The experiments described in this thesis are carried out in the so-called frozen Rydberg gas regime, where the atoms do not move during the excitation. The advantage of working in this regime is the strong interaction leading to fast dynamics and the relatively weak influence of decoherence and loss processes. Interesting physics like spontaneous ordering and emerging long-range correlations can be observed. Such a frozen system resembles a quantum magnet when the atomic ground state is identified with $|{\downarrow}\rangle$ and the Rydberg state with $|{\uparrow}\rangle$ and can be described by an Ising system with power-law interactions in a transverse and longitudinal field [9, 28–32]. Power-law spin Hamiltonians recently attracted a lot of interest due to recent progress in the simulation of quantum dynamics in ion chains with tunable long-range spin interactions [33, 34] and the observation of dipolar exchange interactions with ultracold polar molecules [35]. These long-range interacting systems open up a new field of ultracold quantum physics with a large variety of strongly correlated Hamiltonians waiting for experimental implementation.

This thesis reports on the preparation and high-resolution imaging of Rydberg many-body systems and the observation the emergence of self-organized ordering. We facilitate well-controlled techniques for manipulation of ultracold atoms in optical lattices to prepare initial ground state atom distributions for Rydberg experiments. For the first time we combine the possibilities of Bose-Hubbard physics with Rydberg excitation in a single experimental setup. The optical lattice is not only used for initial state preparation but also for detection of the Rydberg atoms. They are stimulated back to the ground state after excitation and are recaptured in the lattice for high-resolution fluorescence imaging. This enables a new class of well-controlled Rydberg experiments with adjustable initial atomic sample distribution and at the same time high-fidelity imaging of single Rydberg atoms with single-site resolution in the lattice. On the basis of these techniques we investigate the emergence of spatial order in a system of ground state atoms coupled to a Rydberg state. The observation of spatially ordered structures in the high-density components of excited many-body states requires post-selection on high Rydberg atom numbers. For the realization of crystalline ground states adiabatic preparation schemes have been proposed [30, 36, 37]. We implement such a technique to deterministically prepare Rydberg crystals in the strongly interacting Ising spin system by controlled coupling to the Rydberg state with optimized time-dependent Rabi frequency and detuning. The demonstrated adiabatic control over such a system constitutes a big step towards quantum simulation of a wide range of long-range interacting many-body systems by ultracold atom systems with tailored Rydberg-based interactions.

Outline

The thesis starts with a basic introduction on atoms in optical lattices and essential techniques for single-site imaging in Chapter 2. After this chapter the focus is shifted to Rydberg physics and an introduction to Rydberg atoms is given (Ch. 3), followed by a technical part about the calculation of Rydberg atom properties (Ch. 4). Chapter 5 then introduces the experimental setup for Rydberg excitation and detection and explains calibration experiments in preparation of the following two chapters. The first of these reports on the observation of spatially ordered structures of Rydberg atoms excited using simple rectangular laser pulses by post-selecting on high-density components of the highly excited many-body states (Ch. 6). In the next chapter we study the dynamics of the formation of Rydberg crystals and their properties. Additionally, the improvements of the control over the experimental system required for this adiabatic preparation of ground states in the Rydberg Hamiltonian are described (Ch. 7). The last chapter then concludes and gives an outlook over the wide range of possible future experiments based on the combination of Rydberg atoms with optical lattices (Ch. 8).

List of publications

The following articles have been published in refereed journals in the context of this thesis. The articles most relevant for this thesis are shown in bold font.

S. Hild, T. Fukuhara, P. Schauß, J. Zeiher, M. Knap, E. Demler,
I. Bloch, C. Gross
Far-from-Equilibrium Spin Transport in Heisenberg Quantum Magnets
Phys. Rev. Lett. **113**, 147205 (2014)

P. Schauß, J. Zeiher, T. Fukuhara, S. Hild, M. Cheneau, T. Macrì, T. Pohl,
I. Bloch, C. Gross
Crystallization in Ising quantum magnets
Science **347**, 1455–1458 (2015)

T. Fukuhara, P. Schauß, M. Endres, S. Hild, M. Cheneau, I. Bloch, C. Gross
Microscopic observation of magnon bound states and their dynamics
Nature **502**, 76–79 (2013)

T. Fukuhara, A. Kantian, M. Endres, M. Cheneau, P. Schauß, S. Hild,
D. Bellem, U. Schollwöck, T. Giamarchi, C. Gross, I. Bloch, S. Kuhr
Quantum dynamics of a mobile spin impurity
Nature Physics **9**, 235–241 (2013)

M. Endres, M. Cheneau, T. Fukuhara, C. Weitenberg, P. Schauß, C. Gross,
L. Mazza, M. C. Bañuls, L. and Pollet, I. Bloch, S. Kuhr
Single-site- and single-atom-resolved measurement of correlation functions
Appl. Phys. B, 'Online First' doi:10.1007/s00340-013-5552-9 (2013)

P. Schauß, M. Cheneau, M. Endres, T. Fukuhara, S. Hild, A. Omran, T. Pohl,
C. Gross, S. Kuhr, I. Bloch
Observation of spatially ordered structures in a two-dimensional Rydberg gas
Nature **491**, 87–91 (2012)

M. Endres, T. Fukuhara, D. Pekker, M. Cheneau, P. Schauß, C. Gross,
E. Demler, S. Kuhr, I. Bloch
The 'Higgs' amplitude mode at the two-dimensional superfluid/Mott insulator transition
Nature **487**, 454–458 (2012)

M. Cheneau, P. Barmettler, D. Poletti, M. Endres, P. Schauß,
T. Fukuhara, C. Gross, I. Bloch, C. Kollath, S. Kuhr
Light-cone-like spreading of correlations in a quantum many-body system
Nature **481**, 484–487 (2012)

M. Endres, M. Cheneau, T. Fukuhara, C. Weitenberg, P. Schauß, C. Gross,
L. Mazza, M. C. Bañuls, L. Pollet, I. Bloch, S. Kuhr
Observation of correlated particle-hole pairs and string order in low-dimensional Mott insulators
Science **334**, 200–203 (2011)

C. Weitenberg, P. Schauß, T. Fukuhara, M. Cheneau, M. Endres,
I. Bloch, S. Kuhr
Coherent Light Scattering from a Two-Dimensional Mott Insulator
Phys. Rev. Lett. **106**, 215301 (2011) [Selected for a PRL 'Viewpoint']

C. Weitenberg, M. Endres, J. F. Sherson, M. Cheneau, P. Schauß, T. Fukuhara,
I. Bloch, S. Kuhr
Single-spin addressing in an atomic Mott insulator
Nature **471**, 319–324 (2011)

2. Single-site- and single-atom-resolved fluorescence imaging

The development of single-site fluorescence imaging techniques in optical lattices was a breakthrough in the detection capabilities for ultracold atom systems. This imaging technique has the outstanding capability to image from one to few thousands of atoms simultaneously with single-site resolution in the optical lattice [20, 21]. The resulting snapshots of the full lattice occupation give access to new observables like spatial correlation functions [14, 15, 38] and high-resolution thermometry based on the detection of single defects in the lattice occupation [16, 21].

2.1. Ultracold atoms in optical lattices

Bosons on a lattice are described by the Bose-Hubbard model, which takes into account the tunnelling of the particles from one lattice site to neighbouring sites and on-site interactions if a lattice site is more than singly occupied. The model can be nicely implemented using rubidium-87 in an optical lattice [11–13, 39]. There is an on-site interaction U for every pair of atoms on the same site, which is repulsive in the case of rubidium-87, and the hopping J between lattice sites can be tuned by changing the depth of the optical lattice. The Bose-Hubbard Hamiltonian is given by

$$\hat{H}_{\mathrm{BH}} = -J \sum_{\langle i,j \rangle} b_i^\dagger b_j + \frac{U}{2} \sum_i \hat{n}_i (\hat{n}_i - 1) - \mu \sum_i \hat{n}_i \ . \tag{2.1}$$

Here $\sum_{\langle i,j \rangle}$ denotes the sum over all neighbouring lattice sites, $b_i^\dagger$ and b_i are the creation and annihilation operators for a boson on lattice site i and $\hat{n}_i = b_i^\dagger b_i$ is the particle number operator for site i. The parameters J and U can be calculated from the lattice and atom properties (Appendix G) and depend only on the scattering length of the involved atoms, the lattice depth and geometry. These parameters can be also measured directly in the experiment, U can be determined by lattice modulation or microwave spectroscopy [40–43], J is often inferred from the measured lattice depth by band spectroscopy, but can also be measured in a high-resolution imaging setup by looking at the single particle tunnelling dynamics [22, 44].

The Bose-Hubbard model features a quantum phase transition from a superfluid to a Mott-insulating state, which has been observed in momentum space [12] as well as in real space with single-site resolution [20, 21]. The phase transition occurs when changing J/U to small values, by either increasing the on-site repulsion or decreasing the tunnelling. We use the lattice depth as control parameter, which predominantly tunes the tunnelling J.

Here we are mainly interested in the Mott-insulator limit, $J/U \to 0$, where all lattice sites in the lattice are decoupled and the physics of the system can be described exactly by a classical theory with only on-site terms. This limit can be exploited to prepare extended regions in the lattice with unity filling. The size of these regions is limited by the harmonic confinement of the trap in the experiment which is typically taken into account via a local density approximation. This assumes that every site in the trapped system is equivalent to a site in an homogeneous system with a chemical potential determined by the harmonic confinement at the considered position. The classical description in the decoupled regime can be derived as the lowest order high-temperature expansion (HTE0) [45]. The observable in the setup is the parity of the number of atoms on every lattice site, i.e. we detect only one atom if the initial number of atoms on that lattice site was odd, as light-induced collisions cause a pairwise loss [20, 21, 46, 47]. The parity density, which is observed in our experiment, can then be calculated by

$$n_p(\mu,U,\beta,n_{\max}) = \frac{\sum_n^{n_{\max}} \mathrm{mod}(n,2) e^{-\beta(\frac{U}{2}n(n-1)-\mu n)}}{\sum_n^{n_{\max}} e^{-\beta(\frac{U}{2}n(n-1)-\mu n)}} \,. \tag{2.2}$$

Here $\beta = \frac{1}{k_\mathrm{B}T}$, $n_{\max}$ is the maximum on-site occupation number and $\mathrm{mod}(n,2)$ is the parity of the on-site occupation number n. The number of neighbouring sites is not relevant, as every site is considered to be decoupled. The model can be used to calculate the in-trap parity density of atomic-limit Mott insulators by applying a local density approximation with low calculation effort (Appendix A.2).

2.2. Setup for single-site fluorescence imaging

The imaging of ultracold quantum gases on a single-site and single-atom level opens many new possibilities to investigate these system and measure previously inaccessible observables, like spatially resolved correlation functions [38]. Our specialized single-site setup with high-resolution objective has been described in detail in previous publications [21, 48, 49], and here we will only shortly summarize the most important information about setup and experimental sequence.

The first cooling stages in the experiment are similar to other rubidium Bose-Einstein condensate (BEC) machines, but the region of the vacuum chamber with best vacuum conditions and the lattice setup ("science chamber") is optimized for high-resolution imaging. In the following a short description of the experiment is given. The atoms from a large reservoir of several grams of rubidium at room-temperature are first cooled transversally in a 2D MOT and then loaded through a differential pumping tube to a 3D magneto-optical trap (MOT). The 3D MOT is then, after a compressed MOT stage, loaded into a unplugged quadrupole trap. In the magnetic trap microwave evaporation is performed but stopped before strong Majorana losses occur. The precooled atoms are then loaded into a single beam transport dipole trap and moved via mechanically shifting the focus to the science chamber. There, we have the setup for a three-dimensional lattice formed by retro-reflected beams. First the retro-reflected beams of the two horizontal beams are blocked and the incoming beams

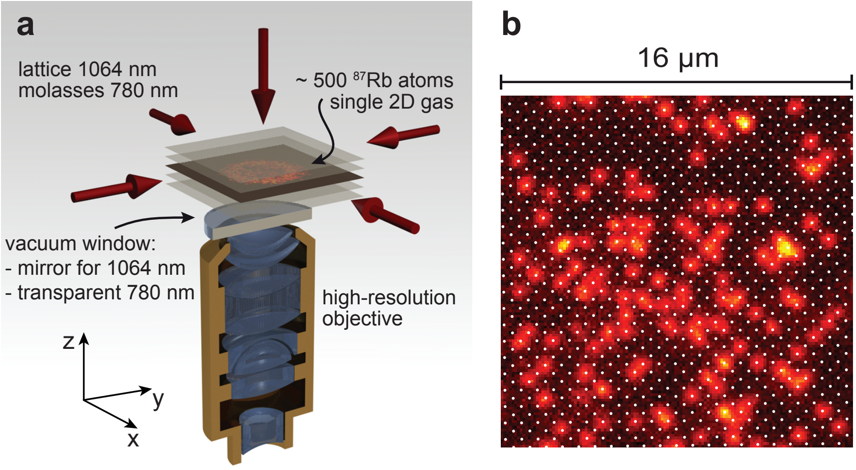

Figure 2.1.: Central part of the singe-site setup. **a**, The schematic shows a single plane of atoms in a vertical standing wave 1064 nm lattice. This 1D z-lattice is created by a retro-reflection from the vacuum-window in front of the objective. This window is coated as a mirror for 1064 nm and is transparent for 780 nm. For imaging the atoms are pinned with the z-lattice and two horizontal lattices and illuminated by red-detuned molasses light, which cools the atoms and scatters photons from the atoms, that are imaged via the high-resolution objective to an EMCCD-camera, **b**, typical image of a dilute cloud of atoms. The red dots are the atoms, their size is determined by the point spread function of the imaging system. The white dots mark the position of the lattice sites. Images adapted from [21].

are used as a crossed dipole trap. Here we evaporate further and can create a BEC. Typically we stop before and load the cold atoms into the vertical z-lattice. This lattice is formed by a beam incident from above and the retro-reflected beam from the horizontal window before the objective, which sits below the vacuum chamber. This window is coated as mirror for the lattice laser wavelength of 1064 nm and is transparent for the imaging light at 780 nm.

At that stage we have the atoms distributed over several slices of the vertical standing wave lattice. We prepare a single slice of atoms by transferring all atoms to the other hyperfine state ($F = 2$) using a microwave sweep and only a single slice back, which we can separate in frequency by a strong magnetic field gradient along the z-axis. Removing all the other atoms leaves us with around 1000 atoms in a single slice of the vertical lattice. This is the starting point for further evaporation to the target atom number. For the evaporation we use a horizontal gradient, implemented by the superposition of a vertical gradient field and an horizontal offset field, and an additional dimple to increase the trapping frequency. Typically we reduce the atom number down to around 200 atoms and then increase the horizontal lattice depth to drive the two-dimensional system over the superfluid-Mott-insulator transition. For detection the atoms in the single slice of the vertical lattice are pinned in the 3D optical lattice by increasing the lattice depth to 3000 E_r in all three directions, where

$E_\mathrm{r} = h^2/(2m\lambda^2)$ is the recoil energy of the lattice with $\lambda = 1064\,\mathrm{nm}$ and m the mass of rubidium-87. The magnetic fields are then switched to compensated zero-field and red-detuned molasses light is used to scatter photons and simultaneously cool the atoms in the lattice. The photons are collected via a high-resolution objective with a numerical aperture of 0.68, which allows with a resolution of about 700 nm to determine which sites are occupied in the lattice with 532 nm spacing. The image is taken using an EMCCD camera and an illumination time of typically one second.

For high densities in the lattice the extraction of the site occupation is challenging, but can be calculated via a computer program ([21], Sec. 2.4). The calculation is simplified by the fact that due to light-assisted collision the parity of the atom number on each site is detected [20, 21], implying a occupation of either zero or one. A typical image of a dilute cloud is shown in Fig. 2.1, where the single atoms are easily distinguishable by eye as red dots using a dark-red (no light) to yellow (high light level) colour map. The residual noise in the pictures is caused by background counts, readout and shot noise of signal and background light (the background light is subtracted via a reference image without atoms).

2.3. Auto-focussing

Due to the high resolution required for single-site imaging the depth of focus of the imaging system is rather small (approximately three sharp planes ≈ 1.5 µm), such that active refocussing is already required for mechanical drifts of the apparatus of approximately a micron. The drifts can be compensated by a high-precision regulated piezo stack (PIFOC P-726) on which the high-resolution objective is mounted. Typically a refocussing is required every 30 min. Assuming a sequence with five images (each takes 30 s) to find the optimal focus position, the refocussing would occupy around 10 % of the measurement time. Additionally repeated non-automated calibrations can easily distract scientists from the real measurement due to many interruptions.

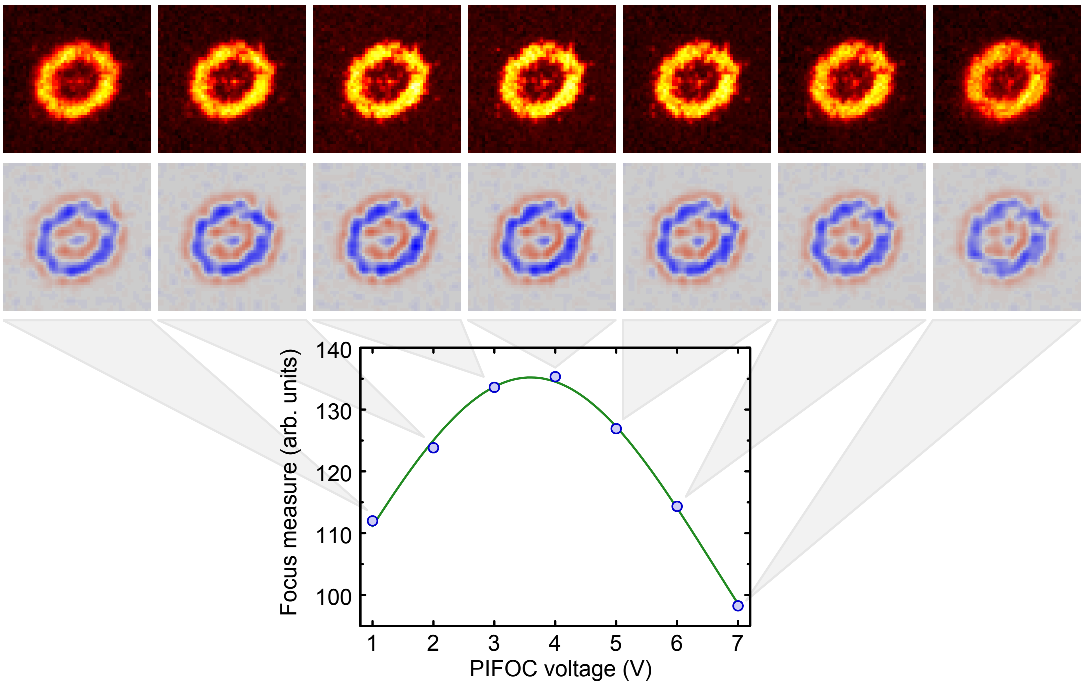

Figure 2.2.: Illustration of the auto focus process. First row: the seven pictures with different PIFOC voltage of the same cloud. Second row: images after post-processing. Graph below: extracted focus measure values (blue points) and Gaussian fit (green line), giving an optimal focus position of 3.6 V for this example data set of a Mott insulator with doubly occupied shell in the centre.

This stability issue can be solved by automatic active feedback on the PIFOC to compensate drifts of the addressed slice with respect to the focus of the high-resolution objective. The idea is to take the seven pictures in a single run of the experiment of the same cloud. If the requirements on the image quality are relaxed, the exposure time can be reduced from 1 s to around 80 ms, which allows for the imaging of the same cloud in several pictures and changing the focusing of the objective in between within 50 ms using the PIFOC. A quite simple technique can be used to extract the focus position automatically from several pictures of the same cloud and the corresponding voltages for the PIFOC. For the automatic determination of the focus an easily calculated measure for the relative focus quality of the images is required. The following method is used in our system: To improve speed, the images are first binned 4×4 (this is still $\approx 500\,\mathrm{nm}$ per pixel). Then we effectively band-pass by applying a 7×7 Laplacian of Gaussian (LOG) filter on the image. This is essentially a numerical second derivative smoothed with a Gaussian of $\sigma = 2$. The result is a 2D picture of the curvature of the initial image, which is largest if the image has strong contrast (Fig. 2.2). To end up with a single number as measure for the focussing quality we sum up the absolute value of the curvature over the whole image. Plotting the focus measure for all images of the series over the PIFOC voltage gives typically a Gaussian-like shape, which is fitted and the position of the maximum is a very good approximation for the optimal focus position. This calculation is included in the experimental control software, such that the focusing is happening without further interaction. The images are taken in the so-called "idle sequence", which is always started automatically if no other measurement sequence is running to maintain thermal equilibrium of the experimental setup. At the beginning of other sequences they are then evaluated to guarantee sharp images of the ultracold atoms.

2.4. Reconstruction algorithm

The reconstruction algorithm is one of the main ingredients of data processing at the experiment. Its main purpose is to detect the occupied lattice sites in fluorescence images and extract a lattice occupation matrix from the image. This lattice occupation matrix is the basis of all further evaluation of experimental data at our setup. The image processing can, of course, only extract information which is in the original picture, this is the parity projected density, and good reconstruction fidelities are only achievable with good imaging quality and especially very low hopping rates during the imaging. Hopping during the imaging is detrimental, as it can cause two signals of the same atom at different positions, making it impossible to guess the initial atom number distribution correctly. The algorithm was first implemented by Stefan Kuhr for the first publication [21], and then further optimized and automated to handle the larger amounts of data that had to be processed for later experimental studies (e.g. [14]). One of the main challenges of such image processing algorithms is reasonable performance without affecting the fidelity. Another important point is to reach a level of reliability that the reconstruction can be run on all images taken at the experiment essentially without interaction.

In the following the main ideas and techniques used in the reconstruction algorithm are discussed. First we argue why the reconstruction is possible for our pictures. The resolution is around $700\,\mathrm{nm}$, but the spacing between neighbouring lattice sites is $532\,\mathrm{nm}$. Because of that further information is required to determine the atom positions. But for our system it is known that atoms can only sit on lattice sites. This information improves the effective resolution, and allows to extract the lattice occupation with high fidelity even in the presence of noise. To exploit the lattice structure during the reconstruction, all its parameters have to be determined quite accurately. There are parameters that are fixed and others that drift from shot to shot. The angles of both horizontal lattices with respect to the camera and the lattice spacing in both directions belong to the first class. They only change during readjustments of the setup. It turns out that small lattice adjustments have vanishing influence on lattice angles, severe effects are only visible for adjustments of the imaging path. Also the lattice spacing can vary slightly due to imaging distortions, but these effects are negligible. These parameters are extracted in separate calibration measurements and are kept fixed during the daily image reconstruction process. The lattice phases along both lattice axes, which determine the absolute position of a lattice site in space, are drifting slowly due to thermal effects. They can be determined using a single picture, by shifting the known lattice structure to coincide with a single atom. All the other atoms in the picture will then lie on this calculated lattice. For the calibration of lattice angles and lattice constant we take images of dilute thermal clouds with lots of isolated atoms, which can be easily individually identified. The position of the atoms can be determined with sub-lattice-site precision by fitting the point spread function. Projecting the positions of all atoms onto a line with certain direction in the plane yields a histogram with a contrast, which is maximal for the line being parallel to one of the lattice axes. The distance of the peaks in the comb structure yields the lattice spacing [48].

In the following the algorithm performed for each image is shortly sketched. It begins with loading the bitmap file. It is corrected for static intensity modulations of the CCD, which are caused by interference on the CCD chip ("etaloning"). The intensity modulation can be calibrated by averaging lots of images with large random atom distributions, which averages out the atom distribution and leaves over the spatial inhomogeneity of the effective sensitivity of the camera chip. Afterwards background level and signal level for single atoms are estimated. This helps to improve the fidelity of the reconstruction for imperfect pictures with background light and low fluorescence signals. Based on this information an algorithm is used to identify isolated single atoms. These atoms are important to determine the phases of the lattice and improve the estimated signal level per atom. Overlapping all of these single atom accurately allows to determine the point spread function of the imaging system with quite good signal-to-noise ratio (Fig. 2.5). For the following steps the coordinate transformation from image coordinates to integer lattice coordinates and backwards are precalculated. The known lattice structure allows for a first estimate of the lattice occupation by just integrating a certain region around the centre of every lattice site using a threshold technique. For higher resolution compared to the lattice spacing this technique would be already sufficient to extract the lattice occupation with very high fidelity. In our case this estimate is quite bad close to unity filling regions. To improve this guess an iterative algorithm is used, which adds or removes occupation or shifts occupation between neighbouring lattice sites. It locally tries to reduce the difference of the real image with a convolution of the reconstructed occupation with the point spread function. The amount of redistributed weight is reduced until convergence. There are two good choices for the point spread function. One is to use a Gaussian, the other possibility is an averaged point spread function determined from isolated single atoms. It turns out that there is no significant difference in reconstruction fidelity for both techniques, but using the measured point spread function leads to slightly improved convergence and lower residuals. The next step is to determine whether a fitted occupation, which converged to a real number, is caused by an atom on the lattice site or just by noise. To this end, we create a histogram of all lattice occupations of the image. If the image quality was reasonable, this will lead to a double-peak structure. One peak at zero for empty sites and another peak corresponding to the singly occupied sites. Fitting Gaussians to both peaks leads to an optimal threshold at the crossing point of both functions to decide between zero or one atom. This threshold is used thereafter to round the occupation to integer values. Sometimes the signal can be so high that it corresponds to two atoms, which is caused in most cases by an atom in another site along the imaging direction. The resulting matrix with integer entries is the main result of the reconstruction. There are some add-ons integrated in the automatic evaluation for often used parameters. For example a radius and position fit of the cloud, the evaluation of addressing coordinates for addressing experiments or additional information about the fidelity of the reconstruction. In the end the results are written to several result files, which are discussed shortly in the following. The main file is in Matlab format ("*_reconstr.mat"), which contains all the information about the reconstructed image, and is saved directly in the folder of the image. For compatibility with older scripts there is also a file containing only the matrix ("*_occ.mat") and one containing the pixel-coordinates of all atoms ("*_coord.mat"). Additionally there is an image overview of the reconstructed image in PNG-format. The main advantage of this picture is that it can be opened with standard image viewers and allows for a fast check of the reconstruction quality and atom distribution in the lattice. For a good overview there is a summary file in ASCII format for every sequence and a global one containing the main parameters for every reconstructed image in a single line.

The following list summarizes the main tasks performed for each picture during the reconstruction.

1. Load image from Andor sif file and apply etaloning correction
2. Determine background level and estimate signal level
3. Find single atoms and fit them for accurate position information
4. Lattice phase fitting using single atoms and determination of signal level, extract point spread function
5. Precalculate coordinate transformation
6. First guess for the lattice occupation
7. Optimize lattice occupation with adaptive steps until convergence
8. Determine threshold signal level for 0/1-atom
9. Round occupation according to threshold to integer value
10. Other evaluation (fidelity estimate, addressing, . . .)
11. Write output

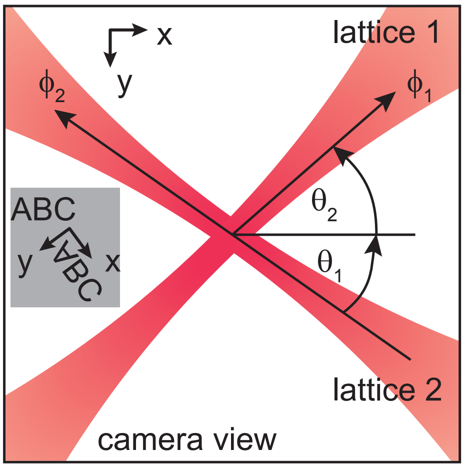

Figure 2.3: Lattice parameter definitions for reconstruction algorithm. The lattice parameters are defined in the coordinate system of the images taken by the fluorescence camera. To fix the geometry of the lattice the two angles of the lattices θ_1 and θ_2 are required. Additionally both lattices shift in phase and the sign of the phases are defined as shown. The grey box shows the coordinate system of the spatial light modulator (SLM) used for addressing (Sec. 7.4.1). The writing "ABC" demonstrates how a text shown upright on an image sent to the SLM is projected onto the atoms as observed by the camera.

2.4.1. Static lattice properties

The lattice angles and lattice constants were fitted the last time 22/11/2012. For the lattice constant we obtain 4.273(3) px consistently for both lattice axes. There is no measurable difference in both directions and over the whole field of view, which demonstrates the high quality of the imaging system. As the lattice spacing is known to be $a_{\text{lat}} = 532\,\text{nm}$, this result yields also a calibration of the camera of 124.50(9) nm/px. The lattice angles can be also determined with high precision. The values are currently $\theta_1 = -44.51(3)^\circ$ for lattice 2 and $\theta_2 = 45.71(1)^\circ$ for lattice 1 with the definition of the angles provided by Fig. 2.3.

For the reconstruction algorithm the coordinate transformations from image to lattice coordinates and backwards are essential. In the following $a = 4.273(3)$ is the lattice constant in pixels.

Lattice to image coordinates The calculation of this transformation is directly derived from the angle definition shown in Fig. 2.3. In the lattice coordinates we label the sites with a pair of integers (i,j) and in the image coordinates the pixels (x,y) with $x,y \in [1;532]$. With these definitions the transformation is

$$\begin{aligned} x &= ia\cos\theta_1 + ja\cos\theta_2 + x_0 \\ y &= -ia\sin\theta_1 - ja\sin\theta_2 + y_0 \ . \end{aligned} \tag{2.3}$$

Here x_0 and y_0 are offsets, which can be chosen as the pixel coordinates of an arbitrary atom in the lattice.

Image to lattice coordinates The transformation in the other direction can be derived by just solving Eq. (2.4.1) for (i,j). As there are several pixels close to the centre of the site the resulting index is determined by rounding towards the nearest integer to get the closest site to the input pixel.

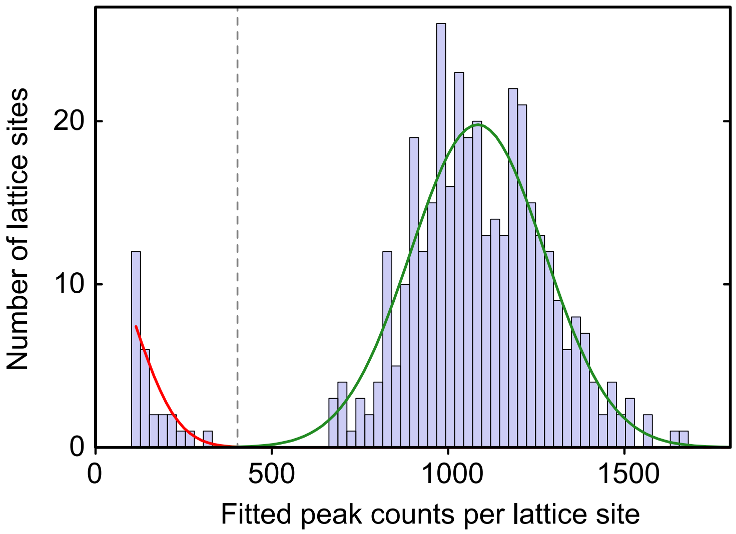

Figure 2.4.: Histogram of single atom counts. The peak counts per lattice site were determined by fitting the PSF per lattice site. Data for a single example picture of a Mott insulator. The background peak (red) and the single atom peak (green) are fitted with Gaussians. The threshold value between no atom and a single atom is marked by the vertical grey line at the crossing point of both Gaussians. Peak counts $\lesssim 100$ are directly discarded and do not appear in the histogram. This evaluation is automatically performed by the reconstruction program for every single image without user interaction.

$$\begin{aligned} i &= \mathrm{round}\left(-\frac{(x-x_0)\sin\theta_2+(y-y_0)\cos\theta_2}{a\sin(\theta_1-\theta_2)}\right) \\ j &= \mathrm{round}\left(\frac{(x-x_0)\sin\theta_1+(y-y_0)\cos\theta_1}{a\sin(\theta_1-\theta_2)}\right) \end{aligned} \tag{2.4}$$

2.4.2. Statistics on reconstructed files

In this section all images taken in 2013 (approximately 85000 reconstructed pictures) are analysed to give some statistical information about the reconstruction.

About 97 % of the pictures were reconstructed in less than 30 s, which is the typical time per experimental cycle in our setup. This means that the reconstruction of the pictures is essentially as fast as the data taking.

During the reconstruction single atom coordinates are determined. Averaging the point spread function (PSF) of many of these single atoms leads to a high-quality picture of the point spread function of the objective. The technique used is a super-sampling of the single atom sub-pictures by a factor of 5 and then aligning the pictures on this finer grid with respect to their fitted centre and then averaging (Fig. 2.5). The point spread function shows a slight asymmetry of the first ring of the Airy-type pattern (Fig. 2.5c). This asymmetry hints to a slight tilt of the objective, but this

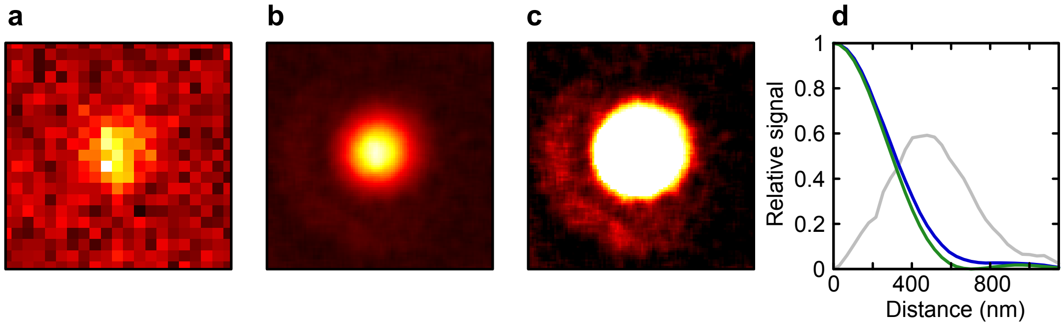

Figure 2.5.: Illustration of the point spread function. a-c, Pictures of the point spread functions (PSF). Full width of the pictures is 20 px of the camera or 2.49 µm, **a**, PSF of a single atom, **b**, PSF of about 1000 aligned and averaged single atoms, **c**, same data as **b**, but focusing on the ring structure by adapted colour scale. **d**, Azimuthal average of the experimental PSF from **b** (blue) and theoretically expected ideal PSF for NA = 0.68 (green) [48], the difference multiplied by 10 is shown in grey. Fitting the numerical aperture to the experimentally measured point spread function yields NA = 0.63, which is a quite close to the expected NA although it contains all dirt effects and the uncertainty in the atom position in a lattice site.

effect is hardly visible in a single picture. Otherwise the point spread function has no further distortions. Neglecting the small ring the PSF can be modelled without further information by a single Gaussian: $P(x,y) = A \exp\left(-\frac{(x-x_0)^2+(y-y_0)^2}{2\sigma^2}\right)$. The size of the PSF can be extracted from pictures with lots of isolated atoms and one obtains $\sigma = 2.15(5)\,\mathrm{px} = 267(6)\,\mathrm{nm}$, which leads to a minimum resolvable distance following the Rayleigh criterion of $d_{\mathrm{min}} = \frac{3.8317}{\sqrt{2}}\sigma = 723\,\mathrm{nm}$, where the numerical prefactor comes from the relation of the first minimum in the Airy pattern to the Gauss curve sigma. The amplitude in counts of the camera for a single atom is fluctuating a bit and also depends strongly on the adjustment of the molasses. For every reconstructed picture a histogram of the signal levels for every single atom is calculated. Typically the peak of the single atom signal is clearly visible. This peak is fitted by a Gaussian of type $\exp\left(-(x-\mu)^2/(2\sigma^2)\right)$, which yields the mean signal per atom μ in a certain picture. The mean of the peak relative to its width σ determines the signal-to-noise ratio in our setup and can be determined to $\frac{\mu}{\sigma} = 4.4(1.2)$ (error is the s.d.). This ratio is stable, while the absolute signal per atom is fluctuating.

Drift of lattice phases

The drift of the horizontal lattice phases depends mainly on thermal effects on the experiment table. With a good climate control and a well-controlled sequence and a matched idle sequence to maintain equilibrium, the lattice phase drift can be suppressed to below 1 site/hour without active phase stabilization (Fig. 2.6a). For sequences with a very low number of sufficiently isolated atoms or even empty pictures in between, the tracking of the phase becomes a bit more noisy, but an accuracy of

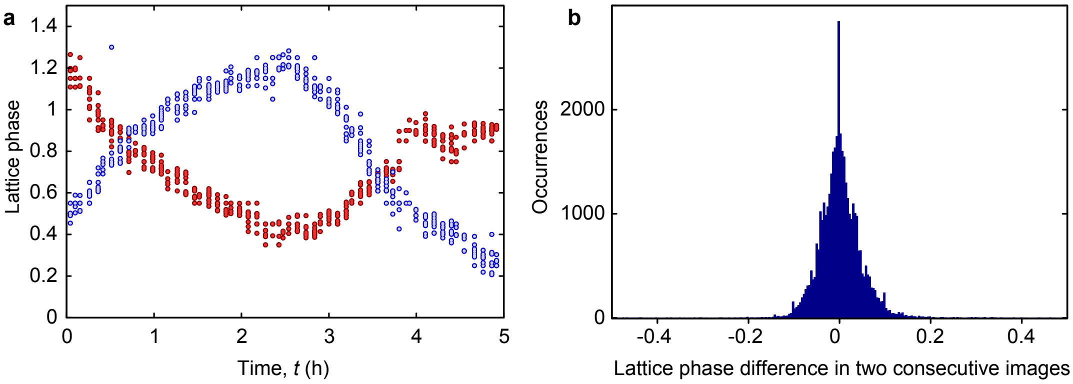

Figure 2.6.: Analysing the lattice phase drifts. **a**, Lattice phase drift from 14/06/2013 over time. Blue dots, lattice 1 phases. Red dots, lattice 2 phases. Every dot corresponds to one lattice phase determination of a single picture. The timing is only correct on the level of a sequence (typically 5 min). The small scatter of the points demonstrates a phase determination error on the order of 0.1 a_{lat} (this is subpixel precision, as 1 px on the image corresponds to 0.23 a_{lat}). There are only very few outliers, e.g. top left, which are often due to a pair of neighbouring atoms being interpreted as a single atom during the phase fit routine. **b**, Histogram of the phase difference for lattice 1 of two consecutive images which were taken typically within 30 s. There is no significant difference for both lattice axes.

0.1 a_{lat} is still within reach. From an one day data set the distribution of the phase difference of consecutive pictures was evaluated, post-selecting on pictures with at least three atoms used in the phase fitting process (Fig. 2.6b). In 96 % the phase difference between successive pictures is below 0.1 a_{lat}, and in 99 % the phase difference is below 0.2 a_{lat}.

2.5. Outlook

Although the imaging of single atoms works nicely in the lattice there are some limitations. Overcoming these would enhance the detection capabilities a lot. Currently only one spin component can be imaged at the same time, as the molasses imaging mixes all hyperfine ground states. In principle it is possible to work in a unity filling Mott insulator [50, 51], which then allows to infer the occupation in the other spin component by imaging one component due to the unity filling constraint. In theory even more information can be extracted and even entanglement can be probed in this way [52]. In practice such techniques have limited applicability, as a very good unity filling preparation is required and no experiment with finite tunnelling in the lattice can be performed with high fidelity in this way. A true two-component spin imaging would enable the measurement of spin-spin correlations for a wider range of applications. Another open question is the detection of doubly occupied sites, especially in combination with two-component spin imaging. The detection of doubly occupied site would be for example necessary to determine on-site correlations (Appendix H.2). These problems can be partly solved by mapping a single slice cloud to two slices in the z-lattice. This would require the imaging of two or more planes behind each other in addition to a splitting operation. To this end, one needs to distinguish for example two atoms in two neighbouring planes behind each other from a single atom. One problem here is that the amplitude per single atom is rather noisy (Fig. 2.4). The dependence of this width on the imaging parameters is not clear yet. In practice the signal turns out to be not exactly twice the signal of a single atom and the signal-to-noise ratio does not allow for a clear decision in this case.

Another challenge arises when trying to determine the lattice phase from very cold clouds. Due to the lower temperatures reached lately, the number of isolated atoms, which were used for the fit of the lattice phases, is rather low and often zero. A new algorithm for extracting the lattice phase from pictures with several closely packed atoms has been developed, but is not yet implemented for production.

Another very different limitations of the experiment turns out to be the cycle time, which sets, although already relatively fast compared to many other experiments with $25 - 30\,\mathrm{s}$, an upper limit of the amount of data that can be taken. This becomes in particular a problem for experiments which require a lot of statistics, like correlation measurements, especially in 2D. This is also true for Rydberg experiments as for many of these the average number of detected Rydberg atoms per experimental cycle is below one, as will become clear in the next chapter.

3. Introduction to Rydberg atoms

Rydberg atoms are highly excited atoms where one of the electrons is in an eigenstate with large principal quantum number. The lifetime of these weakly bound states is typically astonishingly long, as the lifetime is increased due to the very small overlap with the ground state [53].

Rydberg states are available in every atom and molecule and lately even found in excitons [54], so schemes which are based on Rydberg states are generic and applicable in many systems. Additionally there is not only one Rydberg state, but always a bunch of series of Rydberg states. Here we will focus on Rydberg states with exactly one highly excited electron, which is the relevant case for alkali-metal Rydberg atoms. In those atoms the Rydberg states are very close to hydrogen states, only some of these states are shifted due to the overlap with the ionic core. One can account for this shift by introducing an effective principal quantum number n^*, differing from the actual principal quantum number by the quantum defect [55]. This trick is enough to understand the spectrum of Rydberg states and the universal scaling of the Rydberg state properties with effective principal quantum number near the ionization threshold (Tab. 3.1).

The interesting range of Rydberg states typically extends from $30-200$, because the low states have short lifetime and the very high states become more and more difficult to resolve and control in the laboratory, as they are extremely sensitive to electric fields.

This sensitivity is caused by the fact that the electron is on average typically a factor of 100 to 1000 further away from the core compared to a ground state atom, which leads to a strongly enhanced polarizability by many orders of magnitude. This also implies an increase of induced dipole moments and strong forces between the Rydberg atoms due to the resulting van der Waals interaction, which is typically more then ten orders of magnitude stronger than for ground state atoms. These forces can be switched on and off coherently on timescales of less than a microsecond via optical excitation and deexcitation of atoms to Rydberg states. Therefore Rydberg atoms are interesting for quantum information processing and the realization of strongly correlated many-body systems.

In the following sections we first look at the properties of isolated Rydberg atoms, their interactions and then the influence of the interactions on laser excitation to Rydberg states. In the last part we discuss the effects when coupling dense and strongly interacting samples to Rydberg levels.

3.1. Universal scaling of Rydberg atom properties

The main properties of Rydberg atoms can be understood quantitatively within quantum defect theory [55]. The idea of the theory is to introduce quantum defects $\delta(n,l,j)$ for every fine-structure state which correct the principal quantum number to an effective principal quantum number $n^* = n - \delta(n,l,j)$, which then fulfils the Rydberg formula for the absolute transition energy E_{nlj} to the Rydberg level [56–58].

$$E_{nlj} = E_{\text{ion}} - \frac{R^*}{(n - \delta(n,l,j))^2} = E_{\text{ion}} - \frac{R^*}{(n^*)^2} \tag{3.1}$$

Here E_{ion} is the ionization threshold, R^* is the mass-dependent effective Rydberg constant, $R^* = \frac{1}{1+\frac{m_e}{m}} R_\infty$ for an atom with nuclear mass m, with R_∞ the Rydberg constant [53]. The quantum defect $\delta(n,l,j)$ depends mainly on principal quantum number n and the azimuthal quantum number l and becomes close to zero for $l > 2$ due to the low core overlap of these states. There is also a slight dependency on the orbital angular momentum quantum number j, which is often negligible.

In general all properties of Rydberg atoms show a characteristic scaling with n^*, forming a nice tool to find the optimal range of n^* for a certain experiment (Table 3.1). Some of the scalings are extremely strong like the polarizability, while others are rather weak like the dipole matrix elements for Rydberg excitation from the ground state. In the following we will discuss some of the scalings. The radius of the Rydberg atoms scales $(n^*)^2$, as can be analytically calculated for hydrogen. This leads to extremely large wavefunctions for the electron for high n^* and a diameter of typical Rydberg atoms from several hundred nanometres to few micrometres. The binding energy of the Rydberg electron as given by the Rydberg formula decreases and becomes vanishingly small compared to typical binding energy of electrons in atoms. The level separation of neighbouring Rydberg levels decreases with n^* leading to difficulties to resolve individual lines for very high n^*, but this happens in experiments with well-compensated electro-magnetic fields only at $n > 200$ [59, 60]. The lifetime of the Rydberg states increases, which leads to a reduction of the natural linewidth for the high Rydberg states This is a bit counter-intuitive, but can be understood by investigation of the decay channels. The radiative decay scales like the probability of the Rydberg electron to be close to the nucleus, as the overlap to low-lying states, which dominate the radiative decay, is highest there. The radiative lifetime scaling can therefore be estimated by $1/\left|\psi(0)\right|^2$, leading to the scaling $(n^*)^3$, which can be confirmed by calculations. There is also depopulation by so-called blackbody radiation induced transitions to neighbouring Rydberg levels. This is caused by the low transition frequencies between Rydberg states, which have overlap with a blackbody spectrum at typical temperatures, as well as the large dipole matrix elements between neighbouring Rydberg levels. The scaling of the radial matrix element to neighbouring Rydberg states can be derived by assuming that the radial wavefunction is approximately the same for both states, which then leads to an overlap matrix element similar to the one for the orbit radius. Therefore they scale equivalently with $(n^*)^2$. Important for experiments with optical excitation of Rydberg atoms is the scaling of the matrix elements from low-lying levels to Rydberg states. For otherwise constant parameters the

Rabi frequency scales as the matrix element with $(n^*)^{-3/2}$. Most modern Rydberg experiments are performed to exploit the strong interactions between Rydberg atoms. The interactions are in first approximation of van der Waals type and decay with one over the sixth power of the distance between the atoms (Sec. 3.2). The C_6 coefficient scales extremely with a power of eleven with n^* and can cause strong forces, if high-n Rydberg atoms are excited at short distances. The relevant length scale determined by van der Waals interaction and excitation bandwidth is the so-called blockade radius, which is the minimum distance between Rydberg atoms when exciting them with a laser of certain Rabi frequency on resonance (Sec. 3.2.2). Interestingly, the scaling of the blockade radius is much weaker as the interaction strength falls off strongly with distance. In the end it scales approximately as $(n^*)^2$, similar to the orbit radius of the Rydberg atom.

In the following the basic ideas of Rydberg-Rydberg interactions and coherent collective excitation of Rydberg atoms in many-body system are discussed.

property	derivation	scaling $(n^*)^x$	reference
orbit radius	$\langle r \rangle = \frac{a_0}{2}(3(n^*)^2 - l(l+1))$	2	[61, p. 419] [62, p. 121]
binding energy	$E_{n^*} = -\frac{R^*}{(n^*)^2}$	-2	[56–58]
level separation	$E_{(n+1)^*} - E_{n^*}$	-3	
electron probability at core	$\lvert\psi(0)\rvert^2 \propto 1/(n^*)^3$	-3	Sec. B.3
hyperfine structure splitting	$\propto \lvert\psi(0)\rvert^2$	-3	[59]
radiative lifetime	$\tau_0 \propto 1/\lvert\psi(0)\rvert^2$	3	[63]
bbr lifetime	$\tau_{\mathrm{bbr}} = \frac{3\hbar(n^*)^2}{4\alpha^3 k_{\mathrm{B}} T}$	2	[64]
effective lifetime	$\tau_{\mathrm{eff}} = (1/\tau_0 + 1/\tau_{\mathrm{bbr}})^{-1}$	2	[64]
radial matrix element	$\langle 5\mathrm{P} \rvert er \lvert nl \rangle \propto \psi(0)$	$-3/2$	[3]
radial matrix element neighbouring level	$\mu = \langle nl \rvert er \lvert nl+1 \rangle$	2	
polarizability	$\alpha = p/E \propto \frac{\mu^2}{E_{n+1}-E_n}$	$2+2+3=7$	
van der Waals coefficient	$C_6 \propto \frac{(\mu_1\mu_2)^2}{E_{n+1}-E_n}$	$2(2+2)+3$ $= 11$	[65]
Rabi frequency	$\Omega = \langle 5\mathrm{P} \mid dE \mid n\mathrm{S} \rangle$	$-3/2$	
blockade radius	$\sqrt[6]{\frac{C_6}{\hbar\Omega}}$	$(11+\frac{3}{2})/6$ $= 2\frac{1}{12}$	

Table 3.1.: Scaling of properties of Rydberg atoms. For large principal quantum number n Rydberg state properties follow universal scaling laws. See also [3, 66, 67]. The blackbody radiation lifetime is abbreviated as bbr lifetime.

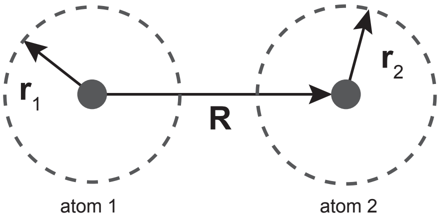

Figure 3.1.: Definitions for Rydberg-Rydberg interaction Hamiltonian. $\boldsymbol{R}$ is the distance vector between the nuclei of both atoms and $\boldsymbol{r}_{1,2}$ the relative position of the electron with respect to the core of atom 1,2.

3.2. Rydberg-Rydberg interactions and pair states

One of the main properties of Rydberg atoms is the interaction between them, which is orders of magnitude stronger than ground state atom interactions [1]. While the short-range interaction between ground state atoms can be typically approximated by a zero-range (delta-function) potential, this is not possible any more for dipolar interactions or interactions, which extend nearly over the whole system size. Here we will discuss the basic ideas how the van der Waals interaction emerges from the induced dipole-dipole interaction between neutral but strongly polarizable Rydberg atoms (based on [68, 69]).

For Rydberg atoms with a single valence electron one can consider the following interaction model. Two interacting Rydberg atoms can be described by two singly positive charged ions and two surrounding electrons. The internal structure of the ionic cores is assumed to be not influenced by the other atom. The spatial configuration can be described by the relative position of the ions $\boldsymbol{R}$, and the relative position of the electron with respect to the corresponding ion $\boldsymbol{r}_{1,2}$ (Fig. 3.1) [68]. The Hamiltonian is then given by $\hat{H}_{dd} = \hat{H}_1 + \hat{H}_2 + V(\boldsymbol{R}) - V(\boldsymbol{R} - \boldsymbol{r}_1) - V(\boldsymbol{R} + \boldsymbol{r}_2) + V(\boldsymbol{R} - \boldsymbol{r}_1 + \boldsymbol{r}_2)$, where $V(\boldsymbol{r}) = \frac{e^2}{4\pi\epsilon_0}\frac{1}{|\boldsymbol{r}|}$ is the Coulomb potential. The terms in the Hamiltonian are the Hamiltonians for the two isolated atoms, and then additional terms for the interaction of both nuclei, the electron of atom 1 with the nucleus of atom 2 and the other way around and also the interaction between the two outer electrons of both atoms. Assuming $\boldsymbol{R} \gg \boldsymbol{r}_{1,2}$ one can apply a multipole expansion in $\boldsymbol{r}_{1,2} \approx 0$ and keep only the first relevant term, which is the dipole-dipole interaction, as the monopole term vanishes because each electron-ion system is neutral (see e.g. [69, p. 25]). The Hamiltonian for the two-atom system is then approximately given by $\hat{H}_{dd} = \hat{H}_1 + \hat{H}_2 + \hat{V}_{dd}(\boldsymbol{R},\boldsymbol{r}_1,\boldsymbol{r}_2)$, where the dipole-dipole interaction operator is given by

$$\hat{V}_{dd} = \frac{e^2}{4\pi\epsilon_0}\left(\frac{\hat{\boldsymbol{r}}_1\hat{\boldsymbol{r}}_2}{R^3} - \frac{3(\hat{\boldsymbol{r}}_1 \cdot \hat{\boldsymbol{R}})(\hat{\boldsymbol{r}}_2 \cdot \hat{\boldsymbol{R}})}{R^5}\right) = \frac{e^2}{4\pi\epsilon_0}\frac{\hat{\boldsymbol{r}}_1\hat{\boldsymbol{r}}_2 - 3(\hat{\boldsymbol{r}}_1 \cdot \hat{\boldsymbol{n}})(\hat{\boldsymbol{r}}_2 \cdot \hat{\boldsymbol{n}})}{R^3}\ , \tag{3.2}$$

where $\hat{\boldsymbol{n}} = \hat{\boldsymbol{R}}/R$ and $R = \left|\hat{\boldsymbol{R}}\right|$. The dipole-dipole interaction scales as $1/R^3$ with the

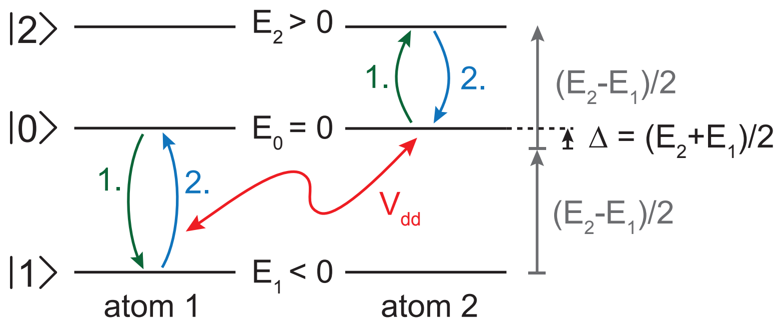

Figure 3.2.: Schematic of Förster exchange process. Rydberg-Rydberg interaction as second order perturbation of the dipole-dipole interaction. Atom 1 jumps in a virtual process to state $|1\rangle$ while atom 2 goes to $|2\rangle$. Afterwards they both go back to the initial state $|0\rangle$. The intermediate state is detuned by the Förster defect $\mathit{\Delta}_F = (E_1 + E_2)/2$.

distance of the two atoms. For the following arguments the angular dependence is neglected to simplify the discussion.

3.2.1. Förster processes in a three-level atom example

In this section we discuss how the van der Waals interaction emerges in a three-level atom model system. For this example we assume two atoms with three energy levels each, which are coupled by a simplified dipole-dipole interaction $\hat{V}_{ds} = \frac{e^2}{4\pi\epsilon_0}\frac{\hat{\boldsymbol{r}}_1\hat{\boldsymbol{r}}_2}{R^3}$ (following [69, p.31]). The interaction arises due to virtual Förster processes, which means that both atoms jump to other levels which have in total a similar energy as the initial state, and then back to the original configuration. As both atoms are coupled by interaction, we need to go to a pair state basis including all nine states $|ij\rangle$, $i,j \in [0,1,2]$. With the assumption $\mathit{\Delta}_F = (E_1 + E_2)/2 \ll 2E_1, 2E_2$, or equivalently $E_1 \approx -E_2$, the states $|11\rangle$,$|01\rangle$,$|10\rangle$,$|02\rangle$,$|20\rangle$ and $|22\rangle$ are far off in energy ($\geq |E_1|, |E_2|$) and can be neglected. The relevant states are now $|00\rangle$,$|12\rangle$,$|21\rangle$. $|12\rangle$ and $|21\rangle$ have the same energy and it turns out that the "dark" state $|d\rangle = 1/\sqrt{2}(|12\rangle - |21\rangle)$ does not couple to $|00\rangle$ with the dipole operator, i.e. $\left\langle d \middle| \hat{V}_{ds} \middle| 00 \right\rangle = 0$, while the "bright" state $|b\rangle = 1/\sqrt{2}(|12\rangle + |21\rangle)$ couples with a factor $\sqrt{2}$ enhanced: $\left\langle b \middle| \hat{V}_{ds} \middle| 00 \right\rangle = \frac{e^2}{4\pi\epsilon_0}\sqrt{2}\left\langle 1 \middle| \hat{\boldsymbol{r}}_1 \middle| 0 \right\rangle \left\langle 2 \middle| \hat{\boldsymbol{r}}_2 \middle| 0 \right\rangle / R^3 = \frac{e^2}{4\pi\epsilon_0}\sqrt{2}d_1 d_2/R^3 = C_3/R^3$. Both results are easily obtained by direct calculation. Here we defined the dipole coupling matrix elements $d_i = \left\langle i \middle| \hat{\boldsymbol{r}}_j \middle| 0 \right\rangle$ and the C_3 coefficient $C_3 = \frac{e^2}{4\pi\epsilon_0}\sqrt{2}d_1 d_2$.

With these preparations the Hamiltonian in the basis $\{|00\rangle, |b\rangle\}$ can be written in matrix form

$$\hat{H}(R) = \begin{pmatrix} 0 & \frac{C_3}{R^3} \\ \frac{C_3}{R^3} & \mathit{\Delta}_F \end{pmatrix}, \tag{3.3}$$

with the so-called Förster defect $\varDelta_F = (E_1 + E_2)/2$. The relevant eigenenergy which is adiabatically connected to energy of $|00\rangle$ in the limit $R \to \infty$ can be calculated to

$$E(R) = -\frac{\varDelta_F}{2}\left(-1 + \sqrt{1 + \frac{4C_3^2}{\varDelta_F^2 R^6}}\right) . \tag{3.4}$$

The energy of the incoming pair state $|00\rangle$ can be approximated in the two limiting cases $R \to \infty$ and $R \to 0$. In the first case one obtains via a series expansion a van der Waals $1/R^6$ potential and in the second case a dipolar $1/R^3$ potential.

The sign of the van der Waals potential is exclusively determined by the sign of the Förster defect $\varDelta_F$. For $\varDelta_F > 0$ it is attractive and for $\varDelta_F < 0$ repulsive. This also leads to the observation that the van der Waals interaction is always attractive for ground states, as the Förster defect will be always positive in this case as all other energy levels have positive energy compared to the ground state and by that also $\varDelta_F > 0$. A repulsive van der Waals interaction is therefore a property that can be only found for excited states.

As discussed above there is a cross-over with distance between the Rydberg atoms between a dipolar potential and a van der Waals potential. Their exact strength is given below.

(a) $R \to \infty$:
$$E(R) \approx -\underbrace{\frac{C_3^2}{\varDelta_F}}_{=:C_6}\frac{1}{R^6}$$

(b) $R \to 0$:
$$E(R) \approx -\operatorname{sign}(\varDelta_F)\frac{C_3}{R^3}$$

One can define a critical radius as the position where the two approximations yield the same interaction energy $R_c = \left(\frac{C_3}{\varDelta_F}\right)^{1/3}$, which gives a coarse estimate up to which distance the $1/R^3$ potential is relevant. At this position the interaction energy is $\varDelta_F$. A Förster resonance occurs, if the detuning $\varDelta_F$ becomes zero. Close to such a resonance the critical radius diverges, which means that the R^{-3} term becomes dominant and the interactions change from van der Waals to dipolar. At large distances beyond R_c also the van der Waals interaction diverges close to the resonance, which allows to tune van der Waals interactions by changing $\varDelta_F$. This is possible in the experiment by shifting the relevant energy levels differentially and is typically done via electric fields, as only moderate electric fields are required due to the high polarizability of the Rydberg levels.

3.2.2. Rydberg blockade

When optically exciting atoms to Rydberg states, the interactions influence the amount of atoms that can be excited. If there are two close-by atoms in the ground-state and one gets excited to the Rydberg state, the Rydberg level of the second atom will be shifted due to the interaction with the first one [1, 2]. If this level shift is now larger

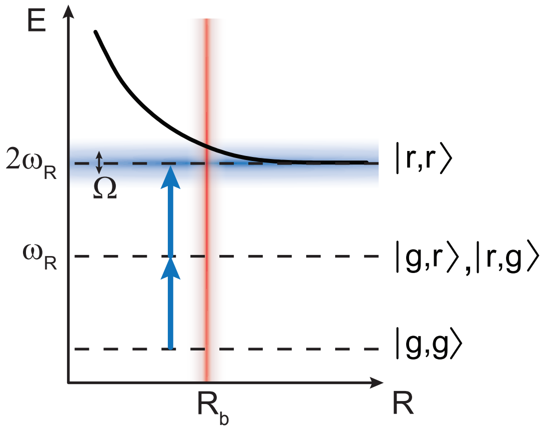

Figure 3.3: Illustration of Rydberg blockade. The picture shows the energy of the pair states $|gg\rangle$, $|rg\rangle$ and $|rr\rangle$ as function of the distance between the two atoms. The doubly excited state $|rr\rangle$ shifts at the blockade radius out of resonance of the Rydberg excitation light.

than the bandwidth of the excitation, the excitation will be off-resonant and will not occur. This leads to the effect that, in a certain range around a Rydberg atom, it is not possible to excite another Rydberg atom without changing the excitation frequency. Typically a stabilized narrow band laser is required for such an experiment.

The phenomenon of Rydberg blockade can be also understood in the pair-state picture (Fig. 3.3). Here the energy shift for several states is shown versus distance of the two atoms. For the state $|gg\rangle$, where both atoms are in the ground state, the energy does not depend on distance. For the state $|rg\rangle$ there is a small dependence if the ground state atom is within the wavefunction of the Rydberg atom, which is negligible on the energy scale discussed here. The picture is very different for the doubly excited state $|rr\rangle$. The energy of this state strongly depends on the distance between the two states (here shown for repulsive interaction). Now it becomes obvious that an excitation laser coupling the states $|gg\rangle$ and $|rg\rangle$ will be only resonant also for the $|rg\rangle \rightarrow |rr\rangle$ transition, if the distance between both atoms is larger than a certain distance. The blockaded volume around a Rydberg atom is given by the condition

$$\frac{C_6}{r^6} > \hbar \max(\Gamma,\Omega)\ . \tag{3.5}$$

For coherent excitation the Rabi frequency needs to be larger than any decay rate, such that the Rabi frequency is typically adjusted to dominate the excitation bandwidth. The distance where the excitation bandwidth equals the interaction shift and is called the blockade radius R_b, which thereby only depends on C_6 and Ω

$$R_\mathrm{b} = \sqrt[6]{\frac{C_6}{\hbar\Omega}}\ . \tag{3.6}$$

The blockade radius is only well-defined in this simple form for an isotropic van der Waals interaction, which is in general not the case (Sec. 4.7). The interaction potential depends on the choice of the Rydberg state, electric and magnetic fields and the relative orientation of the Rydberg atoms. For rubidium S-states the interaction is in general isotropic and repulsive of van der Waals type.

3.3. Coherent collective excitation

Up to now we discussed only effects which can be understood with only two interacting Rydberg atoms. Here we look at a situation where a sample smaller than the blockade radius is optically excited to a Rydberg state.

The relatively long lifetime of Rydberg atoms compared to lower lying electronically excited states allows for the observation of coherent dynamics, in particular Rabi oscillations, on the µs-timescale. The main decoherence sources for the Rydberg states are the Rydberg decay, blackbody radiation, Rydberg-Rydberg interactions (for more than one excited Rydberg atom), motion of the Rydberg atom during excitation and fluctuating electric fields. In most experiments Rydberg atoms are excited with two-photon schemes with off-resonant intermediate state. This leads to additional dephasing mechanisms like light shift noise caused by intensity fluctuations of the two individual laser beams or incoherent scattering at the intermediate state (Appendix C.1). In practice these decoherence sources can be suppressed to allow for the observation of many Rabi cycles [70–72].

The combination of the coherent excitation on the single-particle level with the interactions discussed above, allows for the observation of interesting quantum effects. In the simplest case the whole initial atomic sample is fully blockaded, which means that all atoms are localized in a sphere with diameter much smaller than the blockade radius. If we now excite Rydberg atoms resonantly in this system, we will get at most one Rydberg excitation, as a Rydberg atom on the one edge of the system will still block the excitation at the other end. How does the quantum state look like, if we excite the system globally in a coherent way? As the state with two Rydberg excitations is far off in energy, only basis states are accessible by the excitation which contain exactly one Rydberg excitation at varying positions. As no position of the excitation is energetically favoured, a highly symmetric state of the N atoms is expected. A more detailed investigation shows that only the fully symmetric state, also called W-state, is optically coupled to the ground state [73]. The coupling to this state is enhanced by a factor of $\sqrt{N}$ compared to the single atom Rydberg Rabi frequency $\Omega = \left\langle g_i \middle| \hat{H}_I \middle| r_i \right\rangle / \hbar$, which is easily calculated.

$$\begin{aligned} \hbar\Omega_{\text{collective}} &= \left\langle G \middle| \hat{H}_I \middle| W \right\rangle \\ &= \langle g_1 g_2 ... g_N | \, \hat{H}_I \frac{1}{\sqrt{N}} \sum_{i=1}^{N} | g_1 g_2 ... r_i ... g_N \rangle \\ &= \frac{1}{\sqrt{N}} \sum_{i=1}^{N} \left\langle g_i \middle| \hat{H}_I \middle| r_i \right\rangle \prod_{j=1}^{N-1} \left\langle g_j \middle| \hat{H}_I \middle| g_j \right\rangle \\ &= \sqrt{N} \hbar \Omega \end{aligned} \tag{3.7}$$

Here $|g_1 g_2 ... r_i ... g_N\rangle$ is the basis state in the many-body system where only the atom i is in the Rydberg state and all others in the ground state. The enhanced oscillation frequency has been observed in experiments [72, 74–76]. The situation becomes more complicated if the system is not fully blockaded any more as also basis states with more than one excitation become energetically accessible. One effect of the collective enhancement is the reduction of the blockade radius to ${R_\mathrm{b}}^{\mathrm{collective}} = \sqrt[6]{\frac{C_6}{\hbar\sqrt{N_b}\Omega}} = (N_b)^{-1/12}R_\mathrm{b}$ [77]. Here N_b is the number of atoms within the blockade radius. The scaling looks rather weak, but a change of atom number per blockade radius of a factor of 100 can reduce the blockade radius by around 30 %. For partially blockaded samples models can be found for a better intuitive understanding and approximate calculations. The scaling of various quantities can be derived by a superatom model [78, 79]. Another approach is to treat the system in a basis of Dicke states [80].

3.4. Experimental overview over the field of Rydberg atoms

The field of Rydberg physics has a long history extending far beyond the time of cold atom experiments [1–4, 53, 66, 81]. While the experiments in the beginning were mainly focussed on investigation of Rydberg atom properties by spectroscopic methods, the applications of Rydberg atoms in combination with cold atoms exploded and led to a rapid expansion of the field of Rydberg physics in the last years.

Early experiments The field started with the observation of Rydberg that the lines in atoms follow a scaling with the principal quantum number [56–58]. The large Rydberg wavefunction overlapping with ground state atoms leads to line broadening and shifts, which have been observed in spectroscopy [82, 83]. With dye lasers systematic spectroscopy of Rydberg states became possible [84].

Spectroscopy in glass cells Rydberg spectroscopy in glass cells was one of the first techniques to measure properties of Rydberg atoms. But recently it turned out that even (nearly) Doppler-free spectroscopy of Rydberg atoms is possible in room-temperature glass cells and can be exploited without need for cooling the atoms.

A field that started with spectroscopy in glass cells is Rydberg electromagnetically induced transparency (EIT). The employed two-photon scheme is an almost Doppler free technique for high-resolution Rydberg spectroscopy at room temperature [85]. It has been used to measure the absolute line position of Rydberg states [86] and the hyperfine splitting [87]. Rydberg EIT-spectroscopy became widely used and also has direct applications in electrometry [88]. Recently the technique was also applied in cold atom clouds and has become a good candidate for photon-photon gates (Sec. 3.4.1). The coherence time of Rydberg atoms in gases at or above room temperature is rather short, but it is possible to reach high enough Rabi frequency with pulsed lasers to even show coherent manipulation [89, 90].

Rydberg atoms for microwave photon manipulation and detection Rydberg atoms also enabled the implementation of the challenging idea to employ circular Rydberg states to implement non-demolition measurements of photons [91, 92]. The technique allowed preparation and non-destructive detection of photon states in microwave resonators and was awarded the 2012 Nobel price [93]. The high polarizability of Rydberg atoms that allows to detect single photons can also be exploited to build highly sensitive detector for microwave radiation [94].

Evidence for Rydberg blockade Due to the low thermal movement and low Doppler shift when using cold atoms, it becomes possible to investigate Rydberg blockade. The experimental interest was triggered by proposals how to exploit the Rydberg blockade for two-qubit quantum gates [73, 95], one of the main challenges for neutral atom quantum information processing. First evidence for blockade physics was found by line broadening and saturation of the number of excitations depending on interaction strength [96, 97]. The same physics can be also probed by double-resonance spectroscopy [98, 99]. The very clean experiments with exactly two single atoms interacting while being excited to the Rydberg state [74, 100] showed coherent manipulation of qubits on the Rydberg transition and Rydberg blockade. A two-qubit quantum gate as well as entanglement were demonstrated in the subsequent experiments [101, 102]. Recently also the strength of the van der Waals interaction was measured quantitatively in dependence of the distance of two atoms [103, 104] as well as the anisotropic interaction of D-states [105].

Sub-Poissonian statistics in the excitation Another evidence for Rydberg blockade can be found by looking at the probability distribution of the number of Rydberg atoms $\hat{N}_\mathrm{e}$ excited in a cloud. Historically the distribution function is often characterized by the so-called Mandel Q factor [106, 107] defined as $Q = \frac{\langle \hat{N}_\mathrm{e}{}^2 \rangle - \langle \hat{N}_\mathrm{e} \rangle^2}{\langle \hat{N}_\mathrm{e} \rangle} - 1$, which becomes -1 for a Fock state and 0 for a Poissonian distribution. Due to the blockade radius the number of excitations saturates to a value determined by the volume of the cloud and the blockade radius, leading to a sub-Poissonian counting statistics [108–112]. More systematic studies show the strong dependence of the counting statistics on detuning and Rabi frequency [113, 114] and support the idea of locally ordered patterns in the gas [115].

Microwave spectroscopy As the coupling between Rydberg states is very strong due to their larger dipole moment, Rydberg-Rydberg level transitions are a promising field of study. The transitions lie typically in the few to hundred GHz range and are accessible for example by frequency multiplied microwave sources. There is a long history of microwave spectroscopy on Rydberg atoms, as this type of spectroscopy can be performed in thermal gases and does not require narrow-band Rydberg excitation lasers, because the spectroscopy resolution is determined by the stability of the microwave [59, 116–126]. At some point the observed linewidth is still limited by excitation-scheme independent sources like electric and magnetic stray fields. Microwave fields can also be used to manipulate Rydberg polaritons [127] and could allow for the implementation of a photon quantum gate based on Rydberg polaritons [128].

Rydberg-state mixing by microwaves The possibility to strongly couple Rydberg states via microwaves in absence of strong recoil effects, enables the implementation of schemes which mix Rydberg states via electromagnetic coupling and tune their properties [129–134]. This technique can be used, for example, to eliminate the Stark effect of a certain level by mixing in properties of nearby states [134].

Förster resonances The already strong interactions between Rydberg atoms become even larger nearby Förster resonances [135, 136]. They occur when the energy of a pair of Rydberg states equals the energy of another pair that is coupled to the first one, leading to a possible oscillation between the two coupled pairs. The existence of such resonances at or close to electric zero-field depends on the element-dependent quantum defects. The number of Rydberg states with Förster resonances at zero field is rather low, but often they can be tuned into resonance via electric fields. Förster resonances have been observed [137–139] and also coherence of the interaction has been shown [140, 141]. Förster resonances lead to exchange processes between the two Rydberg states in the two near-resonant pair states [142, 143]. Recently also coherent oscillations caused by the Förster exchange processes have been observed with two atoms [144]. These exchange processes can also lead to a spreading of the Rydberg excitations in presence of other coupled Rydberg atoms [145]. As an extension to the normal Förster process, which leads to a two-body interaction, also four-body interactions have been observed [146].

Trapping of Rydberg atoms In most Rydberg experiments with cold atoms the Rydberg atoms are not trapped. In many cases the movement of the Rydberg atoms during the experiment is negligible and they are anyway ionized and detected afterwards, such that trapping is not relevant. But in the quantum information experiments [1] or experiments with optical detection of Rydberg atoms trapping would be advantageous. Due to their vastly different properties than ground state atoms, it is hard to trap Rydberg atoms in the same traps as ground state atoms. There have been many proposals for Rydberg trapping [147–152]. Of special interest is magic optical trapping, which means that the trapping potential is the same for ground state and Rydberg state. This allows for Rydberg excitations in the trap without excess heating or loss [150, 153]. Magnetic [154], electrostatic [155], optical [156, 157] and magic optical [158] trapping have been successfully demonstrated. While magnetic and electrostatic trapping require rather specialized setups, the optical trapping is generally applicable in cold atom experiments. The absolute value of the so called ponderomotive shift of Rydberg levels in presence of light fields was confirmed in experiments [159, 160].

Quantum information with Rydberg atoms Rydberg atoms offer strong and switchable interactions, which makes them good candidates to implement two-qubit quantum gates [1, 73, 95, 161–163]. A digital quantum computer based on Rydberg atoms could use single atoms in isolated micro traps [1, 164]. Single-qubit rotations can be implemented by addressing the atoms with Raman lasers with a resolution better than the blockade radius [165]. The implementation of gates exploits the strong interaction between Rydberg atoms, which is from a theoretical point of view ideally suited for this purpose. The well-known CNOT-gate has been implemented with locally addressed Rydberg lasers [101], the preparation of bell pairs also works with global excitation to the Rydberg state [102]. Currently the main challenges are the improvement of fidelity and the scalability of these systems. In the first experiments the fidelity is limited by movement of the Rydberg atoms, which can be reduced by trapping of the Rydberg atoms [158]. Other improvements are to reach high Rabi frequencies for faster gates, or cool the atoms close to the ground state of the traps [166, 167]. Also a compensation of light shifts caused by the trap is desirable. The scaling of the number of micro traps is straightforward, but it becomes hard to reach uniform trapping conditions over the array of traps and load exactly one atom into each trap. Arrays of micro traps for neutral atoms have been implemented [168], also with equal trapping for ground and Rydberg state [150, 158]. The sub-Poissonian loading of the traps in such arrays is possible and a probability for a single atom of $50-80\,\%$ has been reached [47, 168, 169], but deterministic loading has remained illusive up to now.

Many-body effects The strong interactions between Rydberg atoms lead to spatial correlations in these many-body systems. In many experiments no spatial resolution is available, but already the line shape of a resonance can give strong indications of collective excitation effects [170–173]. Many-body effects were also found in the Rydberg excitation of a BEC [174]. A striking signal for collective excitation are the $\sqrt{N}$ enhanced Rabi oscillations in fully blockaded clouds. They have been measured via the extracted photons [75], but also directly by detection of the atoms [76]. For two atoms the post-selection on exactly two atoms was performed [72, 74, 76], which enables very good knowledge about the initial state. The observation of coherence in not fully blockaded samples is difficult due to the strong dephasing, but has been achieved [70, 175–179]. Another interesting direction is the spontaneous ordering emerging in these system [115, 180–182] (see also Chapters 6, 7).

3.4.1. New directions

In the following an overview is given over recent developments in the field of Rydberg physics, demonstrating the broad range of physics that can be accessed using Rydberg atoms.

Alkaline earth atoms In alkaline earth-like atoms the Rydberg transitions for both outer electrons are accessible to laser-excitation, which enables the investigation of other interesting effects like auto-ionizing states. Another technique that becomes available is the optical imaging of Rydberg atoms, where only one of the electrons is in a Rydberg state, on the second transition [183, 184]. Another advantage are the available narrow lines and meta-stable states, which allow for experiments involving Rydberg atoms which are not possible with alkali atoms. A meta-stable state can be used as a second optically resolved state to store information. This is not possible in alkali atoms where all electronically excited states decay very fast and only Rydberg atoms allow for only short storage times. The advantage of narrow lines as intermediate states for two-photon excitation schemes is the reduced intermediate state scattering rate.

Rydberg molecules The interaction between the Rydberg electron and neutral ground state atoms can lead to bound states of the ground state atoms in the Rydberg wavefunction. These Rydberg molecules have very large binding length and exotic properties [185]. They are typically detected as additional resonances close to the non-interacting Rydberg resonance [186–190]. Further experiments even allowed to measure coherence in the formation of these short-lived molecules [191] and their properties [192, 193]. When going up in the principal quantum number the binding energies of the Rydberg molecules decrease and in the limit of high quantum number this leads to a mean field broadening and shift of the Rydberg line [194].

Rydberg electrons used for electron-atom scattering With the recent experiments in mind looking at the interaction of a single ion with an ultracold cloud, a Rydberg atom can be seen as an electron trapping an ion. The electron can be that far away from the ion that one could look at an ion interacting with an ultracold atomic cloud without actual ion trap. The other way around the heavy ion is trapping the electron, which allows for the investigation of the interaction of an electron with a Bose-Einstein condensate [60]. These ideas allow to probe low-energy electron-atom scattering and might enable the imaging of the spatial wavefunction of the Rydberg electron [195].

Photon-photon interactions The development in the field of Rydberg-EIT led to the conclusion that Rydberg system are close to ideal to create photon-photon interactions mediated by Rydberg-Rydberg interactions [196]. A first step in this direction was the implementation of a single photon source on the basis of Rydberg blockade [197]. Strong correlation between polaritons led to an anti-correlated photon chain [198]. Such a system also allows for the engineering of effective attractive interactions between photons travelling as polaritons through a Rydberg medium [199]. Rydberg atoms also allowed for the implementation of a switch, which can be flipped with a single photon [200, 201]. Rydberg atoms can also act as an interface between photon-encoded qubits and atomic storage qubits due to the large possible optical depth [202, 203].

Optical Rydberg dressing One of the next big steps for ultracold quantum gases is to control and study long-range interactions in these systems on motional timescales. There are many proposals to admix Rydberg states to the ground state via off-resonant optical coupling. Up to now there was no experimental evidence for the so-called Rydberg dressing, due to limitations by scattering and light-shifts [160, 204]. A first step might be to observe spin squeezing in a Rydberg-dressed sample [205]. Currently the most promising routes are the one-photon dressing with UV-light for alkali atoms or dressing of alkaline-earth atoms from meta-stable states or via narrow transitions.

3.4.2. Summary

The first Rydberg experiments were mainly focussing on spectroscopy and the investigation of the properties of Rydberg atoms. Based on this knowledge it turned out later that interesting many-body physics, many-particle interactions and even photon-photon interactions can be implemented with the help of Rydberg atoms. Rydberg atoms can be used as a tool to implement fundamental Hamiltonians in quantum many-body systems and have the potential to realize controlled long-range interactions in many-body systems. Due to the variety of Rydberg states it is possible to select the Rydberg state which is most suited for an experiment, but this requires the detailed knowledge of their various properties, which are discussed in the next chapter.

4. Calculation of Rydberg atom properties

Many properties of alkali-metal Rydberg atoms can be calculated in the framework of quantum defect theory [206, 207]. Using the experimentally determined quantum defects and a fitted model potential, it is possible the calculate most of the properties of Rydberg atoms without big effort to a reasonable accuracy. There are, of course, more involved schemes (e.g. [208–210]), but for our purposes the standard calculations will be sufficient.

In this chapter we will calculate some of the interesting Rydberg properties based on the Marinescu model potential [211] and experimentally determined quantum defects ([86] for S and D states and [119, 212] for nP states assuming that the difference between ^{85}Rb and ^{87}Rb quantum defects is negligible). Although the calculations are a bit technical, it is important to be sure about the values of the parameters, which are not easily measured, but very important for design of experiments and choice of Rydberg states. We will compare the obtained numbers to other calculations in literature. Atomic units are used for the calculations if not stated otherwise ($e = m_e = \hbar = \frac{1}{4\pi\epsilon_0} = 1$).

4.1. Wavefunctions and radial matrix elements

For alkali-metal Rydberg atoms, all interesting properties can be calculated, if the wavefunction of the outer electron is known. The problem can be reduced to the calculation of the radial wavefunction and is often treated by a semi-empirical approach introducing an effective radial potential caused by the inner electrons and quantum defects which determine the energy levels. Such a technique requires some spectroscopy input, but yields very good results with far less computational effort than other techniques. Once the radial wavefunctions are known, all properties can be derived, in particular the radial matrix elements which determine the coupling strength between different energy levels. The spatial wavefunction of the Rydberg atoms is not significantly different for varying isotopes. This leads to essentially indistinguishable wavefunctions and quantum defects as well as radial matrix elements for both rubidium isotopes. But there are small differences, mainly in the hyperfine structure and small corrections due to the mass difference.

4.1.1. Quantum defects

The main idea of quantum defect theory is to predict properties of atoms by using a semi-empirical approach and fitting the Rydberg formula to the energy levels by introducing a state-dependent correction to the principal quantum number, which is known as quantum defect. This technique has been widely used to investigate complicated level structures [213–215] and is in particular successful in the application to Rydberg states, as the predictions are very precise in this case.

For the determination of quantum defects of Rydberg atoms the energy levels of many Rydberg states are typically measured either via optical spectroscopy [86, 212, 216–218] or microwave spectroscopy [119, 123]. A collection of references to measurements of quantum defects of rubidium is shown in Table 4.1. There are different model functions to fit the quantum defects, typically the function $\delta(n) = \delta_0 + \delta_2/(n - \delta_0)^2$ with the free parameters δ_0 and δ_2 that only depend on l and j is sufficient to fit the experimental data with good accuracy [86, 119]. It turns out that the quantum defects depend strongly on the azimuthal quantum number l for $l \leq 2$, at higher l the overlap of the wavefunction with the core becomes negligible and the quantum defects essentially vanish. The dependence on j is typically rather weak, but still relevant for high-resolution spectroscopy.

4.1.2. Model potential

The radial wavefunctions of alkali-metal Rydberg atoms look like hydrogen wavefunctions. For the outer electrons the positive ion constitutes a perturbation of the $1/r$ potential. The perturbed potential is approximated by a model potential, which is chosen in a way to reproduce the experimentally measured quantum defects. The radial wavefunction is then determined via numerical integration from large r towards $r = 0$ [219].

There are several approaches to find appropriate model potentials. The potential by Marinescu *et al.* [211] is widely used. But also the potential [220] yields the same matrix elements within error bars for the calculations in this thesis. Depending on the targeted accuracy of the calculation various correction terms can be taken into account. The spin-orbit coupling can be also considered explicitly [221], here we could not see any effect of this correction on the order of the error bars based on the variation of quantum defects from different sources.

The calculations here are based on Marinescu *et al.*, [211, eq. (18)]. The potential

isotope	states	reference
^{87}Rb	S,D	[86] (used here)
^{87}Rb	S,D	[217]
^{85}Rb	P	[212]
^{85}Rb, ^{87}Rb	S,P,D	[119]
^{85}Rb	S	[216]
^{85}Rb	F,G	[123]
^{85}Rb	G	[121]
^{85}Rb	$P_{3/2}$	[218]

Table 4.1.: Quantum defect measurements and calculations for rubidium.

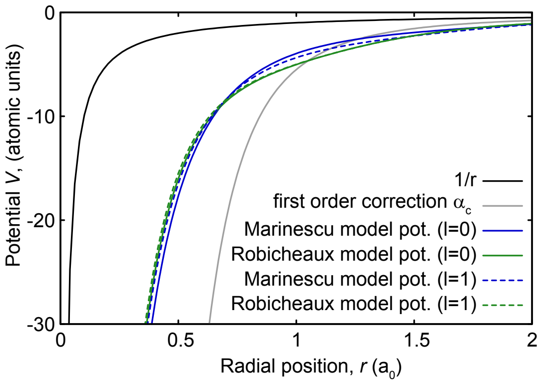

Figure 4.1.: Comparison of model potentials. The simplest correction of the Coulomb potential (black line) is the inclusion of the core polarizability α_c, which corrects the potential at larger r. Shorter distance corrections are introduced by model potentials.

is implemented as a modified Coulomb potential with additional free parameters to fit it to experimental data.

$$\begin{aligned} -\frac{Z}{r} \to -\frac{Z_l(r)}{r} - \frac{\alpha_c}{2r^4}\left(1 - \exp\left(-\frac{r^6}{r_c^6}\right)\right) \\ Z_l(r) = 1 + (Z-1)\exp(-a_1 r) - r(a_3 + a_4 r)\exp(-a_2 r) \\ \text{with } \alpha_c = 9.0760 \text{ for } {}^{87}\text{Rb} \end{aligned} \tag{4.1}$$

The model potential deviates only for small distances from the Coulomb potential and a comparison is shown in Fig. 4.1. For reference the normal $1/r$ potential is depicted, then the first order correction which just takes into account the core polarization and finally the two model potentials, which are quite similar and slightly depend on l.

	$l = 0$	$l = 1$	$l = 2$	$l \geq 3$
a_1	3.69628474	4.44088978	3.78717363	2.39848933
a_2	1.64915255	1.92828831	1.57027864	1.76810544
a_3	-9.86069196	-16.79597770	-11.65588970	-12.07106780
a_4	0.19579987	-0.81633314	0.52942835	0.77256589
r_c	1.66242117	1.50195124	4.86851938	4.79831327

Table 4.2.: Model potential parameters by Marinescu *et al.* Parameters for the model potential Eq. (4.1.2) for rubidium [211].

4.1.3. Computation of radial wavefunctions using the Numerov algorithm

The calculation of the radial wavefunctions requires the integration of the radial differential equation [61]. A very efficient technique for this type of differential equation is the Numerov algorithm [222, 223]. This technique is widely used for the calculation of radial wavefunctions [224–230].

The Numerov method is an integration technique that is very efficient for differential equations of the special second-order form

$$\frac{d^2}{dx^2}\phi = g(x)\phi \ . \tag{4.2}$$

The main problem using the Numerov algorithm is where to start with the integration. It turns out the best way is to begin at a large distance from the core where the wavefunction is known to vanish and then integrate towards the centre. As the wavefunctions drop exponentially for large distances, they are essentially zero at some point, and it becomes possible to just start the integration with zero and a small value (e.g. $1 \cdot 10^{-10}$) as neighbouring value towards the centre. If the starting point is too far out, it might happen that the exponential increase during the integration leads to problems in the numerics if the values get too large. This problem can be solved by rescaling the wavefunction during the integration. The absolute value gets lost using this technique, but the scaling of the wavefunction is anyhow determined by the normalization condition in the end.

The integration formula is then given by [224]

$$\phi_{n-1} = \frac{2\phi_n - \phi_{n+1} + \frac{h^2}{12}\left(10 g_n \phi_n + g_{n+1}\phi_{n+1}\right)}{1 - \frac{h^2}{12} g_{n-1}} \tag{4.3}$$

with

$$\begin{aligned} \phi_{\text{end}} &= 0 \\ \phi_{\text{end}-1} &= 10^{-10} \ . \end{aligned} \tag{4.4}$$

Depending on the radial potential the calculated wavefunction will diverge close the nucleus at $r = 0$. This can be avoided by just using some cut-off and ignore the inner part of the wavefunction. As the wavefunction is oscillating fast in this relatively small volume the contribution to the matrix element is negligible. This has been also checked numerically [225]. The cut-off error is typically below the systematic error of this approach. Here we use the square root scaling as used in [225], which has the advantage to avoid numeric problems during integration due to fast oscillating parts in the wavefunction and allows high accuracy already for quite large step sizes. A detailed derivation of the radial differential equation as well as the transformation of the wavefunctions can be found in the Appendix B.2. The numerical integration was checked against the analytical hydrogen wavefunction (Fig. 4.2) and within the numeric precision no deviation was found. In Fig. 4.3 we compare the scaled wavefunction $\chi(u)$ of ^{87}Rb with the hydrogen wavefunction. This directly shows the

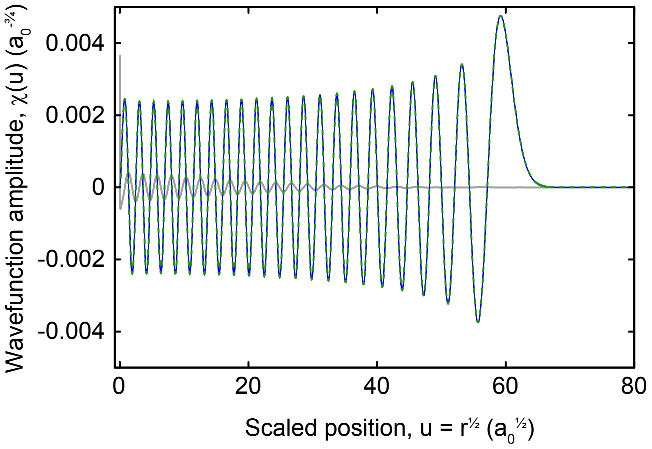

Figure 4.2.: Check of the numerical accuracy of the Numerov algorithm with hydrogen. The analytic scaled wavefunction $\chi(u)$ of 43S hydrogen (green dashed line) is compared with the Numerov result (blue line). The step size for the Numerov calculation is 0.002 and the inner cut-off 0.02. The difference between both curves multiplied by 10^9 (grey line) shows a starting divergence shortly before the cut-off. The Numerov algorithm is performing very well for this differential equation and also much faster than the direct evaluation of the analytical solution.

effects of the corrections of the quantum defects together with the model potential. The main effect is a radial shift of the phase of the oscillation in the probability density and a reduction of the most probable distance of the electron from the core. By transformation of the wavefunction back to physical coordinates also the radial probability distribution of the electron can be calculated which gives a more intuitive view on the wavefunction (Fig. 4.4). The distribution shows that the electron in the 43S Rydberg state is most probably in a thin shell at a certain distance from the core and only with very small probability near the nucleus.

4.1.4. Comparison of the calculated radial matrix elements with literature

To check the calculation of the wavefunctions one can compare the resulting radial matrix elements with measurements and other calculations. In contrast to wavefunctions, numbers for radial matrix elements are given in many publications. There are two regimes, which have to be checked. One is the overlap between Rydberg states, where the quantum defect calculation is expected to be quite precise, and the other the overlap between the ground or intermediate state of the excitation to the Rydberg state. For the second case the quantum defect approach is not the optimal technique, but in many cases reasonable results can be obtained.

The radial matrix elements are directly calculated from the radial wavefunctions $R_{nl}(r)$ by $\mathcal{R}^{nl}_{n'l'} = \int_0^\infty R^*_{n'l'}(r) r R_{nl} r^2 dr$ (Eq. (B.10) for $k = 1$). The calculation of dipole matrix elements was also checked against hydrogen, where they can be com-

Figure 4.3: Comparison of scaled wavefunctions $\chi(u)$ for the 43S state in hydrogen and rubidium. The analytic hydrogen wavefunction for 43S (green line) is shown together with the 43S wavefunction of rubidium-87 (blue line). The difference between both wavefunctions (grey line) shows that the corrections for ^{87}Rb lead essentially to a radial phase shift. Additionally there is some radial shift of the maximum.

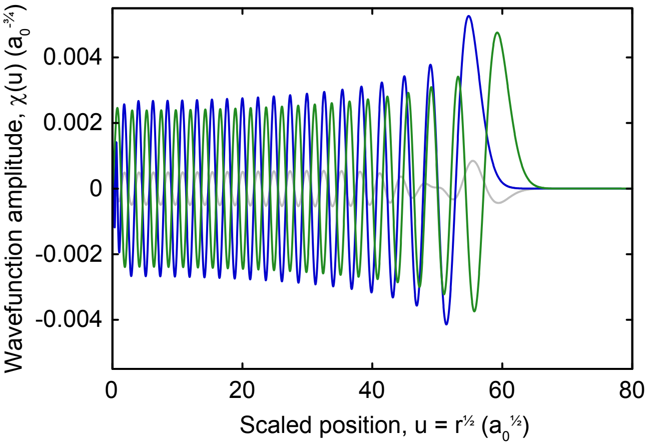

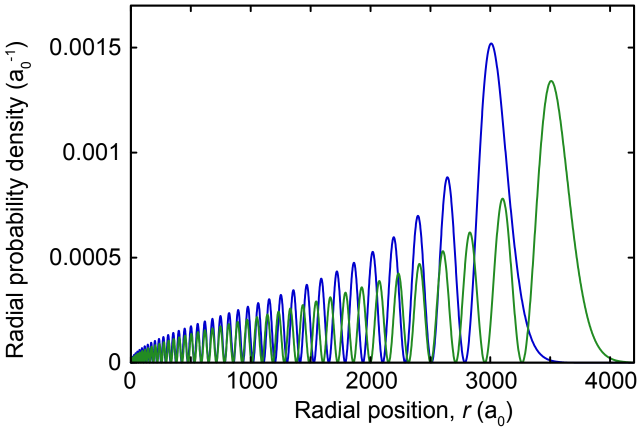

Figure 4.4.: Comparison of the radial probability distribution of the electron for 43S in hydrogen and rubidium. Here we compare the analytical 43S wavefunction for hydrogen (green line) with the numeric 43S rubidium-87 wavefunction calculated using the Numerov algorithm. The radial probability density $r^2 R_{nl}^2$ directly shows the probability to find the electron at a certain distance r from the core. The orbit radius $\langle r \rangle$ of the 43S state is $2384\,\mathrm{a}_0$ and $2774\,\mathrm{a}_0$ for rubidium and hydrogen, respectively.

puted analytically (e.g. [229, p.121][231]). The 1S → nS transitions show very good agreement and only numerical deviations of $< 10^{-9}$ in atomic units. The matrix elements are also compared to experimentally measured matrix elements [208, 232–234]. A comparison with selected matrix elements appearing in various publications shows reasonable agreement of matrix elements of low-lying states to Rydberg states (upper half of Table B.3) and good agreement for matrix elements between Rydberg levels (lower part of Table B.3). There is also quite good agreement with measurements of $5P_{3/2}$ to $nD_{5/2}$ transitions (Table B.2).

For future direct UV-excitation of Rydberg atoms also the calculation and measurement of 5S to nP transitions was investigated (Table B.1). The calculations based on quantum defect theory become by construction more and more inaccurate for lower lying states and are worst for the ground state, but still provide a reasonable guess for the matrix elements. To compare to experimental matrix elements in earlier publications, which are given as oscillator strength, we need to do a conversion. The radial matrix elements can be calculated from the oscillator strengths between a lower level i and an upper level k via $f_{ik} = \frac{2}{3}\frac{\mathit{\Delta} E}{g_i} \left|\langle nlj \mid er \mid n'l'j'\rangle\right|^2$ with the degeneracy of the lower level of the atomic transition $g_i = 2j + 1$ and $\mathit{\Delta} E$ measured in Hartree energies ($E_h = \frac{\hbar^2}{m_e a_0^2}$) [235]. It turns out that the matrix elements from 5S to nP states calculated here are about a factor of two larger than the ones calculated with more sophisticated techniques, which is probably caused by the bad approximation of the 5S ground state by the quantum defect wavefunction.

4.1.5. Scaling of the radial matrix elements

For practical purposes the matrix elements can be approximated by fitting the scaling law (Table 3.1) to the calculated matrix elements, which reduces the information about the matrix elements of a whole series of Rydberg states to a single number.

The radial matrix elements of a low lying state to a series of Rydberg states scale as $(n^*)^{-3/2}$ (Sec. 3.1).

$$\mathcal{R}_{nlj}^{|i\rangle} \approx C_{lj}^{|i\rangle}\,(n^*)^{-3/2} \tag{4.5}$$

The scaling coefficient $C_{lj}^{|i\rangle}$ depends on the initial state $|i\rangle$ and the l and j quantum number of the Rydberg target state. The scalings were fitted to calculations discussed in the previous sections for relevant transitions in ^{87}Rb and are summarized in Table B.4. The most relevant scaling coefficients 5P → nS, nD could be checked to be consistent with other calculations (Table B.5). The summary shows that the matrix elements 5S → nP are relatively small, but the matrix elements increase rapidly when starting from excited states like 5P, 6P or 7P to a Rydberg state. Considering only the upper transition in a two-photon excitation the 6P state becomes already favourable as intermediate state due to the larger matrix element compared to the 5P state.

4.2. Static polarizability

Compared to ground state atoms, where the static polarizability is negligible for ambient electric fields for most purposes, the static polarizability of Rydberg atoms can be extremely high due to the scaling with $(n^*)^7$ (Sec. 3.1). The level shift ΔE due to static electric fields can be directly calculated from the radial matrix elements above for non-degenerate states [236, p.213] and is given by:

$$\begin{aligned} \Delta E &= -\frac{1}{2}\alpha \cdot E_z^2 \\ \alpha &= 2 \cdot e^2 \sum_{n,l,m \neq n',l',m'} \frac{|\langle n'l'm'|z|nlm\rangle|^2}{E_{n',l',m'} - E_{n,l,m}} \end{aligned} \tag{4.6}$$

Here E is the static electric field, which is supposed to be aligned with the z-axis. If there is no other quantization axis like a magnetic field present this choice is always possible. In general Rydberg states, which are isolated in frequency due to a non-zero quantum defect, show a quadratic Stark effect, while (nearly) degenerate levels like states with $l > 2$ in rubidium, shift linear with the electric field [224]. The polarizabilities have a simple scaling with n^* for different states. This allows to determine coefficients for the scaling laws, which has been done for all relevant levels in rubidium [230, p.24]. For example the calculation for the S-states leads to $\alpha_0 = 2.188 \cdot 10^{-9}(n^*)^6 + 5.486 \cdot 10^{-11}(n^*)^7$, which is close to the values obtained from a fit to experimental data: $\alpha_0 = 2.202 \cdot 10^{-9}(n^*)^6 + 5.53 \cdot 10^{-11}(n^*)^7$ [237]. This yields $-17.7\,\mathrm{MHz}/(\mathrm{V/cm})^2$ for the $n = 43$ state ($n^* = 39.87$) of ^{87}Rb, which means that already background electric fields on the order of $100\,\mathrm{mV/cm}$ cause a measurable shift of the Rydberg line.

4.3. Dynamical polarizability and trapping

The forces of Rydberg atoms in far-detuned light fields can be described by the so-called ponderomotive potential of a free electron in a light field, which is a quite good approximation for Rydberg states [147, 149, 238, 239]. The ponderomotive force on electrons is always repulsive, independent of the properties of the laser field.

$$h\nu_{ls} = \frac{e^2 I}{2 m_e \epsilon_0 c (2\pi\nu_L)^2} \tag{4.7}$$

Here ν_{ls} is the light shift measured in Hertz and I is the intensity of the laser field of frequency ν_L. It has been confirmed in experiments [159, 160, 238] that this model gives a good approximation for the forces on Rydberg atoms in laser fields. Due to the large extent of Rydberg atoms, the ponderomotive force has to be averaged over the wavefunction of the electron. This leads for Rydberg atoms to a state-dependence of the ponderomotive potential [156]. Looking at the averaging effect, it turns out that the effective force on Rydberg atoms can change sign in optical lattices for large principal quantum number. This is discussed in the following.

Calculating the tune-out wavelength

In an optical lattice potential the size of the Rydberg atoms with respect to the lattice spacing is typically not negligible and leads effectively to an averaging of the potential

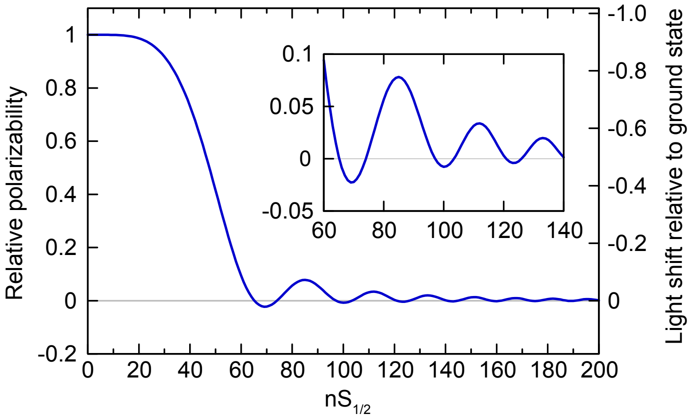

Figure 4.5.: Averaging of the polarizability in a 1064 nm lattice for ^{87}Rb S-states. Due to the large extent of Rydberg atoms compared to the lattice spacing, the polarizability averages over the outer electron wavefunction. Shown here is the relative polarizability of a Rydberg atom in the lattice compared to a homogeneous field. The precise value for 43S is 0.648 . On the second axis the light shift of the Rydberg state compared to the $5S_{1/2}$ ground state is depicted. There are zero-crossings in the relative polarizability for n between 65/66,74/75,97/98,103/104,120/121 and the minima at 69,100,123,143,160,... . The inset shows a magnified view of the region of the first zero crossings and extrema.

over the wavefunction of the Rydberg electron [152]. This averaging effect can be explicitly calculated from the calculated radial wavefunctions. For a retro-reflected lattice with a laser of wavelength λ, the modulation factor is $\langle\cos(2kz)\rangle$, where $k = \frac{2\pi}{\lambda}$ and z is the linear position of the electron along the lattice. For S-states the angular integral can be evaluated analytically to $\int_0^\pi R^*(r)R(r)\cos(2kr)\cos(\theta)d\theta = |R(r)|^2\,\frac{\sin(2kr)}{kr}$. To evaluate the radial integral numerically using the previously determined scaled wavefunctions $\chi(u)$ (Appendix B.2), the integral can be transformed to

$$\langle\cos(2kz)\rangle = \int\limits_0^\infty |\chi(u)|^2\,\frac{\sin(2ku^2)}{ku^2}2u^2du\ . \tag{4.8}$$

In Fig. 4.5 we show the effect of the averaging for the relevant experimental parameters in our setup. As can be seen in the graph, the trapping force decreases for S-states with larger principal quantum number and there are some oscillations around zero. Interestingly, there are zero-crossings at which the Rydberg atom are nearly not affected by the light field as well as minima. For example the 69S state would be an interesting candidate for a state to look at in the experiment, as it experiences the strongest trapping force, which should lead to an enhanced detection efficiency as discussed in Sec. 5.6.5. The trapping force that can be reached in this way is very small in comparison to typical trapping forces on the ground state.

4.4. Calculation of Rabi frequencies

The calculation of Rabi frequencies often leads to confusion due to varying notation and lack of reliable reference values [240]. The calculations here follow the derivation by King [241]. Depending on whether the Rabi frequency is needed in fine or hyperfine coupling basis we use [241, eq. (49)] or [241, eq. (52)]. The radial integral $\mathcal{R}^{nl}_{n'l'} = \int R^*_{n'l'}(r) r R_{nl}(r) r^2 dr$ can be calculated directly from the radial wavefunction. There is also a small dependence on j here, which is omitted in the notation. The radial wavefunction R_{nl} is defined via: $H\psi_{nlm} = E_{nl}\psi_{nlm}$ with $\psi_{nlm}(r,\theta,\phi) = R_{nl}(r) Y_l^m(\theta,\phi)$, where $Y_l^m(\theta,\phi)$ are the spherical harmonics [61]. The following formula demonstrates that the radial overlap integral is the only other atomic parameter next to the quantum numbers required to directly calculate the Rabi frequency [241, eq. (52)]:

$$\Omega_{e\leftarrow g} = \frac{eE_0}{\hbar}(-1)^{2F'+I'+2j+l_>+s'-m'_F}\mathcal{R}^{nl}_{n'l'}\sqrt{(l_>)(2j'+1)(2j+1)(2F'+1)(2F+1)}\cdot \\ \begin{Bmatrix} l' & 1 & l \\ j & s' & j' \end{Bmatrix}\begin{Bmatrix} j' & 1 & j \\ F & I' & F' \end{Bmatrix}\sum_q \epsilon^q \begin{pmatrix} F' & 1 & F \\ -m'_F & q & m_F \end{pmatrix} \tag{4.9}$$

with $E_0 = \sqrt{\frac{2I}{c\epsilon_0}}$ and $l_> = \max(l,l')$. This formula starts out directly with the radial matrix element $\mathcal{R}^{nl}_{n'l'}$, which can be calculated as discussed above (Sec. 4.1.4). For some states, there are also measured values for these radial matrix elements, for example for the 5S ↔ 5P transition it can be extracted to $\mathcal{R}^{5\mathrm{S}}_{5\mathrm{P}} = 5.181(4)$ (Sec. J.1).

Light shifts

The Rabi frequency calculation between all dipole transitions in an atom can be also used to calculate the light shifts caused by laser fields. Assuming that all level shifts are independent, one can calculate the light shift for every pair of states using the Rabi frequency and then add up the shifts. A full diagonalization in a two-level system yields $\mathrm{sign}(\Delta)\frac{\sqrt{\Omega^2+\Delta^2}}{2} - \Delta/2 \approx \frac{\Omega^2}{4\Delta}$, where the approximation holds in the limit $\Delta \gg \Omega$. By that light shifts are easily derived from the Rabi frequency calculation.

4.5. Calculation of the natural linewidth

The natural linewidth of a transition can be calculated conveniently using the formulas [241, eq. (37) and (48)]. As a reminder we note that $A_{g\leftarrow e} = \Gamma_{g\leftarrow e} = 2\pi \cdot \Delta\nu = 1/\tau_{g\leftarrow e}$, where $\tau_{g\leftarrow e}$ is the lifetime and $\Delta\nu$ the FWHM linewidth of the corresponding transition. $\tau_{g\leftarrow e}$ is the lifetime of the upper level, if there is only this one decay channel.

$$\begin{aligned}\Gamma = A_{g\leftarrow e} = A_{|nlj\rangle \leftarrow |n'l'j'm'\rangle} &= \frac{e^2\omega_0^3}{3\pi\epsilon_0\hbar c^3}\,|\langle e\,|\,\hat{r}\,|\,g\rangle|^2 \\ &= \frac{e^2\omega_0^3}{3\pi\epsilon_0\hbar c^3}\cdot\frac{1}{2j'+1}\left|\left\langle n'j'\,\middle|\,\hat{r}C^{(1)}\,\middle|\,nj\right\rangle\right|^2 \\ &= \frac{e^2\omega_0^3}{3\pi\epsilon_0\hbar c^3}\cdot(l_>)(2j+1)\left|\mathcal{R}_{nl}^{n'l'}\begin{Bmatrix} l' & 1 & l \\ j & s' & j'\end{Bmatrix}\right|^2\end{aligned} \tag{4.10}$$

4.6. Rydberg lifetimes

Rydberg lifetimes for rubidium have been calculated [64, 221] and measured [244–246]. The lifetimes can be calculated in good approximation via a scaling formula for all alkali-metal atoms [64]. These values are in good agreement with the measurements of Branden *et al.* [245]. The lifetime of Rydberg atoms is not exclusively determined by the radiative decay of the state directly to lower states, but also limited due to blackbody radiation induced transitions to nearby levels, which are temperature dependent [247]. The blackbody coupling to a neighbouring state is given by $\Gamma_{g\leftrightarrow e,\mathrm{bbr}} = \left(e^{\frac{\hbar|\omega|}{k_\mathrm{B}T}} - 1\right)^{-1} A_{g\leftarrow e}$. The precision of the blackbody induced transition rates is controversial, because the wavelength of the relevant frequencies is on the same length scales as the size of the vacuum chamber, which leads to slight geometry-dependent modifications of the blackbody spectrum. These modifications were investigated in the context of optical lattice clocks [248, 249], where their effect is rather low, but for Rydberg atoms the situation could be different. In Fig. 4.6 the decay rates from 43S and 35P to the various other levels are shown assuming an ideal blackbody spectrum. In general the radiative decay is dominated by the decay rate directly to one of the lowest states. The rate is still quite low due to limited wavefunction overlap

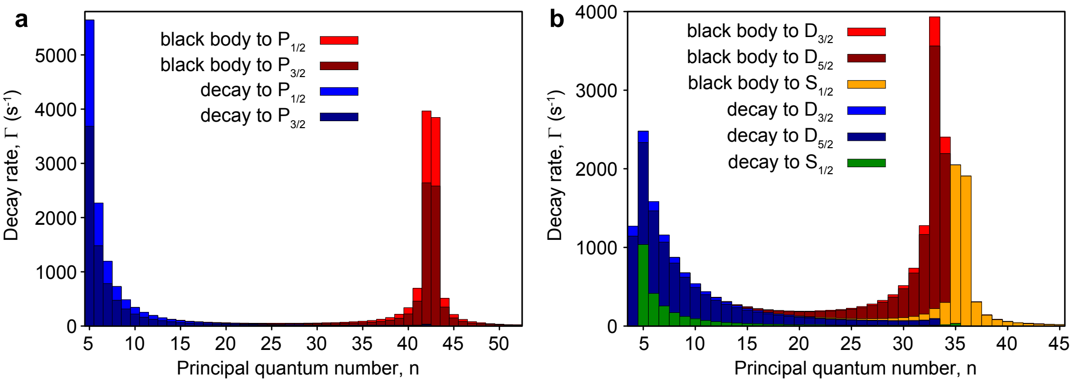

Figure 4.6.: Decay channels of the rubidium 43S and 35P state. a, decay rates from 43S state (see also [3] for 43S diagram), **b**, decay channels for 35P state. There are two main decay types. One is direct radiative decay to lower lying states, the other blackbody coupling to neighbouring Rydberg levels. The blackbody coupling is calculated for $T = 300\,\mathrm{K}$.

reference	$43S_{1/2}$	$35P_{3/2}$	$60D_{5/2}$	$41D_{5/2}$
pure radiative decay, T = 0 K				
[242] (experiment)	99(15)	-	-	-
[64, 243] (theory)	87	76	207	64
[244] (experiment, ^{85}Rb)	99(6)	98(6)	271(16)	87(5)
this thesis (theory)	81	83	172	54
including blackbody depopulation, T = 300 K				
[64, 243] (theory)	44	36	102	39
[245] (experiment, ^{85}Rb)	40(2)	34(2)	-	37(2)
[246] (experiment, ^{85}Rb)	-	-	-	33(4)
this thesis (experiment)	38(12)†	-	-	46(17)†
this thesis (theory)	43	37	95	35

Table 4.3.: Comparison of lifetimes for selected states of rubidium. Lifetimes in micro seconds for pure radiative decay in the upper half and including blackbody depopulation rate in the lower half. The shown values from [244] are calculated from the scaling fitted to the experimental data. There are also early calculations for lower lying states [63, 221]. † only statistical error, for a discussion of systematic errors see Sec. 5.7.5.

between the states. The other main contribution limiting the lifetime is blackbody induced transitions to close-by Rydberg levels. Typically only the 5-10 nearest states are relevant. The effective decay rate of a Rydberg state is given by summation over all radiative decay channels to lower lying states and all blackbody coupling channels to nearby states (Sec. 4.5). The first contribution leads to the radiative lifetime τ_0, while the second to the blackbody lifetime τ_{bbr}. In total this yields the effective lifetime of a Rydberg state $\frac{1}{\tau_{\mathrm{eff}}} = \frac{1}{\tau_0} + \frac{1}{\tau_{\mathrm{bbr}}}$. For practical purposes one can use an empirical scaling law for the zero-temperature lifetime $\tau_0 = \tau_s(n^*)^{\epsilon}$ with constants τ_s and ϵ, which depend on l and j of the Rydberg states. These scaling coefficients were determined for ^{85}Rb by Branden *et al.* experimentally and are shown in Table 4.4.

State	τ_{s}(ns)	ϵ
$nS_{1/2}$	1.4(1)	2.99(3)
$nP_{3/2}$	3.5(4)	2.90(3)
$nD_{5/2}$	1.8(3)	2.84(4)

Table 4.4.: Experimental radiative lifetime scaling by Branden *et al.* [245].

4.7. Calculation of the van der Waals coefficient

The van der Waals coefficient is one of the most important parameters, as it is the measure of the interaction strength between Rydberg atoms. It is worth noting here that the van der Waals coefficient is not only relevant for Rydberg atoms, but also for ground state atoms, as it is directly connected to the scattering length [250, 251]. The van der Waals coefficient can be calculated from the radial matrix elements. Calculations can be found in the literature [252–256] and the following discussion is based on these references. For the rubidium S-states a simple scaling formula for practical applications can be found in Singer *et al.* [253]: $C_6(^{87}\mathrm{Rb,nS}) = n^{11}(11.97 - 0.8486n + 0.003385n^2)$, which yields the widely used value $-1.697 \cdot 10^{19}\,\mathrm{a\,u}$ for the 43S state. In contrast to the simplified view of a spherically symmetric $1/r^6$ potential the van der Waals interaction between rubidium S-states is nearly, but in theory not perfectly isotropic (difference between $\theta = 0$ and $\theta = \pi/2$ is approximately $1\,\%$). This asymmetry is caused by the fine structure splitting of the Rydberg states. When calculating the couplings separately for all fine structure states there is always an angular dependency. Due to these angular-dependent couplings and mixing between several Zeeman states the C_6 calculations can be quite involved. In the following the main ideas of the calculation for a realistic situation will be discussed, which leads to some complications compared to the three level atom model (Sec. 3.2.1). One effect in real atoms is the possibility to change the interaction strength between Rydberg atoms in an experiment by tuning the Förster defect through shifting the involved levels via electric (or magnetic) fields. Another difference is that there are no three-level atoms in reality. But the involved multi-level situation can be partitioned into a set of effective three-level systems, the so-called collision channels, which can be treated separately. For example, for S-states one channel would be $n_1\mathrm{S}_{1/2} + n_1\mathrm{S}_{1/2} \rightarrow n_2\mathrm{P}_{1/2} + n_3\mathrm{P}_{1/2}$, with the Förster defect $\mathit{\Delta}_F(n_1,n_2,n_3) = E(n_2\mathrm{P}_{1/2}) + E(n_3\mathrm{P}_{1/2}) - 2E(n_1\mathrm{S}_{1/2})$. For a polarized sample of Rydberg atoms in a magnetic field the m_j quantum number is well-defined and has to be taken into account.

For the discussion we adopt the following naming convention. We call the atoms involved in the process a and b, their initial states a_i and b_i, the intermediate state a_m, b_m and the final states a_f, b_f. The states are characterised by the quantum numbers (n,l,j,m_j). With this notation the van der Waals interaction energy is given by

$$\begin{aligned}\left\langle a_i,b_i \middle| \hat{V}_{\mathrm{vdW}} \middle| a_f,b_f \right\rangle &= \sum_{a_m,b_m} \frac{\left\langle a_i,b_i \middle| \hat{V}_{dd} \middle| a_m,b_m \right\rangle \left\langle a_m,b_m \middle| \hat{V}_{dd} \middle| a_f,b_f \right\rangle}{\delta_{a_i,b_i,a_m,b_m}} \\ &= \sum_{\nu=(a_m,b_m)} C_6^{\nu} \left\langle a_i,b_i \middle| \hat{D}_{\nu}(\theta,\phi) \middle| a_f,b_f \right\rangle / r^6 \\ &= \frac{C_6(\theta,\phi)}{r^6} \; .\end{aligned} \tag{4.11}$$

The calculation is perturbation theory with virtual intermediate pair states with the Förster detuning $\delta_{a_i,b_i,a_m,b_m} = E(a_m) + E(b_m) - E(a_i) - E(b_i)$. Radial and angular contribution separate for every collision channel $\nu = (a_m,b_m)$ and one can define a m_j-independent C_6^ν coefficient and a matrix $\hat{D}_\nu(\theta,\phi)$, which contains the angular couplings and selection rules [256, (C4)]. The C_6^ν coefficient for every channel is determined only by radial wavefunction overlap integrals and the Förster defect: $C_6^\nu = \sum_{n_{a_m},n_{b_m}} \frac{\mathcal{R}^{a_i}_{a_m}\mathcal{R}^{a_m}_{a_f}\mathcal{R}^{b_i}_{b_m}\mathcal{R}^{b_m}_{b_f}}{\delta_{a_i,b_i,a_m,b_m}}$. When adding up the interactions C_6^ν for all channels, also the angular-dependent coupling strengths in the matrix $\hat{D}_\nu(\theta,\phi)$ come into play, which can lead to a complicated angular dependency of the total C_6 coefficient.

4.8. Photo-ionization of Rydberg atoms

When exciting Rydberg atoms in optical dipole traps they can be ionized by the trapping light. It turns out that the ionization rate is only relevant on typical experimental timescales for Rydberg atoms in strong light fields [149, 257]. The ionization rate depends on the orbital angular momentum l of the Rydberg state. While S-states are quite robust against photo-ionization, the rates for P- and D-states are much higher due to the larger overlap with continuum wavefunctions [149]. Neglecting this special anomaly for low angular momentum states, the ionization rate goes down for Rydberg states with increasing effective principal quantum number n^* and with increasing l for $l > 2$. This can be explained by the fact that ionization happens predominantly when the electron is near the nucleus [258] and this probability becomes smaller for high-angular momentum states. This can be understood in a classical picture as the quasi-free electron far from the core cannot absorb a photon due to momentum conservation. Only in the strong Coulomb potential this process is allowed when the excess momentum is transferred to the nucleus. The ionization also scales with the trapping wavelength. For infrared light the transition to the ionization threshold becomes near-resonant and the ionization rate very high [257]. For example CO_2 lasers photoionize Rydberg states efficiently [159]. But the most often used trapping wavelength of 1064 nm still causes reasonably low ionization rates for most experiments [259], for the 43S states the ionization rate in a typical trap is $\ll 1 \cdot 10^3\,1/\mathrm{s}$ [257].

4.9. Hyperfine structure of Rydberg states

The hyperfine structure splitting is typically very small for Rydberg states, as it scales with the amplitude of the electron wavefunction at the core. The splitting can be extracted from millimetre-wave spectroscopy [59, 119] or optical high-resolution spectroscopy [86, 87]. The hyperfine structure constant scales as $A_{\mathrm{hfs},n^*,l} = \frac{A^*_{\mathrm{hfs},l}}{n^{*3}}$ and for ^{87}Rb the scaling factor is given by $A^*_{\mathrm{hfs,S_{1/2}}} = 18.4(3)\,\mathrm{GHz}$ (combined value with s.e.m. from [87, 117, 119, 260]). Depending on the excitation scheme the hyperfine structure splitting can lead to a broadening of the Rydberg excitation line, but this can be avoided by using an excitation path which couples to only one hyperfine level in the Rydberg state.

4.10. Summary

In this chapter the calculation of various Rydberg atom parameters relevant for experiments was discussed. For the following chapters, we mainly focus on the rubidium-87 43S-state, for which the numbers are summarized in Table 4.5. The calculated values in this thesis were shown to agree generally quite well with the other values found in literature. To demonstrate the extreme properties of Rydberg states, they are compared to the numbers for the 5S state.

The collection of numbers also allows to justify the choice of the 43S state. It has a reasonable lifetime of ∼ 40 µs, not too extreme polarizability and a blockade radius, which is in a range that matches the typical system size in our experiment. The nearly perfect isotropic interaction of the S-state and its simple structure avoid possible issues in the excitation like Förster zero states, which break the blockade condition [255, 261].

property	value 43	calc. this thesis	value 5S
n^*	39.8687 [86]	39.8687 (Sec. 4.1.1)	1.8048
g_j	2.0023		2.0023
hyperfine structure splitting	582(8) kHz (Sec. 4.9)	-	$\sim 6.83\,\text{GHz}$
lifetime τ at 300 K	42 µs [3]	43 µs (Sec. 4.6)	∞
binding energy	$h \cdot -2069.8\,\text{GHz}$ [3]	$h \cdot -2069.703\,\text{GHz}$ (Sec. 3.1)	1010.024 893 3(3) THz [86]
orbit radius	2384.2 a_0 [3]	2384.3 a_0 (Sec. 3.1)	5.6 a_0 [262]
natural linewidth Γ (incl bbr)	$2\pi \cdot 3.76\,\text{kHz}$ [3]	$2\pi \cdot 3.72\,\text{kHz}$ (Sec. 4.5)	$2\pi \cdot 6.0666(18)\,\text{MHz}$ [263]
polarizability α	$-17.7\,\text{MHz}/(\text{V/cm})^2$ [237]	$-17.4\,\text{MHz}/(\text{V/cm})^2$ (Sec. 4.2)	$0.0794(16)\,\text{Hz}/(\text{V/cm})^2$ [263]
transition dipole moment (strongest line, σ, $5P_{3/2} \rightarrow nS_{1/2}$)	0.0103 e a_0 [3]	0.0101 e a_0 (Sec. 4.1.4)	2.989 31(62) e a_0 [263]
radial matrix element $5P_{3/2} \rightarrow 43S_{1/2}$	0.017 86 e a_0 [3]	0.0174 e a_0 (Sec. 4.1.4)	5.181(4) e a_0 (Sec. J.1)
van der Waals coefficient C_6	$-1.697 \cdot 10^{19}$ a u [3, 253]	$-1.710 \cdot 10^{19}$ a u ($\theta = \pi/2$) (Sec. 4.7)	$4.426 \cdot 10^{3}$ a u [211]
blockade radius	$\approx 5\,\mu\text{m}$		$\approx 5\,\text{nm}$

Table 4.5.: Collection of properties of the 43S state of rubidium-87. Literature values are given with references. For derived quantities also a value calculated in this work is given. The properties of the 5S ground state are given for comparison.

5. Rydberg excitation and detection in an optical lattice

5.1. State of the art – Experiments with spatial resolution

In spite of the long history of Rydberg experiments, the number of cold atom experiments with high spatial resolution for Rydberg atoms is quite limited. On the one hand, there are experiments with single atoms or small ensembles in a few well-separated micro traps [70, 101, 102, 264, 265]. On the other hand experiments in homogeneous cold gases allow by a variety of approaches to reach high-resolution images of the Rydberg atom distribution. The experiment in the Raithel-Group uses an ion microscope [180] to image the Rydberg distribution in a volume limited by the excitation beam size in a magneto-optical trap. A very different approach not feasible with alkali atoms is the possibility with alkaline-earth-like atoms to image the Rydberg atoms via a closed transition of the second outer-shell electron [183, 184]. Yet another idea is the electron microscope [266, 267], which might enable to image the spatial distribution of Rydberg atoms via local ionization with an electron beam. Another promising scheme is to exploit the level shift of the ground to Rydberg transition of atoms surrounding a Rydberg atom to enhance the signal. Proposed techniques are based on conditional Raman transfer [268] or electromagnetically induced transparency [269]. The latter proposal has been implemented in experiment, but did not reach the single-Rydberg-atom level yet [145]. The difficulty here is that the scheme requires the coupling to two distinct Rydberg levels, one species which is detected and the other is used as probe. For clean imaging of blockade spheres a two-dimensional arrangement would be required, which makes this type of absorption imaging challenging due to the low optical depth.

There were previous experiments combining Rydberg excitation with optical lattices [110, 157, 197, 270], but they are so far working with 1D lattices and do not reach direct high-resolution imaging of the Rydberg atom distribution.

In contrast to these experiments, we can initialize a near-uniform 2D sample of atoms in the lattice via the superfluid-to-insulator transition, which allows for a more controlled preparation of initial samples in the lattice, especially in combination with local addressing. We then couple the samples to the Rydberg state, remove all ground state atoms from the lattice and image the former Rydberg atoms as ground state atoms via fluorescence imaging. In this way a resolution only limited by lattice discretisation can be reached, which is typically negligible compared to Rydberg blockade length scales.

Our setup opens new possibilities in the field of Rydberg physics, as there is currently no other experiment with degenerate quantum gases and single atom detection on ground state as well as on the Rydberg atom level.

In the following we first discuss possible issues for the experimental implementation and give a general overview over Rydberg detection and excitation schemes to motivate the choices for our experiment. Subsequently the experimental setup, details of the optical detection scheme and first experiments are described.

5.2. Possible issues for a Rydberg lattice experiment

Although the optical excitation of Rydberg atoms was already investigated in some detail, there are possible issues extending these schemes to the excitation in optical lattices. In the following the specific problems encountering for our setup are discussed and based on the introduction of the previous chapters we show that they are not detrimental.

Anti-trapping of Rydberg atoms The excited Rydberg atoms are anti-trapped at the trapping spots of the ground state atoms in red-detuned optical lattices. The strength of the anti-trapping is calculated in Sec. 4.3. It turns out that the absolute value of the shift is on the order of the light shift for the ground state atoms. But the effects of the corresponding acceleration can be suppressed by keeping the time short in which the atoms stay in the Rydberg state. The light shift also leads to a shift of the Rydberg line. This shift is negligible compared to typical Rabi frequencies used in the experiment and should be very stable due to the well-controlled lattice depth.

Detection scheme The molasses imaging at our setup was only tested with sub-microkelvin initial temperature of the atoms before imaging. Optical molasses imaging also works for hotter atoms in optical dipole traps, but it is not clear if the lattice during imaging is deep enough to avoid tunnelling until the molasses cooled down the atoms to a typical equilibrium temperature. For high-fidelity imaging of Rydberg atoms a direct detection is required, as an indirect detection of Rydberg excitations through loss is unfavourable due to the typically low number of Rydberg excitations compared to ground state atoms. If the Rydberg atoms are too hot after the sequence, a recapturing and imaging of the atoms will not work. A model of the detection process shows that the atoms are mainly recaptured in bands with low tunnelling rates which should allow for molasses cooling of the former Rydberg atoms (Sec. 5.6.5).

Photo-ionization For some Rydberg states the photo-ionization rate in the optical lattice is quite high. As the atoms in our setup are typically very cold we need only relatively shallow lattices. This reduces the photo-ionization a lot and leads to negligible ionization rates, at least for S-states (Sec. 4.8).

Unknown electric fields As the setup was not optimized for Rydberg atoms, there is no reliable estimate for electric fields in the setup and no electric field control. The glass windows is about 5 mm away from the atoms and in a symmetric configuration with the opposing window, giving hope that the electric fields are small enough at

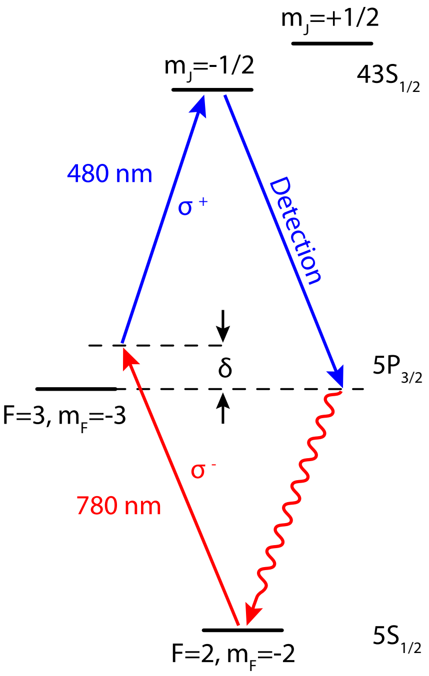

Figure 5.1: Rydberg excitation scheme. The ^{87}Rb Rydberg atoms are excited via a two-photon transition via the intermediate $5P_{3/2}$ state with a detuning $\delta \approx 742\,\mathrm{MHz}$ to the $43S_{1/2}$ state. Polarizations a chosen in a way to couple a uniquely defined stretched state. For detection the Rydberg atoms are pumped down resonantly via the intermediate state $5P_{3/2}$, which decays very fast due to its short lifetime of 26 ns [263].

least for Rydberg states around $n = 50$. During the experiments, it also turned out that microwave fields at 6.3 GHz which were side-products of our microwave setup and have no effect on ground state atoms, can already create strong light shifts on the order of several Megahertz on Rydberg states. Background electric fields will limit the setup to a certain range of principal quantum numbers. But due the large blockade radius compared to our resolution high Rydberg states are anyways not ideal for most experiments at our setup.

5.3. Optical excitation schemes to Rydberg states

There are currently many schemes actively used for the optical excitation of Rydberg atoms in different laboratories. Here, we will discuss various schemes for the coherent excitation of Rydberg atoms using narrow lasers to selectively couple to a certain Rydberg state.

There is the obvious approach to use only a single laser and couple the ground state directly to a Rydberg state. For such a transition the required laser frequency is typically in the ultraviolet, for ^{87}Rb around 297 nm. Producing such a wavelength requires some effort, as there is not even a high-power solid-state laser source available which can be doubled. Another problem are the rather small matrix elements on these transitions. In spite of all the difficulties the direct excitation to P-states is becoming more popular with the advances in frequency doubling technology [72, 271, 272].

The most commonly used scheme is the two-photon excitation via a near-resonant intermediate transition. Here the accessible states for alkali atoms are the S and D Rydberg states, which offer quite a variety from the isotropic interaction of the S-states to various anisotropic interactions for D-states. For rubidium the required lasers with reasonable power are commercially available.

There are also other schemes based on three or more lasers, but these schemes suffer from low effective Rabi frequencies and intermediate state scattering and are typically used for spectroscopy applications. The big advantage of three-photon-spectroscopy for Rydberg atoms is the possibility to use Doppler-free techniques by designing the laser configuration in a way that the vectorial sum of the recoil velocities of all excitation lasers vanishes [273, 274].

The excitation scheme chosen in this thesis is the most commonly used two-photon scheme for ^{87}Rb with lasers at 780 nm ("red") and 480 nm ("blue"). Here the red laser is slightly detuned from the standard laser cooling line of ^{87}Rb. To reach a reasonable effective Rabi frequency to the Rydberg state, considerable power is required on the upper blue transition, as the power on the lower transition is limited due to strong scattering at the intermediate state. At the first glance it looks like this can be circumvented by a larger intermediate detuning. But a simple scaling argument shows that for constant effective Rabi frequency and fixed coupling on the upper transition, the scattering rate at the intermediate level is already uniquely determined by the scalings $\Gamma_{sc} \propto \Omega_1^2/\Delta^2, \Omega = \frac{\Omega_1 \Omega_2}{2\Delta}$. In order to maintain the same two-photon coupling for larger detuning, one needs to increase the Rabi frequency on the lower transition, which in turn increases the scattering rate. This argument holds, as long as the detuning is much larger than the natural linewidth of the transition and the involved Rabi frequencies. In conclusion, the Rabi frequency is only limited by the available power for the upper transition. To circumvent the power limitation at 480 nm other groups either used pulsed lasers [89] or switched to the two-photon transition via the 6P state in rubidium (420 nm and $\approx$ 1016 nm), where high-power laser systems are available for the upper transition [110, 275].

The two general problems of the two-photon schemes are the light scattering at the intermediate level and light shifts. In the end, the light scattering limits the maximum Rabi frequency for a targeted coherence time. For some experiments, coherent excitation is not necessary or only required for short timescales. In these cases the power on the lower transition can be increased, but at some point the induced light shift will fluctuate due to intensity noise and drifts. In principle it is possible to cancel the light shifts on the two-photon transition by using the same Rabi frequency on the lower and upper transition (Appendix C.1.2). But often it is not feasible to achieve the desired two-photon Rabi frequencies while keeping the Rabi frequencies on lower and upper transition equal.

In our experiment we choose a two-photon excitation starting from the $5\mathrm{S}_{1/2}, F = 2, m_F = -2$ via the $5\mathrm{P}_{3/2}, F = 3, m_F = -3$ intermediate state, which allows for the selection of a well-defined Rydberg state (Fig. 5.1) [3]. With an appropriate choice of polarization, a coupling to the $\mathrm{nS}, m_j = 1/2$ state is strongly suppressed. As the scheme selects exactly one intermediate state leading to a uniquely defined excitation path, such that interference between various possible excitation paths is avoided.

Due to the relatively large matrix element of the red transition the required power of the red laser is rather low. This means that one can afford a rather large intermediate detuning and we decided to go for the largest detuning easily reachable via a standard acousto-optical modulator in double pass. Another choice to be made is the sign of the intermediate state detuning. In the experiment in a quite strong magnetic field of around 30 Gauss we saw considerably more scattering for the red-detuned than for the blue-detuned case for the same absolute detuning to the $F = 3, m_F = -3$ intermediate state. We attribute this to a small fraction of wrong polarization, which scatters off the $F < 3$ states, which are less off-resonant in the red-detuned case.

5.4. Detection techniques for Rydberg atoms

Rydberg atoms are often detected via field-ionization and then guiding the resulting ions to an ion detector. This technique was already used in early experiments [53] and later also with cold atoms [96, 97, 180, 276, 277]. The advantage of this scheme is the possibility to detect very few Rydberg atoms created in a large cloud of neutral atoms, essentially without background signal and with reasonable detection efficiency $\approx 40\,\%$ ([114]: $40\,\%$, [110, 278]: $35(10)\,\%$, [4]: $40\,\%$, [228]: $2\,\%$, [279, 280]: $13.0(15)\,\%$, [281]: $47.8(26)\,\%$). In the case of a single ion detector there is no spatial information, but some information can be calculated from the arrival times, as the timing resolution can be very high. But there is also the possibility to use multi-channel plates to gain spatial resolution [96, 180, 282]. Another way to obtain high resolution is to only locally ionize (for example using focussed light beams [159, 257], or electron beams [266, 267]). In our setup we want to exploit the advantages of optical detection schemes and did not integrate an ion detector into the setup. An optical detection via loss of Rydberg atoms from an optical tweezer was explored before with single atoms [70, 74]. The loss occurs due to a combination of photo-ionization and anti-trapping potential of the Rydberg state in the tightly focussed optical dipole trap used there. In some experiments, a coherent deexcitation of the Rydberg atoms before state-selective imaging is possible [76], which avoids the uncertainty in the Rydberg atom loss. In contrast to that, we want to deexcite Rydberg atoms incoherently to avoid detection problems in systems with several Rydberg excitations, where a coherent deexcitation is almost impossible due to the interaction energies. The idea is to couple the Rydberg state to a short-lived state, which then decays back to the electronic ground state. Such a scheme has been already used before in a context with focus on the retrieved photons [197]. Here we use a laser beam resonant with the Rydberg state to $5P_{3/2}$ transition of rubidium to stimulate the Rydberg atoms back down to the ground state (for details see Sec. 5.6.2). The resulting ground state atoms are then imaged via fluorescence imaging.

5.5. Experimental setup

In the following the beam path as well as the laser setup for the Rydberg excitation in the experiment are described. First we discuss the geometric beam configuration and then the laser setup for the two-photon excitation of Rydberg states. This is followed by a detailed discussion of the frequency offsets due to the frequency stabilization scheme of the lasers. We also look into Rydberg spectroscopy in a glass cell, which

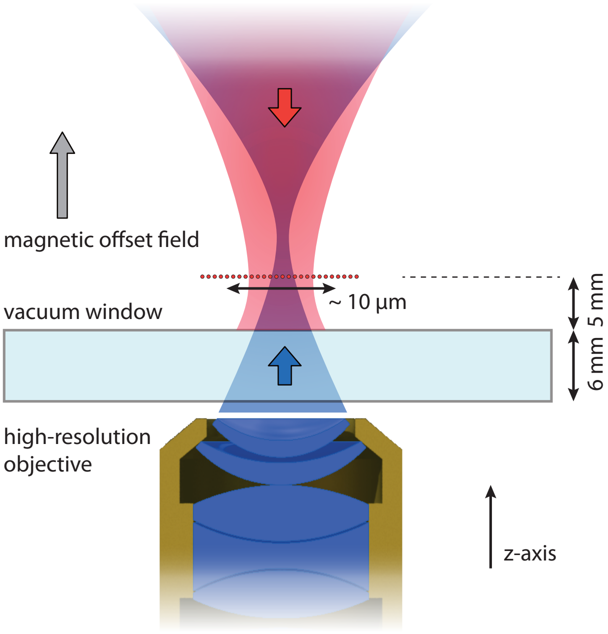

Figure 5.2.: Rydberg excitation beam setup. The two Rydberg excitation laser beams are sent counter-propagating along the z-axis to the atoms along the best-controlled magnetic offset field. The blue beam goes through the objective from below and the red beam in the opposite direction towards the camera. The waist of the red beam was around 40 µm, the blue waist is on the order of 5 µm. The beams were adjusted in a way that the atoms are in the focus of the red beam. The size of the blue beam at the atom position is adjusted via a piezo stack (PIFOC P-726), which can move the objective in z-direction over a range of 100 µm [48]. Sketch not to scale.

allows for fast and accurate checks of the absolute frequency of the lasers relative to Rydberg lines.

5.5.1. Beam path and polarization of the two excitation beams

Depending on the intended Rydberg experiment there is a certain advantageous beam configuration. For our excitation scheme we use the polarization to select a certain Rydberg state. For a clean implementation of the scheme a σ^+-σ^- configuration is necessary. To this end, it is required to send the beam along the magnetic field axis, which is in our case typically perpendicular to the atom plane.

To reduce the recoil during Rydberg excitation a counter-propagating beam configuration is preferred. For the low temperature in our system the Doppler broadening is negligible, but the heating due to the recoil of both excitation beams might be harmful. Another problem is the limited optical access in the setup as the components required for single-site imaging take already quite a lot of space. The only reasonable beam configuration at our setup taking these constraints into account turned out to be the

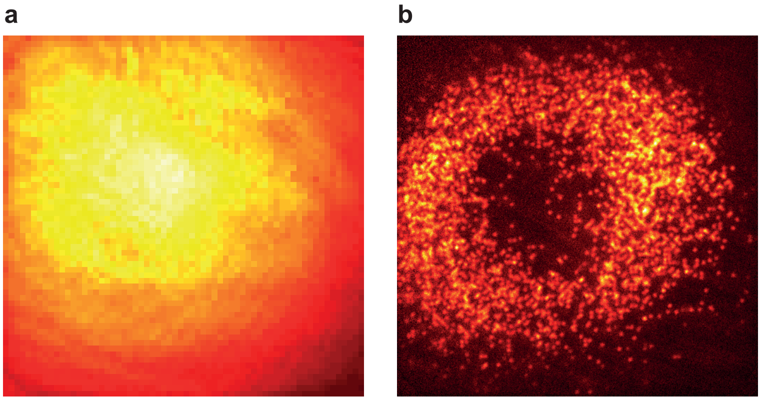

Figure 5.3.: Alignment of Rydberg excitation beams. Our setup allows to check the alignment of the Rydberg beam positions in a single experimental run. **a**, red Rydberg beam imaged directly on the camera, **b**, the light shift of the blue Rydberg beam creates a slightly repulsive potential, which leads to a hole in the atom distribution for low z-lattice depth $< 20\,E_\mathrm{r}$ (for a calculation of the expected light shift see Table 5.3). For both images the field of view is $64 \times 64\,\mathrm{\mu m}^2$.

one shown in Fig. 5.2. With the help of dichroic mirrors the red beam was overlapped with the z-lattice and the blue beam is going in reverse direction along the imaging path. The big advantage of the scheme is also the possibility to check the alignment of the excitation beams in a single shot, as the red beam can be imaged on the camera and the blue beam can be detected by its repulsive potential on the atoms (Fig. 5.3).

The geometric beam configuration described above allows in principle to reach a very good σ^- polarization of the red beam. In order to align the polarization we apply a magnetic offset field that points in the opposite direction as the offset field we want to use later in the experiment to split the magnetic hyperfine states such that they are optically resolved. We set the red laser on the resonance $5\mathrm{S}_{1/2}, |2,-2\rangle \rightarrow 5\mathrm{P}_{3/2}, |3,-3\rangle$ and minimize the absorption using a $\lambda/2$,$\lambda/4$ wave plate combination. Another technique used is to minimize the absorption on the resonance $5\mathrm{S}_{1/2}, |2,-2\rangle \rightarrow 5\mathrm{P}_{3/2}, |1,-1\rangle$ in the final magnetic field, as there is no π-polarization component expected if the beam is sent along the magnetic field direction. The polarization of the blue beam was tuned via preadjusted waveplates-cube setups in the transmitted light through the vacuum chamber. The only problem of this technique is to reach the opposite σ-polarization with respect to the red beam. But this can be checked by spectroscopy on the atoms.

5.5.2. Laser system

The two-photon excitation to Rydberg states requires two laser systems, which are for our choice at 780 nm ("red") and 480 nm ("blue"). The laser system is in some aspect different from the typical laser system for D_1 and D_2 line of rubidium. As the natural linewidth of the Rydberg transition is rather small on the order of few kHz, and also the Rabi frequencies reachable are typically not above 1 MHz for the excitation

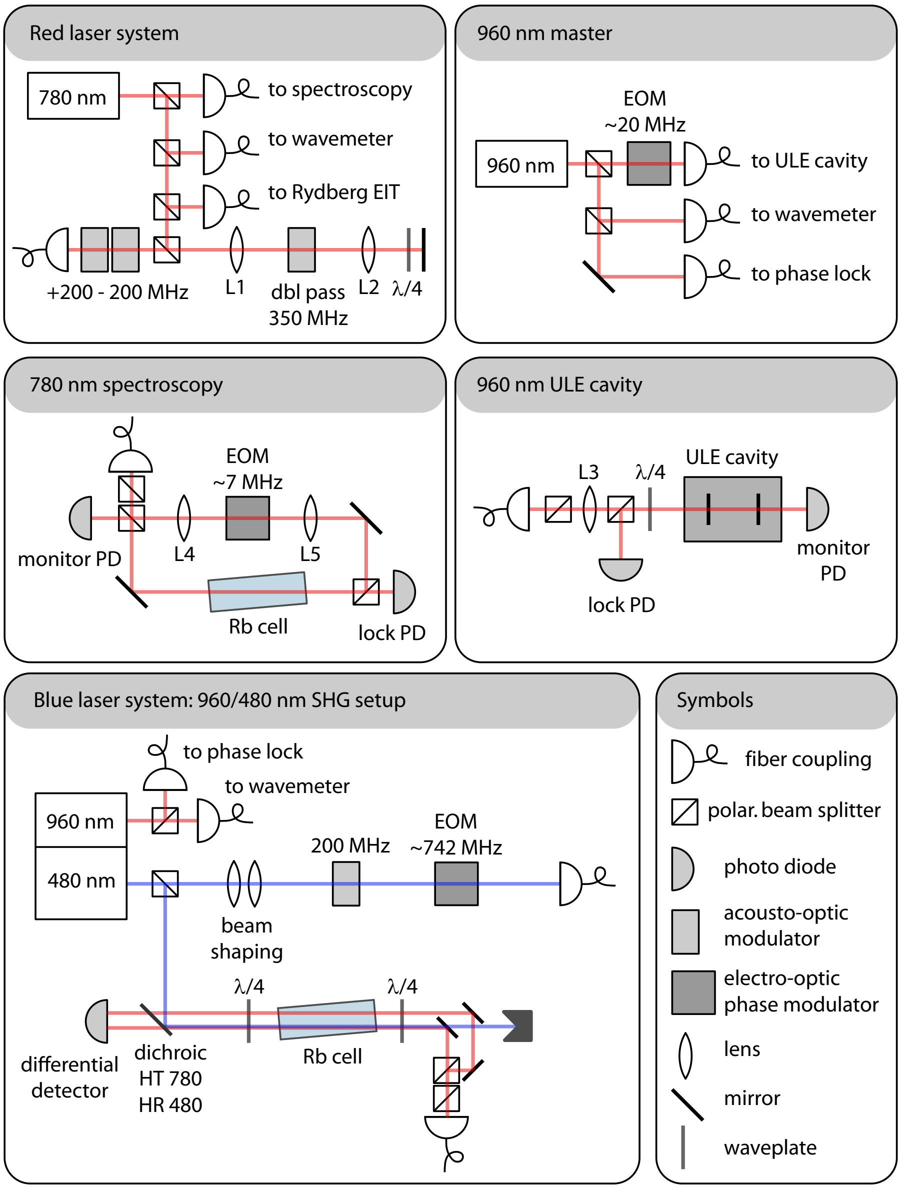

Figure 5.4.: Schematic of Rydberg laser setup. Not all essential components are shown, e.g. $\lambda/2$ plates, lenses and mirrors are mostly left out. L1: $f = 150\,\mathrm{mm}$, L2: $f = 140\,\mathrm{mm}$, focussing through small aperture AOM with small focus to increase switching speed; L2 is large enough for the 0th and 1st diffraction order. L3 mode matching lens for cavity $f = 500\,\mathrm{mm}$. L4, L5: $f = 100\,\mathrm{mm}$ focussing large beam through small aperture EOM.

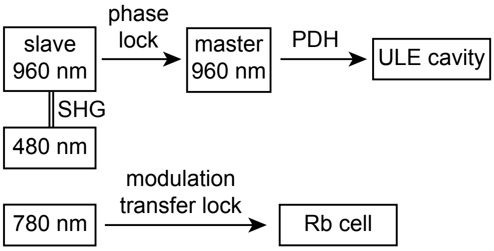

Figure 5.5.: Schematic of the locking scheme. The master is locked to the ULE cavity using a Pound-Drever-Hall-technique. The slave laser is locked to this master laser using an offset phase lock to gain tunability but maintain stability. The red laser is stabilized to a modulation transfer spectroscopy (Appendix C.4).

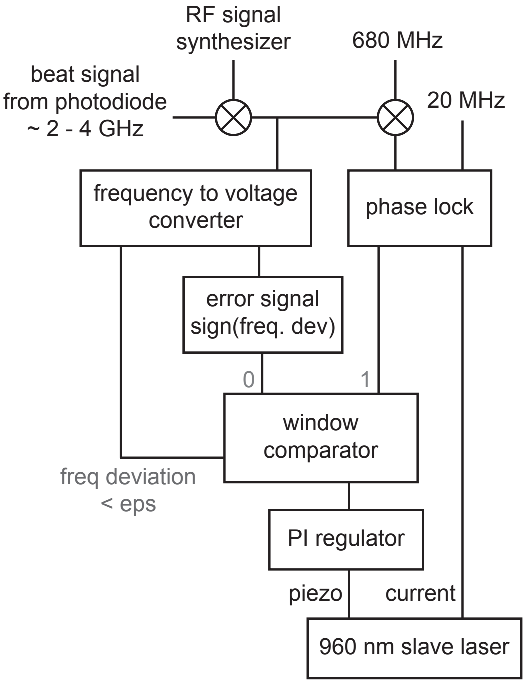

Figure 5.6: Schematic of the phase lock. The beat signal is mixed down in two steps to increase the capture range. The capture range was measured to be as expected around 500 MHz in one direction, limited by the zero-crossing, and typically much larger in the other direction.

of extended ensembles, at least a factor of ten higher stability of the lasers than for laser cooling of rubidium is desirable. Another requirement is some tunability of the laser for the second step of the two-photon excitation, because the Rydberg levels are spaced by around 50 GHz in the range of interest.

The light at a wavelength of 780 nm is generated by a diode laser. Its frequency is stabilised using a modulation transfer spectroscopy in a rubidium vapour cell (see also Appendix C.4, Fig. 5.4). The big advantage of this direct spectroscopy lock is its long-term stability. In contrast, an increase in short-term stability is rather hard to reach in this way. Typically, an additional medium-finesse cavity would be required to narrow down the laser line, but for simplification of the laser system we just used the modulation transfer spectroscopy lock which could be optimized to reach a FWHM linewidth of the red laser of about 50 kHz. This was checked using a beat with a second laser stabilized to an ultra low expansion glass (ULE) cavity.

The stabilized light is then shifted to the blue side of the lock transition $\left|5\mathrm{S}_{1/2}, F=2\right\rangle \rightarrow \left|5\mathrm{P}_{3/2}, F=3\right\rangle$ by a double pass acousto-optic modulator (AOM) at 350 MHz. To further suppress stray light through this AOM we use two additional AOMs with compensating shift frequencies for switching. One of them is also used for the sample-and-hold pulse stabilization. Before we have cold atoms in the vacuum chamber in the experimental sequence, we stabilize the red Rydberg light to a certain power level, which is then reproduced during the pulse for the Rydberg excitation. This way, long-term drifts, e.g. in fibre coupling efficiency, can be compensated.

The light at 480 nm is produced by frequency-doubling light at 960 nm, which is emitted from a diode laser and amplified by a tapered amplifier (Fig. 5.4). This laser is stabilised by a phase-lock to a master laser also operating at 960 nm. The master laser at 960 nm is locked to a temperature stabilised ultra low expansion glass (ULE) cavity in a vacuum chamber (Fig. 5.4). The described locking scheme allows for tuning the frequency of the slave laser while transferring the narrow spectral linewidth of the master laser (Fig. 5.5). This is only possible by using a high-bandwidth offset lock (Fig. 5.6). To reach a high capture range of the lock one can nowadays use a high-bandwidth phase-frequency detector chip. The described setup still uses a chip with only 200 MHz bandwidth (AD9901) in a configuration that limits it to 20 MHz. To increase the capture range to ≈ 500 MHz we use a two-step down-mixing of the beat signal between the slave and master laser. The first signal in the range $0-680$ MHz is fed to a frequency-to-voltage converter and the second signal to a phase-frequency-detector. A window comparator based on the ramp of the frequency-to-voltage converter can now be adjusted to switch to constant output voltages outside the capture range of the phase lock and to the phase-lock error signal in between. In this way the step-like phase-frequency-detector error signal is simply extended in one direction to the point of zero frequency at the frequency-to-voltage converter and in the other direction essentially unlimited. The large capture range allows to stabilize the laser by just flipping the lock switch. By construction, this phase lock stabilizes the beat of both lasers to an offset frequency, which is the synthesizer frequency plus an offset of 660 MHz. The offset is caused by the two down-mixing steps with 680 MHz and 20 MHz.

The short-term linewidth of the slave laser was measured to around 20 kHz using an

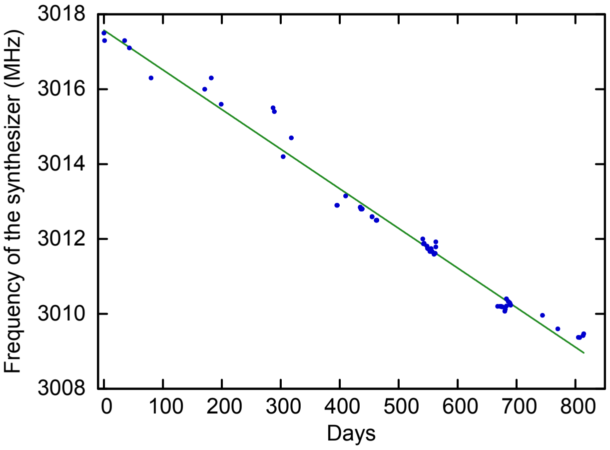

Figure 5.7.: Long term drift of the ULE cavity. Collection of synthesizer frequencies for the 43S Rydberg resonance on the cold atoms over more than two years. Each blue dot corresponds to one resonance curve. Green line, linear fit. We observe a linear drift which can explained by ageing of the ULE glass [284]. The linear drift can be fitted as $-0.010\,58\,\mathrm{MHz/day}\cdot t + 3017.57\,\mathrm{MHz}$, where t is the time in days since 23/01/2012 and the frequency is the synthesizer frequency. The drift corresponds to 122 mHz/s, which is on the same order of magnitude as in other setups ([284]: 63 mHz/s, [285]: 56 mHz/s)

independent resonator (EagleEye, Sirah Laser- und Plasmatechnik GmbH, Germany), which can resolve a linewidth down to $\sim 20\,\mathrm{kHz}$. The reference resonator is not long-term stabilized and therefore does not allow any conclusions about long-term stability of our laser. The best choice for long-term stability checks is the targeted Rydberg line itself. We checked the long-term stability of the two-photon excitation to be 50 kHz over several hours (FWHM of the centre of the line) using an EIT-spectroscopy in a rubidium vapour cell (see also section 5.5.3) [85]. The very slow drift of the ULE cavity due to ageing can be compensated by daily resonance scans or linear extrapolation (Fig. 5.7)

More details on the laser setup can be found in the Masters thesis by Ahmed Omran [283].

5.5.3. Rydberg-EIT spectroscopy in glass cell

In general, electromagnetically induced transparency (EIT) and also the special case with a Rydberg level involved have been studied in depth experimentally [85, 286] as well as theoretically [287]. In our setup we use the EIT-spectroscopy mainly to check our laser system. We are working in a regime with rather high probe-power, such that it is not clearly in the EIT-regime any more. At this point we want to skip the debate about whether these experiments are really in the EIT-regime or not [288], as this is not relevant here. The EIT-spectroscopy in rubidium allows to determine the transitions to Rydberg levels with sub-Megahertz precision and is therefore more

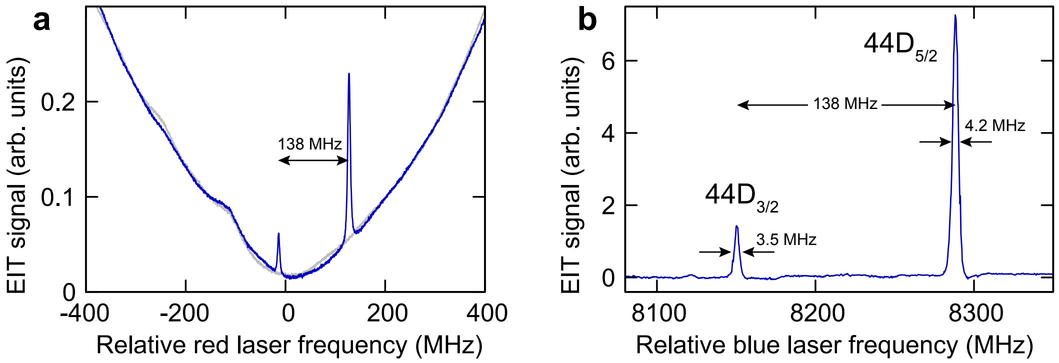

Figure 5.8.: EIT spectrum of the 44D state. **a**, Blue line, EIT spectrum in the glass cell of the 44D state of ^{85}Rb scanning the red probe laser. Grey line, same scan but without the blue coupling laser. The wiggles on the left hand side in signal as well as background trace are Lamb dips due to residual back-reflections in the tilted glass cell. **b**, Same spectrum as in **a**, but scanning the blue coupling laser, which makes the spectrum nearly background free. Outliers due to failure of the doubling cavity following the frequency steps are removed. The peak of the $44D_{3/2}$ and $44D_{5/2}$ are clearly visible using just a balanced amplified differential detector. For higher Rydberg states an additional Lock-in detection could be helpful.

precise than a wavemeter. The typical width of the resonances is lower than the natural linewidth of the D_2 line [85] and in our setup typically 3-5 MHz FWHM.

As an example we show here the EIT spectrum of the 44D state (Fig. 5.8), which was taken by a scan of the blue coupling beam and by that avoiding the Doppler-background of the D_2 line. The fine structure splitting can be extracted quite accurately to 138(1) MHz ([86]: 140.8(11) MHz). The deviation is most probably caused by a residual drift of one of the laser locks during the scan, which were not checked to below 1 MHz during this measurement.

More details on the EIT measurements and further investigations on intensity and magnetic field dependence can be found in the thesis by Ahmed Omran [283].

5.5.4. Calculation of the expected frequencies for the Rydberg resonances

Due to the variety of locks and acousto-optic modulators, calculating the expected frequency for the offset lock of the blue laser for the Rydberg resonance can be quite confusing. The general scheme in our setup to shift the laser system to a certain Rydberg level is the following. The red laser is always fixed in frequency. The master laser for the blue laser has to be locked on a certain mode of the cavity, which is at a convenient frequency offset for the phase lock of typically $2-5$ GHz. Afterwards the phase lock is used to fine-tune the blue laser to the Rydberg resonance. This is done via tuning the frequency of the synthesizer, which is used in the first down-mixing step.

In the following a calculation example for 43S to determine the target beat frequency is discussed. We used the cavity mode at a frequency of $\nu_{\mathrm{master}} = 311.858\,34(4)\,\mathrm{THz}$ (error is reproducibility of our wavemeter, but not the absolute accuracy). For the following calculations we use the literature value for the absolute transition frequency $5\mathrm{P}_{3/2}, F = 3 \rightarrow 43\mathrm{S}_{1/2}$: $\nu_{43\mathrm{S}} = 623.724\,510\,7\,\mathrm{THz}$ [86]. We consider the frequencies before the second harmonic generation, so the offset frequency of the master laser compared to the Rydberg transition is $\nu_{43\mathrm{S}}/2 - \nu_{\mathrm{master}}$. The slave laser is shifted up in addition to the synthesizer frequency by 660 MHz due to the phase lock design. After second harmonic generation there is a shift of +200 MHz of the slave laser by the switching and stabilization AOM. There is also a contribution caused by the intermediate detuning introduced by the +350 MHz double pass AOM of the red laser. In total the AOMs cause therefore a frequency correction of (200 MHz+700 MHz)/2. In general, also the differential Zeeman shift of the ground state $\varDelta\nu_g^Z$ and Rydberg state $\varDelta\nu_r^Z$ plays a role. For the Rydberg S-states this term cancels, as the magnetic shift for both levels is the same. The two-photon resonance is magnetic field insensitive. We attribute the deviations from the expected value to a wavemeter calibration error, which we fit to the data for the 43S state. The determined value $\nu_{\mathrm{werror}} = 210(50)\,\mathrm{MHz}$ is not a surprisingly large error for the wavemeter at 960 nm as it was calibrated for the D_2 line of rubidium.

With these considerations, the synthesizer frequency for the resonance to the 43S state can be calculated to

$$\nu_{43\mathrm{S}}/2 - \nu_{\mathrm{master}} + \nu_{\mathrm{werror}} - 660\,\mathrm{MHz} - (200\,\mathrm{MHz} + 700\,\mathrm{MHz})/2 + \underbrace{(\varDelta\nu_r^Z - \varDelta\nu_g^Z)/2}_{=0 \text{ for S-states}} = 3015\,\mathrm{MHz}\,. \tag{5.1}$$

For the EIT spectroscopy the AOMs for red and blue laser are not in the relevant beam path. The magnetic field in the glass cell is close to zero field and we can neglect the magnetic field shifts. Therefore we get a 450 MHz larger synthesizer frequency for the EIT resonance.

$$\nu_{43\mathrm{S}}/2 - \nu_{\mathrm{master}} + \nu_{werror} - 660\,\mathrm{MHz} = 3465\,\mathrm{MHz} \tag{5.2}$$

On 06/12/2012, the following beat frequencies for the resonance were obtained. For the EIT spectroscopy it was 3465.0(3) MHz for the resonance of the cold atoms 3014.7(3) MHz. The frequency for the EIT should be always $(700 + 200)/2$ MHz = 450 MHz higher, which is exactly the value observed in the experiment.

To check the values and confirm the wavemeter error we can look at the data for the 41D state (2012-12-03): The resonance of the state $41\mathrm{D}_{3/2}$ was found in an EIT spectrum at 2616 MHz synthesizer, $41\mathrm{D}_{5/2}$ at 2701 MHz synthesizer. With the literature value $\nu_{41\mathrm{D}_{3/2}} = 623.701\,857\,8\,\mathrm{THz}$ and $\nu_{41\mathrm{D}_{5/2}} = 623.702\,029\,5\,\mathrm{THz}$ [86] and the master frequency $\nu_{\mathrm{master}} = 311.8479\,\mathrm{THz}$ the calculation yields 2580 MHz and 2670 MHz for $41\mathrm{D}_{3/2}$ and $41\mathrm{D}_{5/2}$, respectively.

The calculated values coincide within wavemeter reproducibility with the experimentally determined position of the resonance. Based on the high-precision EIT data in [86], all the accessible levels can be found without any search by calculation to wavemeter precision.

5.6. Optical detection of Rydberg atoms

In the following we describe the experimental sequence for excitation and detection of Rydberg atoms in more detail and characterize the properties of the optical detection technique. In particular, details of the depumping technique are explained and the detection efficiency is estimated in several different ways.

5.6.1. Experimental sequence for Rydberg excitation and detection

Our experimental sequence begins with the preparation of a two-dimensional degenerate gas of a few hundred ^{87}Rb atoms confined to a single antinode of a vertical (z-axis) optical lattice [14]. The gas is then brought deep into the Mott-insulating phase by adiabatically raising an additional square optical lattice with period $a_{\mathrm{lat}} = 532\,\mathrm{nm}$ in the xy-plane. The atom number in the Mott insulator can be adjusted to a certain system radius of typically up to $R = 6\,\mu\mathrm{m}$, within which more than 80 % of the lattice sites are singly occupied. The atoms start out in the state $\left|5\mathrm{S}_{1/2}, F = 1, m_F = -1\right\rangle$ and are transferred via a HS1 microwave sweep [289, 290] to the hyperfine state $|g\rangle \equiv \left|5S_{1/2}, F = 2, m_F = -2\right\rangle$ which is then coupled to the Rydberg state $|e\rangle \equiv \left|43S_{1/2}, m_j = -1/2\right\rangle$ (Fig. 5.1).

This is reached by two excitation laser beams counter-propagating along the z-axis, with an intermediate-state detuning $\delta/(2\pi) = 742(2)\,\mathrm{MHz}$. During the sequence, a magnetic offset field of $B \simeq 30\,\mathrm{G}$ in z-axis-direction defines the quantization axis. The field is created by the same coil as the slicing gradient but approximately half in magnitude ("half gradient"). The gradient of the magnetic field is aligned along the z-direction and the magnetic field is homogeneous in the atom plane for experiments in two dimensions. The excitation pulse was formed by switching the laser at 780 nm while the laser at 480 nm was on (Fig. 5.9). The temporal resolution of our measurement is therefore set by the rise time of the 780 nm light, which is $\simeq 40\,\mathrm{ns}$, limited by the focus size in the 350 MHz AOM. Immediately after the excitation pulse, we use near-resonant circularly polarized laser beams to drive the closed cycling transition $\left|5\mathrm{S}_{1/2}, F = 1\right\rangle \rightarrow \left|5\mathrm{P}_{3/2}, F = 2\right\rangle$ and the repump transition $\left|5\mathrm{S}_{1/2}, F = 2\right\rangle \rightarrow \left|5\mathrm{P}_{3/2}, F = 3\right\rangle$ to remove all ground state atoms, with a fidelity of 99.9 % in a few µs. The repumper is required to remove very few atoms from the $F = 1$ state which for example stayed there because of the imperfect state preparation. It turns out that all parameters for this ground state pushout have to be carefully optimized to reach the required high fidelity. We aligned the polarization of both pushout and repump beam on the atom cloud to σ^-. The pushout Rabi frequency should be not too large compared to the magnetic field splitting to avoid off-resonant saturation of non-addressed transitions, which constitute a leak out of the cycling transition. For the repumping transition we use as high power as available to repump also the shifted states in the $F = 1$-manifold. When all the ground state atoms are gone, the Rydberg atoms were pumped down to the ground state by resonantly driving the $\left|43\mathrm{S}_{1/2}, m_j = -1/2\right\rangle \rightarrow \left|5\mathrm{P}_{3/2}, F = 3, m_F = -3\right\rangle$ transition for $2\,\mu\mathrm{s}$ (for details see Sec. 5.6.2).

The former Rydberg atoms are then recaptured in a very deep three-dimensional

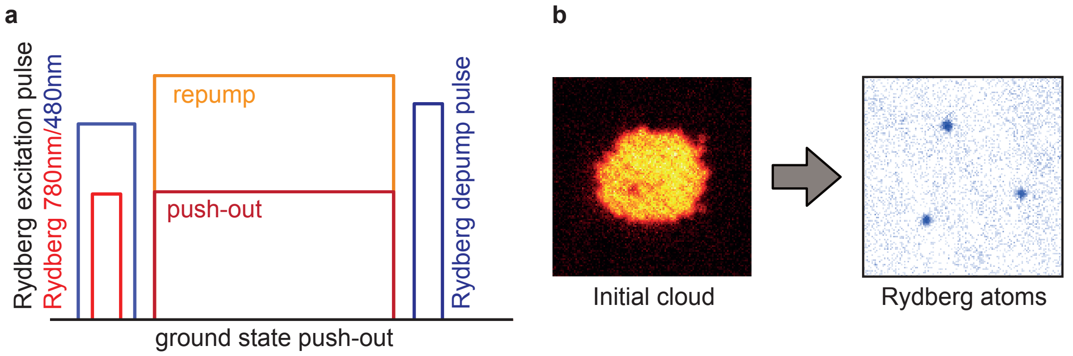

Figure 5.9.: General sequence used for Rydberg excitation and detection. **a**, The Rydberg sequence starts with few µs excitation pulses, followed by the ground state push-out and the deexcitation of the Rydberg atoms to the ground state. The atoms are typically less than 15 µs in the Rydberg state. **b**, Exemplary images of an initial Mott insulator shown in a red to yellow colour map and the three detected Rydberg atoms shown in a white to blue colour map throughout this thesis.

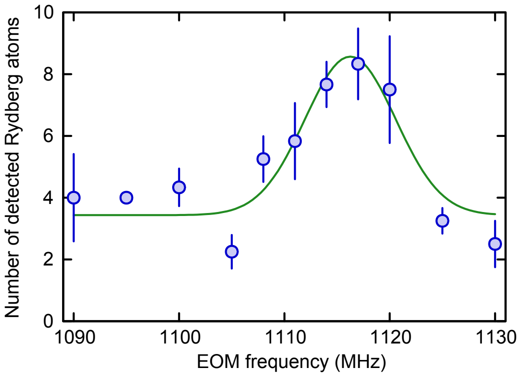

Figure 5.10: Depumping resonance $F = 1$. Probability to detect Rydberg atoms by depumping via the $F = 1$ intermediate state. The number of detected Rydberg atoms is enhanced by about a factor of two around 1116(2) MHz. The background is caused by recapture of spontaneously decayed Rydberg atoms.

lattice. The lattices are switched on within about 1 µs to about 3000 E_r each. Now the atoms are back in the lattice configuration where we can perform fluorescence imaging in an optical molasses, but the magnetic field needs to switched off slowly within $\sim$ 50 ms before switching on the molasses light. The imaging then takes place as demonstrated earlier at the experiment [21].

5.6.2. Depumping Rydberg atoms to the ground state

Alkali Rydberg atoms themselves are not suited to direct imaging techniques that leave them in the Rydberg state. Due to the decay from the Rydberg state and the fact that they are not trapped in typical optical lattices, it is also desirable for detection to transfer population from Rydberg states back to ground states. To improve the detection we stimulated the Rydberg atoms down to the $|5\mathrm{S}_{1/2}, F = 2, m_F = -2\rangle$ ground state as fast as possible after a Rydberg experiment by resonantly driving the $|43\mathrm{S}_{1/2}, m_j = -1/2\rangle \rightarrow |5\mathrm{P}_{3/2}, F = 3, m_F = -3\rangle$ transition. The Rabi frequency

intermediate F state	EOM frequency (MHz)
$F = 3$	740
$F = 2$	980
$F = 1$	1110
$F = 0$	1156

Table 5.1.: Depump resonances from the 43S state. Resonances were calculated for the half gradient of about 28.6 G. The depumping resonances via $F = 3$ and $F = 1$ were observed, the transition via $F = 2$ has no obvious advantage. The $F = 0$ transition would have the wanted decay properties, as atoms would decay from there with unity efficiency to $F = 1$, but a transition from the Rydberg state to the $F = 0$ intermediate state is forbidden.

associated with this resonant single-photon transition was typically several MHz. In combination with the short lifetime of the $5P_{3/2}$ state of 26 ns, this allows for a very efficient and fast pumping to the ground state within $< 2\,\mu s$. The laser light resonant with the transition between the Rydberg and the intermediate states is generated by a resonant free-space electro-optical modulator (EOM) in the path of the blue Rydberg laser at 480 nm, which creates a side-band at the desired intermediate-state detuning $\Delta/(2\pi) = 742\,\text{MHz}$. The other side-band and the carrier have negligible influence on the atoms in the de-excitation phase since they are off-resonant. The EOM also allows for the required fast switching of the deexcitation light within $< 1\,\mu s$.

We will discuss in the following, how the required frequency of the EOM is determined and which intermediate states are accessible for this technique. The applied magnetic offset field causes a differential shift on the $|F = 1, m_F = -1\rangle \leftrightarrow |F = 2, m_F = -2\rangle$ transition of -60.086 MHz with respect to the zero-field transition. This corresponds to $B = -60.086\,\text{MHz}/(3 \cdot 0.7\,\text{MHz/G}) = 28.6\,\text{G}$ magnetic field. The expected resonance for the side-band of the EOM hitting the $F = 3$ line of the $5P_{3/2}$ state is therefore $700\,\text{MHz} + (-2 \cdot 0.70\,\text{MHz/G} + 3 \cdot 0.93\,\text{MHz/G})B = 740\,\text{MHz}$. For the $F = 1$ line the calculation is $700\,\text{MHz} + (-2 \cdot 0.70\,\text{MHz/G} + 1 \cdot 0.93\,\text{MHz/G})B + 266.650\,\text{MHz} + 156.947\,\text{MHz} = 1110\,\text{MHz}$ (Rubidium data from [263]). The depumping via $|F = 3, m_F = -3\rangle$ has the advantage that from there only the transition to $|F = 2, m_F = -2\rangle$ is allowed, which could make some m_F dependent detection scheme possible in the future. It would be desirable to pump down via a path that forces the atoms to decay into the $F = 1$ ground state. It seems that this is impossible, as the transition via the $F = 0$ state is forbidden. The next best way is the $F = 1$ intermediate state, which gives a 83 % probability. This number is given by the branching ratio for the decay from the $F = 1$ intermediate state ($\frac{5}{24} + \frac{5}{24} = \frac{5}{12}$ to $F = 1$ and $\frac{1}{20} + \frac{1}{40} + \frac{1}{120} = \frac{1}{12}$ to $F = 2 \implies P(F = 1) = \frac{10}{12} = 83.3\,\%$). The was checked at the experiment where the probability to end up in the $F = 1$ ground state was measured as 80(4) %.

5.6.3. Detection efficiency estimates

The detection efficiency for Rydberg atoms in our setup is limited by the lifetime of the Rydberg state and by the anti-confining character of the optical lattice potential for Rydberg atoms. If a Rydberg atom decays to the ground state during the push-out pulse, it will be removed as well and not detected. The residual motion of the Rydberg atoms in the lattice potential also leads to a reduction of the detection efficiency when the atoms move away from the focal plane of the imaging system, which has a depth of focus of order 1 µm. Both effects can be minimised by decreasing the time the atoms spend in the Rydberg state after the excitation pulse. The most obvious way to do that is by increasing the efficiency of the removal pulse for the ground state atoms which allows for a reduction of this pulse time.

Determining the detection efficiency in a setup is quite difficult, as it is a parameter intrinsically connected with the detection apparatus. There are many ways to estimate the detection efficiency, but a fully independent check is not possible due to the lack of a second detection technique. But the consistency of several estimates for our detection allows to pin down the detection efficiency quite well. We will show in the following that all detection efficiency estimates yield values consistent with 65(10) %.

Detection efficiency from lifetime measurement

A measurement of the effective lifetime of Rydberg atoms in the lattice allows to estimate the detection efficiency. We assume that at a vanishing delay the extrapolation curve of the lifetime should start at 100 % detection efficiency. For longer waiting times the detection efficiency is assumed to go down (Sec. 5.6.5). We measured a lifetime of $\tau = 25(5)\,\mu\mathrm{s}$ [291] and later of 38(12) µs (Sec. 5.7.5). This corresponds to a detection efficiency estimate of 65(5) % for the experimental sequence used in Ch. 6 and a detection efficiency of 77(8) % for Ch. 7. The problem of this technique is that it assumes an exponential decay, which is not the expected shape from theory (Sec. 5.6.5). But in practice the decay can be very well approximated by an exponential function.

Detection efficiency from time evolution

Another technique is to compare measurements with theoretically calculated time evolutions for well-defined initial atom configurations. This was for example done for Fig. 6.7. Here the theoretical prediction matched the data best when assuming a detection efficiency of $\sim 75\,\%$.

A more direct check is to use the single-atom resonance and Rabi oscillation curves (Sec. 5.7.3). The maximum probability to detect a Rydberg atom there was $\approx 60(10)\,\%$. Noting that the signal will be also reduced by failure of preparing any atom in this sequence making this rather a lower bound on the detection efficiency.

Detection efficiency from Fock states

In section 7.5 we observed a staircase of Rydberg excitation number in the system. Such a measurement allows to fit the detection efficiency to the average signal of the

event	seq. no.	count
$N_\mathrm{e} = 7$, perfect	(256-1) 183-4 261-5	3(1)
$N_\mathrm{e} = 7$, 1 missing	149-2 181-2 214-2 200-3 206-3 (215-3) (149-4) 151-4 234-4 259-4 274-5	11(3)
$N_\mathrm{e} = 8$, perfect	201-5	1(1)
$N_\mathrm{e} = 8$, 1 missing	159-3 (222-3) 242-3 213-4 175-5 179-5 (252-5)	7(3)

Table 5.2.: Estimating the detection efficiency by the occurrence of near-perfect Rydberg crystals. The 413 pictures from 06/08/2013 were checked by hand and the number of events with perfect Rydberg crystals and crystals with one Rydberg atom missing were counted. For reference to the data sequence and picture numbers are given. Error bars are estimated based on images which could not be clearly assigned.

stairs with known excitation number and we obtained 62(5) % in this case.

Detection efficiency from crystal observation

Comparing the number of perfect crystals with the number of crystals with one atom missing allows to estimate the detection efficiency from the dataset with $N_\mathrm{e} = 7$ and $N_\mathrm{e} = 8$ crystals (Sec. 7.7).

The following formula allows to estimate the detection efficiency from the ratio of crystals with one atom missing to the number of perfect detected crystals. For this estimate we need to assume a high preparation fidelity and a detection efficiency that does not depend on the crystal configuration.

$$\frac{\binom{N_\mathrm{e}}{1}\alpha^{N_\mathrm{e}-1}(1-\alpha)^1}{\alpha^{N_\mathrm{e}}} = \frac{\text{number of } N_\mathrm{e}\text{-crystal events with one atom missing}}{\text{number of perfect } N_\mathrm{e}\text{-crystal events}} \tag{5.3}$$

With α the detection efficiency of a single Rydberg atom at the correct place and N_e the number of atoms in the perfect crystal. The experimental numbers required for this calculation are summarized in Table 5.2.

Solving the equation for both datasets we end up with a detection efficiency estimate of about 60(10) %.

5.6.4. Spatial resolution of the detection

Due to the lattice geometry the detection resolution of Rydberg atoms is of course limited by the lattice, which leads to discretisation of the possible positions of detected Rydberg atoms to the lattice spacing of 532 nm. Two effects reduce the spatial resolution of our detection technique compared to this ideal case. The first one is the residual hopping of the atoms during the fluorescence imaging phase. We found that such an event can occur in our experiment with a probability of approximately 1 %

per particle. When this happens, the moving atom will yield a fluorescence signal on two adjacent sites, which can be falsely attributed to two distinct atoms by the reconstruction algorithm. This detection artefact results in a correlation signal at short distances $r < 1\,\mu\mathrm{m}$ (Fig. 6.6a). However, due to their rarity these events have negligible influence on the spatial resolution. The second effect is the possible motion of the Rydberg atoms in the optical lattice potential before imaging. For Rydberg atoms, the lattice potential has similar amplitude but opposite sign compared to ground state atoms (Sec. 4.3). An excited atom therefore finds itself at a maximum of the periodic potential and can move in the xy-plane with an average velocity of $\sim 30\,\mathrm{nm}/\mu\mathrm{s}$, for a typical depth of the optical lattice potential of $V_{\mathrm{lat}} = 40\,E_{\mathrm{r}}$. Both effects lead to a possible motion of the Rydberg atoms by about one lattice site during the $\leq 10\,\mu\mathrm{s}$ of the removal pulse. The recoil velocity acquired in the two-photon excitation process is insignificant in comparison as it is oriented along z-direction and only of smaller magnitude $\simeq 4\,\mathrm{nm}/\mu\mathrm{s}$.

The spatial resolution can be also checked experimentally based on the single atom Rabi oscillation data (Sec. 5.7.3). As the position of the single initial atom is known, a measurement of the positions of Rydberg atoms allows to infer the movement of the atom from excitation to detection. For the preparation of a single atom via the spatial light modulator [50] the position is due to the phase drifts of the lattice only known to be in a 2×2 lattice site region. A measurement shows that about 5 % of the single atom events for the normal addressing are outside this region, for the distribution of the Rydberg atoms afterwards we measure about 20 %. This suggests that the Rydberg excitation causes some broadening, but consistent with the estimation above only on the order of one lattice site.

The tunnelling rate of an atom in the lattice depends exponentially on the band index, which leads to the expectation that it is either tunnelling around or fixed in position. A slowly moving atom in a deep lattice is quite unlikely. This means that the average movement of a particle is not the best measure for the spatial resolution of the Rydberg detection. A better view is that many atoms are detected more or less exactly at the initial position, while for few atoms recaptured in higher bands, the detected position is probably totally uncorrelated with the initial position. From the measurement discussed above, we can conclude that this fraction is $\lesssim 15\,\%$ of the detected Rydberg atoms. Recent experiments indicate that this fraction is lower for the 68S state [292].

5.6.5. Simplified theoretical model for the detection efficiency

In this section we will look at a very simplified model as an upper theoretical bound for the detection efficiency. We do a 1D calculation and assume that the atoms start in the lowest band Wannier function, which then expands in a repulsive lattice potential for some time t and is then recaptured in a deep optical lattice. In our setup there is some hold time for ramping magnetic fields in the deep lattice before molasses cooling sets in. Hence we assume that only atoms in states with a maximum tunnelling rate of 10 Hz are detected. This number comes from the fact that the Rydberg experiment is performed in a magnetic field, but the imaging requires zero field. In practice we have to wait for $\sim 50\,\mathrm{ms}$ before switching on the optical molasses for the fluorescence imaging to make sure that the absolute value of the magnetic field is below $100\,\mathrm{mG}$, which is required for the molasses to work properly. During this time, the population in higher bands tunnels through the lattice. As the tunnelling rate depends exponentially on the band index, the results only slightly depend on the exact tunnelling rate used as cut-off. The calculation of tunnelling matrix elements for very deep lattices is numerically unstable using the standard techniques. To avoid problems we use an extrapolation to determine the number of bands with tunnelling rates smaller than $10\,\mathrm{Hz}$. A fit yields for the number of these bands $\mathrm{floor}(0.24866 \cdot V_{\mathrm{recapture}}^{0.60853})$, as a function of the recapture lattice depth $V_{\mathrm{recapture}}$ in recoil energies. For $3000\,E_{\mathrm{r}}$ this gives 32 bands.

The calculation is done as follows: The Wannier functions are determined in a standard way by summing up all Bloch functions in a certain band [293]. They are then time-evolved using a matrix exponential taking into account the ponderomotive potential seen by the Rydberg atoms in the 1064 nm lattice (Sec. 4.3). The ponderomotive potential used here for $43\mathrm{S}_{1/2}$ is $V_{\mathrm{Rydberg}} = -0.6 V_{\mathrm{latt}}$ (where $0.600 = 0.925 \cdot 0.648$, the first factor is the free electron ponderomotive potential, the second one due to averaging in the lattice). Afterwards the overlaps to all Wannier functions on-site and off-site in all bands of interest are calculated. These calculations were checked using a full lattice diagonalization and overlaps with Bloch functions. In the end, the sum of all overlap probabilities with all Wannier functions in a band has to equal the sum of the overlap probabilities with all Bloch functions with varying q in a band, which can be used as consistency check.

Figure 5.11a shows a 1D calculation for typical parameters. The on-site recapture probability of Rydberg atoms decreases strongly for expansion times longer than $10\,\mu\mathrm{s}$. Surprisingly, the full recapture rate goes up again for longer times, as the Rydberg atoms can also be recaptured in neighbouring sites. The dependency on the initial lattice depth is illustrated in Fig. 5.11b. There is some effect of the initial lattice depth, but it is mainly negligible for relevant lattice depths and times below $10\,\mu\mathrm{s}$. The effect of the slightly changing shape of the initial ground state wavefunction is below 1 % and barely visible in the figure. The basic calculation has been also checked in an experiment with ground state atoms in the lattice using a release-and-recapture experiment and can reproduce the correct timescale of atom loss (Appendix G.8).

The 1D calculation allows to determine the 3D recapture probabilities by assuming separability of x/y/z directions. For the around $10\,\mu\mathrm{s}$ evolution time of the Rydberg state in the experiment we calculate a recapture probability of 0.76 (Fig. 5.11c), which is close to the experimentally determined values of 0.75(10) [291] and 0.62(5) [294].

Although the detection efficiency fits quite well the experimentally determined values, the calculations have to be taken with care, as some effects have been neglected here. In the following we list some of these in descending order of estimated relevance for our specific experiment:

1. molasses might not cool atoms in high lying bands efficiently
2. interaction between Rydberg atoms
3. decay of Rydberg atoms

4. recoil due to Rydberg excitation
5. forces due to electric field gradients
6. calculation only 1D (assumes separability of x/y/z and perfectly isotropic Rydberg state)
7. gravity

The dependency of the molasses detection efficiency on band index is very hard to estimate and to measure. It would be interesting to know the detection efficiency in molasses imaging in dependence of the initial band index, but such measurements would require a lot of effort. The interactions between Rydberg atoms can vary by orders of magnitude depending on the exact distance between the atoms. As the Rydberg atoms can typically only be excited with interaction energies within the effective excitation bandwidth, one can estimate the acceleration at the blockade distance, where it is largest, by: $a \approx \frac{6}{m}\left(\frac{(\hbar\Omega)^7}{C_6}\right)^{1/6}$, which leads to movements of less than 100 nm within 10 µs for our parameters. As the forces depend on the actual configuration of Rydberg excitations, the effect on the detection is not easily estimated and depends on the performed experiment, in particular on the detuning (Sec. 5.7.1).

If the Rydberg atoms decay during the expansion in the lattice, the resulting effect on the recapture probability is not clear, as this depends on the current position in the lattice potential. Probably this leads to an averaging of the depump detection efficiency and the spontaneous-decay detection efficiency. The recoil of the Rydberg excitation for the counter-propagating configuration is negligible, as it should cause movement of less than 40 nm in 10 µs. The neutral Rydberg atoms are in first order not affected by electric fields and electric field gradients over the size of the Rydberg atom are probably small. The movement due to gravity is negligible compared to the error sources above and can be estimated to less than 1 nm in 10 µs. From the calculations it seems desirable to go to a Rydberg state around 70S, as the effect of the lattice potential is reduced and a detection efficiency of > 0.9 is expected (Fig. 5.11d).

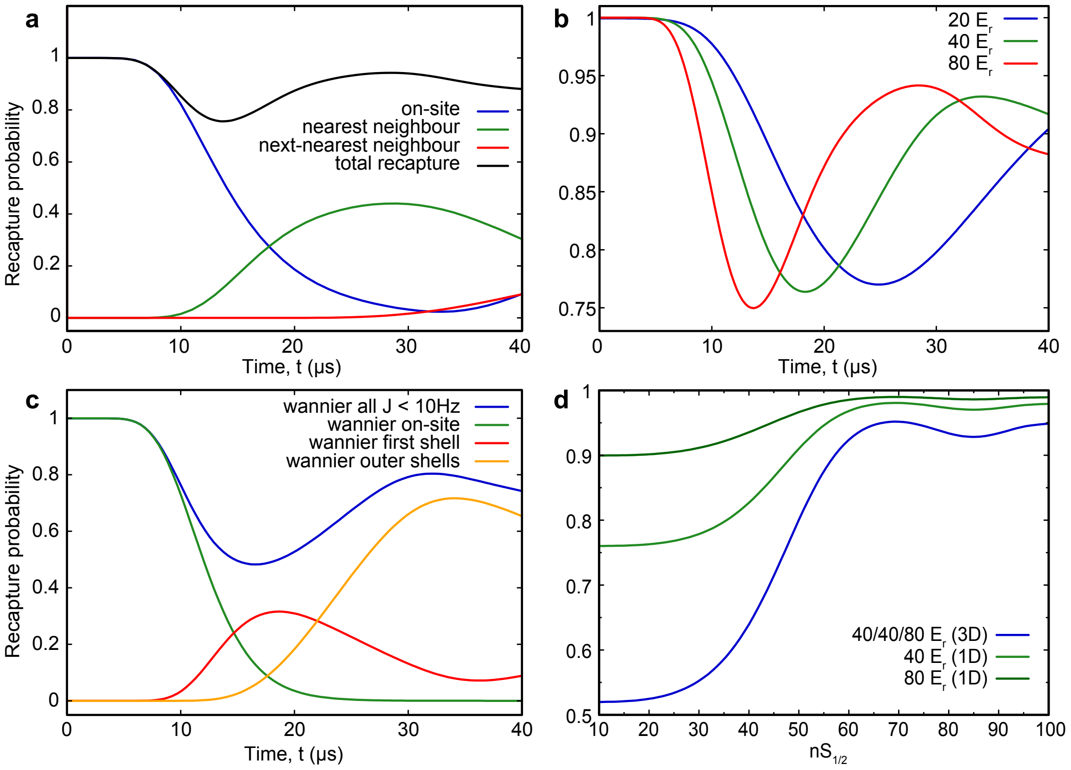

Figure 5.11.: Recapture probability calculations. **a**, Probability to recapture in neighbouring lattice sites in 1D. The atoms are released from a $80\,E_\mathrm{r}$ lattice and recaptured in a $3000\,E_\mathrm{r}$ lattice. The effect of recapturing atoms on neighbouring sites is negligible for $t < 10\,\mu\mathrm{s}$. **b**, Probability to recapture versus initial lattice depth in 1D. The recapture efficiency increases for lower initial lattice depth, as the spreading of the wave packet becomes slower. But the effect is not very big and is probably screened in the experiment due to other effects at lower lattice depth. The revival of recapture probability around $30\,\mu\mathrm{s}$ will be strongly suppressed in the experiment due to the lifetime of the Rydberg states, which is on the same timescale. **c**, Probability to recapture Rydberg atoms in a 3D lattice for the experimentally used configuration from $40/40/80\,E_\mathrm{r}$ to $3000\,E_\mathrm{r}$. Shown is the total recapture probability in any Wannier state on nearest and next nearest neighbour sites (sites further away are not occupied significantly in the given time). **d**, Probability to recapture versus Rydberg state. This graph shows directly the effect of the ponderomotive force on the recapture probability from a $40/40/80\,E_\mathrm{r}$ lattice in a $3000\,E_\mathrm{r}$ lattice after an expansion time of the Rydberg atom of $10\,\mu\mathrm{s}$. The calculations predict that the recapture probability increases tremendously when changing to a Rydberg state around 70S, which resembles the sign change of the Rydberg trapping potential in the lattice for these states (Sec. 4.3). For reference also the 1D recapture probabilities for initial lattice depth $40\,E_\mathrm{r}$ and $80\,E_\mathrm{r}$ are shown. These were used to calculate the 3D recapture probability.

5.7. Rydberg experiments with ultracold atoms

In this section experiments involving the Rydberg excitation of ultracold atoms are discussed. These experiments contribute to the understanding of our system, but are also required to determine important parameters for the following experiments, in particular the Rydberg resonance position and Rabi frequency.

5.7.1. Rydberg resonance determination

As the Rydberg atoms are interacting, the measurement of the isolated atom resonance to the Rydberg level is not as straightforward as for non-interacting systems. Our detection scheme for the Rydberg atoms does not allow for very thin large-volume clouds, as the detection volume is limited by the field of view of $\approx 64 \times 64\,\mu\text{m}^2$, the depth of focus as well as the volume of sufficient lattice depth for molasses imaging. For a typical blockade radius on the order of $5\,\mu\text{m}$, the maximum number of Rydberg atoms that can be detected is limited by the maximum area of the 2D system that can be prepared. For a dilute cloud with $\approx 40\,\mu\text{m}$ diameter, a maximum of around 50 Rydberg atoms is expected. In practice, the maximum observed is on the order of 20, due to detection efficiency and other imperfections. But this can only be achieved for very dense clouds, which is not favourable for resonance scans, as the resonance line is strongly broadened due to density-dependent interaction effects. For the optimal signal-to-noise ratio and low interaction broadening of the resonance, we use large and dilute clouds of atoms. In the optimal case the atoms should all have a distance a bit larger than the blockade radius. A resonance curve which is taken in this regime is shown in Fig. 5.12, where the linewidth of the resonance is only slightly broader than expected from the Fourier limit.

In practice it is hard to control the density of the dilute clouds accurately, especially there will be always a non-zero probability that two atoms are closer than the blockade radius. Already preparing a dilute and cold cloud is kind of a contradiction, as a cold cloud will always get dense at the centre of the harmonic confinement. We aim for a cold cloud here, as band excitations in the system can easily lead to tunnelling before or during imaging and thereby can cause uncontrolled detection errors.

In Fig. 5.13 we investigate the broadening of the Rydberg resonance for systems with varying density, comparing clouds that are diluted on purpose with a unity filling Mott insulator. We observe an increasing blue shift of the resonance with increasing density starting from the dilute cloud to the cloud with higher density and the Mott insulator. But the shift is always on the order of the width of the resonances. We note that the shape of the resonances depends on the pulse parameters, which are chosen similar for the presented curves. For the dense large clouds (purple curve), the resonance looks slightly bimodal with one peak coinciding with the low density thermal cloud resonance and one with the high-density MI resonance, which indicates that there are high- and low-density regions in the large clouds. This is one of the main issues while working with dense large clouds, as the effects of the high-density regions are always smeared out by excitations in the larger low density regions. This can be circumvented by using a Mott insulator, as we get a very homogeneous density

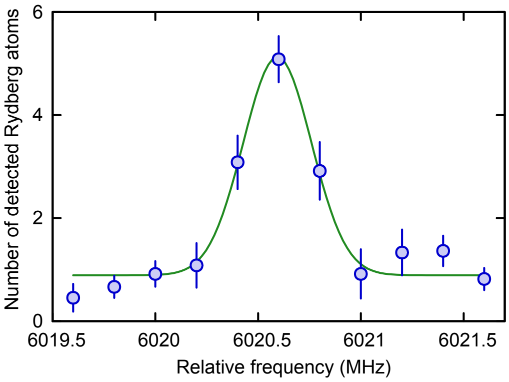

Figure 5.12: Narrow Rydberg resonance in dilute cloud. Blue points, experimental data, averaged over 12 scans. Green line, Gaussian fit. The Rydberg line is still broader than expected from the laser linewidth and Rabi frequency. The width is still broadened due to interactions and the Fourier limit of the pulse, as it does not make sense to use too long excitation pulses as this decreases detection efficiency (Section 5.6.3). Also the offset is most probably caused by the interaction broadening in the dense centre of the cloud. On the x-axis twice the synthesizer frequency is shown. The fitted FWHM is 390 kHz. Pulse length for the excitation was 2 µs, which leads to a Fourier limited FWHM of 302 kHz.

of one atom per lattice site. Also the resonance line is less broadened compared to the high-density cloud due to the more controlled initial state with lower atom number fluctuations. This controlled initial state then also allows to observe sub-Poissonian fluctuations in the number of excited Rydberg atoms (Fig. 5.13b). Sub-Poissonian fluctuations in Rydberg excitation numbers have been measured before [108–110, 114, 115] and were typically characterized by the Mandel Q parameter, which is defined as $Q = \mathrm{var}(N_\mathrm{e})/\mathrm{mean}(N_\mathrm{e}) - 1$. It becomes -1 for a Fock state and 0 for a Poissonian distribution. The Q factor cannot be lower than $-\alpha$, where α is the detection efficiency for a single Rydberg atom (Appendix C.3). We observe clearly sub-Poissonian excitation number fluctuations of $Q = -0.38(12)$ (Fig. 5.13b), but they are not saturating the bound set by the detection efficiency. This is not surprising, as we do not use pulses optimized for this purpose. The data indicates that the minimum Q factor arises not at the resonance of a single atom but at the interaction shifted resonance position in the Mott insulator. We compare the resonance data as well as the Mandel Q data with theory calculations. To make calculations feasible, typically the basis set is reduced to states where all Rydberg excitation have a minimum distance, the cut-off radius R_c (Appendix D). For resonant excitation of Rydberg atoms, a cut-off radius below the blockade radius gives already good results. Due to the blue-detuned excitation in the resonance curve, the situation is different here, as interaction shifted pair states become resonant on the blue side of the resonance. A simple estimate shows that $R_c \ll \left(\frac{C_6}{\hbar\varDelta}\right)^{1/6}$ is required for accurate results. This shows that R_c should be smaller than 5.5 sites for $\varDelta = 2\pi \cdot 4\,\mathrm{MHz}$ in our experiment for the 43S state. As a calculation with $R_c < 5.0\,\mathrm{sites}$ is challenging, we show data for varying R_c. While the calculation on the red side shows no effect on varying cut-off radius, a much

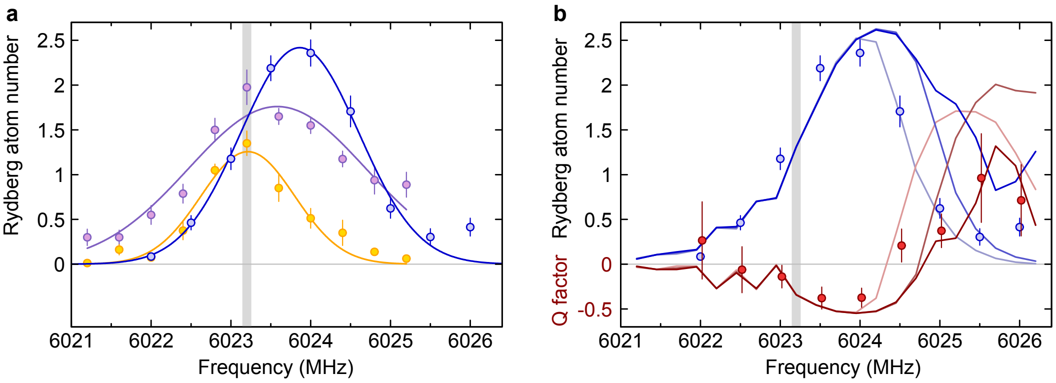

Figure 5.13.: Rydberg resonance scan in Mott insulator. **a**, Comparison of resonance scans with rectangular pulses with varying initial atom conditions. Blue points, resonance scan in Mott insulator of 192(12) atoms and radius 8.1(8) sites. The blue line is a Gaussian with centre 6023.9 MHz and sigma 0.37 MHz. The dataset consists of around 70 pictures per frequency and the excitation used the same 4 µs amplitude modulation as the sweep in Fig. 7.6a but without frequency chirp. For reference we show also two resonance curves taken with simple pulsed excitation in thermal clouds and because the Rydberg atom number is much higher here, the data is scaled down a factor of 10. Orange points, resonance curve in dilute thermal cloud, orange line, Gaussian fit ($\mu = 6023.2\,\text{MHz}, \sigma = 0.59\,\text{MHz}$). Purple points, resonance curve in a more dense cloud, purple line, Gaussian fit ($\mu = 6023.6\,\text{MHz}, \sigma = 1.11\,\text{MHz}$). For this resonance curve the line shape is asymmetrically broadened. We note that the used synthesizer frequency is half the frequency shown on the x-axis. The vertical grey bar marks the resonance position determined by the yellow data. **b**, Blue points, Mott insulator resonance curve from **a**. Red points, Mandel Q factor for the same data (slightly offset to avoid overlapping error bars). The minimum Q value for the non-optimized excitation pulse here is $-0.38(12)$. We compared these data with theoretical calculations for an ideal disc-shaped system with 197 atoms (8 sites radius) with varying cut-off radius R_c of 6.0, 5.5 and 5.0 sites (lines, light to dark colour). The theory calculations take into account a detection efficiency of 62 %.

smaller R_c is required for convergence on the blue side. For more than 2 MHz blue detuning, it is not clear that the calculation is well-converged, but the interaction energy for two Rydberg atoms at 5 sites distance is already 6.9 MHz, such that it should not be possible to excite these pairs. A comparison of the calculation with $R_c = 5$ with the experimental data shows reasonable agreement. For the resonance curve the theory fits very well on the red side, while a higher signal is expected compared to the experiment on the blue side of the resonance. For a blue-detuning of more than 1 MHz the detection efficiency in the experiment is probably reduced, as the interaction energy between the excited Rydberg atoms in this regime is high enough to cause motion of the atoms and a reduced recapture efficiency of the atoms (Sec. 5.6.5). Interestingly, the unexpectedly high signal at the rightmost experimental point of the resonance curve in Fig. 5.12b is reproduced in the theory. This is probably related to a pair excitation resonance of Rydberg atoms at a certain distance in the lattice. The Mandel Q parameter obtained by theory matches quantitatively quite well over the full detuning range. In the theory as well as the experiment we see a shift of the strongest sub-Poissonian counting statistics to the blue side of the single-atom resonance. There is also a region with significant super-Poissonian statistics but only on the blue side of the resonance in accordance with theory. Similar asymmetric behaviour in the Rydberg resonances and the Mandel Q factor has been recently observed by Schempp *et al.* [115].

5.7.2. Light shift calibration of the red Rydberg beam

The two-photon excitation scheme to the Rydberg state can be mapped to a two-level system by adiabatically eliminating the intermediate state as shown in the Appendix C.1.2. This model is good to calculate the Rabi frequency. But there are additional effects, which are often not considered in this simplification. The main effects in our system are the light shifts of the two individual laser beams. The blue power in our system is not big enough to create considerable light shifts (Table 5.3). Most of the expected light shifts are only one the order of a few ten Kilohertz and typically sufficiently stable that they can be neglected. The one light shift that exceeds all others by orders of magnitude is the light shift of the red Rydberg beam. It shifts the intermediate state and the ground state. Only the strong light shift on the ground state is relevant, as the magnitude of the light shift is small compared to the intermediate state detuning of > 700 MHz. The light shift does not cause any trouble if it is stable and calibrated. During the experiments, it turned out that there is a slight back-reflection of a few percent of the red beam from the window in front of the objective, which creates a modulation of the light-shift depending on the exact slicing position in the vertical standing wave. This is caused by the incommensurate wavelength of 780 nm of the Rydberg beam and 1064 nm of the lattice beam. By changing the adjustment of the beam we could reduce this effect to a tolerable intensity modulation of $< 10\,\%$. To allow for the compensation of the light shift, a calibration is required. For this purpose a measurement of the Rydberg resonance for various red power would do the job, but that would be rather tedious. A more effective way is to use microwave spectroscopy on the transition $|F = 1, m_F = -1\rangle \rightarrow |F = 2, m_F = -2\rangle$

light shift on ground state		
light	light shift scaling	typical light shift
red Rydberg	$371.4\,\mathrm{Hz/(W/m^2)}$	$1.66\,\mathrm{MHz}$ for $P = 22.8\,\mu\mathrm{W}$ and $w_0 = 57\,\mu\mathrm{m}$
blue Rydberg	$1.10\,\mathrm{mHz/(W/m^2)}$	$17.6\,\mathrm{kHz}$ for $P = 10\,\mathrm{mW}$ and $w_0 = 20\,\mu\mathrm{m}$
lattice (1D)	$-2.762\,\mathrm{mHz/(W/m^2)}$	$-143.5\,\mathrm{kHz}$ for $P = 100\,\mathrm{mW}$ and $w_0 = 70\,\mu\mathrm{m}$
lattice (1D)	$-1\,E_\mathrm{r}/E_\mathrm{r}$	$40\,E_\mathrm{r} \rightarrow -81\,\mathrm{kHz}$

light shift on 43S state		
light	light shift scaling	typical light shift
red Rydberg	$0.52\,\mathrm{mHz/(W/m^2)}$	$2.3\,\mathrm{Hz}$ for $P = 22.8\,\mu\mathrm{W}$ and $w_0 = 57\,\mu\mathrm{m}$
blue Rydberg	$4.2\,\mathrm{mHz/(W/m^2)}$	$67\,\mathrm{kHz}$ for $P = 10\,\mathrm{mW}$ and $w_0 = 20\,\mu\mathrm{m}$
lattice (1D)	$2.556\,\mathrm{mHz/(W/m^2)}$	$86.1\,\mathrm{kHz}$ for $P = 100\,\mathrm{mW}$ and $w_0 = 70\,\mu\mathrm{m}$
lattice (1D)	$0.600\,E_\mathrm{r}/E_\mathrm{r}$	$40\,E_\mathrm{r} \rightarrow 48.6\,\mathrm{kHz}$

Table 5.3.: Summary of light shifts of required laser beams on ground state and 43S Rydberg state. The red Rydberg beam is 742(2) MHz blue-detuned with respect to the $5\mathrm{P}_{3/2}, |F = 3, m_F = -2\rangle$-line, the blue Rydberg the same amount red-detuned with respect to the $5\mathrm{P}_{3/2}, F = 3 \rightarrow 43\mathrm{S}_{1/2}, F = 2$ transition. The retro-reflected lattice beam has a wavelength of 1064 nm and the intensity given is the incoming beam intensity. One important result here is that the lattice for the Rydberg states has a factor of -0.6 compared to the ground state, which means it is weaker in magnitude but repulsive. The most relevant light shift is the red light shift on the ground state. The light shifts of blue beam and lattice are constant as the intensity of these beams is actively stabilized. The red light shift on the Rydberg state is negligible.

(Fig. 5.14). The differential light shift equals essentially the absolute light shift of the $|F = 2, m_F = -2\rangle$ state as the detuning of the red beam is only $\approx 740(2)$ MHz and is 6 GHz farther detuned for the $F = 1$ ground state. As the scattering on the transition is too strong to perform a microwave sweep of several milliseconds for spectroscopy, we use a π-pulse. The main practical problem for the measurement is now to find the resonance, as the width of the resonance given by the microwave Rabi frequency of around $2\pi \cdot 8.9(3)$ kHz is much smaller than the light shift. In the end this limits the maximum light shift that can be measured to the point where the shot-to-shot fluctuations of the light become larger than the width of the resonance.

It would be nice to measure the intensity of the blue beam the same way as the calibration of the red beam, but the far detuning of the beam leads to extremely low differential light shifts, which are below the typical microwave spectroscopy resolution. The differential light shift of the blue beam on the $|F = 1, m_F = -1\rangle \leftrightarrow |F = 2, m_F = -2\rangle$ transition for σ^- polarization is $0.012\,\mathrm{mHz/(W/m^2)}$, which leads to a 193 Hz shift for $P = 10\,\mathrm{mW}$ and $w_0 = 20\,\mu\mathrm{m}$, which is impossible to detect for realistic magnetic field stabilities. On the field insensitive transition $|F = 1, m_F = 0\rangle \leftrightarrow |F = 2, m_F = 0\rangle$ the expected differential light shift for the parameters above is 0.5 Hz, which is also hard

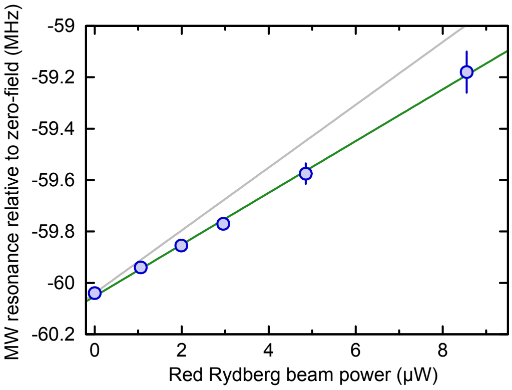

Figure 5.14.: Measured light shift of the red Rydberg beam. Blue dots, experimentally determined resonance using microwave spectroscopy. Green line, fit to the data. Grey line, theoretically expected light shift for a perfectly centred beam with the independently measured beam waist of 44(1) µm. We see a ≈ 20 % reduced light shift compared to the expectation which is probably caused by a slight misalignment. A stability measurement shows that there are about 10 % fluctuations on the light shift which are possibly caused by interference of back-reflections from the lower vacuum-window.

to measure.

5.7.3. Single-atom Rabi oscillation

The most clean technique to determine the unshifted Rydberg resonance is to prepare an isolated single atom. This is quite challenging in our setup, but using the single-site addressing techniques [22] we can prepare a single atom with about 80 % fidelity at a certain lattice site. One can then use the single atom as initial configuration for the Rydberg excitation. This method comes with the huge disadvantage of quite low signal of less than one atom per experimental run. This low signal makes the whole measurement process very time-consuming, as the maximum information per minute is 2 bit. Also the preparation of the single atom has to be checked regularly as it is expected to see no atom in most of the pictures in such an experiment. Nevertheless it is still possible to calibrate the Rabi frequency in this way, as shown in Fig. 5.15. It turns out that it is also crucial to determine the resonance position accurately enough because typical interaction effects (as discussed in Sec. 5.7.1) cause shifts of the line which are too large to measure the correct Rabi frequency. In the end the optimal way is to also check the Rydberg resonance on a single atom. An exponentially decaying oscillation is fitted to the data and yields a 1/e-decay constant of about 3 µs (Fig. 5.15). This quite fast decay of the Rabi oscillation can be explained by modelling the dephasing and decay (Appendix C.1.2). The expected 1/e-decay time of the oscillation is $\tau = 1/\mathit{\Gamma}_d = \left(\frac{1}{2}(\gamma_1 + \gamma_2 + \gamma_i) + \frac{3}{4}\mathit{\Gamma}_r\right)^{-1} \approx 4\,\mu\text{s}$ for the parameters of this experiment (Red Rabi frequency $\mathit{\Omega}_1 = 2\pi \cdot 35\,\text{MHz}$, blue Rabi frequency $\mathit{\Omega}_2 = 2\pi \cdot 13\,\text{MHz}$, intermediate detuning $\mathit{\Delta} = 2\pi \cdot 742\,\text{MHz}$, red laser linewidth $\gamma_1 = 2\pi \cdot$

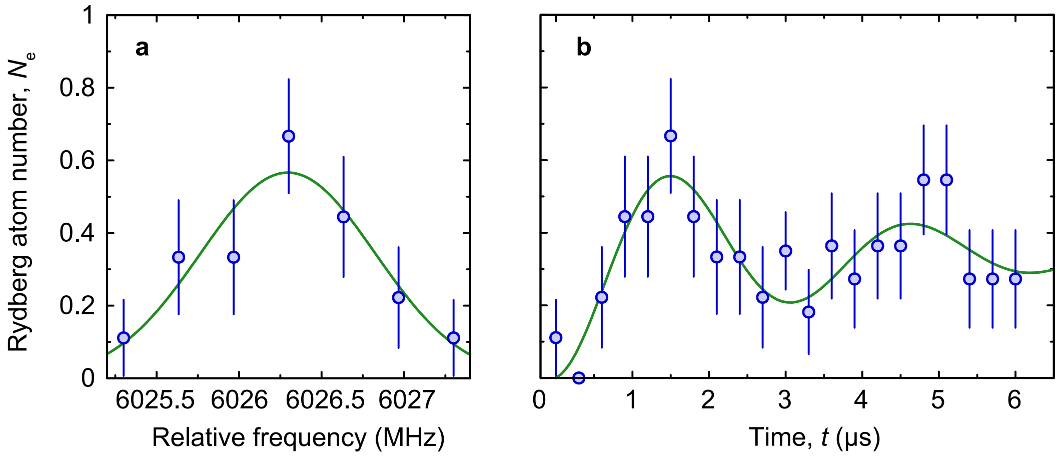

Figure 5.15.: Single atom Rydberg resonance and Rabi oscillation to the 43S state. a, single atom Rydberg resonance. On the y-axis the uncorrected probability to detect a Rydberg atom per shot is shown. The maximum signal on resonance is around 0.6, limited by detection efficiency, preparation fidelity and not perfectly optimized π-pulse for the scan. Fitted FWHM-width is 820 kHz. **b**, single atom Rydberg Rabi oscillation. Blue points, experimental data averaged over about 10 measurements per point. Green line, damped sine fit. Resulting parameters are: $\Omega \approx 320\,\mathrm{kHz}$ and $1/e$-decay time $\tau \approx 3\,\mu\mathrm{s}$.

50 kHz, blue laser linewidth $\gamma_2 = 2\pi \cdot 20\,\mathrm{kHz}$, effective dephasing due to intermediate state $\gamma_i = 2\pi \cdot 3\,\mathrm{kHz}$, Rydberg depopulation rate $\gamma_r = 2\pi \cdot 4\,\mathrm{kHz}$, for details see Appendix C.1.2). Other effects leading to a loss of visibility in the Rabi oscillation, that are not included in the model discussed above, are the finite number of two-atom events in the preparation and a drop in the detection efficiency due to the longer pulse time. In conclusion it becomes obvious from the calculation that the dephasing is dominated here by the linewidth of the red laser with FWHM-linewidth γ_1. Recent measurements with an improved locking to a cavity show nearly no decay over the first oscillation [292], confirming the findings above.

5.7.4. Investigation of 41D states

Besides the Rydberg 43S state, we also had a look at the resonances of a D-state in the experiments with cold atoms. We decided for the 41D state, as it is closest to the 43S state. As described in section 5.5.4, one can calculate the position of the expected resonances quite accurately. For the experiment the start state $5S_{1/2}, F = 2, m_F = -2$ and the σ^--polarization of the red beam were kept fixed while the blue polarization was set to an equal σ^+-σ^--mixture. For this configuration we expect to see three resonances: $41D_{3/2}, m_j = -1/2$, $41D_{5/2}, m_j = -1/2$ and $41D_{5/2}, m_j = -5/2$. The following table summarizes the resonance frequencies for the experiment at about 28.6 G and for the EIT spectroscopy in zero-field.

From the Rydberg EIT data we get a fine-structure splitting of 171.2(12) MHz for the

state	g_j	magnetic shift	synth. freq.	synth. freq. calc.	EIT synth. freq.
$41\mathrm{D}_{3/2}, m_j = -1/2$	0.8	−16.0 MHz	2174.7(8) MHz	2141 MHz	2615.5(5) MHz
$41\mathrm{D}_{5/2}, m_j = -5/2$	1.2	−120.3 MHz	2209.7(3) MHz	2175 MHz	2701.1(3) MHz
$41\mathrm{D}_{5/2}, m_j = -1/2$	1.2	−24.1 MHz	2259.95(10) MHz	2223 MHz	2701.1(3) MHz
$43\mathrm{S}_{1/2}, m_j = -1/2$	2.0	−40.1 MHz	3014.8(3) MHz	3015 MHz	3465.0(3) MHz

Table 5.4.: Spectroscopy data for 41D states. The magnetic field shift is given for the offset field in the experiment of 28.6 G. The expected synthesizer frequency is calculated using the formulas in Sec. 5.5.4. They are consistent with the measured values within the wavemeter calibration uncertainty of 40 MHz. 43S data for reference.

41D state, which is consistent with literature (from [86]: $\mathrm{D}_{5/2}$: 623.702 029 5(8) THz and $41\mathrm{D}_{3/2}$: 623.701 857 8(8) THz, this gives a splitting of 171.7(11) MHz). The difference frequency of the magnetic sub-levels of the $41\mathrm{D}_{5/2}$ state of 100.5(3) MHz, which is close to the expected differential magnetic shift of 96 MHz at 28.6 G. The reason for this slight deviation is unclear, it might be due to electric fields or non-linear magnetic shifts. Assuming an electric field and fitting the position of all three measured resonances yields a rather uncontrolled electric field estimate of roughly 400 mV/cm, which would be rather large (Table I.1). A much better way to check the electric field is to go to higher n Rydberg states as the polarizability scales with $(n^*)^7$ (Table 3.1). Disregarding the minor quantitative deviations on the order of a few percent the spectroscopy is well-controlled and all Rydberg levels were found at the expected frequencies.

5.7.5. Rydberg lifetime measurement

As the optical lattice might have an influence on the lifetime of Rydberg atoms, we checked the lifetime in a 3D lattice with depths 20/20/40 E_r. This is half the lattice depth we used for the 43S state measurements, but there is no influence within this factor of two in lattice depth on the lifetime of the 43S state. In contrast to that, we observed a slight reduction in detection efficiency of the 41D state for the higher lattice depth. For the following measurements we used the standard sequence described in Sec. 5.6.1 and varied the length of the push-out. This will kick out all atoms that decay back to the ground state while the push light is on. A problem of lifetime measurements with our detection scheme is that the time the Rydberg atoms are repelled by the lattice is also increased. This effect leads to a reduced detection efficiency for atoms that stayed longer in the Rydberg state. This looks like a reduced lifetime of the Rydberg state in the data which means that we can only measure an effective lifetime including detection efficiency, which, however, is the relevant timescale for our experiments. There is another systematic effect in the measurement, which can lead to higher lifetimes. In principal, we measure the room-temperature lifetime of the Rydberg atoms, as the deexcitation laser is state-sensitive. But atoms in other Rydberg states can also decay down to the ground state and get captured in the lattice, which mixes in a bit of zero-temperature lifetime into the measured value. The fitted lifetimes are both about 40 µs and within error bars compatible with the theoretical expectations for the lifetime at 300 K. The rather large error bars do not allow any detailed conclusion about the effects of the recapture efficiency, which should lead to oscillations on the decay curve (Sec. 5.6.5). Maybe the poor convergence of the points at certain times hints towards effects of the lattice. To conclude, we observed lifetimes of the Rydberg atoms significantly longer than the typical timescales the atoms are in the Rydberg state in our experiment and we find no clear effect on the lifetime that can be uniquely attributed to the lattice.

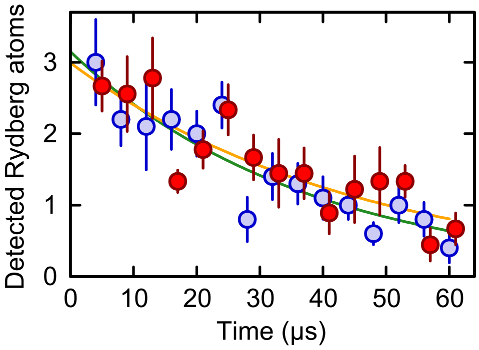

Figure 5.16: Rydberg lifetime measurement in the lattice. Blue points, average number of detected Rydberg atoms over push-out time for $43S_{1/2}, m_j = -1/2$. Red points, same for $41D_{5/2}, m_j = -1/2$. The fitted lifetimes ($1/e$-decay times) are 38(12) µs and 46(17) µs, respectively. The red points are slightly shifted in time to avoid overlapping error bars. For interpretation of the measurement and systematic errors see text.

5.8. Conclusion and Outlook

In this chapter we showed that the imaging of single Rydberg atoms can be implemented with the help of an optical lattice. We did spectroscopy of the Rydberg lines and see strong density-dependent effects on the line shape that can be explained by pair excitations at distances shorter than the blockade radius, which become resonant due to the van der Waals interaction.

The demonstrated technique to image Rydberg atoms is very promising for future experiments, as it allows on the one hand single-site imaging of Rydberg atoms and on the other hand leaves the former Rydberg atoms in the lattice, which could be used for further experiments. The optical lattice allows to scale up experiments performed in few optical dipole traps to hundreds of atoms and also allows for the implementation of techniques to map the Rydberg population back to another spin state in the ground state manifold.

The technique of exciting and imaging Rydberg atoms in an optical lattice is new and not exhaustively investigated yet. For example the effects limiting the detection efficiency are not fully understood and require further studies. Theoretically it should be possible to reach very high detection efficiencies around 90 %. There are several ideas that could improve the detection efficiency. Many variations of the detection sequence have been already tried, but up to now only a reduction of the time from excitation to recapture of the Rydberg atoms after depumping improved the detection considerably. A further decrease in time could be reached by either reducing the push-out time by applying more advanced push techniques (Appendix F) or by depumping the Rydberg atoms to another ground state and then detect only one of the ground state spin states. The problem with the spin-selective methods is that high-fidelity ground state manipulation techniques are required, caused by the huge imbalance in the number of ground state atoms and Rydberg atoms of more than a factor of hundred. This asks for ground state spin-flip or spin-selective imaging (Appendix G.3) with $> 99\,\%$ fidelity, which is probably feasible, but demanding. For example, we implemented a push-out for the $F = 1$ ground state on the $5\mathrm{S}_{1/2}, F = 1 \rightarrow 5\mathrm{P}_{3/2}, F = 0$ transition using light with mixed $\sigma^{+,-}$,π polarization, but the fidelity of this pushing technique is limited due to low hyperfine splitting of ^{87}Rb in the upper state. Maybe it is possible to increase the pushing on this line by using very low saturation of the transition, but then the pushing would become very slow. Another way to improve detection efficiency would be to find some scheme to trap the Rydberg atoms in the optical lattice. The only practical idea up to now is to go to a Rydberg state where the ponderomotive potential of the lattice averaged over the Rydberg wavefunction is slightly attractive (Sec. 4.3). But this is far from a real trap for the Rydberg atoms or magic trapping. Other techniques typically rely on special trapping laser frequencies, but in our setup there is no alternative for the lattice laser wavelength of 1064 nm. One can think about two-photon schemes involving one lattice photon for trapping, but from the numbers these ideas seem to create far too low trapping forces.

Another uncertainty in our setup is the lack of knowledge about electric stray fields. We have no electric field plates in vacuum to measure Stark shifts and the stainless steel chamber prohibits the installation of electric field plates outside the vacuum. This will limit the setup at some point to medium high Rydberg states. Recent measurements with the state 68S still show no strong electric field effects and coherence times of several microseconds [292]. From that we can conclude that the electric fields, or at least the fluctuations of the electric field are negligible for the 43S state. In principal it is also possible to reduce the electric field sensitivity of the targeted Rydberg states by mixing them with neighbouring states using off-resonant microwave fields [134], which could make the compensation of electric fields unnecessary.

6. Observation of spatially ordered structures using pulsed excitation

This chapter is based on the publication [291].

6.1. Introduction

For long times spontaneous appearance of ordering during the excitation of Rydberg atoms in ultracold atomic systems has been expected, but experimental confirmation turned out to be challenging [28, 295–304]. Observables without spatial resolution provide only indirect access to ordering and can be also misleading as they rely on the validity of the theoretical model. Nevertheless, many experiments found indirect evidence for spatial correlations [110, 115, 182, 270]. But the used detection techniques can hardly provide any detailed information about the shape of the correlation function between Rydberg atoms. The most convincing evidence is still direct imaging, even if spatial correlations can be theoretically extracted from a measurement of the full counting statistics [305].

First spatial correlations were observed by Schwarzkopf *et al.* using an field-ion-microscope, which allows for very large magnification and is not subject to the optical diffraction limit [180, 306]. This experiment resolved the blockade radius, but the effective resolution obscured information about the correlation function on distances on the order of the blockade radius. The resolution was limited due to the point spread function of the ion imaging system. Elaborate evaluation allows to model the influence of their point spread function, which reaches an extension of up to 50 % of the blockade radius, on the correlation function. In contrast, we have very precise knowledge about the point spread function in our experiment and also space is discretized by the lattice. This leads to a resolution of about the lattice spacing of 532 nm, which is approximately a factor of ten smaller than the typical blockade radius for the 43S Rydberg state used throughout this chapter. Thereby the influence of the point spread function is negligible in our setup.

One of the main new features of our experimental setup for imaging of Rydberg atoms is the very high resolution and at the same time good detection efficiency. In a series of experiments we demonstrate the possibility to excite and image Rydberg atoms in spatially ordered configurations with high resolution and extract correlation functions with high precision. The single-site resolved imaging directly allows for the determination of arbitrary spatial correlation functions [38]. This enables us to probe the spatial order of the high-density components of the excited correlated Rydberg many-body states.

6.2. Modelling of the experimental system

The physical system under study is a two-dimensional lattice of ultracold alkali atoms. The gas is prepared deep in the Mott-insulating phase, ensuring uniform filling with one atom per site within a disc of radius $R \simeq \sqrt{N_{\mathrm{at}} a_{\mathrm{lat}}^2/\pi}$, where N_{at} is the total number of atoms and a_{lat} the lattice spacing. The atoms were initially in their electronic ground state, $|g\rangle$, and then resonantly coupled to a Rydberg state $|e\rangle$. The internal dynamics of the atoms is governed by the many-body Hamiltonian:

$$\hat{H} = \frac{\hbar\Omega}{2}\sum_{\boldsymbol{i}}\left(\hat{\sigma}_{eg}^{(\boldsymbol{i})} + \hat{\sigma}_{ge}^{(\boldsymbol{i})}\right) + \sum_{\boldsymbol{i}\neq\boldsymbol{j}}\frac{V_{\boldsymbol{ij}}}{2}\hat{\sigma}_{ee}^{(\boldsymbol{i})}\hat{\sigma}_{ee}^{(\boldsymbol{j})} \,. \tag{6.1}$$

Here, the vectors $\boldsymbol{i} = (i_x, i_y)$ label the lattice sites in the plane. The first term in this Hamiltonian describes the coherent coupling with Rabi frequency Ω of the ground state to the excited state on every lattice site, where $\hat{\sigma}_{ge}^{(\boldsymbol{i})} = |e_{\boldsymbol{i}}\rangle\langle g_{\boldsymbol{i}}|$ and $\hat{\sigma}_{eg}^{(\boldsymbol{i})} = |g_{\boldsymbol{i}}\rangle\langle e_{\boldsymbol{i}}|$ are the local transition operators. The second term is the van der Waals interaction potential between two atoms in the Rydberg state. In our case it is repulsive with the asymptotic form: $V_{\boldsymbol{ij}} = -C_6/r_{\boldsymbol{ij}}^6$, with the van der Waals coefficient $C_6 < 0$ and $r_{\boldsymbol{ij}} = a_{\mathrm{lat}}|\boldsymbol{i} - \boldsymbol{j}|$ the distance between the two atoms at sites $\boldsymbol{i}$ and $\boldsymbol{j}$. The projection operator $\hat{\sigma}_{ee}^{(\boldsymbol{i})} = |e_{\boldsymbol{i}}\rangle\langle e_{\boldsymbol{i}}|$ measures the population of the Rydberg state at site $\boldsymbol{i}$. This model is valid as long as the mechanical motion of the atoms and all decoherence effects can be neglected [170, 171]. We will show in the following that this assumption is justified in our setup.

6.2.1. Validity of the model

The validity of the Hamiltonian in Eq. (6.1) for our experimental system relies on two main assumptions, which are discussed in this section: the positions of the atoms is frozen during the dynamics and all decoherence sources can be neglected.

Movement of the atoms during the dynamics

The ground state atoms were confined in a three-dimensional optical lattice of depth $V_x = V_y = 40(3)\,E_{\mathrm{r}}$ in the xy-plane and $V_z = 75(5)\,E_{\mathrm{r}}$ along the z-axis, where $E_{\mathrm{r}} = (2\pi\hbar)^2/(8ma_{\mathrm{lat}}^2)$ denotes the recoil energy of the lattice, and m the atomic mass of ^{87}Rb. For the minimum lattice depth used in the experiment of $V_{\mathrm{lat}} = 40\,E_{\mathrm{r}}$, the time associated to the inverse of the tunnelling matrix element was $\hbar/J \simeq 700\,\mathrm{ms}$, and therefore negligible compared to the timescale of the internal dynamics. The Rydberg atoms move in the lattice potential with a typical velocity of $30\,\mathrm{nm}/\mu\mathrm{s}$ (see discussion in Section 5.6.4), which can also be neglected. The acceleration of the Rydberg atoms due to their interactions is in general relevant [307]. In our case the effect is rather small with around $100\,\mathrm{nm}$ movement within $10\,\mu\mathrm{s}$ for typical experimental parameters (Sec. 5.6.5).

Light scattering from the intermediate state

The main source of decoherence when exciting Rydberg atoms via two-photon excitation schemes is typically light scattering from the intermediate state. The laser beam off-resonantly driving the ground-to-intermediate-state transition had a detuning of 742 MHz and an intensity of $\sim 450\,\mathrm{mW/cm^2}$, yielding a scattering rate of $9 \cdot 10^4\,\mathrm{s}^{-1}$. This corresponds to a coherence time of 11 µs, which is a factor of ten longer than the typical timescale of the many-body dynamics.

Laser linewidth

The finite spectral width of the optical radiation driving the transition to the Rydberg state acts as a decoherence source and was reduced by carefully stabilising the frequency of the excitation lasers with high bandwidth. We could achieve a two-photon linewidth of $\approx 70\,\mathrm{kHz}$ on a 1 s timescale, leading to a coherence time of $\sim$ 3 µs (Sec. 5.7.3). Technical details on the laser setup can be found in Section 5.5.2.

6.2.2. Properties of the frozen Rydberg gas Hamiltonian

The dynamics of the strongly correlated system governed by the frozen Rydberg gas Hamiltonian can be understood intuitively from its energy spectrum in the absence of optical driving. It is instructive to group the large number of many-body states, 2^{N_at}, according to the number of Rydberg excitations, N_e, contained in each state (Fig. 6.1). All singly excited states ($N_\mathrm{e} = 1$) with different positions of the Rydberg atom have identical energies and form a N_at-fold degenerate manifold. For multiply excited states ($N_\mathrm{e} > 1$), this degeneracy is lifted by the strong van der Waals interaction, giving rise to a broad energy band (Fig. 6.1). On the lattice the spectrum is in principle discrete, but due to the strong scaling of the $1/r^6$-potential there are extremely small as well as very large level shifts. For typical Rabi frequencies the spectrum is unresolved, but it might be possible to resolve discrete states by detuning the excitation from resonance and probing distances smaller than the on-resonance blockade radius. Starting from the ground state, the creation of the first excitation is resonant, while the sequential coupling to many-body states with larger number of excitations is rapidly detuned by the interactions. In fact, the rapid variation of the van der Waals potential with distance prevents the excitation of all those states where Rydberg atoms are separated by less than the blockade radius, R_b, defined by $\hbar\Omega = -C_6/R_\mathrm{b}^6$ (Sec. 3.2.2). The existence of this exclusion radius has a striking consequence: while the total many-body state exhibits long-range correlations on a scale of R_b [28], its high-density components with a Rydberg atom density approaching the one of a closest packing of hard spheres with radius $R_\mathrm{b}/2$ should display an ordered structure, in the sense that the position of the Rydberg atoms is correlated over the whole system size.

The excitation dynamics of all configurations should occur in a coherent fashion, resulting in highly non-classical many-body states. First, the approximate rotational symmetry of our system leads to symmetric superpositions of all microscopic configurations with different orientation but identical relative positions of the Rydberg atoms. Second, since the coupling addresses all states within an energy range $\sim \hbar\Omega$,

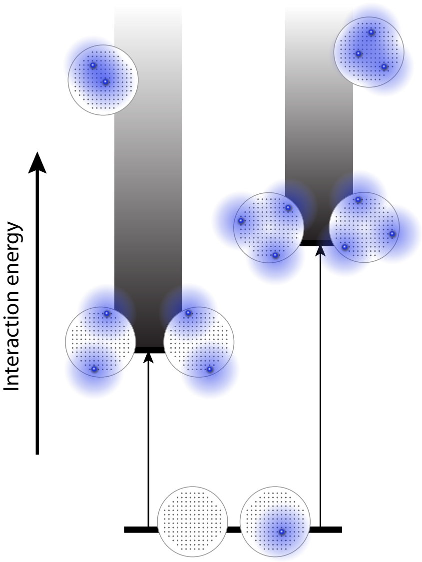

Figure 6.1.: Schematic many-body spectrum. Energy spectrum in the absence of optical driving. States with more than one excitation form a broad energy band (grey shading) above the degenerate manifold containing the ground state and all singly excited states. For each excitation number $N_\mathrm{e} > 1$, the states with lowest energy correspond to spatially ordered configurations, which maximize the separation between the Rydberg excitations. The minimal interaction energy for each excitation number (black arrows) is determined by the finite system size and increases with N_e. Possible spatial configurations of the excitations (blue dots) in the initial Mott-insulating state (black dots) are shown schematically as circular insets next to their respective interaction energy. The blockade radius is depicted by the blue shaded disc around the excitation.

it produces a coherent superposition of many-body states with different number of excitations and slightly different separation between the Rydberg atoms (Fig. 6.1). This collective nature of the excited many-body states dramatically changes the timescale on which their dynamics occurs. The coupling strength to the state with a single excitation is enhanced by a factor $\sqrt{N_\mathrm{at}} \gg 1$ [73] and the coupling to states with $N_\mathrm{e} > 1$ is similarly enhanced, with N_at replaced by the number of energetically accessible configurations in each N_e-manifold [36].

6.3. Experimental sequence

Our experiments begin with a Mott-insulator in a two-dimensional plane of about 150-390 ^{87}Rb atoms [14]. These atom numbers yield a system radius $R = 3.5$-$5\,\mu\mathrm{m}$, within which typically 80 % of the lattice sites are singly occupied. The atoms are prepared in the state $|g\rangle \equiv \left|5\mathrm{S}_{1/2}, F = 2, m_F = -2\right\rangle$, which is then coupled to the Rydberg state $|e\rangle \equiv \left|43\mathrm{S}_{1/2}, m_j = -1/2\right\rangle$ (Sec. 5.6.1). The coupling is achieved via a two-

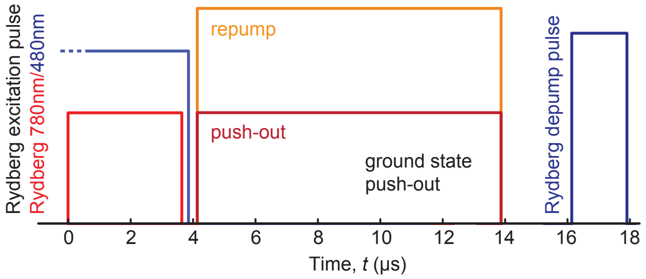

Figure 6.2.: Pulsed excitation and detection sequence. The excitation and detection sequence used throughout this chapter. A general description can be found in Sec. 5.6.1. For the excitation we used an up to 4 µs long rectangular excitation pulse, where the exact timing is done via the red beam. This is followed by the ground state push-out which takes 10 µs followed by a waiting time of 2 µs and the depump pulse of 2 µs. The purpose of the wait time is to exclude any overlap of the pump down pulse with the push-out pulse.

photon process using lasers of wavelengths 780 nm and 480 nm as described in detail in Sec. 5.3. The two-photon Rabi frequency is determined as $\Omega/(2\pi) = 170(20)\,\mathrm{kHz}$ by a Rabi-frequency measurement using the method described in Sec. 5.7.3, leading to a theoretically expected blockade radius of $R_\mathrm{b} = 4.9(1)\,\mu\mathrm{m}$. For all measurements in this chapter the waists of the red and blue laser are 57(2) µm and 17(5) µm, respectively (Sec. 5.3). The largest systems studied here have a radius of 5.4 µm, causing a variation in the coupling strength to the Rydberg state by $< 20\,\%$ over the whole system. From the waists, the power calibration of the red Rydberg beam and the two-photon Rabi frequency we extract the individual Rabi frequencies of $\sim$ 70 MHz for the red and $\sim$ 4 MHz for the blue Rydberg beam.

Following the initial preparation, the laser coupling to the Rydberg state is suddenly switched on for a variable duration t. After the excitation pulse the Rydberg atoms are detected by removing the ground state atoms from the trap, depumping the Rydberg atoms to the ground state and finally determining their position using high-resolution fluorescence imaging (Sec. 5.6.1).

The accuracy of the measurement is limited by the probability of 75(10) % to detect a Rydberg atom and by a background signal due to on average 0.2(1) non-removed ground state atoms per picture (Sec. 5.4). The spatial resolution of our detection technique is limited to about one lattice site by the residual motion of the atoms in the Rydberg state before deexcitation (Sec. 5.6.4). Repeating the experiment many times allows for sampling the different spatial configurations of Rydberg atoms constituting the many-body state and to measure their relative statistical weight.

6.4. Ordered structures in the excitation pattern

The experimental sequence described above allows to image many microscopic configurations with $N_\mathrm{e} = 2$-5 Rydberg excitations and we show typical images in Fig. 6.4. In

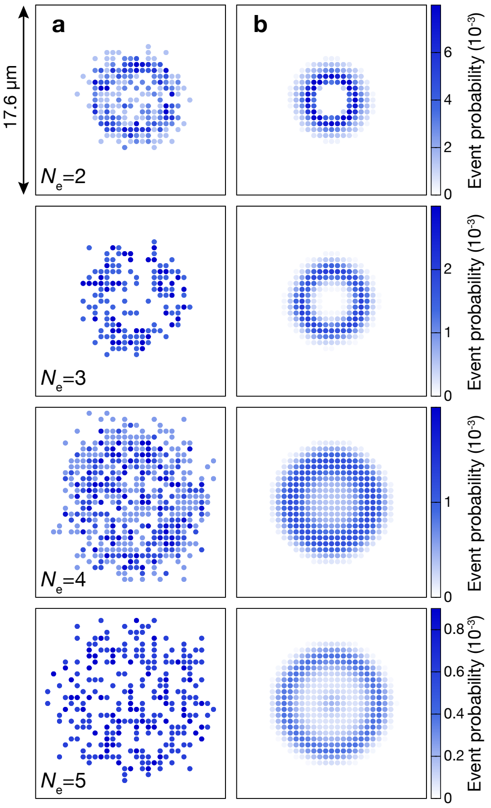

Figure 6.3: Spatial distribution of excitations before rotation. **a**, Histograms constructed from the experimental data for a number of excitations of $N_\mathrm{e} = 2$-5 (top to bottom row). The resulting ring-shaped excitation region is clearly visible for $N_\mathrm{e} = 2$ and 3. The contrast decreases for $N_\mathrm{e} = 4$ and 5 due to the lower number of occurrences in the experiment and the stronger influence of the detection efficiency. The initial atom distribution had a diameter of 7.2(8) µm and 10.8(8) µm for $N_\mathrm{e} = 2$-3 and $N_\mathrm{e} = 4$-5, respectively. **b**, Theoretical predictions for the excitation from initial clouds of same temperature and atom number as in the experiment.

order to analyse the structure of the many-body state, we group the individual images according to their number of excitations and determine the density of the excitations, $\rho_e(\boldsymbol{i}) = \left\langle \hat{\sigma}_{ee}^{(\boldsymbol{i})} \right\rangle$, where $\langle \cdot \rangle$ denotes the average over repeated measurements. These distributions display a typical ring-shaped profile (Fig. 6.3a), which results from the blockade effect and the rotational symmetry of the system. For the larger initial atom samples states with a Rydberg atom in the centre become energetically accessible, leading also in the theory to finite densities in the middle of the ring. Spatially ordered structures become evident once each microscopic configuration has been centred and aligned to a fixed reference axis (Fig. 6.4b).

The centring and alignment procedure is based on the digitised atom distribution reconstructed from the raw fluorescence images (Sec. 2.4, [21]). They reflect the Rydberg atom distribution in a circular region of interest with radius $R_\mathrm{max} = 1.5 \times R$ to reduce the effect of tunnelled atoms. Each individual image was aligned in the following way. First, we set the origin of the coordinate system to the centre of mass of the Rydberg atom configuration. Then, we determined for each atom the angle between its position vector and a reference axis, and rotated the images about the origin by the mean value of these angles (repeating this operation would leave the configuration unchanged). The histograms contain accumulated data taken at different evolution times up to 4 µs, as we found no significant temporal dependence of the excitation patterns. The theoretical calculations use the same parameters as in the experiment (including temperature and atom number distribution of the initial state) and follow the same procedure to determine the Rydberg atom densities. Both the experimental and theoretical histograms are normalised such that the value at each bin represents the probability to observe a microscopic configuration with a Rydberg atom located at this position.

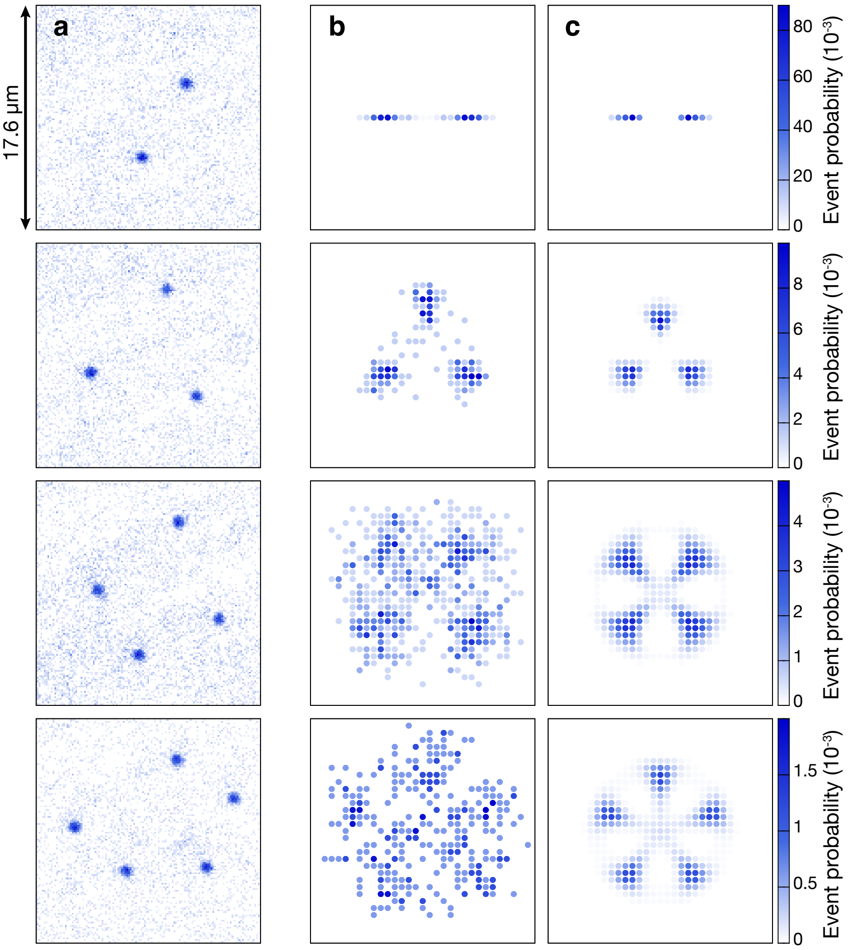

Figure 6.4.: Spatially ordered components of the many-body states. Spatial distribution of excitations for the observed microscopic configurations sorted according to their number of excitations $N_\mathrm{e} = 2$-5 (top to bottom row). **a**, Examples of false-colour fluorescence images in which deexcited Rydberg atoms are directly visible as dark-blue spots. **b**, Histograms of the spatial distribution of Rydberg atoms obtained after centring and aligning the individual microscopic configurations to a reference axis. **c**, Theoretical prediction from numerical simulations of the excitation dynamics governed by the many-body Hamiltonian of Eq. (6.1) for the same conditions as in the experiment (see Fig. 6.3).

For our smallest sample with radius $R \approx 3.5\,\mu\mathrm{m}$ we observe strong correlations between $N_\mathrm{e} = 2$ excitations that are localized at a distance $\sim 6\,\mu\mathrm{m}$. This directly resembles the interaction blockade. In the same dataset, configurations with $N_\mathrm{e} =$

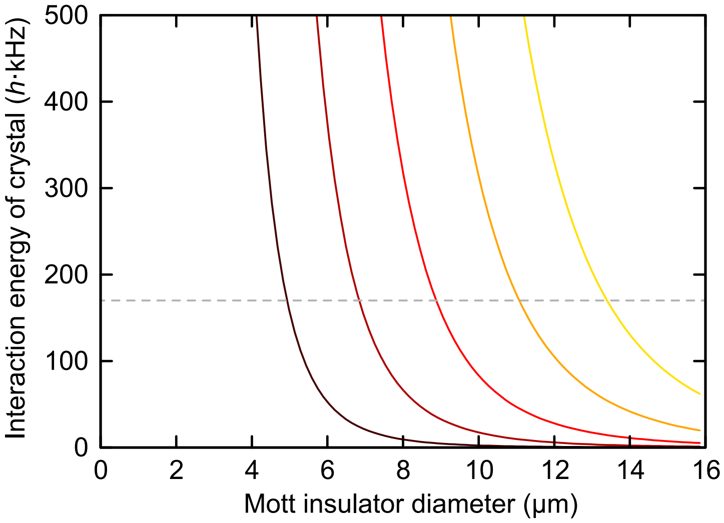

Figure 6.5.: Calculated interaction energy of crystalline configurations. From the theoretical value for the C_6 coefficient of the 43S state we obtain the interaction energy of the symmetric configurations with 2 to 6 excitations (dark red to yellow) on the border of a disc-shaped sample. The horizontal dashed grey line marks the Rabi frequency as the relevant energy scale.

3 Rydberg atoms show an arrangement on an equilateral triangle, revealing both strong radial and azimuthal ordering. These correlations persist for larger numbers of Rydberg excitations, which we can prepare in larger atomic samples with a radius $R \approx 5\,\mu\text{m}$. They form quadratic and pentagonal configurations for $N_\text{e} = 4$ and $N_\text{e} = 5$, respectively. However, since their interaction energy is larger and the coupling to states with higher N_e weaker, these states are populated only with low probability, leading to a reduced signal-to-noise ratio. At which radii a certain number of excitations can occur, becomes clear by calculating the interaction energy of the symmetric crystalline states with all atoms on the border of a disc-shaped sample (Fig. 6.5). A comparison of the interaction energy with the Rabi frequency of the excitation demonstrates that no more than 3 and 5 excitations are energetically accessible for the initial samples size of 7.2(8) µm and 10.8(8) µm, respectively (Figs. 6.3, 6.4).

Our experimental data is in good agreement with numerical simulations of the many-body dynamics according to the Hamiltonian of Eq. (6.1). The calculations use the same atom numbers, temperature and laser parameters as in the experiment (Figs. 6.3b, 6.4c) and are based on a truncation of the underlying Hilbert space, exploiting the dipole blockade, and neglect any dissipative effects ([36] and Sec. D.2). The spatial distributions of excitations provided by the simulation reproduce all the features observed in the experiment. The only apparent discrepancy is the overall slightly larger size of the measured structures, which can be attributed to the spatial resolution of our detection method, as discussed below.

6.5. Spatial correlation functions

For a more quantitative analysis of spatial correlations, we also measured the pair correlation function (Fig. 6.6a)

$$g^{(2)}(r) = \frac{\sum_{\boldsymbol{i}\neq\boldsymbol{j}} \delta_{r,r_{\boldsymbol{ij}}} \langle \hat{\sigma}_{ee}^{(\boldsymbol{i})} \hat{\sigma}_{ee}^{(\boldsymbol{j})} \rangle}{\sum_{\boldsymbol{i}\neq\boldsymbol{j}} \delta_{r,r_{\boldsymbol{ij}}} \langle \hat{\sigma}_{ee}^{(\boldsymbol{i})} \rangle \langle \hat{\sigma}_{ee}^{(\boldsymbol{j})} \rangle} , \tag{6.2}$$

which characterizes the occurrence of two excitations at a distance r from each other (see also Appendix H.3). Similar correlation functions have been investigated theoretically [28, 299, 308] and experimentally [180] in the context of Rydberg systems. Here $\delta_{r,r_{\boldsymbol{ij}}}$ is the Kronecker symbol that restricts the sum to sites $\boldsymbol{i}$,$\boldsymbol{j}$ with a distance $r_{\boldsymbol{ij}} = r$. For the numerical evaluation we use a bin width of 0.5 µm. In contrast to the spatial distributions presented above, the average includes now data with all values of N_e.

The pair correlation function $g^{(2)}(r)$ shows a strong suppression at distances smaller than $r = 4.8(2)\,\mu\mathrm{m}$, which coincides with the expected blockade radius $R_\mathrm{b} = 4.9(1)\,\mu\mathrm{m}$. Moreover, we find a clear peak at $r = 5.6(2)\,\mu\mathrm{m}$ and evidence for weak oscillations extending to the boundaries of our system. Such a correlation function is expected for a gas of quantum hard spheres [309], but the peak could be also caused by finite size effects. The fast decay of oscillations in the correlation function indicates that the overall many-body state only exhibits finite-range correlations, but without data in larger systems this is undecidable. Our theoretical calculation of $g^{(2)}(r)$ (grey line in Fig. 6.6a) exhibits similar features, but shows more pronounced oscillations and vanishes perfectly within the blockade radius. These discrepancies can be attributed to several imperfections of the detection technique. The sharp peak at short distances $r \lesssim 1\,\mu\mathrm{m}$ results from hopping of single atoms to adjacent sites during fluorescence imaging with a small probability of approximately 1 %, which is falsely detected as two neighbouring excitations. The non-zero value of $g^{(2)}(r)$ for distances $r \lesssim 3\,\mu\mathrm{m}$ arises from the imperfect removal of the ground state atoms. Finally, the shift and slight broadening of the peak in the correlation function is attributed to the residual motion of the Rydberg atoms before imaging (Sec. 6.2.1). When accounting for these independently characterized effects in the theoretical calculations (green line in Fig. 6.6a), we obtain excellent agreement with the measurements.

Since our system size is comparable to the blockade radius, the excitations in states with $N_\mathrm{e} > 1$ are localised along the circumference of the system. This essentially freezes out the radial degree of freedom leading approximately to an effective 1D system in the angular variable of the system with periodic boundary conditions. We characterize the angular order by introducing an azimuthal correlation function that reflects the probability to find two excitations with a relative angle $\mathit{\Delta}\phi$ measured with respect to the centre of mass of the distribution of excitations:

$$\tilde{g}^{(2)}(\mathit{\Delta}\phi) = \int \frac{\mathrm{d}\phi}{2\pi} \frac{\langle \hat{n}(\phi)\hat{n}(\phi+\mathit{\Delta}\phi)\rangle}{\langle \hat{n}(\phi)\rangle \langle \hat{n}(\phi+\mathit{\Delta}\phi)\rangle} . \tag{6.3}$$

Here $\hat{n}(\phi) = \sum_{\boldsymbol{i}} \delta_{\phi,\phi_i} \hat{\sigma}_{ee}^{(\boldsymbol{i})}$ is the azimuthal distribution of excitations, with $(r_{\boldsymbol{i}}, \phi_{\boldsymbol{i}})$ the polar coordinates of the site $\boldsymbol{i}$. As can be seen in Fig. 6.6b, the spatially ordered

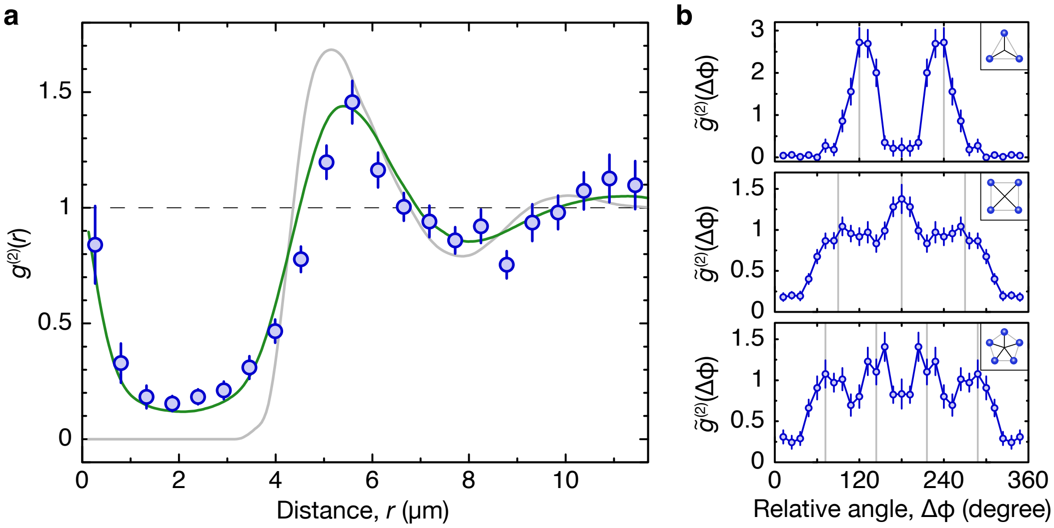

Figure 6.6.: Spatial correlation functions of Rydberg excitations. **a**, Pair correlation function. The blockade effect results in a strong suppression of the probability to find two excitations separated by a distance less than the blockade radius $R_\mathrm{b} = 4.9(1)\,\mu\mathrm{m}$. Moreover, we observe a peak at $r \simeq 5.6\,\mu\mathrm{m}$ and a weak oscillation at larger distances. The initial atom distribution had a diameter of $10.8(8)\,\mu\mathrm{m}$. The experimental data (blue circles) are compared to the theoretical prediction both taking into account the independently characterized imperfections of our detection method (green line) and disregarding these imperfections (grey line). The dashed line marks the value of $g^{(2)}$ in the absence of correlations. The error bars represent the standard error of the mean (s.e.m.) of $g^{(2)}(r)$ determined from the variance of random sub-samples. **b**, Azimuthal correlation function. The spatially ordered structure of the high-density components is best visible in the angular correlations around the centre of mass of the distribution of excitations, characterized by the correlation function $\tilde{g}^{(2)}(\Delta\phi)$ defined in Eq. (6.3). By construction, this function is symmetric around 180°. Correlations are observed at the angles expected for the respective configurations shown in the insets. The peaks close to 180° are more pronounced since the centre of mass of a configuration is likely to lie close to the intersections of the diagonals, due to the blockade effect. Error bars, s.e.m.

structure is clearly visible as correlations at relative angles $\Delta\phi = \nu \times 360°/N_\mathrm{e}$, with $\nu = 1, 2, \ldots, N_\mathrm{e}$, even for the largest excitation numbers.

6.6. Excitation dynamics

We finally analyse the many-body excitation dynamics of the system. In Fig. 6.7a we show the time evolution of the average number of Rydberg excitations, $\bar{N}_\mathrm{e} = \sum_i \left\langle \hat{\sigma}_{ee}^{(i)} \right\rangle$, which quickly saturates to a small value $\bar{N}_\mathrm{e} \simeq 1.5$, much smaller than the

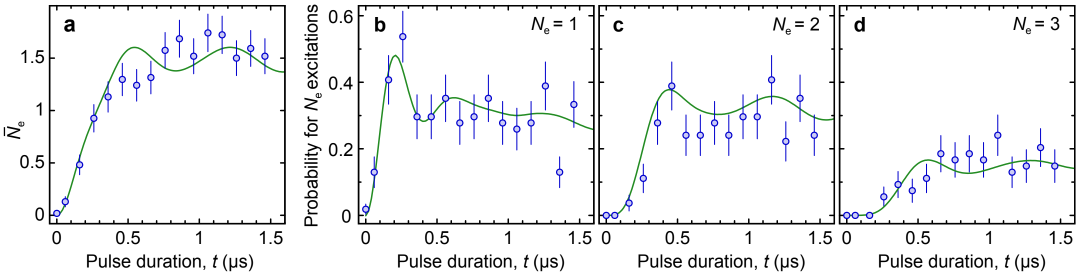

Figure 6.7.: Time evolution of the number of Rydberg excitations. a, Average number of detected Rydberg atoms as a function of the excitation pulse duration. Error bars, s.e.m. **b-d**, Time evolution of the probability to observe $N_\mathrm{e} = 1$ (**b**), $N_\mathrm{e} = 2$ (**c**) and $N_\mathrm{e} = 3$ (**d**) Rydberg excitations. The experimental data (blue circles) are compared to the theoretical prediction (green line), which is based on initial ground state atom distributions observed in the experiment and neglects all decoherence effects. It takes into account the finite detection efficiency as a free parameter (75 %). Error bars, s.e.m.

total number of atoms in the system, $N_\mathrm{at} = 150(30)$. This low value already shows that our system is strongly dominated by the blockade. The saturation is reached in ~ 500 ns, a factor of ten faster than the Rabi period $2\pi/\Omega$, due to the collective enhancement of the optical coupling strength. The probability to observe N_e Rydberg excitations shows a similar saturation profile for each excitation number N_e (Fig. 6.7b-d), but on a timescale that increases with N_e, from about 200 ns for $N_\mathrm{e} = 1$ to about 600 ns for $N_\mathrm{e} = 3$. This can be attributed to the variation of the collective enhancement factor associated with the number of energetically accessible microscopic configurations for a given N_e (Sec. 3.3). The theoretical excitation dynamics corresponding to the Hamiltonian (6.1) shows remarkable agreement with the experimental data when including the finite detection efficiency (Appendix C.2). This provides evidence that the dynamics observed in the experiment is coherent on the observed timescales, which is expected, as the dynamics proceeds on a timescale much shorter than the lifetime of the Rydberg state of 25(5) µs in the lattice and the decoherence time due to other effects discussed in Sec. 6.2.1. The absence of high-contrast Rabi oscillations in the time evolution of the average number of Rydberg excitations is caused by the strong dephasing between many-body states with different interaction energies arising from the different spatial distribution of excitations. However, remnant signatures of Rabi oscillations can still be observed, as predicted [310]. In particular, the population of the singly excited states shows a peak around $t = 200(50)$ ns (Fig. 6.7b), which matches the π-pulse time of the enhanced Rabi frequency $\pi/\left(\sqrt{N_\mathrm{at}}\Omega\right) = 240(40)$ ns. Although the dynamics does not look coherent, observations indicate that time evolution is coherent, but the measurement basis is highly unsuited to uncover the coherence. To provide further evidence for the coherence of the dynamics we took additional data to look at the spatially resolved dynamics of the excitation.

For this purpose, we focus on the subset of microscopic configurations with only one excitation. Because the blockade radius is only slightly smaller than the system

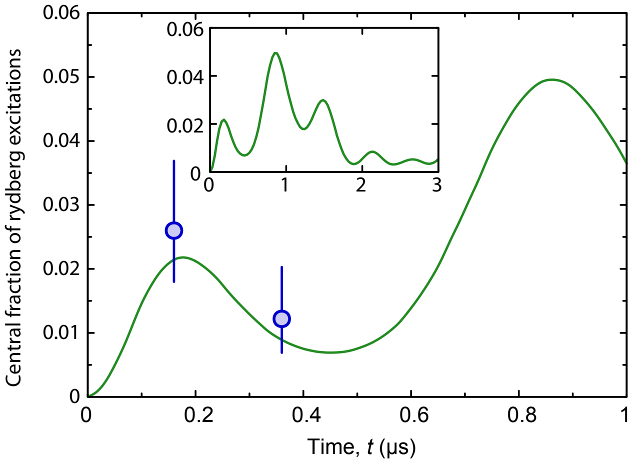

Figure 6.8.: Excitation dynamics at the centre of the system. Relative number of excitations in the central nine sites as a function of the excitation pulse duration for microscopic configurations with a single excitation $N_e = 1$. The theoretical calculation (green line, inset) reveals the coherent evolution, which is hardly visible in the time evolution of the total excitation number. Two experimental points (blue circles) were obtained from an additional dataset containing about 800 images per pulse duration. It was characterized by the temperature of the initial state $T = 9(2)\,\mathrm{nK}$, the atom number $N_{\mathrm{at}} = 210(30)$ and the radius $R = 4.2(5)\,\mu\mathrm{m}$. These experimental parameters were included in the numerical simulation. The error bars denote one standard deviation of the mean (s.e.m.).

diameter, only those configurations in which the excitation is located close to the edge of the system are significantly coupled to configurations with two excitations. This results in unequal time constants for the dynamics at different distances r from the centre and leads to a strong spatial dependence of the dynamics. We have investigated this effect theoretically by calculating the time evolution of the relative probability for the excitation close to the centre of the system (green line in Fig. 6.8). In contrast to Fig. 6.7, we now observe Rabi-like oscillations with notable amplitude over much longer timescales. We performed the corresponding measurement in the experiment for two pulse durations (blue circles) and find reasonable agreement. This kind of measurement requires a huge amount of statistics as most of the observed events show more than one excitation but we postselect for the evaluation on single atom events. But already the two data points show that the dynamics is not consistent with a simple saturation curve and the consistency with theory indicates coherence in the collective excitation.

6.7. Summary and Outlook

In conclusion, we demonstrated the techniques to optically detect Rydberg atoms with unprecedented spatial resolution and good detection efficiency by recapturing them in an optical lattice. The strongly correlated excitation dynamics of a resonantly driven frozen Rydberg gas was characterized, indications for coherent dynamics were found and we observed ordered Rydberg configurations of the excited many-body states by post-selecting to the components with highest Rydberg atom numbers. Our measurements triggered further theoretical work [302], confirming the distribution of Rydberg atoms and the spatial correlation function using a semi-classical approach. The demonstrated excitation of ordered states is not deterministic and only visible due to the post-selection on fixed excitation numbers. We will show in the next chapter, how ordered Rydberg crystals can be prepared deterministically by using an adiabatic scheme, which involves laser sweeps with amplitude and frequency modulation.

7. Crystallization in Ising quantum magnets with power-law interactions

This chapter is based on the publication [294].

7.1. Introduction

While the non-deterministic preparation of ordered Rydberg atom configurations in the last chapter required post-selection and the observed many-body state did not show crystalline order, the main goal of this chapter is to show how to obtain crystalline states in a Rydberg system using an adiabatic preparation scheme. The preparation of crystalline structures corresponds to the preparation of the ground state of the system and not a highly excited state as in the last chapter. This asks for advanced control techniques, as the long-range interactions couple all parts of the system, such that not only local but also global adiabaticity is required to prepare ground states in such a many-body system with long-range correlations. We consider both the detuning from resonance and the Rabi frequency as time-dependent control parameters of the Hamiltonian to drive the system to the targeted crystalline state. Two major advances form the basis of our measurement. First, we use an improved initial state preparation, which starts from a Mott insulator with unity filling, that is then cut to the desired pattern using the single-site addressing technique (Sec. 7.4.1). Second, we implemented excitation pulses with amplitude and frequency modulation, given by theoretically calculated waveforms, to transfer the system to a crystalline state as adiabatically as possible.

The Hamiltonian describing our system maps to a quantum Ising model with power-law interactions, as demonstrated in the next section, and the preparation therefore corresponds to the realisation of magnetic states with long-range correlations. The van der Waals interaction potential between the Rydberg atoms is not long-range in the strict sense [311], but it spans nearly the whole finite system size and therefore couples the system over long distances in relation to the system diameter. Ising spin models with power-law interactions have been investigated theoretically as tractable model systems [252, 312–317]. Recently there has been an increasing interest in long-range interacting quantum spin systems [9], especially in the propagation dynamics of spin Hamiltonians with long-range interactions [33, 34]. This also is caused by the recent success of the first spin-exchange experiments with ultracold molecules in an optical lattice [35]. Rydberg atoms offer stronger interactions leading to orders of magnitude faster timescales in the dynamics and making the Rydberg approach to spin physics complementary to these systems.

7.2. Mapping the Rydberg Hamiltonian to a quantum Ising model

In comparison with the Hamiltonian used in Chapter 6 the excitation to the Rydberg states has to be modelled here including the time-dependent Rabi frequency and detuning. The system is then described by the following Hamiltonian:

$$\hat{H} = \frac{\hbar\Omega(t)}{2}\sum_{\boldsymbol{i}}\left(\hat{\sigma}_{eg}^{(\boldsymbol{i})} + \hat{\sigma}_{ge}^{(\boldsymbol{i})}\right) + \sum_{\boldsymbol{i},\boldsymbol{j},\boldsymbol{i}\neq\boldsymbol{j}} \frac{V_{\boldsymbol{ij}}}{2}\hat{\sigma}_{ee}^{(\boldsymbol{i})}\hat{\sigma}_{ee}^{(\boldsymbol{j})} - \hbar\Delta(t)\sum_{i}\hat{\sigma}_{ee}^{(\boldsymbol{i})} \; . \tag{7.1}$$

Here, the vectors $\boldsymbol{i} = (i_x, i_y)$ label the position of the atoms on the lattice and we use the same definitions for the operators as in the Hamiltonian Eq. (6.1). The difference to the Hamiltonian discussed in the previous chapter is the time-dependence of the Rabi frequency and the additional term taking into account a time-varying detuning $\Delta(t) = \omega_l(t) - \omega_0$ of the laser frequency ω_l from the atomic resonance ω_0. The Hamiltonian Eq. (7.1) can be rewritten as a quantum Ising spin model with van der Waals interactions. To that end, we identify the two spin-states as $|\downarrow\rangle \equiv |g_{\boldsymbol{i}}\rangle$ and $|\uparrow\rangle \equiv |e_{\boldsymbol{i}}\rangle$. Here we omit the site label in the spin description to simplify the notation. With this definition the operators $|\uparrow\rangle\langle\downarrow|$ and $|\downarrow\rangle\langle\uparrow|$ describe a spin flip from the ground state $|\downarrow\rangle$ to the Rydberg state $|\uparrow\rangle$ and vice versa, while the operators $|\uparrow\rangle\langle\uparrow| = \hat{n}_\uparrow$ and $|\downarrow\rangle\langle\downarrow| = \hat{n}_\downarrow$ represent the local Rydberg and ground state population. We identify the coherent coupling in the first term $\frac{1}{2}\left(\hat{\sigma}_{eg}^{(\boldsymbol{i})} + \hat{\sigma}_{ge}^{(\boldsymbol{i})}\right)$ with the $\hat{\sigma}_x$ spin-1/2 operator, defined as $\hat{\sigma}_x = (|\uparrow\rangle\langle\downarrow| + |\downarrow\rangle\langle\uparrow|)/2$. The other terms are rewritten by noting that $\hat{\sigma}_{ee}^{(\boldsymbol{i})} = \frac{\mathbb{1}}{2} + \hat{\sigma}_z$, where $\mathbb{1}$ is the identity operator and $\hat{\sigma}_z = (|\uparrow\rangle\langle\uparrow| - |\downarrow\rangle\langle\downarrow|)/2$. Neglecting constant offset energies this leads to the second and third term in the spin Hamiltonian (7.2), where we defined $\mathcal{I}_i = \sum_{\boldsymbol{j},\boldsymbol{i}\neq\boldsymbol{j}} \frac{V_{\boldsymbol{ij}}}{2}$. Finally we obtain the following spin Hamiltonian

$$\hat{H} = \hbar\Omega(t)\sum_{\boldsymbol{i}}\hat{\sigma}_x^{(\boldsymbol{i})} + \sum_{\boldsymbol{i}}[\mathcal{I}_{\boldsymbol{i}} - \hbar\Delta(t)]\hat{\sigma}_z^{(\boldsymbol{i})} + \sum_{\boldsymbol{i},\boldsymbol{j},\boldsymbol{i}\neq\boldsymbol{j}}\frac{V_{\boldsymbol{ij}}}{2}\hat{\sigma}_z^{(\boldsymbol{i})}\hat{\sigma}_z^{(\boldsymbol{j})} \; . \tag{7.2}$$

The first two terms of the Hamiltonian describe a transverse and longitudinal magnetic field. The former is controlled by the coherent coupling between ground and Rydberg state with the time-dependent Rabi frequency $\Omega(t)$. The detuning $\Delta(t)$ determines the longitudinal field and can be used to counteract the here positive energy offset $\mathcal{I}_i$. The offset $\mathcal{I}_i$ is spatially dependent and causes a pinning of the first two excitations for $N_\mathrm{e} > 1$ to the boundary. It becomes homogeneous and therefore irrelevant for infinite systems. The third term, a $\sigma_z\sigma_z$ interaction, arises due to the van der Waals interaction potential between two atoms in the Rydberg state.

This Hamiltonian has been at the focus of theoretical and experimental interest due to its rich variety of strongly correlated magnetic phases [29, 31, 33, 34, 110, 318, 319]. By varying Rabi frequency and detuning the different phases can be explored. In contrast to typical cold atomic models like the Bose-Hubbard model, here all states with $\Omega > 0$ only exist in the presence of continuous optical driving. This will of course limit the lifetime of the system, but dynamics can be much faster than dissipation and allows for the study of these phases.

In the following we discuss the phase diagram in more detail. In the classical limit ($\mathit{\Omega} = 0$) and for $\mathit{\Delta} > 0$, the many-body ground states are crystalline states with vanishing fluctuations in the total magnetization M. For fixed total atom number N, the magnetization $M = 2N_\uparrow - N$ is determined by the spin-$\uparrow$ component $N_\uparrow = \sum_{\boldsymbol{i}} \langle \hat{n}_\uparrow^{(\boldsymbol{i})} \rangle$ up to the constant offset given by N. The magnetization density $m = M/N$ grows in steps with increasing $\mathit{\Delta}$. The stability range of a state with a certain magnetization density depends on the change in interaction energy with a spin flip. In the thermodynamic limit the magnetization density m forms a complete devil's staircase [320] as a function of $\mathit{\Delta}$. Due to the large blockade radius compared to the distance between neighbouring atoms, we are limited in the experiment to a low magnetization $N_\uparrow \ll \ell$, corresponding to the regular part of the devil's staircase with magnetization densities $1/\ell, 2/\ell, \ldots$. In a one-dimensional chain in this regime, the number of spin-$\uparrow$ atoms increases by one at the critical detunings $\ell^6 \hbar \mathit{\Delta}_\mathrm{c} \approx 7 \, |C_6| \, N_\uparrow^6 / a_\mathrm{lat}^6$ separating successive crystal states with a lattice spacing $a_\mathrm{lat} \ell / (N_\uparrow - 1)$ [36]. In practice the experimental parameters do not allow to observe this staircase in $\mathit{\Delta}$, as the required accuracy and range for the detuning are illusive to reach in an experiment. There might be a parameter range that allows for the observation of parts of the devil's staircase, but this requires a blockade radius on the order of the lattice spacing. For our system extreme detunings of hundreds of Megahertz would be required, but already simple estimations show that such high-density excited configurations cannot be stable on a timescale required for detection (Sec. 5.6.5).

Non-vanishing laser coupling introduces quantum fluctuations that first cause defects in the crystal and for strong coupling destroy the order [29, 31, 318, 321]. The corresponding scenario is shown schematically in Fig. 7.1a. Due to the finite size of the system the transitions are slightly broadened in the $(\mathit{\Omega}, \mathit{\Delta})$ parameter space (the figure was calculated for $N = 7$), but extended lobes corresponding to crystalline states can still be well identified. The scaling of the axes in Fig. 7.1a is chosen such that several crystalline phases for one system size are visible. Due to the strong scaling of the van der Waals interaction with distance, typically maximally two lobes are experimentally accessible for a fixed system size.

The deterministic preparation of crystalline states requires fast dynamical control due to the short lifetime of the Rydberg states of typically several tens of microseconds compared to the gaps in the many-body spectrum. Our initial state with all atoms in their electronic ground state ($N_\uparrow = 0$) coincides with the many-body ground state of the system for negative detuning and $\mathit{\Omega} = 0$. Since for small coupling strength $\mathit{\Omega}$ the energy gap to the first excited state closes at the transition points $\mathit{\Delta}_\mathrm{c}$ between successive $N_\uparrow$-manifolds, $\mathit{\Omega}$ and $\mathit{\Delta}$ have to be varied simultaneously in order to maximize the adiabaticity of the preparation scheme. An intuitive and simple choice of the path $(\mathit{\Omega}(t), \mathit{\Delta}(t))$ starts by slowly switching on the coupling $\mathit{\Omega}(t)$ at a large negative detuning $\mathit{\Delta}(t) = \mathit{\Delta}_\mathrm{min}$ [30, 36, 37]. This brings the system into the disordered phase, where the change of $N_\uparrow$ can be adiabatic. Next, the detuning is increased to the desired final blue-detuned value $\mathit{\Delta}_\mathrm{max} > 0$, followed by a gradual reduction of the coupling strength

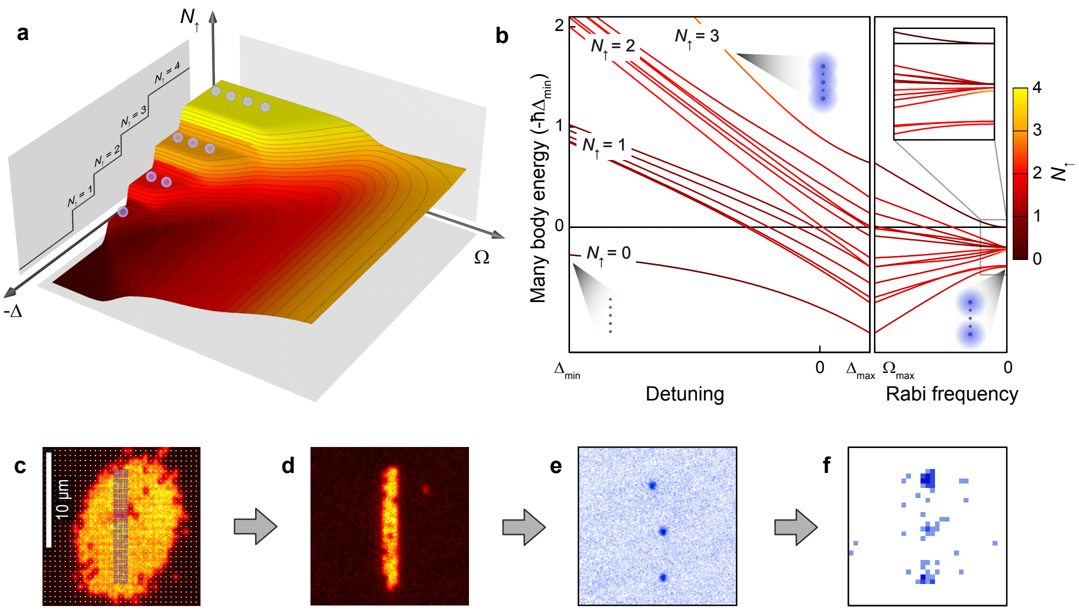

Figure 7.1.: Schematic illustrating the phase diagram, energy spectrum and experimental sequence. a. Schematic phase diagram. The colour scale indicates the number of spin-↑ atoms $N_\uparrow$ in the many-body ground state of a one-dimensional system. $N_\uparrow$ is also visualized in the crystalline phase by the small spheres. For illustration, the detuning $\varDelta$ and Rabi frequency $\varOmega$ axes are rescaled by their sixth root. **b**, Schematic illustrating the evolution of the many-body spectrum during a sweep, where coupling strength $\varOmega(t)$ and detuning $\varDelta(t)$ are controlled. The spectrum was calculated for an exemplary 1D system of five atoms, where the individual states can be still distinguished in the graph. First, the detuning is changed from $\varDelta_{\mathrm{min}}$ to $\varDelta_{\mathrm{max}}$ at constant Rabi frequency $\varOmega_{\mathrm{max}}$, with $\varDelta_{\mathrm{max}}$ chosen to prepare $N_\uparrow = 2$ (left panel). Subsequently, the Rabi frequency is reduced linearly from $\varOmega_{\mathrm{max}}$ to 0 (right panel). The inset is a zoom into the end of the sweep focussing on the shrinking gap between the energy levels. The colour of each line indicates the mean number of spin-↑ atoms in the many-body state. For large negative detuning the four different manifolds correspond to the crystalline states with fixed magnetization given by $N_\uparrow$ as indicated in the figure. In three limiting cases in which the states become classical the spatial distribution is shown schematically (blue circles: Rydberg atoms, grey circles: ground state atoms). **c-e**, Exemplary fluorescence pictures from different times in the experimental cycle. **c**, Mott insulator with lattice sites (white dots) and spatial light modulator pattern (semi-transparent overlay). **d**, Initial atom configuration, **e**, Single shot Rydberg or spin-↑ pattern. **f**, Spatial Rydberg density or magnetization density after averaging 40 experimental runs (darker colour corresponds to more detected atoms).

Ω to zero. Choosing Δ_{max} between the critical detunings Δ_{c} of adjacent $N_{\uparrow}$-manifolds, thereby yields a crystalline state with a well-defined and controllable magnetization. In the final stage of this last step the energy of several many-body states becomes nearly degenerate, as illustrated in Fig. 7.1b for an exemplary system of five atoms. These lowest many-body excited states all belong to the same $N_{\uparrow}$-manifold but show a finite density of dislocations with respect to the perfectly ordered classical ground state. In practice this leads to unavoidable non-adiabatic transitions at the end of the laser pulse, resulting in non-classical crystalline states composed of spatially localized collective magnetic excitations [36]. For states with Rydberg atoms spaced by approximately the blockade radius the interaction energy changes strongly for large dislocations, and only states with very small spatial deviations from the ground state are contained in the superposition. If the magnetization density is lower, also states with more and larger dislocations are energetically close-by.

7.3. Adiabatic transfer – From qubits to many-body systems

Adiabatic state preparation is most often considered in two-level systems. A basic example is the adiabatic transfer of the state $|0\rangle$ to $|1\rangle$ in a qubit. When the qubit is implemented by the two hyperfine states $|F = 1, m_F = -1\rangle$ and $|2, -2\rangle$ in rubidium, this can be accomplished by an HS1 sweep, as used in our experiment [290]. The gap is large in the beginning and the end of the sweep and in between the avoided crossing exhibits a gap determined by the Rabi coupling. By that the timescale for an adiabatic transition is only limited by Rabi frequency and the transition probability can be approximated by the Landau-Zener formula [322].

One can look at the intermediate regime between a single qubit adiabatic transfer and a transfer in a many-body system by investigating a system of many qubits with variable interaction [323]. In systems with power-law interactions, many excited states have very low interaction energies. This comes with the existence of low excitations gaps, which limit the timescale for the adiabatic transition. In the Rydberg system discussed here, the Rabi frequency is typically not limiting the speed of the preparation but the small excitation gaps in the absence of optical driving. This leads to the general difficulty to stay adiabatic in the end of a sweep, as one is typically interested in the preparation of states which survive after the laser is switched off. While the timescale for the sweep at strong optical driving is determined by the Rabi frequency, during the switch-off process the Rabi frequency has to be reduced. At some point the intrinsic gaps of the many-body system determine the required timescale of the sweep.

In conclusion, the minimum time for adiabatic transfers in many-body systems is theoretically limited by the gaps in the spectrum in absence of optical driving, whereas in a two-level system very high speeds can be reached by just increasing the Rabi frequency. This already suggests that the last part of the adiabatic sweep needs to be rather long for our system. For the search of a good choice for an adiabatic sweep we use optimizations based on numerical simulation of the Hamiltonian (Appendix E).

7.4. Experimental sequence

The basic experimental sequence is similar to the one used in Chapter 6. For our measurements we chose line- or disc-shaped atomic samples of well-controlled length or radius. The line had a width of three lattice sites and a variable length ℓ. Since this width was much smaller than the blockade radius of approximately nine sites, this geometry can theoretically be described by an effective one-dimensional chain with a collectively enhanced Rabi frequency $\sqrt{3}\Omega$. We checked this equivalence explicitly by a numerical calculation for a system length of 23 sites and both results coincide to a precision of 1 %.

To minimize fluctuations in cloud size and position, we prepared the initial atomic density distribution precisely by cutting out the desired cloud shape from the initial Mott insulator using a spatial light modulator (Sec. 7.4.1). The final preparation step was to transfer the remaining atoms via a microwave sweep to the $|2,-2\rangle$ state. The average filling was 0.8 atoms/site and at the edge it dropped to below 0.1 atoms/site within one lattice site.

The coupling to the Rydberg state was realized as described before (Chapter 6) [291]. Detailed coupling beam parameters are summarized in Table 7.1. Fast control of the Rabi frequency $\Omega(t)$ and the detuning $\Delta(t)$ was implemented by tuning intensity and frequency of the red coupling laser (Sec. 7.4.2). Finally, the Rydberg atoms were detected with high spatial resolution by fluorescence imaging after removing the ground state atoms from the trap and depumping the Rydberg state back to the ground state (Fig. 7.1e and Sec. 5.6). The excitation and detection sequence was shortened compared to previous measurements by optimizing the push-out pulse (Fig. 7.2). The spatial distribution of Rydberg atoms and, therefore, the magnetization profile was measured by averaging over at least 40 realizations (Fig. 7.1f).

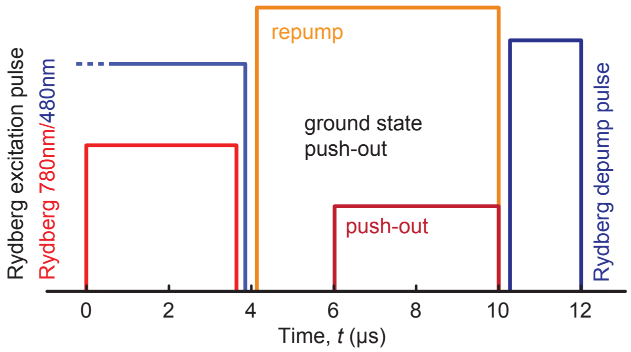

Figure 7.2.: Excitation and detection sequence for sweeps. The excitation and detection sequence used throughout this chapter. A general description can be found in Sec. 5.6.1. For the excitation we use a 4 µs long sweep, where the timing, the Rabi frequency and the detuning are adjusted via the red beam. This is followed by the ground state push-out which takes 6 µs, where the push beam itself is only switched on the last 4 µs. Directly afterwards the depump pulse of 2 µs is applied.

		red laser 1D	red laser 2D	blue
max. Rabi freq 2photon	$(2\pi \cdot \mathrm{kHz})$	250(25)	420(42)	-
max. Rabi frequency	$(2\pi \cdot \mathrm{MHz})$	29(2)	49(3)	13(2)
max. intensity	$(\mathrm{mW/cm^2})$	76(5)	215(14)	$1.4(3) \cdot 10^6$
beam waist	(µm)	44(2)	44(2)	17(5)
max. light shift	$(2\pi \cdot \mathrm{kHz})$	236(35)	670(100)	57(9)

Table 7.1.: Parameters of the Rydberg laser beams for sweep experiments. The red laser parameters for the 1D experiments are shown in the first column, for 2D in the second column. The blue laser has the same parameters in 1D and 2D (third column). Errors, s.d.

7.4.1. Initial atom preparation via single-site addressing

The idea of our initial state preparation is to produce a large unity filling region in the optical lattice and cut out the wanted atom pattern for the experiment. For the realization of large systems we used a deconfining beam to reduce the harmonic potential induced by the lattice beams and thereby enlarged the spatial extension of a single occupancy Mott insulating state [51] (Fig. 7.1c). The light at 670 nm for this deconfinement beam was generated using a super-luminescent diode with a linewidth of ≈ 5 nm to reduce interferences on this beam. It is amplified in two consecutive tapered amplifiers to reach the required power level. This technique allows to reach unity filling regions of a diameter of up to 15 µm. Only for very large systems (cf. Fig. 7.7a, $\ell > 27$ and Fig. 7.12c, rightmost panel) we had to allow for double occupancy in the central part.

We prepared the targeted initial atom distribution by the single-site addressing technique, first demonstrated with a single beam [22] and later optimized with a spatial light modulator [50]. We start from a Mott insulator with unity filling over a region larger than the target pattern and prepare the atoms in the state $|F = 1, m_F = -1\rangle$. Then we use a light pattern of the shape of the target pattern to create a spatially dependent light shift. The light pattern is created in real space with a digital mirror device (DMD) [324]. The DMD consists of nearly a million micromirrors, which can be switch between two stable positions. To allow for high resolution and even local intensity control, we image 350(50) pixels to the area of one point spread function of the objective (60(10) pixels for $532 \times 532\,\mathrm{nm}^2$). Intensity, polarization and detuning of the light pattern were chosen to create a differential light shift on the transition $|1, -1\rangle \leftrightarrow |2, -2\rangle$ of approximately 50 kHz, but nearly no absolute shift of the $|1, -1\rangle$ state. To this end, we use σ^--polarized light at 787.555(1) nm between D_1 and D_2 line [48]. As we cannot optimize the polarization perfectly due to technical reasons, we adjusted the wavelength slightly compared to the theoretical optimum to minimize the light shift on the $|2, -2\rangle$ state. Then we apply a microwave sweep to transfer all non-addressed atoms to $|2, -2\rangle$ on the bare resonance. All the atoms in the addressing light will stay in the state $|1, -1\rangle$. A subsequent push beam on the cycling transition $5\mathrm{S}_{1/2}, |2, -2\rangle \leftrightarrow 5\mathrm{P}_{3/2}, |3, -3\rangle$ can efficiently remove the atoms in $|2, -2\rangle$ without

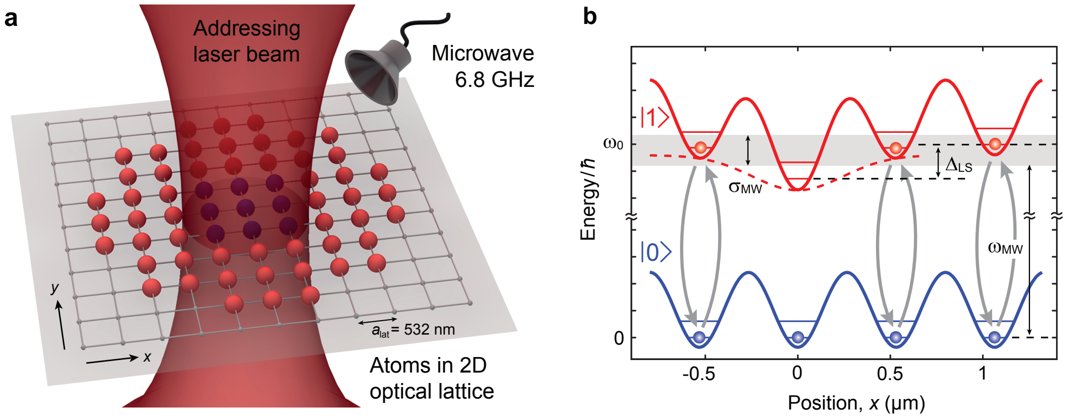

Figure 7.3.: Schematic illustrating the addressing. An addressing pattern is used to shift all atoms in the targeted pattern out of resonance, then the non-shifted atoms are transferred to the other spin state and removed from the lattice. **a**, Schematic showing the beam and the spin states of the atoms after the transfer. The blue atoms stay in state $|0\rangle = |F = 1, m_F = -1\rangle$, while the red atoms were flipped by a microwave sweep to $|1\rangle = |2, -2\rangle$. **b**, light shifts of the atoms when addressing one atom out of four. Only the addressed atoms are not transferred due to the strong light shift $\mathit{\Delta}_{\text{LS}}$, the others experience a small light shift, but their resonance frequency is still within the bandwidth of the microwave sweep σ_{MW}. Image adapted from [22].

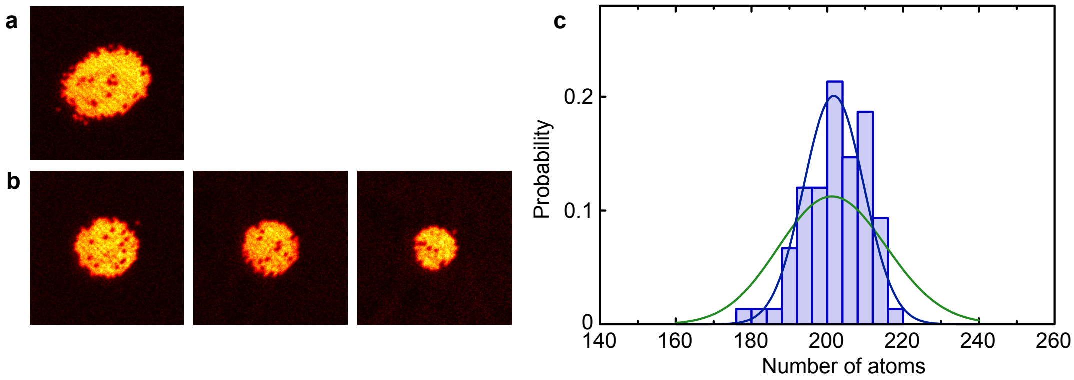

Figure 7.4.: Sub-Poissonian atom number fluctuations by addressing. **a**, Deconfined initial cloud, here with 421 atoms. **b**, Clouds after cut-out with addressing for three circular addressing patterns with varying radius. The prepared configurations shown have 256, 209, 128 atoms. **c**, Distribution of atom numbers for the medium sized pattern in **b**. Dataset contains 75 images taken as reference interlaced with a Rydberg measurement over one day. The atom number was 202(8) (mean and standard deviation) and the radius 8.4(1) sites.

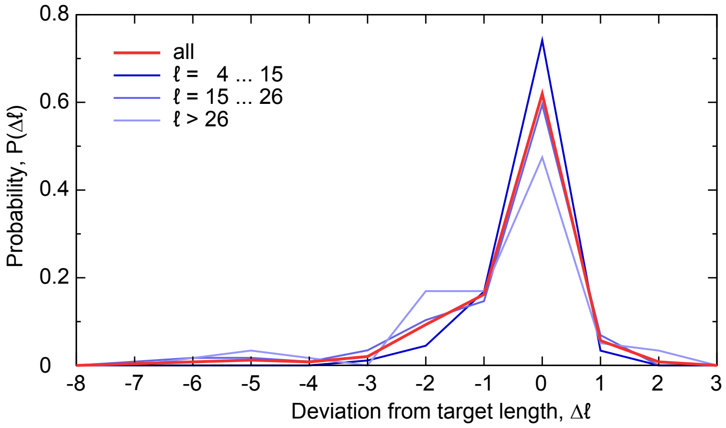

Figure 7.5.: Length fluctuations of prepared 1D systems. Probability distribution of the length deviation extracted from experimental reference images compared to the target length. These distributions were taken into account for the theory calculations in Fig. 7.10.

heating the addressed atoms. Afterwards we are left with an atom pattern reflecting directly the light distribution (Fig. 7.1d and 7.4b).

For this scheme to perform well we work typically in a deep lattice of $40\,E_\mathrm{r}$, as residual imperfections can easily induce tunnelling at lower lattice depths. We observe sub-Poissonian atom number fluctuations of the resulting atom pattern (Fig. 7.4c). The filling factor of the pattern is typically above 0.8 atoms/site, limited mainly by the initial Mott insulator and heating during the hold time of the addressing sequence.

For the 1D systems the fluctuations in the length are most relevant for Rydberg experiments. We measured the length fluctuations, which are in absolute values similar for all 1D systems, independent of their absolute length (Fig. 7.5). There is a slight tendency to prepare lines with a length one site shorter than targeted, which is mainly caused by errors in the sub-lattice-site positioning of the addressing pattern with respect to the lattice phase. But also residual light shifts of the addressing pattern can cause tunnelling of atoms especially at the edges of the addressing pattern. The slightly worse length fluctuations for the longest 1D systems are caused by atom number fluctuations in the initial Mott insulator, as we could not prepare initial atom numbers which were large enough that the Mott insulator size was always larger than the addressing pattern within atom number fluctuations. Therefore the addressing pattern was with a small probability not fully overlapping with the initial atom distribution.

7.4.2. Implementation of the laser sweeps

For the implementation of the sweeps a fast frequency and amplitude modulation of the two-photon coupling is required. This is realized in the experiment by changing the parameters of the red beam (780 nm), while the parameters for the blue beam (480 nm) are held constant. Fast amplitude and frequency modulations are implemented using a single acousto-optical modulator in double-pass configuration at a centre frequency of 350 MHz. For the frequency sweep a synthesizer with large frequency modulation bandwidth is used to drive the acousto-optical modulator. The amplitude is shaped using a fast, calibrated variable attenuator after the synthesizer. Long-term drifts are minimized by a sample-and-hold intensity stabilization technique.

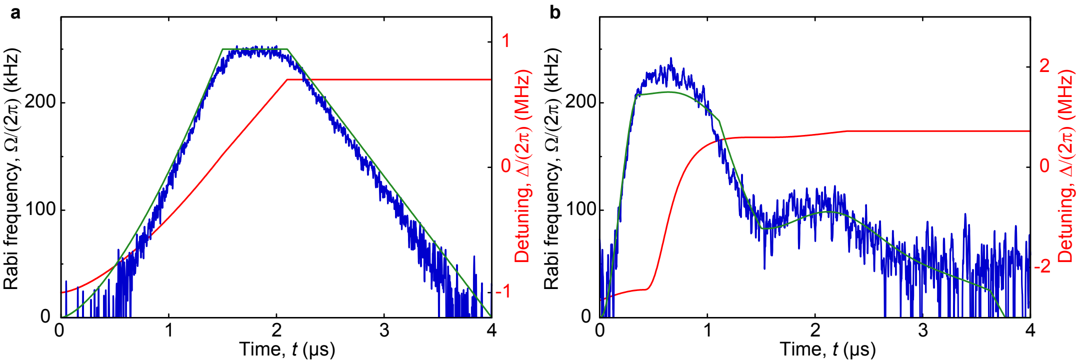

Figure 7.6.: Frequency and amplitude modulation of the sweeps in 1D and 2D. Time dependence of Rabi frequency and detuning during the sweep used in the experiments with 1D systems (**a**) and 2D systems (**b**). Green line, targeted two-photon Rabi frequency. Red line, targeted detuning. Blue line, two-photon Rabi frequency obtained by a calibrated photo diode. The noise is due to the low light level on the high-bandwidth photo diode. For the 2D systems the sweep was not optimized using the full procedure discussed in Appendix E, since the limiting factor here were fluctuations of the cloud shape. For the largest 2D systems (Fig. 7.12, rightmost column) the Rabi frequency was scaled up by a factor of 1.9(1) compared to **b**.

To assure the absolute frequency stability of the two-photon excitation with respect to the Rydberg resonance we took a Rydberg resonance curve on every measurement day. To avoid interaction induced broadening and shifts we use a very dilute cloud. Over consecutive days the line centre was reproducible within about 200 kHz, limited by a combination of Fourier width and interaction broadening. The linewidth of the Rydberg lasers is 50 kHz for the red laser and $\lesssim 20$ kHz for the blue laser. To measure the Rabi frequency Ω of the two-photon coupling we prepared a single atom using our addressing technique and observed its Rabi oscillations as discussed in Sec. 5.7.3.

The use of the red laser to implement the amplitude modulation leads to a time-dependent ac Stark shift on the ground state, which causes an additional detuning of the transition to the Rydberg state. This effect has to be compensated during the sweep, as it can easily exceed the two-photon Rabi frequency. For this purpose we modify the time-dependent detuning correspondingly. The ac Stark shifts of the intermediate and Rydberg states are negligible, the former due to the vanishing influence of the level shift compared to the intermediate state detuning of $\Delta = 2\pi \cdot 742$ MHz, the latter due to the weak coupling. The amplitude and frequency modulation throughout the sweeps are shown in Fig. 7.6.

The relatively small beam waist of the coupling laser beams (Table 7.1) leads to a spatial variation of the Rabi frequency $\varOmega$ across the system. For most of the measurements the difference in coupling strength was less than 30 %, but for the largest one-dimensional systems with $\ell > 26$ up to 40 %. We checked theoretically that the influence of such variations on the adiabatic sweep is on the order of the experimental error bars.

7.5. Staircase in 1D

In this section we demonstrate the adiabatic preparation of crystalline states in an elongated quasi-one-dimensional geometry. The experimentally realizable number of spin-↑ atoms $N_\uparrow$ is limited for fixed system size by the interaction energy due to the weak scaling of the longitudinal magnetic field with $\varDelta$. Large detunings lead to a reduction in detection efficiency due to extremely strong interactions and sweeps into small crystalline lobes pose extreme stability demands on the atom number distribution and frequency. Hence, instead of varying the detuning, we changed the length ℓ of the initial system to explore the characteristics of the Rydberg crystals [36]. In this way the interaction energy scales approximately linearly with $N_\uparrow$ and not with the sixth power. We measured the mean number of Rydberg atoms $N_\uparrow$ for varying length ℓ using a numerically optimized sweep (Sec. 7.6, Appendix E). In the optimization the sweep duration was set to 4 µs, which is a reasonable compromise between the decreasing detection efficiency for longer sweeps and adiabaticity. The results for the sweep to a final detuning of $\varDelta_{\mathrm{max}} = 2\pi \cdot 700(200)\,\mathrm{kHz}$ shown in Fig. 7.7a exhibit clear plateaus in $N_\uparrow$ and agree well with numerical predictions which take into account the measured initial atomic density, the actual sweep and as the only free parameter the detection efficiency $\alpha = 0.62(5)$. The value of the detection efficiency determined in this way is consistent with independent measurements in Fig. 7.10c and Fig. 7.12 (see also Sec. 5.6.3). On the plateaus the theory predicts strong overlap with states of fixed total magnetization (Fig. 7.8). Exploiting that varying the system size ℓ is approximately equivalent to varying the detuning $\varDelta_{\mathrm{max}}$, we extract the susceptibility $\chi \equiv \frac{\partial N_\uparrow}{\partial \varDelta_{\mathrm{max}}} \approx \frac{\ell}{6\varDelta_{\mathrm{max}}} \frac{\partial N_\uparrow}{\partial \ell}$ from our data (Appendix E). As shown in Fig. 7.7b, χ is found to vanish in the plateau regions, as expected for crystalline magnetic states. The finite values in between result from the small energy gaps between crystalline states of slightly different magnetization around $\varDelta_{\mathrm{c}}$, leading to the preparation of compressible superposition states.

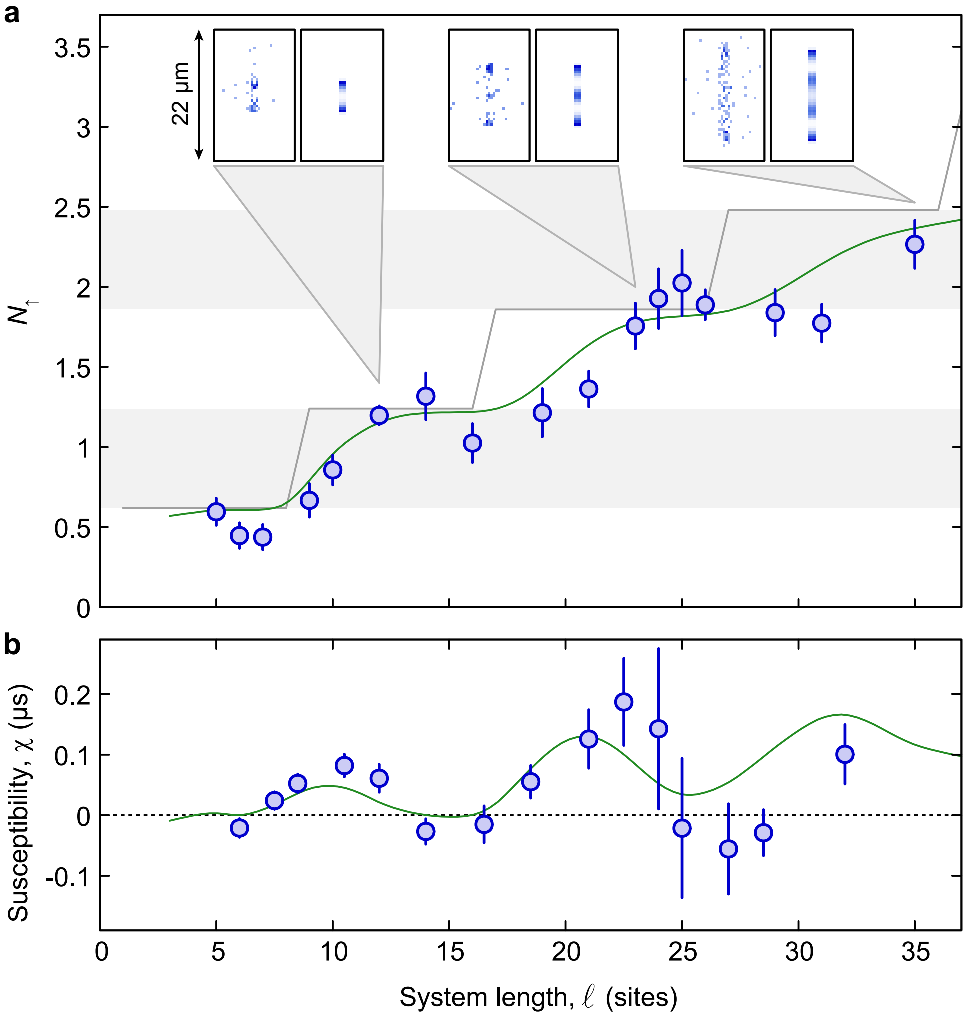

Figure 7.7.: Identification of the crystalline phase. **a**, Mean spin-↑ number $N_\uparrow$ versus system length ℓ for an elongated system. Blue circles correspond to the experimental mean number of Rydberg atoms $N_\uparrow$ after the optimized sweep, which is kept the same for all ℓ. The green line is the result of the numerical simulation for the experimental initial states, taking into account an initial state filling of 0.8 and length fluctuations of the order of one site as shown in Fig. 7.5. The grey line is the classical ($\Omega = 0$) prediction. The only free parameter used to fit the theory to the experimental data is the detection efficiency $\alpha = 0.62$. Insets: Measured spatial distribution of the magnetization (left) and corresponding theory (right) for system lengths ℓ of 12, 23 and 35 sites. The brightness (light to dark) translates to the normalized number of spin-↑ atoms. **b**, Susceptibility χ of the prepared states. Blue circles are derived from the experimental data shown in **a** using a numerical symmetric second-order approximation of the derivative (Appendix E). The green line is a numerical calculation of $\chi = dN_\uparrow/d\Delta|_{\Delta_{\max}}$ for each system size ℓ. All error bars s.e.m.

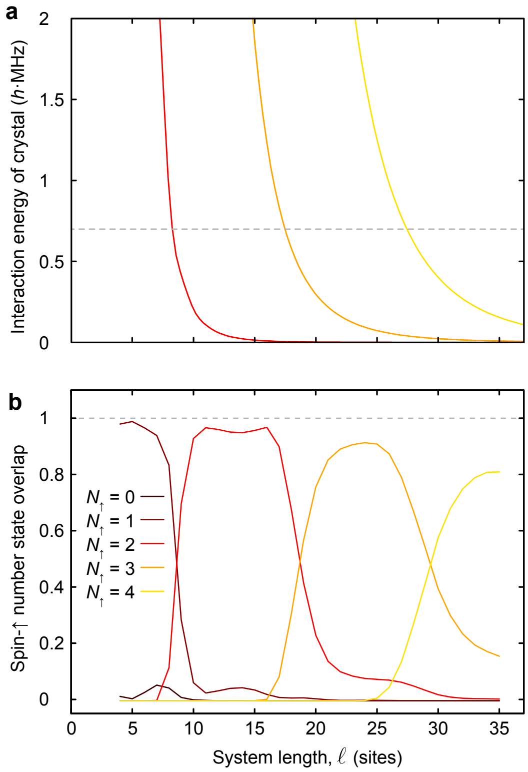

Figure 7.8: Population of many-body states with fixed Rydberg atom number after the sweep for varying system length. **a**, Calculated energy of crystalline configurations in 1D. For the theoretical value of the C_6 coefficient of the 43S state the interaction energy of the classical linear crystalline configurations with 2 to 4 excitations (red to yellow) is calculated. The horizontal grey line marks the final detuning of the sweep as the most relevant energy scale. The positions of the crystal interaction energies crossing the final detuning line determine approximately at which length ℓ the Rydberg number after the sweep steps up by one. **b**, Calculated dependence of the population of many-body states with fixed Rydberg atom number after the sweep on the system length. The calculation was done for an ideal $3 \times \ell$ system with unity filling. Curves for the number of spin-↑ atoms $N_\uparrow = 0 \ldots 4$ are shown. For $N_\uparrow \geq 4$ the efficiency of the preparation drops significantly due to smaller gaps on the trajectory of the sweep.

7.6. Dynamical crystallization in 1D

The adiabatic preparation requires the crossing of a phase boundary [29, 31, 318], which becomes possible in our system due to its finite-size gap, and during transit the system undergoes complex correlated quantum dynamics. To study the crystallization process along the sweep trajectory $(\Omega(t), \Delta(t))$ we abruptly switch off the coupling at different times, thereby projecting the many-body state onto the eigenstates of the uncoupled system ($\Omega = 0$). For the measurement we choose the optimized sweep for the $N_\uparrow = 3$ crystalline manifold in a system of 3×23 sites. In Fig. 7.9 we show the theoretical prediction for the time evolution during this sweep for an ideal system. The small amount of oscillations in the occupations of the different Fock states of Rydberg atom numbers during the sweep indicate adiabaticity of the sweep. Oscillations are typically caused by coherences between two states with different energy, which do not occur in adiabatic sweeps as all amplitude should stay in the ground state. This optimized sweep can reach approximately $90\,\%$ fidelity for the $N_\uparrow = 3$ state. The corresponding path through the phase diagram is shown in Fig. 7.10a as black line with markers 1–7 for the times where measurements were performed. The implemented sweep crosses the boundary to the crystalline lobe with $N_\uparrow = 3$ between point 5 and 6 at a blue-detuning of approximately $2\pi \cdot 700\,\mathrm{kHz}$. The linear scale of the axis shows the dramatically different scale of the phases for varying Rydberg atom number. The region with $N_\uparrow = 4$ is already out of scale and the phase with $N_\uparrow = 2$ is barely visible and limited to a very small region around $\Delta = 2\pi \cdot 100\,\mathrm{kHz}$ and $\Omega < 2\pi \cdot 10\,\mathrm{kHz}$.

For each evolution time along the sweep trajectory we measured the Rydberg number histogram, from which we extracted the mean $N_\uparrow$ and the normalized variance $Q = \frac{\langle(\sum_i \hat{n}_\uparrow^{(i)})^2\rangle - N_\uparrow^2}{N_\uparrow} - 1$ (Fig. 7.10b). During the sweep $N_\uparrow$ increases until we observe a saturation behaviour which we interpret as the onset of crystallization (Fig. 7.9). Simultaneously, the Q factor decreases from the Poissonian value $Q \approx 0$ to $Q \approx -0.5(1)$, which reflects the approach to the crystalline state. Due to our detection efficiency we cannot measure the ideal value $Q \approx -1$. The lowest value that can be expected is $Q \approx -\alpha$ (for a derivation see Appendix C.3). This bound is nearly saturated by the obtained experimental value. The measurement of the full counting statistics along the sweep trajectory allows for a more quantitative comparison with theory (Fig. 7.10c). However, the finite detection efficiency strongly affects the observed histograms and leads to a tail of the distributions towards lower spin-↑ atom numbers (Appendix C.2). Nevertheless, when taking $\alpha = 0.62$ into account in the theoretical prediction, we find very good agreement with the experimental observations. We observe notable features for times 6 and 7. At time 6 the observed probability for events without Rydberg atoms is astonishingly low, which provides a lower bound for the detection efficiency and at time 7 the distribution looks cut above $N_\uparrow = 3$, which confirms that we do not have more than three Rydberg atoms in the system.

The high-resolution detection scheme allows for an even more detailed study of the dynamics via the spatial magnetization density, which is largely unaffected by the detection efficiency, which mainly reduces the amplitude of the signal here. For our quasi-one-dimensional systems, crystallization becomes directly visible in the magnet-

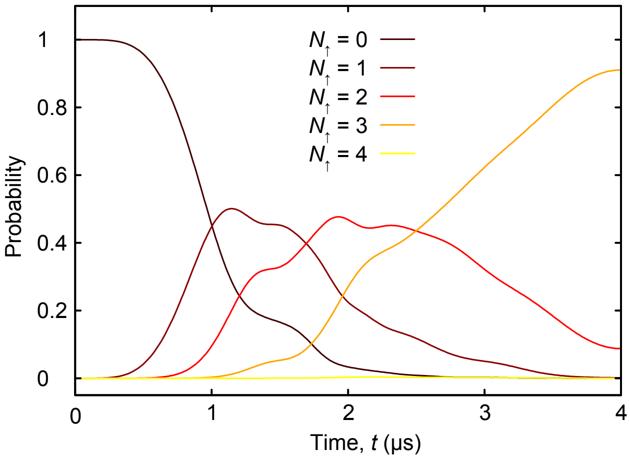

Figure 7.9: Calculated time-evolution of the population of many-body states with fixed $N_\uparrow$ during the optimized sweep in 1D. The evolution of the occupation was calculated for an ideal 3×23 system with unity filling for the sweep in Fig. 7.6a. Curves for $N_\uparrow = 0 \ldots 4$ are shown, all states with higher number of spin-$\uparrow$ atoms have vanishing amplitude.

ization density, where it provides here similar information as the correlation function $\langle \hat{n}_\uparrow^{(i)} \hat{n}_\uparrow^{(j)} \rangle$ due to a breakdown of translational symmetry. The high interaction energy required to compress crystals with $N_\uparrow > 1$ leads to an effective pinning of the two outer $N_\uparrow$-spins to the edges of the system. All other states with same $N_\uparrow$ and no spin-$\uparrow$ at the edge lie higher in energy. We look at the magnetization density as for the measurements above at several times during the sweep. At the beginning of the pulse we observe delocalized Rydberg atoms throughout the system (Fig. 7.10d), characteristic for the magnetically disordered phase in this parameter regime. For longer times spin-$\uparrow$ atoms start to accumulate at both ends of the line-shaped cloud and finally the full Rydberg atom density crystallizes to the expected triple-peak configuration. The dynamics of this crystallization process matches well with the theoretical expectations. The slight broadening of the observed peaks could be caused by slightly non-adiabatic transitions during the sweep, but it is also still compatible with the spatial resolution of the detection of one lattice site (Sec. 5.6.4)

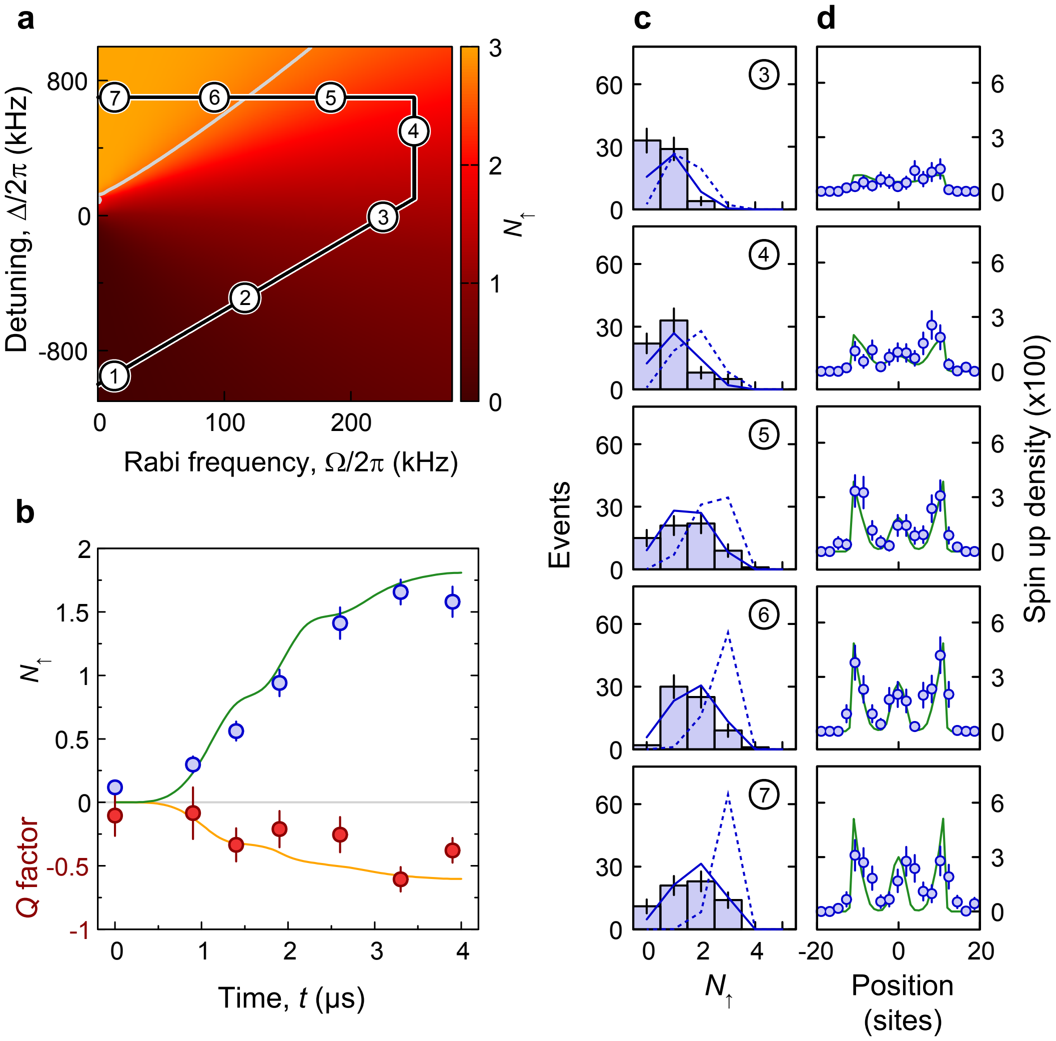

Figure 7.10.: Dynamical crystallization in 1D. a, Illustration of the laser sweep. The black line shows the path of the sweep through the phase diagram, the numbered positions mark the measurements (cf. **c**). The colour scale indicates the number of spin-↑ atoms $N_\uparrow$ of the ground state for every pair (Ω, Δ). The grey line indicates the boundary of the crystalline lobes, where the Q factor drops below -0.9. The phase diagram was calculated for the experimental parameters. **b**, Mean number of Rydberg atoms (blue circles) and Q factor (red circles) for the seven times marked in **a** together with the theoretical prediction. Each of the seven data points is based on at least 65 independent experimental repetitions. **c**, Experimental and theoretical probability distributions of the number of Rydberg atoms along the sweep (cf. **a**). Blue boxes show experimental data and the dashed and solid lines represent the theoretical result for detection efficiencies of $\alpha = 1$ and $\alpha = 0.62$, respectively. **d**, Transversally averaged distributions (probability per site) of the spin-↑ atoms for the same times as in **c** with a binning of two sites (blue circles). The slight asymmetry towards the right might be due to a gradient in the Rabi frequency (Sec. 7.4.2). The green line is the numerical result. All error bars s.e.m.

7.7. Adiabatic preparation in 2D

In a different set of experiments we investigate the adiabatic preparation in a disc-shaped spin system of up to 400 spins. We use the spatial light modulator to prepare the initial distribution with a controlled radius. The preparation can be optimized to allow for radius fluctuations of less than one lattice site (Sec. 7.4.1). Here, the dynamical preparation turns out to be more challenging, since effects of the fluctuating boundary are much more pronounced in two dimensions than in the effective one-dimensional geometry discussed above. Nevertheless, a proper frequency chirp of the coupling laser provides substantial control of the many-body dynamics and the preparation of energetically low-lying many-body states. This is demonstrated in Fig. 7.12 where we compare the magnetization density at constant detuning to the result of a chirped coupling from $\Delta_{\mathrm{min}} < 0$ to Δ_{max} (Fig. 7.6b). In the former case the magnetization is almost uniformly distributed across the atomic sample, while in the latter low energy states with a localized magnetization density are prepared. The initial system size permits to control the number of spin-↑ atoms. With increasing $N_{\uparrow}$ the configuration with all Rydberg atoms located along the circumference becomes energetically unfavourable compared to configurations with an extra Rydberg atom in the centre. Fig. 7.11 shows the corresponding crystal configurations explicitly and their theoretical interaction for the 43S state.

The series of configurations with one Rydberg atom in the centre becomes lowest in energy between $N_{\uparrow} = 6$ and $N_{\uparrow} = 7$. The very small separation of the two configurations with $N_{\uparrow} = 6$ might lead to an instability and could explain why we did not observe many of these configurations in the experiment. The structural change from $N_{\uparrow} = 6$ to $N_{\uparrow} = 7$ is directly visible in the observed patterns shown in Fig. 7.12. The occurrence of the other respective configurations is strongly suppressed, though it can happen that a $N_{\uparrow} = 8$ configuration can be observed as a $N_{\uparrow} = 7$ ring configuration due to detection efficiency. But this detection problem can be avoided by looking at the magnetization density (Fig. 7.12b), where we see in the middle panel of the right grey box no peak in the centre, while the peak appears for the initial atom distribution size of the rightmost panel.

To show the existence of resolvable crystalline phases we tried to observe a staircase of excitations as in 1D (Sec. 7.5). The definition of a staircase in 2D with respect to system size is not well-defined because of the discretisation of the lattice, which leads to irregular 2D shapes when increasing the radius by steps of one or less and leads to a non-uniform increase of the atom number. We performed a measurement of the number of Rydberg atoms versus frequency offset of the sweep in 2D, but the result does not deviate significantly from a linear increase with atom number (Fig. 7.13). We compare data from three separate data sets, which are consistent within error bars, but show stronger fluctuations than expected. It might be that the used sweep here was not as adiabatic as thought such that it caused strong fluctuations and showed extreme sensitivity to all parameters. Possible other reasons for the failure to resolve the staircase in 2D is the much smaller width of the stairs with respect to system size and smaller spacing of crystal configurations in energy due to the additional degree of freedom. Nevertheless the data shows a negative Q factor for all configurations, down

Figure 7.11: Cross-over in the crystal structure. For circular initial atom distributions there is a cross-over in the structure of the crystals between six and seven excitations, which is illustrated here by the calculation of static crystal energies. **a**, crystal configuration with 3-8 Rydberg atoms on a ring. **b**, Crystal configuration with one Rydberg atom in the centre and the rest on a ring. **c**, Comparison of the interaction energies of the configurations in **a** and **b**. Here the interactions energies were calculated for a cloud with radius 11 sites and the theoretical C_6 coefficient of the 43S state.

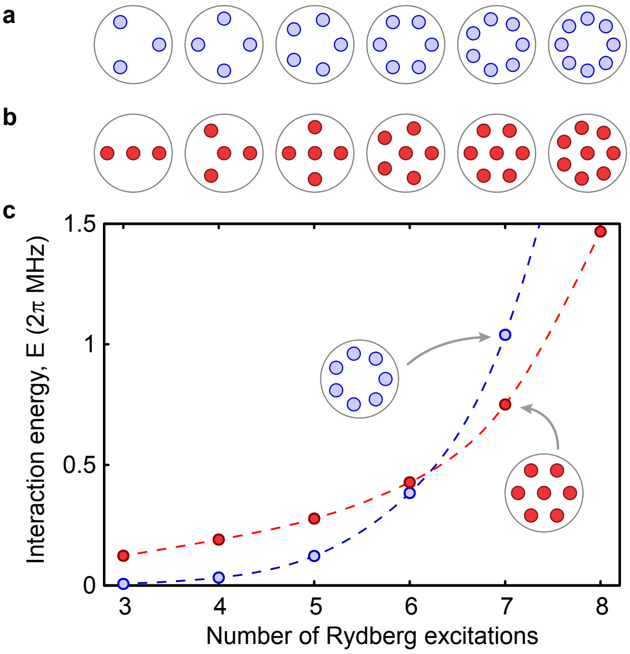

to about $Q = -0.5(1)$, probably limited by detection efficiency. The average number of excitations seems to saturate around 2.5, corresponding to αN_e for $\alpha = 0.62$ and $N_\mathrm{e} = 4$, which is the expected maximum Rydberg atom number for a cloud with radius around seven sites.

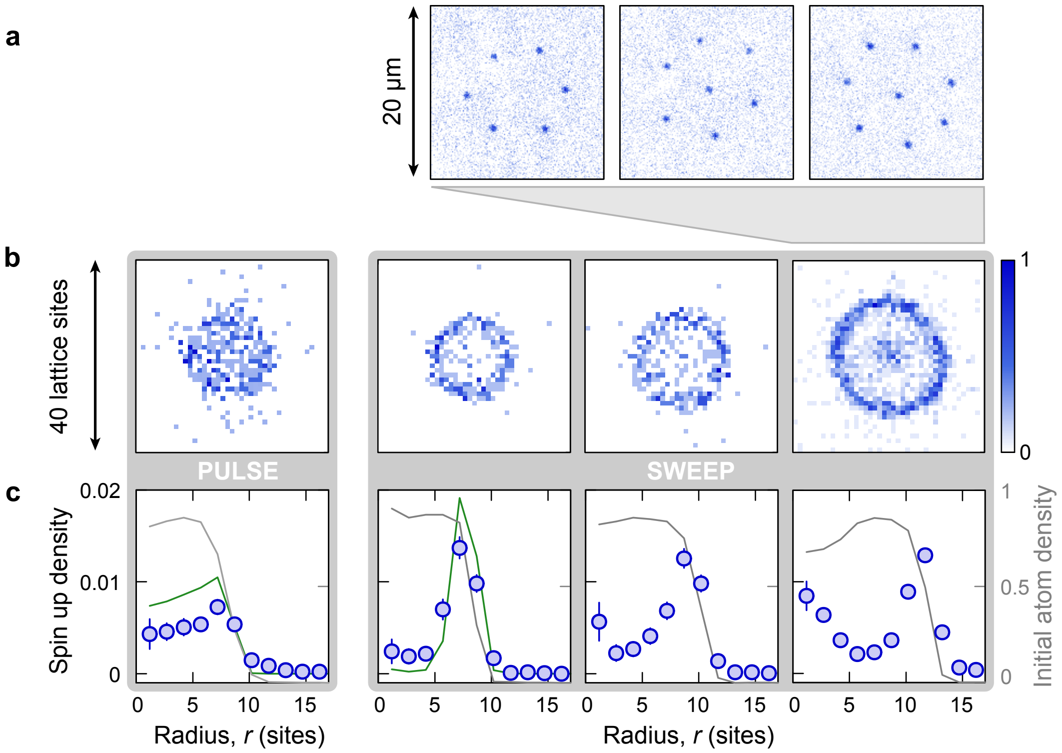

Figure 7.12.: Preparation of low-energy states in disc-shaped samples. a, Unprocessed experimental single shot pictures with 6, 7 and 8 Rydberg atoms from the rightmost data set. Each blue point corresponds to a single atom. The low probability to observe these perfect crystal events is consistent with the detection efficiency (Sec. 5.6.3) **b, c**, Magnetization densities for pulsed (left grey box) and sweeped laser coupling with increasing system size from left to right are shown in the right grey box. The pulsed coupling was done with the same amplitude modulation as for the sweep (Fig. 7.6b), but the detuning $\varDelta$ was held constant (averaged data for $\varDelta = 2\pi \cdot 260\,\mathrm{kHz}$ and $\varDelta = 2\pi \cdot 760\,\mathrm{kHz}$ is shown). The system radius was $8.2(2), 8.3(1), 10.0(3), 11.8(2)$ lattice sites (left to right). **b**, Measured two-dimensional distribution of the magnetization. The colour scale represents the normalized counts per site. **c**, Azimuthally averaged density distribution (probability per site) of the data shown in **b** (blue dots), and comparison with theory (green line). The theoretical calculation was only feasible for small clouds and is based on representative experimental initial atomic samples. The average density of the initial systems is shown in grey on the right axis. The density dip in the centre for the largest radius is caused by the vicinity to the doubly occupied Mott lobe. Error bars s.e.m.

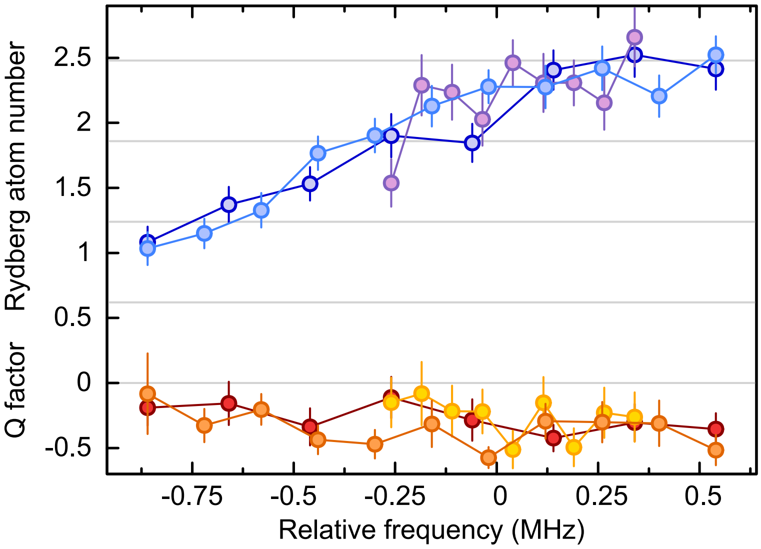

Figure 7.13.: Attempt to resolve the staircase in 2D. The curves in dark-blue, blue, purple show the mean detected Rydberg atom number, and the ones in red, orange, yellow the corresponding Q factor of three datasets. The staircase is not resolved and we see strong fluctuations in the data maybe caused by non-adiabaticity of the sweep. It looks like we see a step in the dark-blue dataset, but this is not reproduced in the other curves. We used a 6 µs sweep with start at a detuning $\Delta = -1.5\,\mathrm{MHz}$ and end at 1.5 MHz with respect to the centre frequency, which is reached at 1 µs. The centre frequency of the sweep with respect to the Rydberg resonance is shown on the x-axis. The initial atom distribution is a Mott insulator with 150(8) atoms and radius 7.1(1) sites. The grey lines marks the expected levels of the plateaus of the staircase for a detection efficiency of 62 %. There is a systematic uncertainty of up to 200 kHz in the global offset of the x-axis. Every data point shown is based on an average over 40-65 experimental images.

7.7.1. Radial correlation function

For comparison with the correlation function shown with pulsed excitation (Fig. 6.6), we also calculated the radial ↑-↑-correlation function (Fig. 7.14) for the rightmost dataset in Fig. 7.12. Without the azimuthal averaging one obtains the full 2D correlation function (Fig. 7.14a). The circular anti-correlation region corresponding to the blockade sphere is clearly visible, while further details are hardly observable due to the noise. No azimuthal dependency is visible, which confirms the expectation of an isotropic interaction of the 43S state and justifies averaging along this dimension. The averaging helps to suppress the noise and in the resulting data (Fig. 7.14b) and even a second correlation peak becomes visible. It shows up at a distance which corresponds to the diameter of the cloud and mainly events with three Rydberg atoms on a line contribute to this correlation. As the observed crystal structures are still finite-size dominated, the distances between Rydberg atoms depend slightly on the number of

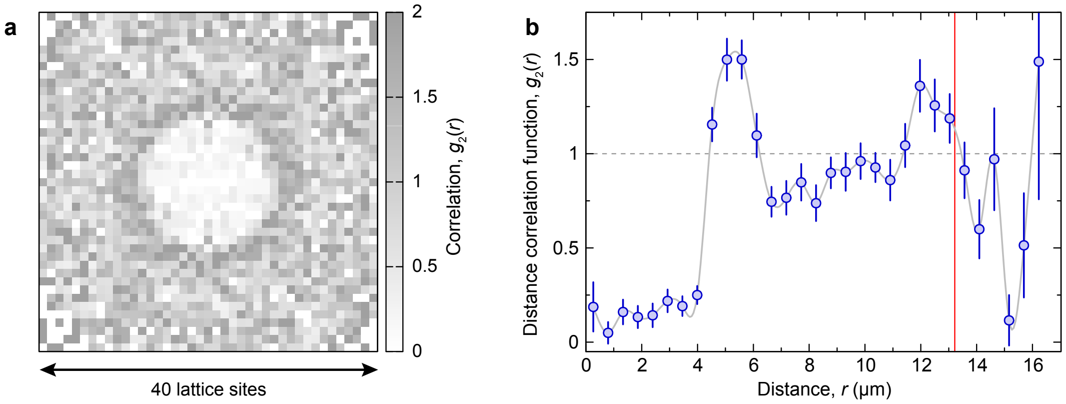

Figure 7.14.: Correlation function in 2D. a, two-dimensional spatial correlation function for the largest disc-shaped initial system, shown in Fig. 7.12. There is a clear circular anti-correlation region in the centre with a ring around. A second ring is barely visible due to the noise caused by limited statistics. Due to the symmetry in the correlation function the graph is point symmetric around the centre. **b**, Blue points show the radial correlation function calculated as defined in Eq. (6.2) and used in Fig. 6.6. The red line marks the diameter of the system and the grey line is a guide to the eye.

Rydberg atoms in the state. This effect will wash out the contrast of the spatial correlation function for larger distances and also causes the reduced anti-correlation between the first and second correlation peak around $r = 8\,\mu\text{m}$. To observe correlation functions with several clear peaks much larger initial atom distributions would be required or Rydberg states with much smaller blockade radius in order to increase $N_\uparrow$. In principle we could reduce the blockade radius by using Rydberg atoms with weaker interactions or going to much higher Rabi frequency, but this would require some changes at the experiment which are discussed in the outlook (Ch. 8).

7.7.2. Dynamics in 2D

The study of the dynamics during the adiabatic preparation, as shown for one-dimensional systems in Sec. 7.6 can be also extended to two-dimensional disc-shape ensembles. In Fig. 7.15 we show the full counting statistics of the Rydberg atom number as well as the spin-$\uparrow$ density for five times during the sweep. Theory predicts predominantly events with four spin-$\uparrow$ atoms. The experimental results are well described by theory assuming the detection efficiency of $\alpha = 0.62$ as above. In the spin-$\uparrow$ density we observe the transition of a nearly homogeneous density to the appearance of a hole in the centre of the system, which becomes most prominent for the full sweep of $4\,\mu\text{s}$ (Fig. 7.15b, rightmost graph). A comparison of the initial atom density with the observed ring in the spin-$\uparrow$ density demonstrates that the Rydberg atoms appear at the border of the system. The build-up of the hole can be also investigated by determining the relative number of spin-$\uparrow$ atoms in the centre of system (Fig. 7.16). We see a

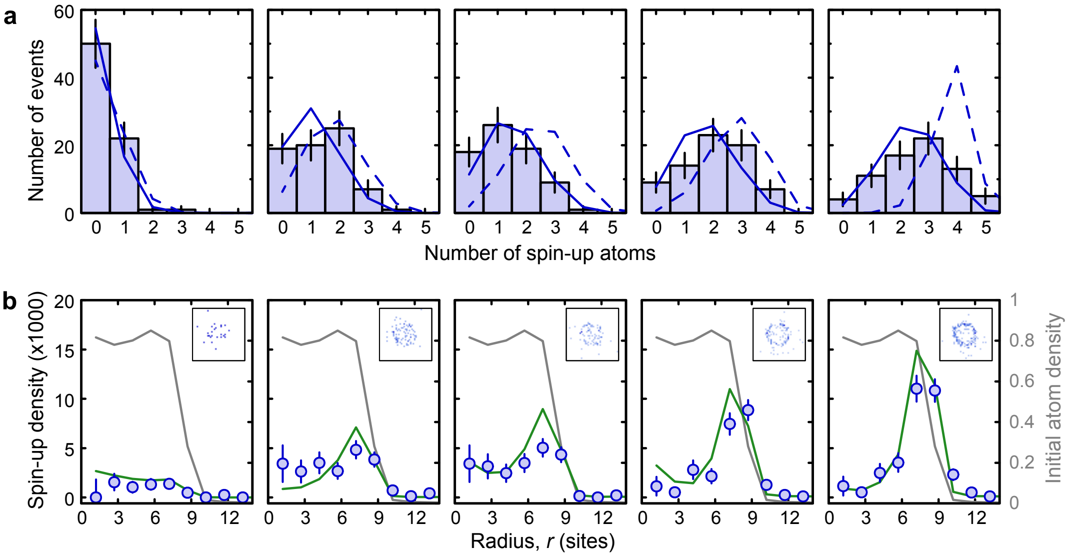

Figure 7.15.: Dynamical crystallization in disc-shaped samples. **a**, Histograms of $N_\uparrow$ for the adiabatic sweep shown in Fig. 7.6 cut at times $0.44, 0.94, 1.14, 2.14, 3.94\,\mu\mathrm{s}$ (from left to right, pulse length was read off from oscilloscope to reduce influence of AOM rise time). The experimental data is shown as bar histogram, the theory taking into account the detection efficiency of $\alpha = 0.62$ as continuous line. The theory with $\alpha = 1$ is shown as dashed line. Calculations take into account the experimental scatter of initial atom densities by averaging over the dynamics of 57 experimental atom configurations with a radius of 8.24(13) sites and a mean atom number of 192(10). **b**, Blue points, experimental azimuthally averaged spin-$\uparrow$-density for the same times as in **a**. Green line, theory including $\alpha = 0.62$. For reference the initial atom density is shown as grey line on the right axis. The insets show the full 2D density of the Rydberg atoms.

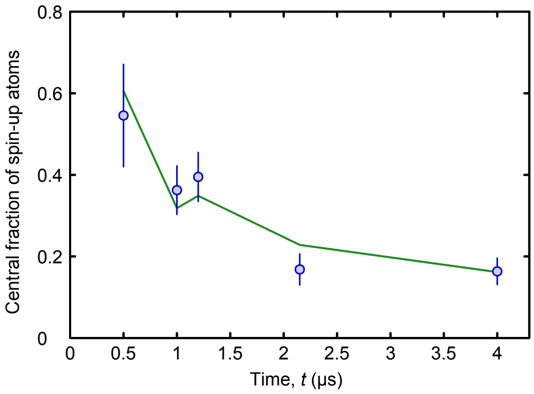

Figure 7.16: Central density during dynamical crystallization in 2D. Blue points, experimentally determined relative density in the central circle with radius 6.5 sites of the system over the length of the cut sweep. Green line, central density extracted from the theory results shown in Fig. 7.15.

strong drop in the beginning of the sweep and then a saturation which sets in around the middle of the sweep. This behaviour indicates a phase transition to the crystalline phase. The theory calculation shows good agreement with the experimental data.

7.8. Summary and outlook

The measurements in this chapter demonstrated the possibility to achieve the required amount of control over a many-body system with power-law interactions to deterministically prepare ordered magnetic states. We showed evidence for Rydberg crystals by direct imaging of the magnetization density as well as a staircase in the total magnetization when changing the length of a quasi-one-dimensional system (Sec. 7.5). By a time-dependent measurement we traced the evolution of the many-body system when crossing the phase transition to the ordered phase, showing directly how the order builds up. The adiabatic preparation technique was also demonstrated in 2D, but here already small fluctuations in the atom number washed out the staircase. But still it was possible to show that states with much lower energy compared to a pulsed excitation can be prepared. A more detailed study of the phase transition might enable to observe the two-stage melting of the crystalline states via a floating crystal phase [31, 318]. By implementing additional controlled dissipation to our system, the investigation of long-range quantum correlations and dissipative quantum magnets in strongly interacting Ising-type spin systems would become possible [325–327]. Similar studies are also possible with anisotropic Rydberg-Rydberg interactions, leading to a richer structure of the crystalline phases [328].

8. Conclusion and outlook

In this thesis the high-resolution and single Rydberg atom sensitive imaging of Rydberg many-body systems has been demonstrated, which allowed for the direct observation of ordering. We reach unprecedented resolution for the imaging of Rydberg atoms and have unmatched control over the preparation of arbitrary ultracold initial atom configurations in the lattice for Rydberg experiments. In contrast to previous experiments our detection technique allows to image many ground state atoms as well as many Rydberg atoms with single-particle sensitivity.

Using pulsed Rydberg excitation we observed spatially ordered structures by post-selection on the high-density components of the many-body states. The imaging technique and in particular the detection efficiency and resolution were investigated in detail. The high-quality imaging allowed to sort images of Rydberg atom configurations by the number of Rydberg atoms. In this way we directly revealed the ordered structures by alignment of the Rydberg atom configurations. A more quantitative analysis has been performed by calculation of the azimuthal and radial correlation function between Rydberg atoms, which also allows to extract the blockade radius. Measurements focussing on the dynamics of close to fully blockaded samples hint towards coherent dynamics with strong dephasing due to a wide energy spread of the excited states.

With the implementation of more advanced excitation techniques a quantum simulation of a quantum Ising model with power-law interactions in a transverse and longitudinal field became feasible. The adiabatic control technique for this strongly interacting Hamiltonian allowed to realize Rydberg crystals and measure their correlations which extend over the whole system size. In contrast to the first measurements of ordered structures the Rydberg crystals are close to the ground state of the many-body Hamiltonian and show ordering without post-selection. To make these experiments possible, we improved the initial state preparation in the lattice by applying a single-site addressing technique. In addition we implemented full control over the time-dependent Rabi frequency and detuning of the adiabatic sweeps to realize theoretically optimized trajectories through the phase diagram. This adiabatic preparation technique enabled us to measure properties of the many-body ground state like its vanishing susceptibility or local magnetization densities.

Outlook

The amount of control reached over Rydberg systems allows for the quantum simulation of long-range interacting many-body systems. The approach to many-body physics using Rydberg atoms is very different from other techniques starting from more complex particles like magnetic atoms or molecules. The big advantage of Rydberg atoms is the high control over ground state atoms, which can be exploited before Rydberg excitation for cooling and state preparation and afterwards for imaging. Also the type of interactions can be selected by the choice of the Rydberg state, which has yet to be explored for the other systems. While the production of ultracold polar ground-state molecules [329–331] and magnetic atoms [332–334] has been successfully demonstrated, the stability of these systems with respect to collisions is still a field of active study [335–337]. In contrast, the essential single atom physics as well as binary interactions for alkali-metal Rydberg atoms can be calculated with high precision. Rydberg atoms allow to access much of the physics targeted by molecules and magnetic atoms, while avoiding much of the complexity of these systems. Although Rydberg atoms are not stable on motional timescales, many experiments can be performed in the frozen gas regime where the whole experiment can be extremely fast due to the strong Rydberg-Rydberg interaction. An even more powerful technique is Rydberg dressing, which would extend ultracold Rydberg physics to motional timescales.

Frozen Rydberg gas The current Rydberg setup allows for many more interesting experiments even without further additions. A recent project is the investigation of collective excitation in fully blockaded clouds using the 68S state [292]. With the help of the addressing technique atomic samples with sub-Poissonian atom number fluctuations can be prepared, which allow for the observation of collective Rabi oscillations with better contrast than measured so far [75, 76].

Another interesting perspective is to go for a nearly vanishing intermediate state detuning in the two-photon excitation and monitor the distribution of Rydberg atoms in such an electromagnetically-induced transparency scheme. A system like this allows future studies of magnetic Hamiltonians with tunable dissipation [325–327, 338].

With additional coupling to a second Rydberg state, either by microwave or a second Rydberg laser, coherent exchange processes between Rydberg atoms could be observed [339]. These can form the basis for the simulation of novel long-range interacting spin models [9].

The investigated system of a unity filling lattice combined with the possibility of Rydberg excitation is also very promising for quantum information processing [1], as there are good perspectives to fulfil all DiVincenzo criteria [340]. The high-fidelity initialization of the lattice with atoms in a certain hyperfine state has been realized [21]. Every atom on a lattice site can be used as a single qubit. The manipulation of single qubits on the lattice is possible via the single-site addressing technique [22]. Here single qubit flips at arbitrary positions have been demonstrated, but no full local single-qubit control yet. In combination with site-selective excitation of Rydberg atoms in the lattice, which could be implemented with similar effort as the single-site addressing, two-qubit gates between many pairs of atoms in the lattice would become possible. The high-resolution imaging then in the end allows for the detection of all atoms in the lattice simultaneously.

Rydberg dressing One of the big open challenges in the field of many-body Rydberg physics is the demonstration of Rydberg dressing [6, 7, 23–27]. The idea is to couple off-resonantly with a laser to a Rydberg state and by that admix a bit of the Rydberg state, in particular its long-range interaction, to the ground state. The implementation of these ideas would enable the investigation of quantum many-body systems with tunable long-range interactions and would allow Rydberg systems to directly compete with ultracold molecules and magnetic atoms in the field of long-range interacting many-body systems.

One might consider to implement Rydberg dressing using the two-photon scheme described in this thesis, but the numbers looked hopeless (Table 8.1). This estimation was also confirmed by up to now unsuccessful tries in other groups [160, 204]. It turns out that alkaline-earth-like atoms might allow for better excitation schemes due to the existence of long-lived intermediate states [205, 341]. For ^{87}Rb it turned out that the only realistic implementation of Rydberg dressing with relevant interaction strength requires a direct coupling with a single ultraviolet laser to the Rydberg state. This laser system is currently being built into our setup by Johannes Zeiher [342].

Single-photon Rydberg P-state excitation In this section we discuss the possibilities of using a single ultraviolet laser for the coupling to the Rydberg state instead of a two-photon excitation. A first observation is that the set of accessible Rydberg states changes from S- and D-states to P-states, as they are the only dipole-allowed transitions directly from the ground state in rubidium. The main reason why this direct excitation scheme is not widely used is the necessity of an ultraviolet laser with sufficient power and stability and the larger Doppler broadening in the case of thermal atoms. With the availability of better laser technology an increasing number of experimental groups started to work on single-laser excitation schemes [72, 271, 272, 343, 344]. The big advantage of direct coupling is the possibility to reach higher Rabi frequencies with lower light shifts and excess scattering rates than for the two-photon schemes in rubidium. Higher Rabi frequencies allow for a smaller blockade radius, which can be further reduced in a 1D geometry due to the angular dependence of the interaction. This might allow for the observation of larger Rydberg crystals. The higher Rabi frequency relative to scattering rates makes the ultraviolet excitation scheme much better suited for Rydberg dressing than the two-photon setup, as will be discussed in the next section.

Advantages of single-photon Rydberg dressing In the following we will discuss the differences between two-photon Rydberg dressing schemes and a direct single-photon scheme. To this end, we first have to consider the underlying physics. The general idea of optical Rydberg dressing is to couple the ground state to a Rydberg state off-resonantly with detuning $\varDelta$ by a laser of Rabi frequency $\varOmega$ [6, 7, 23–27]. Similar to what happens in a typical dipole trap, the upper state is admixed to the ground state. To avoid strong scattering at the upper state the coupling has to be off-resonant $|\varOmega/\varDelta| \ll 1$. The resulting admixture of the Rydberg state to the ground state corresponds to a probability to find the atom in the Rydberg state of $\beta = \left(\frac{\varOmega}{2\varDelta}\right)^2$. The very large C_6 coefficient of a Rydberg atom is reduced to $\tilde{C}_6 = \left(\frac{\varOmega}{2\varDelta}\right)^4 C_6$. Due to the Rydberg blockade, the dressing becomes less efficient for atoms too close together

Parameter	value $36P_{3/2}$	value $43S_{1/2}$
τ_{eff} [64]	$38\,\mu s$	$44\,\mu s$
β	$7.6 \cdot 10^{-4}$	$8.8 \cdot 10^{-4}$
Ω_{red}	-	$1\,\mathrm{MHz}$
Ω_{blue}	-	$140\,\mathrm{MHz}$
Δ_i	-	$700\,\mathrm{MHz}$
Ω	$13\,\mathrm{MHz}$	$0.1\,\mathrm{MHz}$
Δ	$230\,\mathrm{MHz}$	$1.7\,\mathrm{MHz}$
$\tilde{V}$	$270\,\mathrm{Hz}$	$3\,\mathrm{Hz}$
C_6	$-2 \cdot 10^{-60}\,\mathrm{Jm}^2$	$-1.6 \cdot 10^{-60}\,\mathrm{Jm}^2$
R_c	$1.4\,\mu m$	$3.0\,\mu m$

Table 8.1.: Parameter comparison for Rydberg dressing. Approximate parameters for realistic laser power for Rydberg dressing with rubidium via the direct single-photon dressing or the two-photon scheme for a targeted lifetime of 50 ms.

and the dressed-atom interaction potential becomes constant for distances lower than $R_c = \left(\frac{C_6}{2\hbar|\Delta|}\right)^{1/6}$. Effectively the potential is of soft-core type $U(r) = \frac{\tilde{C}_6}{r^6+R_c^6}$. The relevant energy scale to observe this potential is the height of the soft core $\tilde{V} = \frac{\tilde{C}_6}{R_c^6} = \hbar\frac{\Omega^4}{(2|\Delta|)^3} = \hbar\Omega\beta^{3/2}$, which interestingly is independent of C_6 and depends only on laser parameters.

To check if the dressing is realistic we compare the parameters for dressing via the two-photon excitation and the direct ultraviolet transition to a P-state. We require a lifetime of the dressed-atom state of 50 ms, which is the typical motional timescale of the atoms. The effective lifetime of a Rydberg-dressed atom is $\tau_{\mathrm{dress}} = \beta^{-1}\tau_{\mathrm{eff}}$, which directly determines the maximum allowed scattering rate. To observe interesting effects via Rydberg dressing it is required to look at systems which are larger than the range of the the soft core R_c. Therefore we assume a beam waist of $20\,\mu m$. For the direct comparison we have to assume available Rabi frequencies and consider realistic laser powers in the UV and at 480 nm of 100 mW and 1 W, respectively. By fixing these parameters and the Rydberg states $36P_{3/2}$ and $43S_{1/2}$, all other quantities follow. In the case of the UV light the detuning Δ is determined via the definition of β by $\Delta = \frac{\Omega}{2\sqrt{\beta}}$. In the two-photon case the scattering rate is limited by the intermediate state scattering. This then determines the maximum tolerable red Rabi frequency and together with the available blue power the two-photon Rabi frequency via $\Omega = \frac{\Omega_{\mathrm{red}}\Omega_{\mathrm{blue}}}{2\Delta_i} = \frac{\Omega_{\mathrm{blue}}}{\sqrt{\tau_{\mathrm{dress}}\Gamma}}$. Here the intermediate detuning of the two-photon transition is not relevant in the limit of far detuning.

The values in Table 8.1 show that only a very small Rabi frequency is available for dressing to avoid too much scattering in the case of the two-photon scheme. The interaction potential height of $\sim 3\,\mathrm{Hz}$ is smaller than all typical energy scales in the system and probably impossible to observe. The reason behind this low effect is the scattering rate at the intermediate state, which renders high Rabi frequencies on the lower transition impossible. For the UV dressing the potential height is a factor of about hundred higher, but still much smaller than the typical interaction energy U of $\sim 1\,\mathrm{kHz}$ for rubidium-87. As the total interaction energy in the system increases with the number of atoms, an interaction energy of this magnitude could probably be observed.

Applications of Rydberg dressing The successful implementation of Rydberg dressing would be a milestone towards the quantum simulation of long-range interacting Hamiltonians with motional degree of freedom. With standard absorption imaging the effect of Rydberg dressing can be rather hard to detect [23]. One clear signature would be spin-squeezing due to the strong non-linear interactions [205, 345]. If strong enough Rydberg dressing can be reached, in principle the mysterious supersolid state could be realized [6, 7, 346–348]. This is a crystalline phase, which simultaneously shows superfluidity. Its existence and the interpretation of experiments that claimed the observation of supersolidity in ^{4}He are still controversial [349–351]. An implementation with cold atoms, which is based on microscopically different physics, might allow for a larger superfluid fraction and more convincing evidence [348]. Another interesting regime is Rydberg dressing in an optical lattice [27], which also has the experimental advantage that possible collisions at short distance between Rydberg-dressed atoms should be suppressed. Rydberg dressing in optical lattices could clear the path towards implementing the extended Bose-Hubbard model, which is a generalization of the Bose-Hubbard model with additional beyond on-site interactions. A very interesting phase featured by the extended Bose-Hubbard model is the so-called Haldane insulator with hidden string-order [352–356], which could be detected the same way as already demonstrated for string order in a Mott insulator [14]. Rydberg dressing to anisotropic P-states is also a path towards simulation of the dynamical gauge field emerging in a quantum spin ice [256].

Appendix A.

Supplementary material for Chapter 2

A.1. Parity projection

The effect that we detect only an atom on a lattice site if the initial occupation was odd is an intrinsic property of the single-site fluorescence imaging in our setup. The main disadvantage is the loss of information about the initial absolute density. Under certain assumptions the density can be reconstructed for rather low densities. The typical assumption is a Poissonian distribution of the on-site occupation before parity projection, which is expected for a Bose-Einstein condensate and thermal gases. In this case some information about the average of the Poissonian distribution can be extracted from the parity projected density. The main limit here is the signal-to-noise ratio in the experiment, as the uncertainty in the estimation of parameters of the Poissonian distribution from parity-projected densities grows exponentially with the error on the measured parity density.

We assume Poissonian atom number distribution $p_\lambda(k) = \lambda^k \frac{e^{-\lambda}}{k}$ on-site with average occupation λ. The probabilities to detect even parity $p_{0,\lambda}$ and to detect odd parity $p_{1,\lambda}$ can be calculated analytically:

$$\begin{aligned} p_{0,\lambda} &= \sum_{\text{k even}} p_\lambda(k) = e^{-\lambda}\cosh(\lambda) = \frac{1+e^{-2\lambda}}{2} \\ p_{1,\lambda} &= \sum_{\text{k odd}} p_\lambda(k) = e^{-\lambda}\sinh(\lambda) = \frac{1-e^{-2\lambda}}{2}\ . \end{aligned} \tag{A.1}$$

This can be solved for λ to extract the mean density before parity projection $\lambda = -\frac{1}{2}\ln(p_{0,\lambda} - p_{1,\lambda})$. Calculating the error on the determined value yields $\varDelta\lambda = \sqrt{\left(\frac{\varDelta p_{0,\lambda}}{2(p_{0,\lambda}-p_{1,\lambda})}\right)^2 + \left(\frac{\varDelta p_{1,\lambda}}{2(p_{0,\lambda}-p_{1,\lambda})}\right)^2} = \frac{e^{2\lambda}}{2}\sqrt{\varDelta p_{0,\lambda}^2 + \varDelta p_{1,\lambda}^2}$, which obviously increases exponentially with λ.

As an example the loss of signal due to parity projection of a density wave around a mean density of λ is given by the derivative $e^{-2\lambda}$. The signal decays exponentially and already at a mean density of 0.5 the signal is decreased to 37 %. This leads to the observation that density modulations in Bose-Einstein condensates can be only detected with reasonable fidelity in a low-density regime in the presence of parity projection.

A.2. HTE0 on arduino

In the following a HTE0 implementation to simulate Mott insulator occupations. The code below is numerically stable also for floating point arithmetic, which allows to run it on an arduino uno.

```
#define N_SITES 16
float meannmod2HTE0_ext(float mu,float U,float B,int Zorder) {
  float expSubtract = 0;
  start:
  float Z = 0;
  float meann=0;

  for (int myn=0; myn<=Zorder; myn++) {
      float arg = -B*(U/2.*myn*(myn-1)-mu*myn)+expSubtract;
      float tmp;
       if (arg < -10) {
         tmp = 0;
       } else {
         tmp = exp(arg);
       }
      if (isinf(tmp)) {
        expSubtract -= arg;
        goto start;
      }
      Z = Z + tmp;
      meann=meann + (myn % 2)*tmp;
  }
  return meann/Z;
}
void calculateDistribution(int localGrid[N_SITES][N_SITES],
                           float T, float mu0, float r0) {
  int center = N_SITES/2.;
  int Zorder = 3;
  float U = 1; // all other values in units of U
  float B = 1/T;
  for (int i = 0; i < N_SITES; i++) {
     for (int j=0; j < N_SITES; j++) {
       float distGridVal = sqrt((i-center)*(i-center)+(j-center)*(j-center));
       float muGridVal = mu0-(distGridVal/r0)*(distGridVal/r0);
       localGrid[i][j] =
     meannmod2HTE0_ext(muGridVal, U, B, Zorder)>random(1000)/2000.0;
     }
  }
}
```

Appendix B.

Supplementary material for Chapter 4

B.1. Analytic hydrogen wavefunctions

A simple reference for the calculation of the radial wavefunctions of the Rydberg atoms are the hydrogen wavefunctions. For reference we write down here the analytical results explicitly [61], which were used for comparison with the calculated Rydberg wavefunctions. The version below uses the same definition as Mathematica for the Laguerre polynomials.

The normalized hydrogen wavefunction in spherical coordinates is given by

$$\begin{aligned}\psi_{nlm}(r,\theta,\phi) &= R_{nl}(r)\cdot Y_l^m(\theta,\phi)\\ &= \sqrt{\left(\frac{2}{na_0}\right)^3\frac{(n-l-1)!}{2n(n+l)!}}e^{-\rho/2}\rho^l L_{n-l-1}^{2l+1}(\rho)Y_l^m(\theta,\phi)\\ \text{with } \rho &= \frac{2r}{na_0}\text{ and the normalization}\\ &\int\limits_0^\infty dr\int\limits_0^\pi d\theta\int\limits_0^{2\pi} d\phi\,\psi_{nlm}(r,\theta,\phi)^*\cdot\psi_{n'l'm'}(r,\theta,\phi)r^2 = \delta_{nn'}\delta_{ll'}\delta_{mm'}\ .\end{aligned} \tag{B.1}$$

Here, a_0 is the Bohr radius, L_{n-l-1}^{2l+1} the generalized Laguerre polynomials and $Y_l^m(\theta,\phi)$ the spherical harmonics.

The normalized radial part of the hydrogen wavefunction is:

$$\begin{aligned}R_{nl}(r) &= \sqrt{\left(\frac{2}{na_0}\right)^3\frac{(n-l-1)!}{2n(n+l)!}}e^{-\rho/2}\rho^l L_{n-l-1}^{2l+1}(\rho)\\ \text{with normalization } &\int\limits_0^\infty R_{nl}^*\cdot R_{n'l'}(r)r^2dr = \delta_{nn'}\delta_{ll'}\ .\end{aligned} \tag{B.2}$$

B.2. Derivation of the radial differential equation for Rydberg atoms

Here we derive the radial wavefunction in scaled coordinates, optimized for numerical integration via the Numerov algorithm. The whole calculation is done in atomic units.

Analogous derivations can be found in [228, pp 33–35][175, pp.6–11] [230, pp. 15–17]. We start from the Schrödinger equation with spherically symmetric potential

$$\begin{aligned} \left(-\frac{\Delta}{2\mu} + V(r)\right)\Psi &= E\Psi \\ \mu &= \left(m_e^{-1} + m_p^{-1}\right)^{-1} \ . \end{aligned} \tag{B.3}$$

For the following we use Δ in spherical coordinates, given as

$$\Delta = \frac{\partial}{\partial r^2} + \frac{2}{r}\frac{\partial}{\partial r} + \frac{1}{r^2 \sin\theta}\frac{\partial}{\partial\theta}\left(\sin\theta\frac{\partial}{\partial\theta}\right) + \frac{1}{r^2\sin^2\theta}\frac{\partial^2}{\partial\phi^2} \ . \tag{B.4}$$

The difference between hydrogen and rubidium is due to the quantum defects and the effective potential seen by the outer electron. The potential used for rubidium is given in Section 4.1.2. For hydrogen the potential is just the Coulomb potential $V(r) = -\frac{1}{r}$. For alkali-metal Rydberg atoms there are various approximations possible. A simple approximation taking into account the basic effect of the other electrons leads to the following potential [207].

$$\begin{aligned} V(r) &= -\frac{Z}{r} + V_p(r) \\ &\text{with} \\ V_p(r) &\approx -\frac{\alpha_d}{2r^4} \end{aligned} \tag{B.5}$$

One can apply the standard separation ansatz to split off the radial part of the wavefunction.

$$\Psi = R_{nl}(r)Y_{lm}(\theta,\phi) = \frac{1}{r}U_{nl}(r)Y_{lm}(\theta,\phi) \tag{B.6}$$

With $Y_{lm}(\theta,\phi)$ the spherical harmonics the radial Schrödinger equation reduces to:

$$\left(-\frac{1}{2\mu}\frac{d}{dr^2} + V(r) + \frac{l(l+1)}{2r^2\mu}\right)U_{nl}(r) = EU_{nl}(r) \ . \tag{B.7}$$

For numeric integration it is favourable to use scaled coordinates [225],[226, p.36], which lead to a nearly constant oscillation period of the wavefunction in space. These wavefunctions can then be integrated numerically without loss in precision with fixed step size methods. The spatial coordinate and the wavefunction are rescaled as $u = \sqrt{r}$ and $\chi(u) = u^{-\frac{1}{2}}U_{nl}(u^2)$ or equivalent $\chi = r^{3/4}R(r)$ with $R(r) = \frac{U(r)}{r}$ [225].

To apply this transformation of the radial Schrödinger equation (B.7) one first needs to transform the second derivative

$$\frac{d^2}{dr^2}U(r) = \frac{1}{4}u^{-\frac{3}{2}}\frac{d^2}{du^2}\chi(u) - \frac{3}{16}u^{-\frac{7}{2}}\chi(u) \ , \tag{B.8}$$

where $U(r) = r^{1/4}\chi(\sqrt{r})$.

We plug in the result above into the radial Schrödinger equation and obtain a scaled radial differential equation for $\chi(u)$.

$$\begin{aligned}
\left(-\frac{1}{2\mu}\left(\frac{1}{4}u^{-\frac{3}{2}}\frac{d^2}{du^2}-\frac{3}{16}u^{-\frac{7}{2}}\right)+V(u^2)\sqrt{u}+\frac{l(l+1)}{2u^4\mu}\sqrt{u}\right)\chi(u) &= E\sqrt{u}\chi(u)\\
\left(-\frac{1}{8\mu u^2}\frac{d^2}{du^2}+\frac{\frac{3}{16}+l(l+1)}{2\mu u^4}+V(u^2)\right)\chi(u) &= E\chi(u)\\
\text{using }\frac{3}{16}+l(l+1) &= \frac{1}{4}\left(\frac{1}{2}+2l\right)\left(\frac{3}{2}+2l\right)\\
\left(-\frac{1}{8\mu u^2}\frac{d^2}{du^2}+\frac{(\frac{1}{2}+2l)(\frac{3}{2}+2l)}{8\mu u^4}+V(u^2)\right)\chi(u) &= E\chi(u) \qquad \text{(B.9)}\\
\frac{d^2}{du^2}\chi = \left(\frac{(\frac{1}{2}+2l)(\frac{3}{2}+2l)}{u^2}+8\mu u^2V(u^2)-8\mu u^2E\right)&\chi(u)\\
\text{and when using Eq. (B.5)}&\\
\frac{d^2}{du^2}\chi = \left(\frac{(\frac{1}{2}+2l)(\frac{3}{2}+2l)}{u^2}-8\mu-\frac{4\alpha_d\mu}{u^2}-8\mu u^2E\right)&\chi(u)
\end{aligned}$$

Here $E=-\frac{1}{2(n^*)^2}$ is the binding energy of the electron. The reduced mass in atomic units is about one and can be neglected compared to other error sources, especially for a heavy element as rubidium.

To avoid reverse transformations of the numerically obtained scaled wavefunctions for the calculation of matrix elements, we determine the radial overlap integral directly for the scaled wavefunctions $\chi(u)$.

$$\begin{aligned}
\mathcal{R}_{nl}^{n'l'} &= \int_0^\infty R_{nl}^*(r)r^kR_{n'l'}r^2dr\\
&= \int_0^\infty \frac{U_{nl}(r)}{r}r^k\frac{U_{n'l'}(r)}{r}r^2dr\\
&= \int_0^\infty U_{nl}(r)r^kU_{n'l'}(r)dr \qquad \text{(B.10)}\\
&= \int_0^\infty \sqrt{u}\chi_{nl}(u)u^{2k}\sqrt{u}\chi_{n'l'}(u)2udu\\
&= 2\int_0^\infty \chi_{nl}(u)u^{2k}\chi_{n'l'}(u)u^2du
\end{aligned}$$

B.3. Scaling of the wavefunction at the nucleus with the effective principal quantum number

Assuming that the scaling (see Appendix B.2) transforms the hydrogen wavefunctions in nearly constant amplitude functions, the scaling of $\psi(0)$ with the effective principal quantum number n^* can be derived. We start with $\chi(r) = \zeta\theta(r - r_1)$, with r_1 the orbit radius of the Rydberg state. Normalizing this wavefunction and transforming to $R(r)$ leads to $R(r) = \sqrt{\frac{3}{2}}\,(rr_1)^{-3/4}\,\theta(r - r_1)$. To determine the wavefunction at the origin, we integrate the wavefunction up to a small radius $r_0 < r_1$:
$\int_0^{r_0} |R(r)|^2\, r^2 dr = \int_0^{r_0} \left(\frac{r}{r_1}\right)^{-3/2} \theta(r - r_1) r^2 dr = \left(\frac{r_0}{r_1}\right)^{3/2}$. By definition r_0 is independent of n^* and r_1 scales as $(n^*)^2$, so $|\psi(0)|^2$ scales as $(n^*)^{-3}$. Another more technical way to derive this scaling is to look directly at the analytic hydrogen wavefunctions and their behaviour for $r \to 0$ using $L_m^k(0) = \frac{(m+k)!}{m!k!}$.

B.4. Comparison of radial matrix elements with literature

In the tables in this section calculated radial matrix elements are compared to various values in literature. The comparisons show that for most transitions the values are consistent. Only for transitions from the electronic ground state to Rydberg P-states significant deviations become apparent, which are attributed to the poor approximation of the ground state by the model potential.

transition	this work, radial m. el. $[a_0]$	calc. from quoted f-value, radial m. el. $[a_0]$	this work, osc. strength	quoted value, osc. strength
$\langle 5S_{1/2} \vert r \vert 6P_{3/2}\rangle$	$5.69 \cdot 10^{-1}$	$4.41 \cdot 10^{-1}$	$1.56 \cdot 10^{-2}$	$9.37 \cdot 10^{-3}$
$\langle 5S_{1/2} \vert r \vert 7P_{3/2}\rangle$	$2.37 \cdot 10^{-1}$	$1.65 \cdot 10^{-1}$	$3.17 \cdot 10^{-3}$	$1.53 \cdot 10^{-3}$
$\langle 5S_{1/2} \vert r \vert 8P_{3/2}\rangle$	$1.39 \cdot 10^{-1}$	$8.72 \cdot 10^{-2}$	$1.17 \cdot 10^{-3}$	$4.60 \cdot 10^{-4}$
$\langle 5S_{1/2} \vert r \vert 9P_{3/2}\rangle$	$9.55 \cdot 10^{-2}$	$5.65 \cdot 10^{-2}$	$5.72 \cdot 10^{-4}$	$2.00 \cdot 10^{-4}$
$\langle 5S_{1/2} \vert r \vert 10P_{3/2}\rangle$	$7.13 \cdot 10^{-2}$	$3.97 \cdot 10^{-2}$	$3.26 \cdot 10^{-4}$	$1.01 \cdot 10^{-4}$
$\langle 5S_{1/2} \vert r \vert 11P_{3/2}\rangle$	$5.61 \cdot 10^{-2}$	$3.35 \cdot 10^{-2}$	$2.05 \cdot 10^{-4}$	$7.30 \cdot 10^{-5}$
$\langle 5S_{1/2} \vert r \vert 12P_{3/2}\rangle$	$4.59 \cdot 10^{-2}$	$2.54 \cdot 10^{-2}$	$1.38 \cdot 10^{-4}$	$4.25 \cdot 10^{-5}$
$\langle 5S_{1/2} \vert r \vert 13P_{3/2}\rangle$	$3.85 \cdot 10^{-2}$	$2.11 \cdot 10^{-2}$	$9.79 \cdot 10^{-5}$	$2.95 \cdot 10^{-5}$
$\langle 5S_{1/2} \vert r \vert 14P_{3/2}\rangle$	$3.29 \cdot 10^{-2}$	$1.85 \cdot 10^{-2}$	$7.21 \cdot 10^{-5}$	$2.28 \cdot 10^{-5}$
$\langle 5S_{1/2} \vert r \vert 15P_{3/2}\rangle$	$2.86 \cdot 10^{-2}$	$1.43 \cdot 10^{-2}$	$5.48 \cdot 10^{-5}$	$1.36 \cdot 10^{-5}$
$\langle 5S_{1/2} \vert r \vert 16P_{3/2}\rangle$	$2.52 \cdot 10^{-2}$	$1.30 \cdot 10^{-2}$	$4.26 \cdot 10^{-5}$	$1.13 \cdot 10^{-5}$
$\langle 5S_{1/2} \vert r \vert 17P_{3/2}\rangle$	$2.24 \cdot 10^{-2}$	$1.15 \cdot 10^{-2}$	$3.38 \cdot 10^{-5}$	$8.89 \cdot 10^{-6}$
$\langle 5S_{1/2} \vert r \vert 18P_{3/2}\rangle$	$2.02 \cdot 10^{-2}$	$1.03 \cdot 10^{-2}$	$2.73 \cdot 10^{-5}$	$7.16 \cdot 10^{-6}$
$\langle 5S_{1/2} \vert r \vert 19P_{3/2}\rangle$	$1.82 \cdot 10^{-2}$	$9.08 \cdot 10^{-3}$	$2.24 \cdot 10^{-5}$	$5.56 \cdot 10^{-6}$
$\langle 5S_{1/2} \vert r \vert 20P_{3/2}\rangle$	$1.66 \cdot 10^{-2}$	$7.54 \cdot 10^{-3}$	$1.86 \cdot 10^{-5}$	$3.84 \cdot 10^{-6}$

Table B.1.: Comparison of oscillator strengths for ^{87}Rb with experimental data by Caliebe & Niemax [208]. The measurements fit quite well with relativistic calculations [210, 357, 358]. The table shows that the simple quantum defect calculation is not accurate for these transitions and leads to deviations of around a factor of two in the matrix elements for $5S_{1/2}$ to $nP_{3/2}$ transitions.

matrix element	this work $[a_0]$	quoted value exp $[a_0]$	quoted value th $[a_0]$
$\sqrt{2/3}\langle 5P_{3/2} \vert r \vert 20D_{5/2}\rangle$	0.0873	0.084(6)	0.085
$\sqrt{2/3}\langle 5P_{3/2} \vert r \vert 22D_{5/2}\rangle$	0.0748	0.071(6)	0.073
$\sqrt{2/3}\langle 5P_{3/2} \vert r \vert 26D_{5/2}\rangle$	0.0572	0.058(6)	0.056
$\sqrt{2/3}\langle 5P_{3/2} \vert r \vert 28D_{5/2}\rangle$	0.0508	0.050(5)	0.049
$\sqrt{2/3}\langle 5P_{3/2} \vert r \vert 30D_{5/2}\rangle$	0.0456	0.044(4)	0.044
$\sqrt{2/3}\langle 5P_{3/2} \vert r \vert 35D_{5/2}\rangle$	0.0357	0.032(4)	0.035
$\sqrt{2/3}\langle 5P_{3/2} \vert r \vert 37D_{5/2}\rangle$	0.0328	0.031(3)	0.032
$\sqrt{2/3}\langle 5P_{3/2} \vert r \vert 40D_{5/2}\rangle$	0.0290	0.030(3)	0.028
$\sqrt{2/3}\langle 5P_{3/2} \vert r \vert 42D_{5/2}\rangle$	0.0269	0.024(3)	0.026
$\sqrt{2/3}\langle 5P_{3/2} \vert r \vert 44D_{5/2}\rangle$	0.0250	0.023(3)	0.024
$\sqrt{2/3}\langle 5P_{3/2} \vert r \vert 48D_{5/2}\rangle$	0.0219	0.021(3)	0.021

Table B.2.: Comparison of radial matrix elements for ^{87}Rb with experiment and theory from [234, 359]. In the measurements by Piotrowicz *et al.* the matrix elements are given including the angular factor $\sqrt{2/3}$ [359, p.78]. The experimental values are consistent with the values in [233], a comparison can be found in [360].

matrix element	this work (a_0)	quoted value (a_0)	reference	deviation (%)
$\langle 5S_{1/2} \vert r \vert 5P_{1/2} \rangle$	5.46	5.1842	[263]	5.5
$\langle 5S_{1/2} \vert r \vert 5P_{3/2} \rangle$	5.44	5.1776	[263]	5.1
$\langle 5S_{1/2} \vert r \vert 5P_{3/2} \rangle$	5.44	5.14	[100]	5.9
$\langle 5P_{3/2} \vert r \vert 79D_{5/2} \rangle$	0.0125	0.012	[100]	3.8
$\langle 5P_{3/2} \vert r \vert 43D_{5/2} \rangle$	0.031 75	0.029	[70, p.4]	9.5
$\langle 5P_{3/2} \vert r \vert 43D_{5/2} \rangle$	0.031 75	0.031 60	[78, p.30]	0.47
$\langle 5P_{1/2} \vert r \vert 43S_{1/2} \rangle$	−0.017 601	−0.017 600	[78, p.30]	0.01
$\langle 5P_{3/2} \vert r \vert 43S_{1/2} \rangle$	0.017 48	0.017 86	[3, p.6]	2.1
$\langle 5P_{3/2} \vert r \vert 44D_{5/2} \rangle$	−0.0306	0.03	[276, p.3]	2.1
$\langle 56F_{5/2} \vert r \vert 58D_{3/2} \rangle$	2596.0	2594	[74, SI]	0.08
$\langle 58D_{3/2} \vert r \vert 60P_{1/2} \rangle$	2563.3	2563	[74, SI]	0.01
$\langle 46S_{1/2} \vert r \vert 45P_{1/2} \rangle$	1924.5	1924	[132]	0.03
$\langle 50D_{5/2} \vert r \vert 52P_{3/2} \rangle$	1842.7	1840	[361]	0.15
$\langle 48F_{7/2} \vert r \vert 50D_{5/2} \rangle$	1892.8	1893	[361]	0.01
$\langle 35D_{5/2} \vert r \vert 37P_{3/2} \rangle$	876.3	875	[361]	0.15
$\langle 33F_{7/2} \vert r \vert 35D_{5/2} \rangle$	881.6	882	[361]	0.04
$\langle 46D_{5/2} \vert r \vert 48P_{3/2} \rangle$	1550.3	1548	[307]	0.15
$\langle 44F_{7/2} \vert r \vert 46D_{5/2} \rangle$	1585.9	1587	[307]	0.07
$\langle 46D_{5/2} \vert r \vert 47P_{3/2} \rangle$	2708.6	2709	[307]	0.01
$\langle 45F_{7/2} \vert r \vert 46D_{5/2} \rangle$	2694.3	2694	[307]	0.01

Table B.3.: Comparison of radial matrix elements for ^{87}Rb and ^{85}Rb with literature. The pure radial matrix elements from [263] are extracted as described in Sec. J.1. The precision of calculated matrix elements between two Rydberg states (lower half of the table) is much higher than the quality of the matrix elements from the ground state or first excited state to Rydberg states (upper half) due to larger influence of the imperfect model potential on low-lying states.

	$nS_{1/2}$	$nP_{1/2}$	$nP_{3/2}$
$5S_{1/2}$	-	0.9223(11)[0.7%]	1.1689(8)[0.7%]

	$nS_{1/2}$	$nD_{3/2}$	$nD_{5/2}$
$5P_{1/2}$	4.4362(5)[0.5%]	8.2650(3)[0.2%]	-
$5P_{3/2}$	4.4052(5)[0.6%]	8.5730(3)[0.2%]	8.5389(3)[0.2%]
$6P_{1/2}$	8.7444(18)[1.2%]	12.5363(9)[0.5%]	-
$6P_{3/2}$	8.5770(17)[1.2%]	13.1678(60)[0.5%]	13.0956(61)[0.5%]
$7P_{1/2}$	14.2235(10)[2.1%]	17.4035(61)[0.9%]	-
$7P_{3/2}$	13.9598(18)[2.1%]	18.1369(63)[1.0%]	18.0152(63)[1.0%]

Table B.4.: Scaling of radial matrix elements of ^{87}Rb. The scaling coefficients are fitted to the calculated values of matrix elements for $n = 30$ to $n = 100$ (for details see Sec. 4.1.5). The notation is $a(b)[c]$ where a is the scaling coefficient, b the fitting error of the last digit and c the maximum deviation of the fit function from the individual calculated values. As the quantum defect calculation is not the optimal approach to calculate matrix elements involving a low-lying level, systematic errors on the order of 10 % are not surprising. In particular the matrix elements 5S → nP have to be taken with care, as the quantum defect calculation for the ground state wavefunction might be quite inaccurate (Table B.1).

matrix element	this work (a_0)	quoted value (a_0)	reference	deviation (%)
$5P_{3/2} \rightarrow nS_{1/2}$	4.405	4.508	[227, p.296] [175, p.13]	2%
		4.502	[230, p.21]	2%
$5P_{3/2} \rightarrow nD_{5/2}$	8.539	8.475	[227, p.296] [175, p.13]	1%
		8.457	[230, p.21]	1%

Table B.5.: Comparison of fitted scaling coefficients with literature. For details see Sec. 4.1.5.

Appendix C.

Supplementary material for Chapter 5

C.1. Three-level system with dissipation

To establish conventions we repeat the basic physics of three-level systems in ladder configurations and the reduction to an effective two-level system. For a comparison with experiment it is interesting to understand the influence of the various decay channels in the system. As application we will discuss the prerequisites on the parameters to observe Rabi oscillations in such a system. A good overview on the inclusion of decay in the three-level system can be found in [230, p.39]. The following treatment is based on the derivations and results there (similar discussions can be found also for example in [71, 78, 287, 362–366]). For simplification of the treatment we only consider real Rabi frequencies.

C.1.1. Three-level system

The excitation of Rydberg atoms via a two-photon transition is described by a three-level system with two laser couplings. The Hamiltonian can be written in Matrix form in the basis $(|g\rangle, |e\rangle, |r\rangle)$, where $|g\rangle$ is the ground state, $|e\rangle$ the intermediate state and $|r\rangle$ the Rydberg state.

$$\hat{H} = \hbar \begin{pmatrix} 0 & \frac{\Omega_1}{2} & 0 \\ \frac{\Omega_1}{2} & \Delta & \frac{\Omega_2}{2} \\ 0 & \frac{\Omega_2}{2} & \delta \end{pmatrix} \tag{C.1}$$

Here Δ is the intermediate state detuning and δ is the two-photon detuning as defined in Fig. C.1.

Decay due to the natural linewidth of excited levels is given by the following Liouville operator.

$$\hat{\mathcal{L}}(\rho) = \begin{pmatrix} \Gamma_e\rho_{ee} & -\frac{1}{2}\Gamma_e\rho_{ge} & -\frac{1}{2}\Gamma_r\rho_{gr} \\ -\frac{1}{2}\Gamma_e\rho_{eg} & -\Gamma_e\rho_{ee} + \Gamma_r\rho_{rr} & -\frac{1}{2}(\Gamma_e + \Gamma_r)\rho_{er} \\ -\frac{1}{2}\Gamma_r\rho_{rg} & -\frac{1}{2}(\Gamma_e + \Gamma_r)\rho_{re} & -\Gamma_r\rho_{rr} \end{pmatrix} \tag{C.2}$$

Where the density matrix is parametrized as

$$\hat{\rho} = \begin{pmatrix} \rho_{gg} & \rho_{ge} & \rho_{gr} \\ \rho_{eg} & \rho_{ee} & \rho_{er} \\ \rho_{rg} & \rho_{re} & \rho_{rr} \end{pmatrix} . \tag{C.3}$$

Here the direct decay from the Rydberg state to the ground-state is neglected, as the transition is typically forbidden due to parity conservation and therefore the transition rate very small. We take into account the decay from the Rydberg state to the intermediate state Γ_r and the decay from the intermediate to the ground state Γ_e. The off-diagonal terms model the dephasing between the corresponding levels caused by decay events. Additionally there is dephasing for imperfect laser stability, which can be taken into account by the following operator [230]:

$$\hat{\mathcal{L}}_d(\rho) = \begin{pmatrix} 0 & -\gamma_1\rho_{ge} & -(\gamma_1+\gamma_2)\rho_{gr} \\ -\gamma_1\rho_{eg} & 0 & -\gamma_2\rho_{er} \\ -(\gamma_1+\gamma_2)\rho_{rg} & -\gamma_2\rho_{re} & 0 \end{pmatrix} . \tag{C.4}$$

Here $\gamma_{1,2}$ denote the FWHM linewidth of the laser on the lower transition and upper transition, respectively (Fig. C.1).

The dynamics including dissipation is then given by the master equation

$$\dot{\hat{\rho}} = -\frac{i}{\hbar}\left[\hat{H},\hat{\rho}\right] + \hat{\mathcal{L}}(\rho) + \hat{\mathcal{L}}_d(\rho) . \tag{C.5}$$

C.1.2. Reduction to two-level system

In many cases it is not necessary to do calculations in the three-level system as the physics can be also calculated in an effective two-level description [362, 363]. Many experiments are easier to interpret in the resulting two-level model. The reduction scheme is somewhat tricky in the details [367], but the simple adiabatic elimination scheme leads to the correct result. The prerequisite for the adiabatic elimination of the intermediate level is a large intermediate state detuning, i.e. $|\Delta| \gg \max(|\delta|, |\Omega_1|, |\Omega_2|)$ [367, 368]. These conditions can be somewhat relaxed using a bit more complex treatment [369]. The adiabatic elimination scheme can be generalized to many levels and higher order approximations [370].

To simplify the calculation of light shifts, one can typically assume $|\omega_1 - \omega_2| \gg |\Delta|$, which allows to neglect the light shift of laser 1 on transition 2 and laser 2 on transition 1. As written above, we assume $|\Delta| \gg |\Omega_{1,2}|$, allowing to approximate the light shifts of laser 1,2 on transition 1,2 as $\Delta_g^{LS} = \frac{\Omega_1^2}{4\Delta_1} = \frac{\Omega_1^2}{4\Delta}$ and $\Delta_r^{LS} = -\frac{\Omega_2^2}{4\Delta_2} = \frac{\Omega_2^2}{4(\Delta-\delta)}$. The effective light shift on the reduced two-level system is thereby $\Delta_{\text{eff}}^{LS} = \Delta_r^{LS} - \Delta_g^{LS} = \frac{\Omega_2^2}{4(\Delta-\delta)} - \frac{\Omega_1^2}{4\Delta}$.

Finally we end up with an effective two-level description with effective detuning and Rabi frequency. The effective Rabi frequency is $\Omega_{\text{eff}} = \frac{\Omega_1\Omega_2}{2\Delta}$, and the effective detuning $\Delta_{\text{eff}} = \delta + \Delta_{\text{eff}}^{LS} = \delta + \frac{\Omega_2^2}{4(\Delta-\delta)} - \frac{\Omega_1^2}{4\Delta}$. Within this thesis the effective resonant Rabi frequency Ω_{eff} is often simply referred to as Ω. For off-resonant driving the Rabi frequency becomes $\Omega_{\text{detuned}} = \sqrt{\Omega_{\text{eff}}^2 + \Delta_{\text{eff}}^2}$.

Without dissipation the effective description of the three-level system is the well-known two-level system Hamiltonian, where Ω and Δ are replaced by the effective quantities discussed above.

$$H = \hbar \begin{pmatrix} 0 & \frac{\Omega_{\text{eff}}}{2} \\ \frac{\Omega_{\text{eff}}}{2} & \Delta_{\text{eff}} \end{pmatrix} \tag{C.6}$$

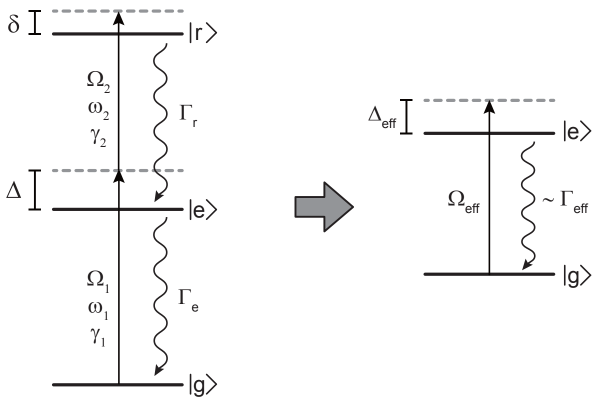

Figure C.1.: Reduction of three level system. By adiabatic elimination of the intermediate state a three-level system (left) can be described in the limit of large intermediate detuning $\varDelta$ by a two-level system (right). The detuning of the laser 1 on transition 1 is $\varDelta_1 = \varDelta = \omega_1 - \omega_{eg}$, where ω_{eg} is the atomic transition frequency. The detuning of laser 2 on transition 2 is $\varDelta_2 = \omega_2 - \omega_{re} = \delta - \varDelta$.

Taking into account the decay and dephasing terms during reduction is tricky, here we use a semi-empirical approach and checked the following Liouville operators numerically against the full three-level calculation.

$$\hat{\mathcal{L}}(\rho) = \begin{pmatrix} \varGamma_r \rho_{rr} & -\frac{1}{2}\varGamma_r \rho_{gr} \\ -\frac{1}{2}\varGamma_r \rho_{rg} & -\varGamma_r \rho_{rr} \end{pmatrix} \tag{C.7}$$

$$\hat{\mathcal{L}}_d(\rho) = \begin{pmatrix} 0 & -(\gamma_1 + \gamma_2 + \gamma_i)\rho_{gr} \\ -(\gamma_1 + \gamma_2 + \gamma_i)\rho_{rg} & 0 \end{pmatrix} \tag{C.8}$$

Here $\gamma_i = \frac{\varGamma_e \varOmega_1^2}{\varGamma_e^2 + 2\varOmega_1^2 + 4\varDelta^2} \approx \frac{\varGamma_e \varOmega_1^2}{4\varDelta^2}$ is a reasonable approximation for the dephasing due to the decay at the intermediate level. For the further calculation we define $\gamma = \gamma_1 + \gamma_2 + \gamma_i$. The time evolution for $\varDelta_{\text{eff}} = 0$ can be solved analytically by transformation of the complex differential equation system to a standard real linear form

$$\frac{d}{dt}\begin{pmatrix} \rho_{gg} \\ \mathrm{Re}(\rho_{gr}) \\ \mathrm{Im}(\rho_{gr}) \\ \rho_{rr} \end{pmatrix} = \begin{pmatrix} 0 & 0 & -\varOmega_{\text{eff}} & \varGamma_r \\ 0 & -\gamma - \varGamma_r/2 & -\varDelta_{\text{eff}} & 0 \\ \varOmega_{\text{eff}}/2 & \varDelta_{\text{eff}} & -\gamma - \varGamma_r/2 & -\varOmega_{\text{eff}}/2 \\ 0 & 0 & \varOmega_{\text{eff}} & -\varGamma_r \end{pmatrix} \begin{pmatrix} \rho_{gg} \\ \mathrm{Re}(\rho_{gr}) \\ \mathrm{Im}(\rho_{gr}) \\ \rho_{rr} \end{pmatrix}. \tag{C.9}$$

The result for the Rydberg state population for an initial state with all population in the ground state is then

$$\rho_{rr}(t) = -\frac{\varOmega^2 e^{-\varGamma_{\text{eff}} t}\left(\varGamma_{\text{eff}} \sin(\varOmega_d t) + \varOmega_d \cos(\varOmega_d t) - \varOmega_d e^{\varGamma_{\text{eff}} t}\right)}{\varOmega_d \left(2\gamma\varGamma_r + \varGamma_r^2 + 2\varOmega^2\right)}. \tag{C.10}$$

To simplify the notation we use $\varOmega = \varOmega_{\text{eff}}$ and define $\varOmega_d = \frac{1}{4}\sqrt{16\varOmega^2 - (\varGamma_r - 2\gamma)^2}$, $\varGamma_{\text{eff}} = \frac{2\gamma + 3\varGamma_r}{4}$, where $\varOmega_d$ becomes real for the oscillatory case $\varOmega \gg \gamma, \varGamma_r$ and represents a slightly modified oscillation frequency. In the case of weak dephasing and weak decay we can approximate the time evolution above, by noting that $\Omega_d \approx \Omega$ and $\Gamma_{\text{eff}} \ll \Omega_d$. This leads to:

$$\rho_{rr}(t) \approx \frac{\Omega^2 \left(1 - e^{-\Gamma_{\text{eff}} t} \cos(\Omega t)\right)}{2\gamma \Gamma_r + \Gamma_r^2 + 2\Omega^2} \approx \frac{1 - e^{-\Gamma_{\text{eff}} t} \cos(\Omega t)}{2} \,. \tag{C.11}$$

The last result shows directly that the effective decay of the Rabi oscillation is given by the time constant $\Gamma_{\text{eff}} = \frac{2\gamma + 3\Gamma_r}{4} = \frac{1}{2}(\gamma_1 + \gamma_2 + \gamma_i) + \frac{3}{4}\Gamma_r$. The requirement to observe Rabi oscillations is therefore $\Omega > \Gamma_{\text{eff}}$. The linewidths of the lasers can be reduced by a good stabilization, but Γ_r, which is approximately $2\pi \cdot 4\,\text{kHz}$ for the 43S state, cannot be changed. The dephasing γ_i caused by decay from the intermediate state is directly determined by the laser intensity for the lower transition. It is clearly desirable to rather increase the Rabi frequency on the upper transition, which has no negative effect on the dephasing. By maximizing $\frac{\Omega}{\Gamma_{\text{eff}}}$, it is possible to calculate the optimal detuning to observe a maximum number of Rabi cycles, which is given by $\Delta_{\text{opt}} = \sqrt{\frac{\Gamma_e}{4\gamma_1 + 4\gamma_2 + 3\Gamma_r}}\Omega_1$. This suggest we should use $\frac{\Delta}{\Omega_1} \approx 5$ for our parameters ($\Gamma_e = 2\pi{\cdot}6\,\text{MHz}, \gamma_1 = 2\pi{\cdot}50\,\text{kHz}, \gamma_2 = 2\pi{\cdot}20\,\text{kHz}, \Gamma_r = 2\pi{\cdot}4\,\text{kHz}$). But this calculation does not take into account dephasing due to light shift variations caused by intensity noise, which limits the intensity on the lower transition. In the end the best way to observe Rabi oscillations is to aim for the highest reachable Rabi frequency on the upper transition, while the optimal Rabi frequency on the lower transition depends on the detuning Δ and the combination of many dephasing and decoherence sources.

C.2. Detection efficiency correction for Rydberg histograms

In an experiment where we detect a certain number of atoms in every picture and every atom is detected with a probability η, we can correct the full counting statistics of the distribution of detected atom numbers $p(n)$ using a linear transformation. The main assumption here is a detection efficiency for a single atom that is constant over time and does not depend on the number of atoms in the picture. We denote the probability to detect n atoms with $p_\eta(n)$ and the underlying real distribution $p(n) \equiv p_1(n)$. $n_{\max}$ is the maximum number of atom that occurs. With these definitions we obtain the following transformations

$$p_\eta(n) = \sum_{m=n}^{n_{\max}} \eta^n (1-\eta)^{m-n} \binom{m}{n} p(m) \tag{C.12}$$

$$p(n) = \sum_{m=n}^{n_{\max}} \left(\frac{1}{\eta}\right)^n \left(1 - \frac{1}{\eta}\right)^{m-n} \binom{m}{n} p_\eta(m) \,. \tag{C.13}$$

The sum can also start at zero as the binomial coefficients are anyway zero in the added range.

To demonstrate consistency of both transformation we show that the second equation is the inverse transformation of the first (the identity used in here can be verified using e.g. Mathematica):

$$\begin{aligned}
p(n) &= \sum_m \left(\frac{1}{\eta}\right)^n \left(1-\frac{1}{\eta}\right)^{m-n} \binom{m}{n} \sum_{m'} \eta^m (1-\eta)^{m'-m} \binom{m'}{m} p(m') \\
&= (\eta-1)^{-n} \sum_{m,m'} (-1)^m (1-\eta)^{m'} \binom{m}{n}\binom{m'}{m} p(m') \\
&= (\eta-1)^{-n} \sum_{m'} (1-\eta)^{m'} p(m') \underbrace{\sum_m (-1)^m \binom{m}{n}\binom{m'}{m}}_{=(-1)^n \delta_{m',n}} \qquad \text{(C.14)} \\
&= (\eta-1)^{-n} (1-\eta)^n p(n) (-1)^n \\
&= p(n)\ .
\end{aligned}$$

C.3. Mandel Q parameter

The Mandel Q parameter, introduced by Mandel in the 70ths [107], is a normalized factorial moment.

There are some special properties of this parameter: It is 0 for a Poissonian distribution and takes a minimal value of -1 for a Fock state. For a parameter Q_η measured with a detection efficiency η in an experiment, the relation $Q_\eta = \eta Q$ holds (Appendix of [106], see also [107]). In the following the proof of this relation is reproduced.

We start from the known mean value and standard deviation of the binomial distribution $p(k) = \binom{n}{k} p^k (1-p)^{n-k}$ (e.g. [371]) and calculate mean and variance:

$$\langle x \rangle = \sum_k k p(k) = \sum_k k \binom{n}{k} p^k (1-p)^{n-k} = np \qquad \text{(C.15)}$$

$$\langle x^2 \rangle - \langle x \rangle^2 = np(1-p) \qquad \text{(C.16)}$$

$$\langle x^2 \rangle = np(1-p) + n^2p^2 = \sum k^2 \binom{n}{k} p^k (1-p)^{n-k} \qquad \text{(C.17)}$$

We define $\langle x \rangle_\eta$ as the average value of the probability distribution x with distribution function $p_\eta(x)$ as used in Appendix C.2. The goal is now to calculate the relation between $\langle . \rangle_\eta$ and $\langle . \rangle$ for x and x^2. We use the relations shown above.

$$\langle x \rangle_\eta = \sum_n n p_\eta(n) = \sum_n \sum_m n \eta^n (1-\eta)^{m-n} \binom{m}{n} p(m) = \sum_m \eta m p(m) = \eta \langle x \rangle \qquad \text{(C.18)}$$

$$\begin{aligned}
\langle x^2 \rangle_\eta &= \sum_n n^2 p_\eta(n) = \sum_n n^2 \sum_m \eta^n (1-\eta)^{m-n} \binom{m}{n} p(m) = \sum_m \left(m^2\eta^2 + m\eta(1-\eta)\right) p(m) \\
&= \eta^2 \langle x^2 \rangle + \eta(1-\eta) \langle x \rangle
\end{aligned}$$

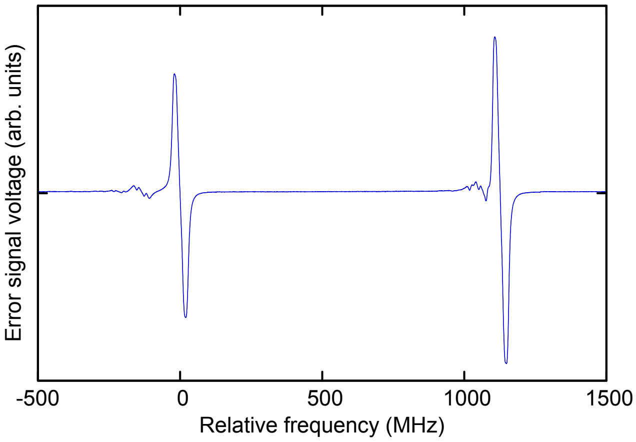

Figure C.2.: Modulation transfer error signal. Modulation transfer error signal for ^{87}Rb (left) and ^{85}Rb (right). The spectroscopy is nearly free of systematic offsets and the residual offset is about 1 % of the peak signal. It is probably caused by electronic offsets and does not depend on laser power. The x-axis is calibrated by the known isotope shift of the line of 1126.5 MHz. The wiggles on the left side of the error signals are probably caused by interference effects due to the other atomic transition nearby. The two large error signals are both around 40 MHz wide with a signal-to-noise ratio of around > 200, allowing to lock to 50 kHz.

Now we calculate Q_η measured in the experiment in terms of the ideal Q parameter.

$$\begin{aligned}
Q_\eta &= \frac{\langle x(x-1)\rangle_\eta - \langle x\rangle_\eta^2}{\langle x\rangle_\eta} = \frac{\langle x^2\rangle_\eta - \langle x\rangle_\eta^2}{\langle x\rangle_\eta} - 1 \\
&= \frac{\eta^2 \langle x^2\rangle + \eta(1-\eta)\langle x\rangle - \eta^2 \langle x\rangle^2}{\eta \langle x\rangle} - 1 \\
&= \frac{\eta \langle x^2\rangle - \eta \langle x\rangle^2}{\langle x\rangle} + (1-\eta) - 1 \\
&= \eta \left(\frac{\langle x^2\rangle - \langle x\rangle^2}{\langle x\rangle} - 1 \right) \\
&= \eta Q
\end{aligned} \tag{C.19}$$

If the experiment exhibits a well-defined detection efficiency η the minimum Q that can be measured is then $-\eta$.

C.4. Modulation transfer spectroscopy

Many often used spectroscopy techniques like saturated absorption spectroscopy, modulation or polarization spectroscopy are quite sensitive to offset drifts, leading easily to drifts of the laser frequency on the order of 10 % of the natural linewidth. For the so-called modulation transfer spectroscopy this problem is strongly reduced. The basic technique is quite an old concept [372–374] and there is even a patent on that [375]. It got broad interest only much later [175, 376–384] and is still actively studied due to its special properties. The idea is to phase-modulate only the saturation beam and detect the transfer of the modulation to the probe beam. After down-mixing this leads to a vanishing error signal far from resonance and a strong dispersive signal on resonance. Compared to other spectroscopy techniques only closed transition cause a strong error signal, but some other lines are also accessible by using different polarizations. Another interesting effect is the low susceptibility to power broadening for this technique. For the typical power of diode lasers we could not observe power broadening, while for normal saturated absorption spectroscopy the Doppler free lines are easily broadened to a degree that they vanish in the noise floor. The main disadvantage of the modulation transfer spectroscopy is that a strongly driven resonant electro-optic modulator is required to reach a reasonably strong error signal. It turns out that the optimal modulation frequency is typically slightly below the natural linewidth of the transition, for higher modulation frequencies several zero crossings of the error signal are observed.

In our setup we were able to reach a linewidth and stability of the laser lock by a modulation transfer spectroscopy of about 50 kHz (Sec. 5.5.2). The corresponding error signal is shown in Fig. C.2. As demonstrated in high-precision spectroscopy [385], locking to ±3 kHz on the D_2-line is possible by using pre-stabilization cavities and advanced lock-in schemes.

Appendix D.

Supplementary material for Chapter 6

The following supplementary material is reproduced from [291].

D.1. Additional information on the datasets

The experimental data results from three different datasets (A, B and C). Each dataset was characterized by a temperature, T, atom number, N_{at}, and diameter, $2R$, which we extracted from a fit to the ground state atom distribution in the initial state [21] (Table D.1). The datasets A and B were used for Fig. 6.4 and 6.6, while the dataset C was used for Fig. 6.7. The distribution of the number of excitations in the datasets A and B is detailed in Table D.2, where we also indicated which subset of images was used for which figures. The dataset C consisted of 54 images per pulse duration and the relative distribution of excitations is directly visible in Fig. 6.7.

	dataset A	dataset B	dataset C
T (nK)	8(4)	13(2)	9(4)
N_{at}	150(30)	390(30)	150(30)
R (µm)	3.6(4)	5.4(4)	3.6(4)

Table D.1.: Temperature T, atom number N_{at} and radius R for the pulsed excitation datasets A, B and C. Errors, s.d.

D.2. Numerical calculations

In order to determine the dynamics governed by the Hamiltonian in Eq. (6.1), we expand the many-body wavefunction, $|\psi\rangle$, of the N_{at}-atom system in terms of Fock-states

$$|\psi\rangle = c^{(0)}|0\rangle + \sum_{\boldsymbol{i}_1} c^{(1)}_{\boldsymbol{i}_1}|\boldsymbol{i}_1\rangle + \sum_{\boldsymbol{i}_1,\boldsymbol{i}_2} c^{(2)}_{\boldsymbol{i}_1,\boldsymbol{i}_2}|\boldsymbol{i}_1,\boldsymbol{i}_2\rangle + \ldots + \sum_{\boldsymbol{i}_1,\ldots,\boldsymbol{i}_{N_{\mathrm{at}}}} c^{(N_{\mathrm{at}})}_{\boldsymbol{i}_1,\ldots,\boldsymbol{i}_{N_{\mathrm{at}}}}|\boldsymbol{i}_1,\ldots,\boldsymbol{i}_{N_{\mathrm{at}}}\rangle\ , \quad \text{(D.1)}$$

	dataset A		dataset B	
number of excitations	number of images	figures	number of images	figures
0	177	–	321	–
1	235	–	375	6.6a
2	191	6.4a, 6.6b	390	6.6a
3	65	6.4a, 6.6b	308	6.6a
4	7	–	177	6.4a, 6.6a, 6.6b
5	1	–	64	6.4a, 6.6a, 6.6b
6	0	–	14	–
7	0	–	5	–

Table D.2.: Distribution of the number of excitations in the pulsed excitation datasets A and B. For each subset of images we have also indicated in which figure it has been used.

where $|\boldsymbol{i}_1, \ldots, \boldsymbol{i}_{N_\mathrm{e}}\rangle$ corresponds to a state with N_e Rydberg excitations located at lattice sites $\boldsymbol{i}_1$ to $\boldsymbol{i}_{N_\mathrm{e}}$, and $c^{(N_\mathrm{e})}_{\boldsymbol{i}_1,\ldots,\boldsymbol{i}_{N_\mathrm{e}}}$ denotes the respective time dependent amplitude. The basis states are eigenfunctions of the Hamiltonian (6.1) in the absence of laser driving, with energy eigenvalues $E^{(N_\mathrm{e})}_{\boldsymbol{i}_1,\ldots,\boldsymbol{i}_{N_\mathrm{e}}} = \sum_{\alpha<\beta}^{N_\mathrm{e}} V_{\boldsymbol{i}_\alpha \boldsymbol{i}_\beta}$. For a system of N_at atoms, this basis set expansion yields a set of 2^{N_at} coupled differential equations (Fig. D.1).

Due to the exponential growth of the number of many-body states with N_at, a direct numerical propagation is practically impossible for the large number of atoms in our experiments, $N_\mathrm{at} \sim 100$. In order to make the calculations feasible, we exploit the blockade effect and discard all many-body states containing Rydberg atom pairs separated by less than a critical distance R_c. For the present simulations, we obtain well-converged results for $R_c \simeq R_\mathrm{b}/2$, where R_b is the blockade radius. The resulting geometric constraint not only reduces the number of relevant many-body states within a given N_e-manifold, but, due to the finite system size, also restricts the total number of excitations N_e necessary to obtain converged results. For the parameters considered in this work, a maximum number of Rydberg excitations of ${N_\mathrm{e}}^{(\mathrm{max})} = 6$ was found sufficient. This procedure allows to significantly mitigate the otherwise strong exponential scaling of the underlying Hilbert space dimension, and yields a power-law dependence $\sim {N_\mathrm{at}}^{{N_\mathrm{e}}^{(\mathrm{max})}}$ of the number of relevant basis states on the total number of atoms. This makes the computations feasible, albeit still demanding, for such large systems as in our experiment.

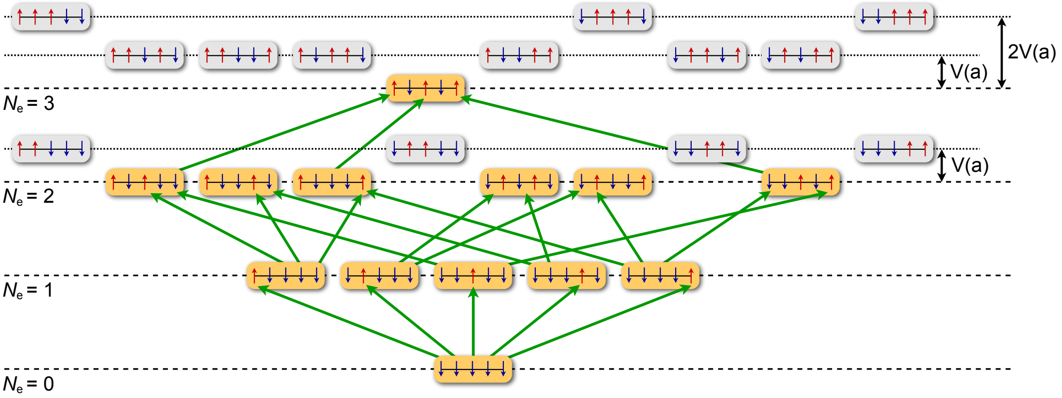

Figure D.1.: Schematic illustrating the Hilbert space truncation for numerical calculations. The underlying many-body level structure is shown for the example of a one-dimensional chain of five atoms. The atomic states are symbolised by effective spins, with spin-down (blue arrows) and spin-up (red arrows) corresponding to the atomic ground and Rydberg state, respectively. In the displayed example, we consider strong interactions $V(a) \gg \hbar\Omega$ between adjacent Rydberg excitations, while next-nearest neighbour interactions $V(2a) = V(a)/64 < \hbar\Omega$ are assumed to be smaller than the laser coupling strength. Consequently, the dynamics of near resonant basis states (orange boxes) is explicitly calculated in the simulations, while strongly shifted states (grey boxes) do not participate in the excitation dynamics and are discarded (see text for further details). The near-resonant laser coupling between relevant many-body states is indicated by the green arrows. Due to the strong geometrical constraint imposed by the interaction blockade combined with the finite system size, many-body states containing more than $N_e = 3$ Rydberg excitations do not need to be considered.

Appendix E.

Supplementary material for Chapter 7

The following supplementary material is reproduced from [294].

E.1. Numerical sweep optimization

Our theoretical calculations are based on a numerical solution of the Schrödinger equation for the Hamiltonian (7.2) in a truncated Hilbert space. To this end, we expand the wave function $|\psi\rangle$ of the N-atom system in terms of states with fixed Rydberg number $N_\uparrow$, which are eigenstates of the classical Hamiltonian (i.e. for $\Omega = 0$)

$$|\psi\rangle = c^{(0)}\,|0\rangle + \sum_{\boldsymbol{i}_1} c^{(1)}_{\boldsymbol{i}_1}\,|\boldsymbol{i}_1\rangle + \sum_{\boldsymbol{i}_1,\boldsymbol{i}_2} c^{(2)}_{\boldsymbol{i}_1,\boldsymbol{i}_2}\,|\boldsymbol{i}_1,\boldsymbol{i}_2\rangle + \ldots + \sum_{\boldsymbol{i}_1,\ldots,\boldsymbol{i}_N} c^{(N)}_{\boldsymbol{i}_1,\ldots,\boldsymbol{i}_{N_{\mathrm{at}}}}\,|\boldsymbol{i}_1,\ldots,\boldsymbol{i}_N\rangle\ , \tag{E.1}$$

where $\left|\boldsymbol{i}_1,\ldots,\boldsymbol{i}_{N_\uparrow}\right\rangle$ corresponds to a state with $N_\uparrow$ Rydberg atoms located at lattice sites $\boldsymbol{i}_1$ to $\boldsymbol{i}_{N_\uparrow}$, and $c^{(N_\uparrow)}_{\boldsymbol{i}_1,\ldots,\boldsymbol{i}_{N_\uparrow}}$ denotes the corresponding time-dependent amplitude. In order to truncate the otherwise exponentially large Hilbert space we only include Rydberg numbers of $N_\uparrow \leq N_{\uparrow c}$ and introduce a cut-off distance R_c, discarding all states that contain Rydberg atoms closer than R_c [291]. The presented results were obtained for $N_{\uparrow c} = 5$ and we verified directly that the inclusion of states with $N_\uparrow = 6{,}7$ did not contribute to the many-body dynamics. In addition R_c was reduced progressively until convergence of the simulated dynamics was achieved [291].

In order to optimize the coupling laser sweep we monitor the fidelity

$$\mathcal{F}(|\psi(t)\rangle\,, |\psi_{\mathrm{GS}}(t)\rangle) = |\langle\psi_{\mathrm{GS}}(t)|\psi(t)\rangle|^2\ , \tag{E.2}$$

i.e., the overlap between the time-evolving wavefunction $|\psi(t)\rangle$ and the many-body ground state $|\psi_{\mathrm{GS}}(t)\rangle$ at time t determined by the actual set of laser parameters $\Omega(t)$ and $\Delta(t)$. First we choose a given trajectory $(\Omega(t), \Delta(t))$ that connects the initial ground state containing no Rydberg atom with the targeted crystalline ground state. The actual path chosen for our experiments is shown in Fig. 7.10a. Next we discretize the path into a large number of sampling points, forming equal linear segments, along which we propagate the Schrödinger equation as described above. A suitable sweep for high-fidelity generation of states with fixed Rydberg number was then obtained by optimizing the local ramp speed for each segment with respect to the decrease of $\mathcal{F}(t)$ between successive sampling points, with the constraint $T = 4\,\mu\mathrm{s}$ for the total sweep duration, T. As described in Chapter 7, non-adiabatic transitions between closely lying states with equal $N_\uparrow$ but finite dislocations are unavoidable in the final stage of the sweep. Hence, for the chosen path, we stop the optimization and fixed the ramp speed once the Rabi frequency drops below 60 kHz. Since the experimentally prepared atomic lattice has a finite filling fraction of ≈ 0.8, this procedure is repeated for several random configurations producing slightly different optimal sweeps. The sweep shown in Figure 7.6a was constructed as a simple and simultaneously good compromise between those numerically obtained sweeps for $\ell = 23$. As demonstrated in Fig. 7.8, this sweep indeed yields a high total fidelity of 0.99, 0.97 and 0.91 for the preparation of many-body states with fixed Rydberg number of $N_\uparrow = 1$, $N_\uparrow = 2$ and $N_\uparrow = 3$, respectively. In our experiments, this sweep was used to obtain the Rydberg blockade staircase shown in Fig. 7.7.

E.2. Estimating the compressibility

In the dilute limit, $N_\uparrow \ll \ell$, the Hamiltonian Eq. (7.2) for a 1D chain can be reformulated in a continuous form. To this end, we scale lengths and energies by $L = \ell a_{\mathrm{lat}}$ and C_6/L^6, and introduce dimensionless operators

$$\hat{\psi}(x_i) = \sqrt{\frac{L}{a_{\mathrm{lat}}}} \left|g^{(i)}\right\rangle \left\langle e^{(i)}\right| = \sqrt{\ell} \left|g^{(i)}\right\rangle \left\langle e^{(i)}\right| \,, \quad \hat{\psi}^\dagger(x_i) = \sqrt{\ell} \left|e^{(i)}\right\rangle \left\langle g^{(i)}\right| \,, \tag{E.3}$$

where $x_i = i a_{\mathrm{lat}}/L$. Taking the continuum limit, this permits to write the lattice Hamiltonian as

$$\hat{H} = B_\perp \int_0^1 (\hat{\psi}^\dagger(x) + \hat{\psi}(x))\,\mathrm{d}x + B_\parallel \int_0^1 \hat{\psi}^\dagger(x)\hat{\psi}(x)\,\mathrm{d}x + \frac{1}{2} \int_0^1\!\!\int_0^1 \frac{\hat{\psi}^\dagger(x)\hat{\psi}^\dagger(x')\hat{\psi}(x')\hat{\psi}(x)}{|x - x'|^6}\,\mathrm{d}x\,\mathrm{d}x' \tag{E.4}$$

with the dimensionless, effective magnetic fields $B_\perp = \sqrt{\ell}\frac{\hbar\Omega}{2}\frac{L^6}{C_6}$ and $B_\parallel = -\hbar\Delta\frac{L^6}{C_6}$. The quantum fields $\hat{\psi}^\dagger$ and $\hat{\psi}$ describe the creation and annihilation of hard-core bosons, where the hard-core constraint is naturally ensured by the Rydberg-Rydberg atom interaction. The Rydberg number, and, hence, the density increases linearly with L, such that $L \to \infty$ defines the thermodynamic limit.

Consequently the Rydberg atom number $N_\uparrow = N_\uparrow(B_\parallel, B_\perp)$ depends on only two parameters and we can re-express the susceptibility $\chi \equiv \frac{\partial N_\uparrow}{\partial \Delta}$ in terms of the derivative of $N_\uparrow$ with respect to ℓ. Neglecting the weak dependence on $B_\perp$, thus, yields

$$\chi = \frac{\ell}{6\Delta}\frac{\partial N_\uparrow}{\partial \ell} \,, \tag{E.5}$$

which we used to calculate the susceptibility χ from the measured dipole-blockade staircase shown in Fig. 7.7. The required ℓ-derivative was obtained from the experimental data, $N_\uparrow^{(i)}$ and $\ell^{(i)}$, by using a second-order symmetric formula [386]: $\left.\frac{\partial N_\uparrow}{\partial \ell}\right|_{\ell = \bar{\ell}^{(i)}} \approx \frac{N_\uparrow^{(i+1)} - N_\uparrow^{(i-1)}}{\ell^{(i+1)} - \ell^{(i-1)}}$ with $\bar{\ell}^{(i)} = \frac{1}{2}(\ell^{(i+1)} + \ell^{(i-1)})$.

In order to verify the quality of the employed approximations, we also determined χ numerically directly from its definition. To this end, we recorded the staircase in the Rydberg atom number using the sweep $(\mathit{\Omega}(t), \mathit{\Delta}(t))$ shown in the Figure 7.6a and for a reference sweep with a small global frequency shift δ, i.e. for $(\mathit{\Omega}(t), \mathit{\Delta}(t) + \delta)$. Within the studied range $|\delta/(2\pi)| < 10\,\mathrm{kHz}$ the number of Rydberg atoms $N_\uparrow$ was found to vary linearly with δ such that the susceptibility can be evaluated directly via $\chi = (N_\uparrow(\delta) - N_\uparrow(\delta = 0))/\delta$. This susceptibility χ is shown in Fig. 7.7b and agrees well with the experimental results obtained from equation (E.5).

Appendix F.

Coherent pushing

One of the limitations in the Rydberg detection technique used is the minimum time required to remove all ground state atoms from the lattice (Sec. 5.4). The limitation is due to the scattering rate on the D_2 line of rubidium, the maximum scattering rate achievable is $R_{sc} = \frac{\Gamma}{2} = \pi \cdot 6.0666(18)\,\mathrm{MHz} = 19.06(1) \cdot 10^6\,\mathrm{s}^{-1}$. As the D_2 line is the strongest line in rubidium it is also not possible to improve by choosing another transition to scatter photons. The maximum force that than be reached by this incoherent scattering is $F_{\mathrm{max,incoh.}} = \hbar k \Gamma / 2$.

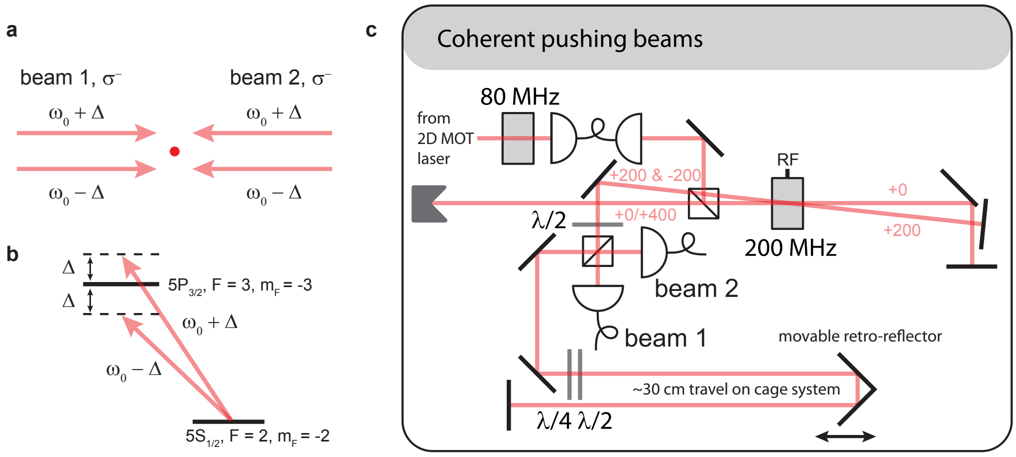

Figure F.1.: Coherent pushing schematic. a, Properties of the two beams with two frequencies each sent counter-propagating onto the atoms. **b**, The two frequency components in the beams shown in a simplified level scheme. Due to the symmetry most of the light shifts on the transition are compensated. **c**, Laser setup for the preparation of the two bichromatic beams. The 80 MHz AOM is required to improve the switching, as the suppression is not good enough with only one AOM. The 200 MHz AOM is operated at a RF power to reach a 50:50 splitting of the light in 0st and 1st order, which also leads to a 50:50 power ratio of the ±200 MHz frequency components in the used output port. Half of the total power is lost in the beam dump at the other output port. The delay of one of the output beams is adjustable by a movable retro-reflector (Thorlabs PS971M-B) on a cage system. The retro-reflector distorts the polarization, but this can be compensated by a $\lambda/2$,$\lambda/4$ wave plate combination. For the setup the same symbols are used as in Fig. 5.4.

There are other techniques that can break the limit of incoherent scattering with the help of coherent two-photon transitions [387–396] or dispersive forces [397, 398]. A realistic technique for our setup is the so-called stimulated bichromatic force (BCF), which uses two bichromatic counter-propagating beams, each with the two frequency components $\omega_0 \pm \varDelta$ where ω_0 is the transition frequency of the atomic line (Fig. F.1a). $\varDelta$ can be chosen in the experiment, but it needs to be in a certain relation to the Rabi frequency $\varOmega$ of all the monochromatic frequency components, which all need to have the same intensity. The force is maximized for $\varOmega = \frac{\pi}{4}\varDelta$, which leads to a theoretical maximum of the stimulated force of $F_{\mathrm{max,bcf}} = \hbar k \varDelta / \pi$ [390]. In practice the range of $\varDelta$ is limited, one the one hand by the achievable Rabi frequency, on the other hand by other levels nearby, as the calculation assumes a clean two-level system.

We tried a configuration with $\varDelta = 200\,\mathrm{MHz}$ on the $|F = 2, m_F = -2\rangle \leftrightarrow |3, -3\rangle$ transition of the rubidium-87 D_2 line in our setup (Fig. F.1b). The frequency shift is still easily implemented with an acousto-optic modulator. The required Rabi frequency is then 157 MHz, which corresponds to 60 µW at a waist of 40 µm. We branched off some light of the 2D MOT laser using a flip mount to have enough power without the requirement for an additional laser. The centre frequency of the laser is already close to the target frequency and we could tune the offset lock to the desired frequency. The two frequency components are then produced by a tricky double pass through a 200 MHz AOM [391]. The next problem is how to send the light to the atoms. For one of the beams we used the same path as for the red Rydberg beam, for the other the one of the z-molasses beam [22]. Both beams have few 10 µm waist. The polarization of the red Rydberg beam was already adjusted to σ^-. The other beam was adjusted the same way as described in Sec. 5.5.1. The Rabi frequency can be measured indirectly via the light shift, which can be determined quite precisely using microwave spectroscopy (Sec. 5.7.2). The light shift in combination with the adjusted detuning yields the Rabi frequency. The last free parameter is the relative phase of the two beat notes in the two counter-propagating beams. Luckily the beat note wavelength is large $\lambda_{\mathrm{beat}} = \frac{c}{2\varDelta} = 0.749\,\mathrm{m}$. We use a double-pass through a retro-reflector delay line which allows to reduce the required mechanical travel to 18.7 cm and at the same time make the setup insensitive to tilts of the retro-reflector. The setup allows to change the phase over the full range with a change in fibre coupling efficiency without readjustment of less than 30 % (Fig. F.1c). In theory this setup should be able to create a force on the atoms which is $\frac{4\varDelta}{\pi\varGamma} = 42$ times larger than the maximum incoherent force. But in practice it did not work as expected. It was only possible to push parts of the atoms within few microseconds, but only with very bad fidelity of $< 90\,\%$. Typical other experiments on stimulated light forces focus on the accelerated atoms and do not investigate the remaining atoms, which are crucial in our case. We think that the main problem is the pumping effect of the coherent pushing beam from the ground state $|F = 2, m_F = -2\rangle$ to $|F = 1\rangle$. As the experiment is performed in an magnetic offset field, the $|F = 1\rangle$ levels are strongly split and not all easily repumped. In the end we were probably limited by the incoherent scattering on other hyperfine levels in the $5P_{3/2}$ manifold which are one the one hand compromising the coherence and on the other hand lead to a loss out of the cycling transition, which we could not compensate by the available repump power.

Appendix G.

Lattice calculation

This chapter summarizes some calculations of cubic lattice parameters required to check the applicability of lattice modulation techniques to coherently transfer atoms to excited bands in the optical lattice in our setup [399, 400]. Especially the combination of these ideas with Bose-Hubbard physics are interesting for our experiment, as they allow for algorithmic cooling and the preparation of larger regions with constant atom number per lattice site [43]. We set up a calculation and checked the parameters in our setup with some calibration measurement described in the following section. We focus mainly on photon-assisted tunnelling in tilted lattices [401–403], as this could allow for spin-dependent transfer of atoms into neighbouring lattice sites.

G.1. Amplitude modulation in a tilted optical lattice

The typical optical lattice configuration in our setup is a 3D configuration with lattice depths of $10 - 80\,E_\mathrm{r}$ for all of the three lattice axes. In most of the experiments we work in a vertical gradient field with an offset of 28.6 G and a gradient corresponding to a shift of $\sim 4/3\,\mathrm{kHz}$ of the $|F = 1, m_F = -1\rangle$ state per site. This typically used gradient is about a factor of 2 smaller than the gradient used for slicing, which corresponds to a shift of 4.0(2) kHz on the transition $|1, -1\rangle \to |2, -2\rangle$ per slice. The half gradient exerts a force on the atoms in our standard starting state $|1, -1\rangle$ which is weaker than gravity and points in the same direction. Gravity causes an energy offset between neighbouring sites in the z-lattice of $mga_\mathrm{lat}/h = 1.13\,\mathrm{kHz}$. We measure these shifts by lattice amplitude modulation in the z-lattice at $20\,E_\mathrm{r}$ without xy-lattices with a modulation time of $50 - 150\,\mathrm{ms}$ and an amplitude $\sim 0.5\,\%$. We expect three resonances, one going to the second band on-site, one to the second band in the upper site and one to the second band in the lower site. Transitions to the first band are not coupled due to the symmetric amplitude modulation. Without gradient we measure resonances at 25.5(1) kHz, 26.6(1) kHz and 27.75(3) , confirming the expected splitting between neighbouring resonances due to gravity of 1.1(1) kHz. For the half gradient we expect an additional shift of $4/3\,\mathrm{kHz} \cdot 4.1/9.7 = 0.56\,\mathrm{kHz}$ per site. This is confirmed with resonances at 25.2(1) kHz, 26.6(1) kHz and 28.25(10) kHz and obtain a splitting of 1.5(1) kHz. The same measurement with the full gradient leads to an even larger splitting of 2.6 kHz (resonances 23.95(10) kHz, 26.6(1) kHz and 29.15(10) kHz). Higher modulation frequencies than $\sim 30\,\mathrm{kHz}$ are problematic via our intensity stabilization. For frequencies of 50 kHz and higher we can use a mixer to add the amplitude modulation and we checked that the stabilization is not considerably disturbed by the modulation as the servo bandwidth is $\lesssim 30\,\mathrm{kHz}$. To see coherence in this kind of lattice modulation, a coupling to a band with negligible tunnelling is required to avoid loss in the upper band. In a $20\,E_\mathrm{r}$ lattice the second band is tunnelling strongly. We went to a $80/80/70\,E_\mathrm{r}$ lattice to check that and observe Rabi oscillation for a modulation frequency of $57\,\mathrm{kHz}$ and amplitude modulation of $\pm 5\,\%$. We observe Rabi oscillations to the second band with a T_1-time of $\sim 9\,\mathrm{ms}$ and a Rabi frequency of $2\pi \cdot 564\,\mathrm{Hz}$, which matches very well the theoretical expectation of $2\pi \cdot 566.85\,\mathrm{Hz}$.

G.2. Spin-dependent photon-assisted tunnelling by modulation of a tilted lattice

One idea to apply these lattice modulation techniques is to implement a spin-dependent transfer of atoms from one lattice site to a neighbouring one. The two resonances can be split in frequency by a magnetic gradient, and also the direction of movement of the atoms can be selected. The main question is the transition matrix element with respect to the driving for the required coupling to neighbouring lattice sites.

To model the system theoretically one first needs to calculate the Wannier functions as quasi-stationary local wavefunctions of the atoms (Appendix G.4). The Rabi frequencies due to lattice amplitude modulation can then be calculated by overlap matrix elements of Wannier functions via

$$\varOmega = \varDelta V \left\langle w_1 \,\middle|\, \cos(kx)^2 \,\middle|\, w_2 \right\rangle / \hbar \,. \tag{G.1}$$

Where $\varDelta V$ is the amplitude of the time-dependent lattice potential $V_A(x,t) = (V_0 + \varDelta V \sin(\omega t)) \cos(kx)^2$.

Similarly the coupling for phase modulation can be calculated [400]

$$\varOmega = 2k\varDelta x V_0 \left\langle w_1 \,|\, \cos(kx)\sin(kx) \,|\, w_2 \right\rangle / \hbar = k\varDelta x V_0 \left\langle w_1 \,|\, \sin(2kx) \,|\, w_2 \right\rangle / \hbar \,, \tag{G.2}$$

where the phase modulated lattice potential is defined by $V_\phi(x,t) = V_0 \cos(k(x + \varDelta x \sin(\omega t)))^2$.

It turns out that neither amplitude nor phase modulation couples atoms in the lowest band to the neighbouring site in the lowest band. So one has to consider the higher tunnelling rates in the target band. We choose the Rabi frequency reachable on such a transition relative to the tunnelling rate in the upper band as a figure of merit. Fig. G.1 shows these fractions as a function of lattice depth for an amplitude modulation of $\varDelta V/V = 0.2$ and a phase modulation of $\varDelta x/a_\mathrm{lat} = 0.2$. The situation looks challenging for the amplitude modulation, as a reasonable coherence time is only possible for very strong driving and only at quite low lattice depth. An intrinsic problem of the amplitude modulation is that the modulation is limited by lattice depth. For phase modulation the situation looks much better. But it is important to note that the phase modulation couples very strongly to the first excited band on-site, such that the resonances are only resolved for quite a strong tilt of the lattice. In contrast to that the phase modulation does not couple to the second band on-site and one could use the transition to the second band on the neighbouring site. At our experiment amplitude

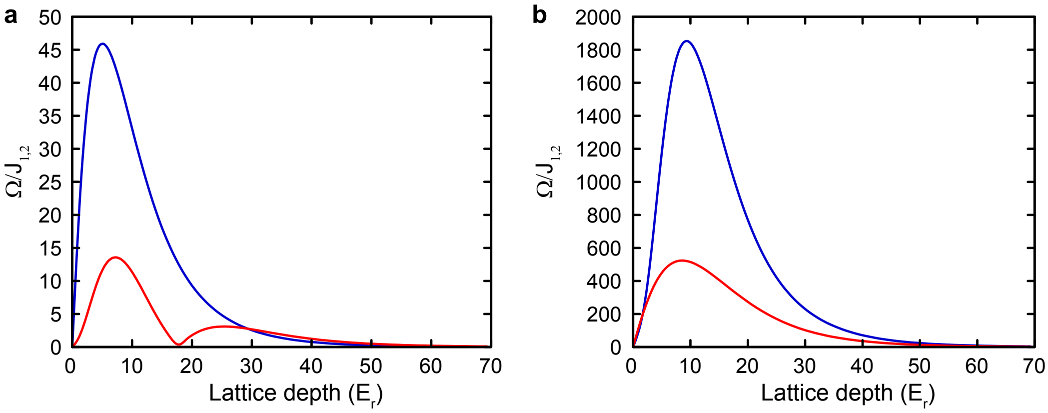

Figure G.1.: Lattice modulation coupling strength to neighbouring sites. Shown is the coupling Rabi frequency from the ground state to a neighbouring site relative to the tunnelling in the target band for the first (blue) and second (red) band for various lattice depths. **a**, for amplitude modulation of the lattice with $\Delta V/V = 0.2$ and **b** phase modulation with $\Delta x/a_{\mathrm{lat}} = 0.2$.

modulation is directly possible via the intensity stabilization of the lattices. Phase modulation is more involved, especially for the vertical lattice, which is retro-reflected in vacuum and the distance from the atoms to the retro-mirror is only $\sim 5\,\mathrm{mm}$. A reasonable phase modulation would require a frequency modulation of the lattice laser of tens of GHz with several ten Kilohertz, which is practically challenging.

G.3. Proposal for detection of spin-spin correlations

If the lattice modulation ideas discussed in the last section would work, then one could use this technique to implement the splitting of two spin components in one slice into two slices with in principle arbitrary distance. A possible protocol is described in the following. Starting with a spin mixture of two spin states $\uparrow$, $\downarrow$ with different magnetic moment, one can freeze the distribution and apply a magnetic gradient along the z-axis. Then it should be possible to selectively drive the transition of the e.g. $\uparrow$-spin component to next slice in z-direction by applying a lattice modulation corresponding to a π-pulse. The $\uparrow$ atoms are then in the second band of the next slice. To iterate the sequence a π-pulse on the 0th $\leftrightarrow$ 1st band on-site transition is required. As this will be possibly not spin-selective, the $\downarrow$ atoms will be afterwards in the second band and the $\uparrow$-atoms in the lowest band again. In principle this could be repeated a few times until a separation is reached, which is optically resolved. The imaging can be then performed by just freezing the atoms and imaging half of the time focussed on the one slice and the other half on the other slice. The would then allow to obtain a single-shot distribution of both spin-components and full access to spin-spin-correlations.

In practice this will be quite hard due to the weak coupling of the lattice modulation off-site compared to the timescales of on-site excitations and intra-band tunnelling. Already a few tunnelling events would compromise the detection efficiency strongly and it might be easier to reach higher detection efficiencies by doing spin physics in unity-filling Mott insulators and just image one spin-component and extract the other one from the slightly imperfect unity-filling restriction. For 1D systems these rather complicated schemes are not required, as on can let the atoms expand in the second dimension in presence of a gradient, leading to a clear splitting of both spin components, which can then be easily distinguished in a single image.

G.4. Calculation of Wannier functions

While the calculation of Wannier function is in general not an easy problem [404], it is straightforward for the separable cubic 3D lattice, where the calculation simplifies to a 1D calculation. Calculations and formulas for parameters J and U of the Bose-Hubbard model can be found for example in [13, 19, 293, 405, 406]. It is important to note that many calculations focus on the lowest band and for higher bands it becomes important to have the correct sign convention for the Bloch functions to apply the standard formula Eq. G.3 [293].

The Wannier function at position R_i in band n is given by:

$$w_n(r - R_i) = \frac{1}{\sqrt{N}} \sum_q e^{-iqR_i} \psi_{nq}(r) \tag{G.3}$$

With the Bloch functions $\psi_{nq}(r) = u_{nq}(r)e^{iqr}$, which are the eigen functions of the lattice Hamiltonian in k-space.

$$\hat{H}_0 \psi_{nq}(r) = \hbar\omega_{nq}\psi_{nq}(r) \tag{G.4}$$

G.5. Tunnelling from Wannier functions

Starting from the definition of the tunnelling matrix element, we show that the tunnelling matrix element is the Fourier transform of the spectrum.

$$\begin{aligned}
J_{R_i - R_j} &= \int dr w_n(r - R_i)\hat{H}_0 w_n(r - R_j) \\
&= \frac{1}{N} \int dr \sum_q \sum_{q'} e^{iqR_i} \psi^*_{nq}(r)\hat{H}_0 \psi_{nq'}(r) e^{-iq'R_j} \\
&= \frac{1}{N} \int dr \sum_q \sum_{q'} e^{i(qR_i - q'R_j)} \psi^*_{nq}(r)\hbar\omega_{nq'}\psi_{nq'}(r) \\
&= \frac{1}{N} \sum_q \sum_{q'} \hbar\omega_{nq'} e^{i(qR_i - q'R_j)} \int dr \psi^*_{nq}(r)\psi_{nq'}(r) \\
&= \frac{1}{N} \sum_q \sum_{q'} \hbar\omega_{nq'} e^{i(qR_i - q'R_j)} \delta_{q,q'} \\
&= \frac{1}{N} \sum_q e^{iq(R_i - R_j)} \hbar\omega_{nq}
\end{aligned} \tag{G.5}$$

G.6. Harmonic approximation for U

While it is possible to obtain the interaction energy U in the lattice from direct integration of Wannier function overlaps, the calculation based on a harmonic approximation is still reasonably precise and a good check for the numerics. The harmonic oscillator approximation for the interaction energy (e.g. [13, p.899], [293, (2.59)]) can be extended to the case where the atom is in different bands in every dimension. The harmonic approximation gives an upper bound on U, as the harmonic oscillator wavefunction is more localized than the Wannier state.

The harmonic oscillator frequency of a lattice site is given by $\omega = \sqrt{\frac{2(VE_r)k^2}{m}}$ with V the lattice depth in units of E_r, where $E_r = \frac{\hbar^2 k^2}{2m}$. We call the 3D harmonic oscillator wavefunction approximating the Wannier function of a lattice site $\psi_{ho,\boldsymbol{n}}(\boldsymbol{x}) = \prod_{i=1}^{3} \psi_{ho,n_i}(x_i)$. Here n_i is the band-index of the wavefunction in dimension i. To evaluate the interaction energy U, approximated by the integral $U_{ho} = g \int d^3x \, |\psi_{ho,\boldsymbol{n}}|^4$ with $g = \frac{4\pi\hbar^2 a_s}{m}$, it is reasonable to first integrate the 1D harmonic oscillator functions.

$$\int d^3x \, |\psi_{ho,n_i}|^4 = \sqrt{\frac{m\omega_i}{2\pi\hbar}} C_{n_i} \tag{G.6}$$

The band-index dependent constants C_n can be calculated exactly using e.g. Mathematica and are shown in the Table below for $n = 0 \dots 4$.

n	C_n
0	1
1	3/4
2	41/64
3	147/256
4	8649/16384

With these preparations the calculation of the generalized harmonic approximation for U is straightforward.

$$\begin{aligned}
U_{ho} &= g \int d^3x \, |\psi_{ho,\boldsymbol{n}}|^4 \\
&= g \prod_i^3 \sqrt{\frac{m\omega_i}{2\pi\hbar}} C_{n_i} \\
&= g \left(\frac{m}{2\pi\hbar}\right)^{3/2} \left(\frac{2}{m}\right)^{3/4} \prod_i^3 \left(V_i E_r^i k_i^2\right)^{1/4} C_{n_i} \\
&= g \left(\frac{m}{2\pi^2\hbar^2}\right)^{3/4} \prod_i^3 \left(V_i E_r^i k_i^2\right)^{1/4} C_{n_i} \\
&= g \left(\frac{m}{2\pi^2\hbar^2}\frac{\hbar^2}{2m}\right)^{3/4} \prod_i^3 V_i^{1/4} k_i C_{n_i} \qquad \text{(G.7)} \\
&= g (2\pi)^{-3/2} (2\pi)^3 \prod_i^3 \frac{V_i^{1/4}}{\lambda_i} C_{n_i} \\
&= g (2\pi)^{3/2} \prod_i \frac{V_i^{1/4}}{\lambda_i} C_{n_i} \\
&= \frac{4\pi\hbar^2 a_s}{m} (2\pi)^{3/2} \prod_i^3 \frac{V_i^{1/4}}{\lambda_i} C_{n_i} \\
&= \frac{2\hbar^2 (2\pi)^{5/2} a_s}{m} \prod_i^3 \frac{V_i^{1/4}}{\lambda_i} C_{n_i}
\end{aligned}$$

This result can be further simplified for the symmetric ground state case $C_{n_i} = 1$ and $V_i = V$ and $\lambda_i = \lambda$:

$$\begin{aligned}
&= \frac{2\hbar^2 (2\pi)^{5/2} a_s}{m} \frac{2m}{\hbar^2 k^2} \frac{V^{3/4}}{\lambda^3} E_r \\
&= 4 (2\pi)^{1/2} a_s \frac{V^{3/4}}{\lambda} E_r \qquad \text{(G.8)} \\
&= \sqrt{\frac{8}{\pi}} 2\pi a_s \frac{V^{3/4}}{\lambda} E_r
\end{aligned}$$

G.7. Analytic formula for expansion of a Gaussian wave packet

For the calculation of the detection efficiency in Sec. 5.6.5 the free expansion of a Wannier function has to be calculated. In many cases it is accurate enough to use the expansion dynamics of a Gaussian wave packet as approximation.

The release and recapture of a single atom in an optical lattice can be modelled using a harmonic oscillator approximation for the Wannier function of the ground state, which is then time-evolved analytically and then projected back to a basis of lattice states. The trap frequency of a lattice site in a standard retro-reflected lattice

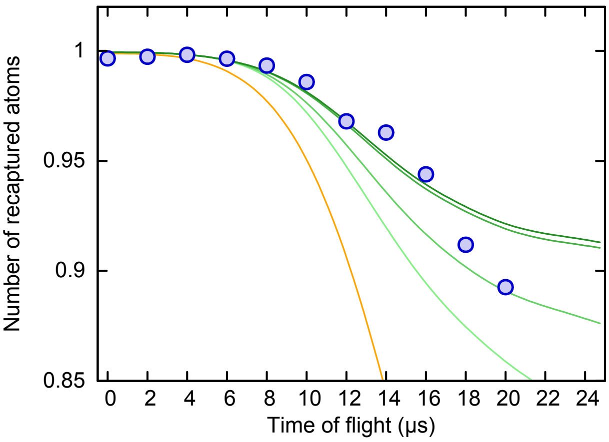

Figure G.2: Mott insulator recapture. Shown is the recaptured fraction of atoms over the time of flight (for details see text). Blue points, experimental data in a Mott insulator. Green and orange curves are theory calculations. The green curves form dark to light assume that atoms in the lowest 32,31,30,29 bands of the lattice are imaged, including atoms that are recaptured in neighbouring sites. The orange curve assumes 32 bands and neglects the probability to recapture atoms in neighbouring sites.

is given by $\omega = \sqrt{\frac{2VE_\mathrm{r}k^2}{m}}$ with the recoil $E_\mathrm{r} = \frac{\hbar^2 k^2}{2m}$ and $k = \frac{2\pi}{\lambda}$ with λ the wavelength of the lattice laser.

With this trapping frequency the expansion dynamics of the local harmonic oscillator ground state after lattice switch off is given by: $\Psi_\mathrm{HO}(t) = \left(\frac{\alpha(t)^2}{\pi}\right)^{1/4} \exp^{-\frac{1}{2}\alpha(t)^2 x^2}$ with the definitions $\alpha(t) = \left(\frac{1}{\alpha_0^2} + \alpha_0^2 \hbar^2 t^2 / m^2\right)^{-1/2}$ and $\alpha_0 = \sqrt{\frac{m\omega}{\hbar}}$.

G.8. Check of the recapture calculation with ground state atoms

To check the calculation of the recapture calculation used for the detection efficiency estimation (Sec. 5.6.5), we took a test data set with a Mott insulator where we switched off the lattice at $40/40/80\,E_\mathrm{r}$ and recaptured the atoms in a 3D lattice of $\sim 3000\,E_\mathrm{r}$ in all directions. The switch-off was performed by fast RF switches for the AOMs of all three lattice axes to avoid limitations by the lattice stabilization. We measured the number of atoms that stayed in a radius of 1.3 times the Mott insulator radius (defined as the radius where the centre density dropped to 0.5) after the free time of flight. The atoms had $\sim 50\,\mathrm{ms}$ to tunnel away between recapture and imaging, which is approximately the time we need to ramp the field for the fluorescence imaging. Fig. G.2 shows a comparison of the experimental data with various theory calculations. The orange theory curves shows that after 10 µs the probability to recapture atoms in the initial site drops significantly. The experimental data is consistent with the green theory calculations that assume that all atoms in the lowest 30-32 bands are detected. All of the lowest 32 bands have a tunnelling rate of $< 10\,\mathrm{Hz}$ and are expected not to tunnel within the time before imaging. Because the orange curve, that neglects recapture in neighbouring sites, is strictly below the data, the deviation of the data from the green curve for 32 sites can be explained by effects due to nearest neighbour recapture. Maybe some of the atoms recaptured on neighbouring sites are not detected as they lead to doubly occupied sites in the Mott insulator, which are imaged as empty sites after parity projection. But they could also tunnel and then are detected on different sites. In summary the recapture data can be quite well explained by the theory calculations.

Appendix H.

Spatial correlation functions

This chapter will look at some correlation functions, their properties, and some examples, to illustrate what is measured by certain spatial correlation functions.

H.1. Pair correlation in 1D

Here we look at some basic properties of a pair correlation function. We use a simple system as an example here: A 1D lattice of length ℓ with constant atomic density. A correlation is introduced by emptying two sites at a distance d and repeating this N times (it does not matter if the sites were empty before or not). To calculate correlation functions we then look at an ensemble of these 1D systems. The question to answer using the correlation function is: How many pairs are hidden in the data?

The model discussed above is implemented by the following ensemble of densities, where we use the definitions listed in Table H.1.

$$n(x) = (\mathrm{rand}() < n_0) \prod_{i=1}^{N} (1 - \delta(x - x_i))(1 - \delta(x - x_i + \mathrm{randdir}())) \tag{H.1}$$

For a low density of pairs the mean resulting density can be calculated by assuming non-overlapping pairs, if the background density is known (each emptied position removes n_0/ℓ from the density): $\langle n \rangle = n_0 - 2Nn_0/\ell$

If the background density is unknown the number of pairs can still be extracted in this system via the normalized pair correlation function $C = \frac{\langle n(x)n(x+1)\rangle}{\langle n(x)\rangle\langle n(x+1)\rangle}$. It measures essentially the number of pairs in the system, which we will show in the

d	distance of pair (1 for neighbouring atoms)
$\mathrm{randdir}() \in \{-d,d\}$	random number $d \cdot (2 \cdot (\mathrm{rand}() > 0.5) - 1)$
$\mathrm{rand}() \in [0,1[$	random number
n_0	background density
N	number of pairs
ℓ	length of the system
x_i	random position of a pair $[-d+1,\ell+d]$

Table H.1.: Definitions for correlation example. The random position of the pairs is chosen to give a flat density distribution in the range $[1..\ell]$.

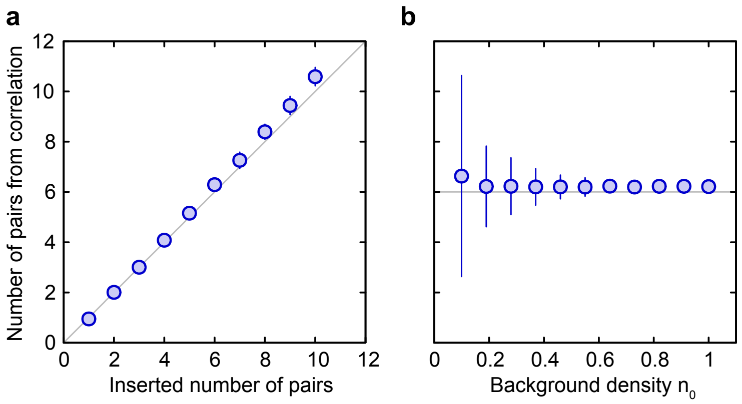

Figure H.1.: Reconstructing the number of pairs from pair correlations. **a**, Pair number determined from correlation versus inserted pair count. For pair densities $> 10\,\%$ we see a systematic error due to overlapping pairs. **b**, Extracted pair count versus background density at a fixed number of inserted pairs of 6. At lower density the statistics gets worse, but there is no systematic shift. This shows that an extraction of the number of pairs is in principle also possible for densities below 1, where the pairs cannot be identified by eye. For all calculations a 1D chain of length 100 was used and 50000 random samples. These configurations were grouped in 50 sub-samples of 1000 samples each to calculate error bars.

following. A simple consideration ignoring edge effects and overlapping pairs leads to $C = \frac{\frac{(\ell-3N)\cdot n_0^2}{\ell}}{\left(\frac{(\ell-2N)\cdot n_0}{\ell}\right)^2} = \frac{(\ell-3N)\ell}{(\ell-2N)^2}$ (only valid in the limit of low density of pairs). Solving this for the number of pairs N yields $N = \frac{\ell(4C(\ell-1)-3\ell-\sqrt{9\ell^2-8C(\ell^2+\ell-2)})}{8C(\ell-1)} \approx (C-1)(\ell+3)$, where the assumptions for the approximation are $\ell \gg 1$ and $C \approx 1$.

There is also the other definition of a pair correlation as $\langle n(x)n(x+1)\rangle - \langle n(x)\rangle \langle n(x+1)\rangle$ [14], which has the disadvantage that the resulting numbers still depend on the absolute density. But the big advantage of this correlation function are the almost constant error bars for varying density, as the division in the definition before leads to diverging error bars for low densities.

H.2. Spatial correlation at zero distance

The spatial on-site correlation is in principle an interesting observable. Here we show that the on-site correlation vanishes always in presence of parity projection. With the definitions

$$\begin{aligned} \hat{n}(x) &\equiv a^\dagger(x)a(x) \\ n(x) &\equiv \langle \hat{n}(x)\rangle \end{aligned} \tag{H.2}$$

the correlation can be directly calculated:

$$
\begin{aligned}
g^{(2)}(x) &= \frac{\left\langle a^\dagger(0)a^\dagger(x)a(x)a(0)\right\rangle}{\left\langle a^\dagger(x)a(x)\right\rangle \left\langle a^\dagger(0)a(0)\right\rangle} \\
&= \frac{\left\langle a^\dagger(0)a^\dagger(x)a(x)a(0)\right\rangle}{n(x)n(0)} \\
&= \frac{\left\langle a^\dagger(0)a(0)a^\dagger(x)a(x) - a^\dagger(0)\left[a(0),a^\dagger(x)\right]a(x)\right\rangle}{n(x)n(0)} \\
&= \frac{\left\langle \hat{n}(0)\hat{n}(x) - \hat{n}(0)\delta_{x,0}\right\rangle}{n(x)n(0)} \\
&= \frac{\left\langle \hat{n}(0)\hat{n}(x)\right\rangle - n(0)}{n(x)n(0)} \\
&= \begin{cases} \frac{\left\langle \hat{n}(0)\hat{n}(x)\right\rangle}{n(0)n(x)} & \text{if } x \neq 0 \\ \frac{\left\langle \hat{n}(0)^2\right\rangle - n(0)}{n(0)^2} & \text{if } x = 0 \end{cases}
\end{aligned} \tag{H.3}
$$

Here we used $\left[a(x),a^\dagger(y)\right] = \delta_{x,y}$. For a measurement of the density with parity projection the only possible results for the local density in a single shot are 0 and 1. This leads to the fact that $\left\langle \hat{n}(x)^2\right\rangle = \left\langle \hat{n}(x)\right\rangle$. We conclude that parity projection in a lattice boson system leads to $g^{(2)}(x=0) = 0$ without further assumptions.

H.3. Density-density correlation function definition and examples

The g_2 density-density correlation function is usually defined as

$$
g_2(\boldsymbol{x},\boldsymbol{y}) = \frac{\left\langle n(\boldsymbol{x})n(\boldsymbol{y})\right\rangle}{\left\langle n(\boldsymbol{x})\right\rangle \left\langle n(\boldsymbol{y})\right\rangle} \,. \tag{H.4}
$$

Where $\langle . \rangle$ is the ensemble average. In 2D this function has still 4 parameters, which makes it nearly impossible to reach suitable statistics. Especially at cold atom experiments the cycle time is not as fast to easily get several thousand images. As the system is typically symmetric in some of the parameters, it is possible to average without losing considerably in accuracy. In practice, typically a $g_2(\boldsymbol{r})$ function is used, which only depends on the difference vector $\boldsymbol{r} = \boldsymbol{x} - \boldsymbol{y}$. In many cases $g_2(\boldsymbol{r})$ only depends on the length of $\boldsymbol{r}$ and makes it possible to also perform an azimuthal average. This reduces the correlation function to $g_2(r)$ with a single parameter.

There are essentially two ways to perform the reduction to a radial g_2 function, either to divide first and then average spatially ($g_2^{(a)}$) or the other way around ($g_2^{(b)}$). The results are in general not the same as division and averaging do not commute.

$$
g_2^{(a)}(\boldsymbol{r}) = \int dx \frac{\left\langle n(\boldsymbol{x})n(\boldsymbol{x}+\boldsymbol{r})\right\rangle}{\left\langle n(\boldsymbol{x})\right\rangle \left\langle n(\boldsymbol{x}+\boldsymbol{r})\right\rangle} \Big/ \int dx \tag{H.5}
$$

$$
g_2^{(b)}(\boldsymbol{r}) = \frac{\int dx \left\langle n(\boldsymbol{x})n(\boldsymbol{x}+\boldsymbol{r})\right\rangle}{\int dx \left\langle n(\boldsymbol{x})\right\rangle \left\langle n(\boldsymbol{x}+\boldsymbol{r})\right\rangle} \tag{H.6}
$$

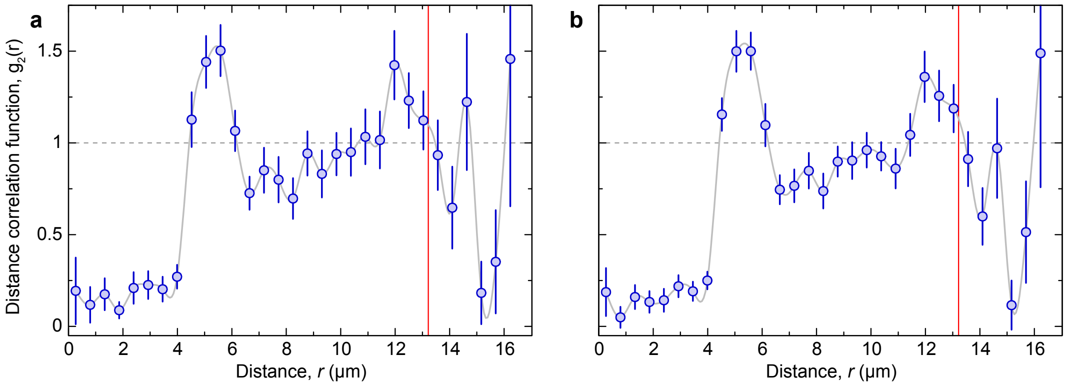

Figure H.2.: Radial correlation function for different averaging. Comparison of the radial correlation function for the two different averaging techniques $g_2^{(a)}$ (**a**) and $g_2^{(b)}$ (**b**) for the largest initial clouds investigated in Fig. 7.12. The differences are within error bars. For both curves there is a second maximum visible, corresponding to the position of the next-nearest neighbour in the crystal.

Here we implicitly include the average over the angular degree of freedom of the difference vector $\boldsymbol{r}$ in the spatial averaging, as it seems reasonable to perform all spatial averages in one step. It turns out that both definitions are present in publications. The type (a) averaging was for example used in [407], while other publications apply type (b) averaging, e.g. [269, 408]. The correlation function defined in [14] corresponds to $g_2^{(b)} - 1$. Although both definitions yield nearly the same results for most practical purposes, they are different and in certain cases one or the other can produce a larger correlation signal. Examples for these cases are presented in the next section. There is another definition in words by [28]: "The correlation function is defined to be the probability that two atoms separated by a distance R are both excited divided by the square of the probability an individual atom is excited." At this position we note that the probability to excite a Rydberg atom is about the same as the Rydberg density in our experiment, if we excite from a Mott insulator with unity filling. There might be still some correction due to some defects of the Mott insulator, but the correlation function is anyway insensitive to uncorrelated density offsets. Therefore $g_2^{(a)}$ and $g_2^{(b)}$ can also be calculated with $n(x)$ replaced by $p(x)$. Where $p(x)$ is the probability to excite an atom $p(x) = \frac{n_{\text{Rydberg}}(x)}{n_{\text{initial}}(x)}$.

Correlation examples 1D

To understand the properties of the correlation function defined in Eq. (H.5), the best is to look at some examples. For simplicity we choose a 1D system, as the main properties can be explained already in 1D. For the examples (Fig. H.3) we consider the following situation: We create 10000 samples of a 1D system of length $\ell = 100$ with 0 or 1 atom on each place. To generate correlations we use a probability function $P(\{\alpha_i\},\{\beta_j\},x)$ which depends on random variables α_i, fixed parameters β_j and the spatial position x. For every sample we get a different probability function from which we get the probability for each position x to place an atom.

For the discussions of the differences between the two correlation definitions (Eq. (H.5)), we consider the following examples.

$$P_1(\{\},\{\lambda\},x) = \sin\left(\frac{\pi}{\lambda}x\right)^2 \tag{H.7}$$

Constants: $\lambda = 40$

$$P_2(\{\phi\},\{\lambda\},x) = \sin\left(\frac{\pi}{\lambda}+\phi\right)^2 \ , \tag{H.8}$$

where ϕ is a uniformly distributed random variable in the range $[0; 2\pi]$.

Constants: $\lambda = 40$

$$P_3(\{x_0\},\{n_0,\sigma,d\},x) = \left(n_0 + \exp\left(-\frac{(x-x_0)^2}{2\sigma^2}\right) + \exp\left(-\frac{(x-x_0-d)^2}{2\sigma^2}\right)\right)/2 \ , \tag{H.9}$$

where x_0 is a uniformly distributed random variable in the range $[1; \ell]$.

Constants: $\sigma = 2, d = 50, n_0 = 0.1$

$$P_4(\{x_0\},\{n_0,\sigma,x_1,d\},x) = \left(n_0 + 4\exp\left(-\frac{(x-x_1)^2}{2\sigma^2}\right) + 4\exp\left(-\frac{(x-x_1-d)^2}{2\sigma^2}\right)\right. \tag{H.10}$$

$$\left. + \exp\left(-\frac{(x-x_0)^2}{2\sigma^2}\right) + \exp\left(-\frac{(x-x_0-d)^2}{2\sigma^2}\right)\right)/10 \ ,$$

where x_0 is a uniformly distributed random variable in the range $[1; \ell]$.

Constants: $n_0 = 0.1, \sigma = 2, d = 50, x_1 = 30$

$$P_5(\{X_0\},\{n_0\},x) = \left(n_0 + 2\exp\left(-\frac{(x-X_0)^2}{2\sigma^2}\right) + 2\exp\left(-\frac{(x-X_0-d)^2}{2\sigma^2}\right)\right)/(4+n_0) \ , \tag{H.11}$$

where X_0 is a Gaussian distributed random variable
with mean 20 and standard deviation 3.

Constants: $n_0 = 0.3, \sigma = 2, d = 50, x_1 = 30$

There first example Eq. (H.7) shows that a sample derived from a single probability distribution is not correlated, the correlation is 1, independent of the density. Here the first difference between $g_2^{(a)}$ and $g_2^{(b)}$ shows up. The function $g_2^{(a)}$ becomes unstable for low densities and is much more noisy in low density regions due to the low statistics in the denominator. The second example Eq. (H.8) shows the typical correlation by a sine-pattern with shot-to-shot phase fluctuation. This resembles directly the situation encountered for a spin spiral [409]. Here the mean density becomes flat and the correlation signal is strongly modulated with alternating correlation and anti-correlation. To show effects of localized functions, example three models two Gaussians, with fixed distance but random offset (Eq. (H.9)). The density is flat neglecting finite size effects. The correlation function shows a signal at zero distance, which is an autocorrelation of each of the Gaussians and at the distance of the two Gaussians the desired peak. As directly visible in the figure, the difference of the two variations of the correlation function is negligible for these two examples. To focus more on the differences we will now give one example where $g_2^{(a)}$ yields a stronger correlation signal (Eq. (H.10)) and another one where $g_2^{(b)}$ dominates (Eq. (H.11)). For the first one we look at two Gaussians as in Eq. (H.9), but here we consider two additional Gaussians, which are fixed in space but higher in probability and have accidentally the same distance as the first ones. In this case there should be intuitively a correlation, as adding uncorrelated atoms to a correlated system does not destroy the correlation. As visible in Fig. H.3, $g_2^{(a)}$ still finds a strong correlation at the expected distance, while $g_2^{(b)}$ is blinded by the density modulation and is totally flat within error bars. This example directly demonstrates the weakness introduced in $g_2^{(b)}$ by only using the globally averaged density in the calculation. To show that also $g_2^{(b)}$ can show stronger correlation signals, a bit more fine-tuned example is required. We use a similar configuration as in Eq. (H.9), but now the absolute position of the pairs of Gaussians is normally distributed. For this example also a constant background density with a certain value is necessary. In this situation $g_2^{(b)}$ can create an overshooting correlation signal, which exceeds the one seen by $g_2^{(a)}$.

In conclusion, the difference between these two correlation definitions (Eq. (H.5)) arises in special situations involving spatially inhomogeneous density. If the density is perfectly homogeneous, $\langle n(\boldsymbol{x})\rangle$ is constant in space and both definition are exactly the same. $g_2^{(a)}$ has the intrinsic problem that the denominator is quite noisy unless there is a lot of statistics for every point in space. In particular in low density regions the probability to find positions in space with zero average density is non-zero for a finite number of samples. This leads to a division by zero, which than can be handled in various ways, e.g. by ignoring these points in the calculation. The definition $g_2^{(b)}$ avoids these problems, but the result is not properly normalized, if correlation and density are spatially varying and correlated in a strange way. For all normal cases $g_2^{(b)}$ is totally fine and gives the same correlation function in the limit of large data sets.

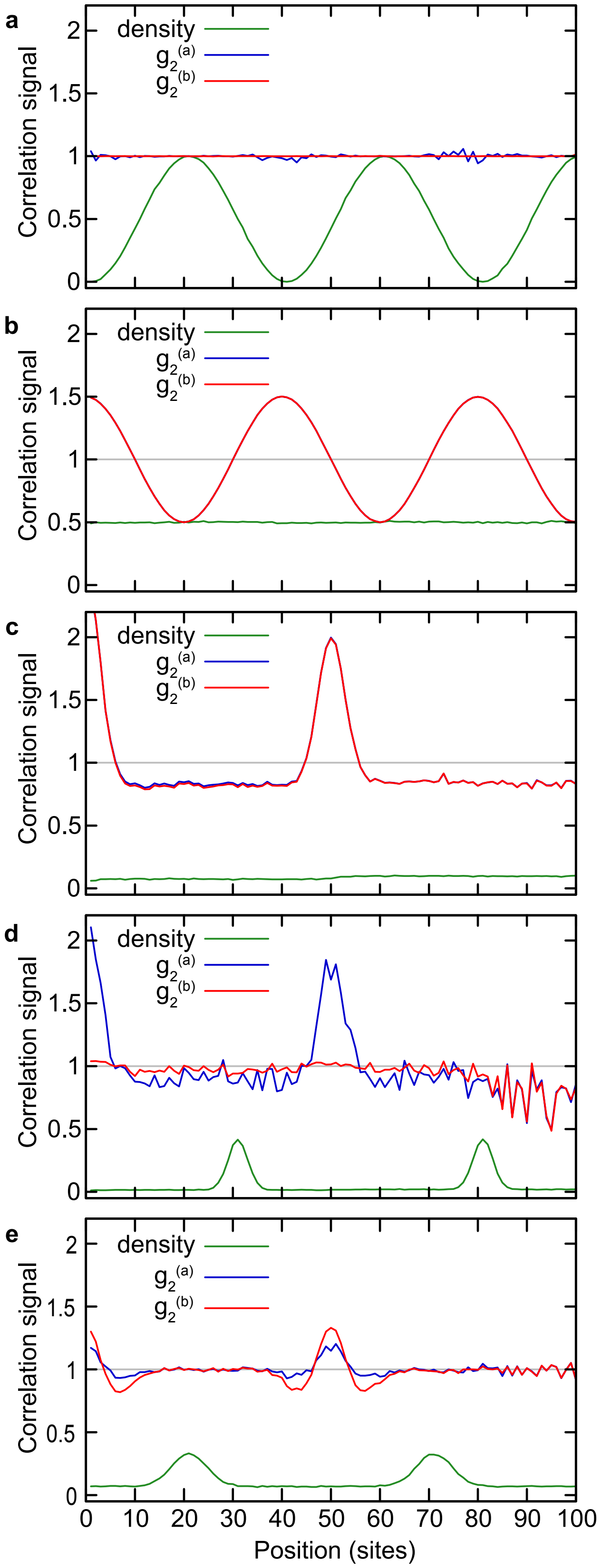

Figure H.3: Correlation function for sample configurations. For the density the x-axis shows the absolute position and the y-axis the density. For the correlation functions the x-axis shows the relative position adn the y-axis the correlation. In the following a short description of the test cases. For details see text. **a**, fixed sine pattern. **b**, random phase sine pattern. **c**, two Gaussians with correlated distance and uniformly distributed position, **d**, additionally to **c** two fixed Gaussians with the same distance. **e**, two Gaussians with correlated distance and Gaussian distributed position with offset density.

Appendix I.

Overview of parameters in other experiments

In Table I.1 we summarize typical parameters for Rydberg atom excitation in other experiments. The experiments with few atoms [74, 100] reach quite high Rabi frequency by strongly focussed beams. The large detuning in the case of [100] helps to get long coherence times. In the experiment [74] the intensity on the lower transition is chosen so high that the scattering rate on the intermediate state starts to saturate, which helps in this case to increase the number of observable Rabi cycles. All experiments use intensities above the saturation intensity (for the D_2 line and σ-polarized light on cycling transition this is $1.669\,\mathrm{mW/cm^2}$ [263]). But what is relevant here is the off-resonant scattering rate, which is given by $\varGamma_{\mathrm{sc}}(I) = \frac{\varGamma}{2}\frac{I/I_{\mathrm{sat}}}{1+I/I_{\mathrm{sat}}+(2\varDelta/\varGamma)^2}$ [410]. An interesting regime is when this scattering rate starts to saturate as the ratio $\varOmega/\varGamma_{\mathrm{sc}}$ will increase then. The only problem of this approach is the strong light shifts and the very fast timescales of the Rabi oscillations on the order of $\varGamma$. To estimate the theoretical number of observable Rabi cycles also $\varOmega/\varGamma_{\mathrm{sc}}$ is shown in the table for the theoretical value of the scattering rate $\varGamma_{\mathrm{sc}}$ of the scattering rate. Obviously these values are much larger than the number of cycles observed in the experiment caused by additional decoherence effects in the experiment as for example increased scattering due to laser linewidth, amplified spontaneous emission background of the diode lasers and the lifetime of the Rydberg states. The Rabi frequencies of other Rydberg experiments given in Table I.1 were checked to be consistent with calculations. Only for the publication [110] the expected Rabi frequency was not reproduced, maybe due to a misinterpretation of the numbers given there.

Group	Bloch [291]	Bloch [294]	Saffman [100]	Grangier [74]	Arimondo [110]	Raithel [180]	Pfau [176]	Weidemüller [178]
Rydberg state	$43S_{1/2}$,$m_j = -1/2$	$43S_{1/2}$,$m_j = -1/2$	$79D_{5/2}$,$m_j = 1/2$	$58D_{3/2}$	$53D_{5/2}$	^{85}Rb $70D_{5/2}$	$43S_{1/2}$	$31D_{5/2}$
Intermediate state	$5P_{3/2}$	$5P_{3/2}$	$5P_{3/2}$	$5P_{1/2}$	$6P_{3/2}$	$5P_{3/2}$	$5P_{3/2}$	$5P_{3/2}$
Intermediate detuning†	+742 MHz	+742 MHz	−2.4 GHz	+400 MHz	+0.5−1 GHz	≈ 0 MHz	+478 MHz	+140 MHz
Wavelength λ_1 (nm)	780	780	780	795	420	780	780	780
Wavelength λ_2 (nm)	480	480	480	474	1010 − 1030	480	480	480
Optical power 1 (mW)	0.023	0.0038	0.002	7	20	[0.004]	≈ 0.05 [242, p. 5]	[0.014]
Optical power 2 (mW)	0.5	6	26.2	30	150	n/a [10]	55 [242, p. 4]	40
Beam 1 waist (µm)	57(2)	44(2)	12 and 7‡	130	120	750	550 [242, p. 4]	1100
Beam 2 waist (µm)	17(5)	17(5)	11 and 9	25	150	8	35 [242, p. 4]	$d = 100\,\mu$m flattop
Intensity 1 (mW/cm^2)	450	125	1490	26400	88400	≈ 5	11	275
$\Gamma_{\mathrm{sc},1}/(\Gamma/2)$	$4.5 \cdot 10^{-3}$	$1.3 \cdot 10^{-3}$	$9.5 \cdot 10^{-4}$	$2.3 \cdot 10^{-1}$	$6.2 \cdot 10^{-3}$	-	$2.7 \cdot 10^{-4}$	$7.2 \cdot 10^{-2}$
$\Omega/\Gamma_{\mathrm{sc}}$	12	84	177	10	34	-	261	23
Intensity 2 (kW/cm^2)	0.1	1.3	15.7	3.1	0.4	n/a [10]	2.9	0.5
Polarization 1	σ^-	σ^-	π	π	n/a	σ^+	σ^+	[σ^+]
Polarization 2	σ^+	σ^+	π	σ^+	n/a	σ^+	σ^-	[σ^+]
Rabi frequency 1	[$2\pi \cdot 70$ MHz]	$2\pi \cdot 37$ MHz	[$2\pi \cdot 105$ MHz]	$2\pi \cdot 260$ MHz	[$\sim 2\pi \cdot 80$ MHz]	[$\sim 2\pi \cdot 7$ MHz]	$2\pi \cdot 9.7$ MHz	$2\pi \cdot 55$ MHz
Rabi frequency 2	[$2\pi \cdot 4$ MHz]	$2\pi \cdot 13$ MHz	[$2\pi \cdot 27$ MHz]	$2\pi \cdot 21$ MHz	[$\sim 2\pi \cdot 12$ MHz]	n/a [$\sim 2\pi \cdot 33$ MHz]	$2\pi \cdot 21$ MHz	$2\pi \cdot 27$ MHz
eff. Rabi frequency	$2\pi \cdot 170(20)$ kHz	$2\pi \cdot 320(20)$ kHz	$2\pi \cdot 510$ kHz	$2\pi \cdot 6.5$ MHz	$2\pi \cdot 30$ kHz	n/a	$2\pi \cdot 210$ kHz	[$2\pi \cdot 5$ MHz]
Magnetic field (Gauss)	30	30	11.5	9	n/a	n/a	0.89 (magn. trap)	n/a (MOT off)
Electric field	no control	no control	no control	no control	< 1 mV/cm	< 100 mV/cm	2 V/cm [242]	160 mV/cm
Pulse length (µs)	≤ 4	≤ 4	≤ 4	< 0.35	< 8	< 0.4	< 20	< 0.35
Full laser width (kHz)	< 70	< 70	< 1	< 700 [412]	< 300	∼ 1000	< 1500 (1 ms)/130(5 µs)	∼ 2000

Table I.1.: Rydberg excitation parameter comparison between several experiments. Comparison of selected parameter sets of various publications. Values in [ ] are own calculations for values not given directly in the paper from the given parameters. The numbers for the lower transition are marked by 1 the upper by 2. Experiments work with ^{87}Rb if not indicated otherwise. † intermediate detuning, positive means blue detuning. ‡ beam is elliptic with both waists given.

Appendix J.

^{87}Rb properties

J.1. Radial matrix element of the rubidium D$_2$ line

In [263] only the rubidium matrix elements $\langle j = 1/2 \,|\, r \,|\, j' = 1/2\rangle = 2.989318(20)$ and $\langle j = 1/2 \,|\, r \,|\, j' = 3/2\rangle = 4.22752(87)$ are given. For comparison with the matrix elements calculated using the radial wavefunction, these matrix elements need further reduction. This can be done using [263, eq. (37)]

$$\begin{aligned} \langle j \,|\, r \,|\, j' \rangle &= \langle lsj \,|\, r \,|\, l's'j' \rangle \\ &= \langle j \,|\, r \,|\, j' \rangle \, (-1)^{J'+L+1+S} \sqrt{(2j'+1)(2l+1)} \begin{Bmatrix} l & l' & 1 \\ j' & j & s \end{Bmatrix} \end{aligned} \tag{J.1}$$

and leads to a matrix element $\mathcal{R}_{5\mathrm{S}}^{5\mathrm{P}} = \langle l = 0 \,|\, r \,|\, l' = 1\rangle = 5.181(4)$ ($\sqrt{2l+1} = 1$ here).

J.2. Collection of references for rubidium properties

isotope	states	reference
^{85}Rb	F$_{7/2}$	[413]
^{85}Rb	S,D	[217]
^{85}Rb and ^{87}Rb	S	[216]
^{87}Rb	S,D	[86]

Table J.1.: References for absolute transition frequencies to Rydberg states of rubidium

data	states	reference
Laser cooling properties	5S → 5P	[263]
Polarizability / dipole matrix element	$5S \rightarrow 5P_{1/2}$	[414]
Dipole matrix elements and polarizability	5S and 5P	(theory) [358]
Hyperfine structure	$6P_{3/2}$	[415]
Hyperfine structure, nuclear moments	$S,P_{3/2}$	[416]
Spectroscopy	$5S \rightarrow P_{1/2}$	[417]
Oscillator strengths	5S → nP	(theory) [210]
Radial matrix element / oscillator strength	5S → nP	(theory) [357]
Oscillator strengths	5S → nP	[208]
Single-photon spectroscopy	5S → nS, nP, nD	[418]
Spectroscopy	$5S_{1/2} \rightarrow 5D_{5/2}$	[419]
Polarizability	5D	[420]
Dipole matrix element	5S → 4D	[421]
Hyperfine structure, energy level	$4D, 5P_{3/2} \rightarrow 4D$	[422, 423]
Dipole matrix elements	$5P_{3/2} \rightarrow nD_{5/2}$	[234]
Oscillator strengths	$5P_{3/2} \rightarrow nD_{5/2}$	[233]
Spectroscopy data	5S → 7S	[424]
Transition frequency	$5P_{3/2} \rightarrow 7S$	[425]
Anti-relaxation coating	5S	[426]
Review hyperfine structure		[427]
Compilation of energy levels		[428, 429]
Nuclear moments		[430]
Quasi-metastable levels		[431]

Table J.2.: Collection of publications with precision data of ^{87}Rb properties

Bibliography

1. Saffman, M., Walker, T. & Mølmer, K. Quantum information with Rydberg atoms. *Rev. Mod. Phys.* **82,** 2313–2363 (2010).
2. Comparat, D. & Pillet, P. Dipole blockade in a cold Rydberg atomic sample [Invited]. *J. Opt. Soc. Am. B* **27,** A208 (2010).
3. Löw, R. *et al.* An experimental and theoretical guide to strongly interacting Rydberg gases. *J. Phys. B At. Mol. Opt. Phys.* **45,** 113001 (2012).
4. Hofmann, C. S. *et al.* An experimental approach for investigating many-body phenomena in Rydberg-interacting quantum systems. *Front. Phys.* doi:`10.1007/s11467-013-0396-7` (2013).
5. Baranov, M. Theoretical progress in many-body physics with ultracold dipolar gases. *Phys. Rep.* **464,** 71–111 (2008).
6. Henkel, N., Nath, R. & Pohl, T. Three-Dimensional Roton Excitations and Supersolid Formation in Rydberg-Excited Bose-Einstein Condensates. *Phys. Rev. Lett.* **104,** 195302 (2010).
7. Pupillo, G., Micheli, A., Boninsegni, M., Lesanovsky, I. & Zoller, P. Strongly Correlated Gases of Rydberg-Dressed Atoms: Quantum and Classical Dynamics. *Phys. Rev. Lett.* **104,** 223002 (2010).
8. Feynman, R. P. Simulating physics with computers. *Int. J. Theor. Phys.* **21,** 467–488 (1982).
9. Hazzard, K. R. A. *et al.* Quantum correlations and entanglement in far-from-equilibrium spin systems. *Phys. Rev. A* **90,** 063622 (2014).
10. Georgescu, I. M., Ashhab, S. & Nori, F. Quantum simulation. *Rev. Mod. Phys.* **86,** 153–185 (2014).
11. Jaksch, D., Bruder, C., Cirac, J., Gardiner, C. & Zoller, P. Cold Bosonic Atoms in Optical Lattices. *Phys. Rev. Lett.* **81,** 3108–3111 (1998).
12. Greiner, M., Mandel, O., Esslinger, T., Hänsch, T. W. & Bloch, I. Quantum phase transition from a superfluid to a Mott insulator in a gas of ultracold atoms. *Nature* **415,** 39–44 (2002).
13. Bloch, I., Dalibard, J. & Zwerger, W. Many-body physics with ultracold gases. *Rev. Mod. Phys.* **80,** 885–964 (2008).
14. Endres, M. *et al.* Observation of correlated particle-hole pairs and string order in low-dimensional Mott insulators. *Science* **334,** 200–3 (2011).
15. Cheneau, M. *et al.* Light-cone-like spreading of correlations in a quantum many-body system. *Nature* **481,** 484–7 (2012).

16. Endres, M. *et al.* The 'Higgs' amplitude mode at the two-dimensional superfluid/Mott insulator transition. *Nature* **487,** 454–8 (2012).
17. Jaksch, D. & Zoller, P. The cold atom Hubbard toolbox. *Ann. Phys. (N. Y).* **315,** 52–79 (2005).
18. Bloch, I., Dalibard, J. & Nascimbène, S. Quantum simulations with ultracold quantum gases. *Nat. Phys.* **8,** 267–276 (2012).
19. Jaksch, D. Bose-Einstein Condensation and Applications. PhD thesis (1999).
20. Bakr, W. S. *et al.* Probing the superfluid-to-Mott insulator transition at the single-atom level. *Science* **329,** 547–50 (2010).
21. Sherson, J. F. *et al.* Single-atom-resolved fluorescence imaging of an atomic Mott insulator. *Nature* **467,** 68–72 (2010).
22. Weitenberg, C. *et al.* Single-spin addressing in an atomic Mott insulator. *Nature* **471,** 319–24 (2011).
23. Honer, J., Weimer, H., Pfau, T. & Büchler, H. P. Collective Many-Body Interaction in Rydberg Dressed Atoms. *Phys. Rev. Lett.* **105,** 160404 (2010).
24. Maucher, F. *et al.* Rydberg-Induced Solitons: Three-Dimensional Self-Trapping of Matter Waves. *Phys. Rev. Lett.* **106,** 170401 (2011).
25. Glaetzle, A. W., Nath, R., Zhao, B., Pupillo, G. & Zoller, P. Driven-dissipative dynamics of a strongly interacting Rydberg gas. *Phys. Rev. A* **86,** 043403 (2012).
26. Li, W., Hamadeh, L. & Lesanovsky, I. Probing the interaction between Rydberg-dressed atoms through interference. *Phys. Rev. A* **85,** 053615 (2012).
27. Macrì, T. & Pohl, T. Rydberg dressing of atoms in optical lattices. *Phys. Rev. A* **89,** 011402 (2014).
28. Robicheaux, F. & Hernández, J. Many-body wave function in a dipole blockade configuration. *Phys. Rev. A* **72,** 063403 (2005).
29. Weimer, H., Löw, R., Pfau, T. & Büchler, H. P. Quantum Critical Behavior in Strongly Interacting Rydberg Gases. *Phys. Rev. Lett.* **101,** 250601 (2008).
30. Schachenmayer, J., Lesanovsky, I., Micheli, A. & Daley, A. J. Dynamical crystal creation with polar molecules or Rydberg atoms in optical lattices. *New J. Phys.* **12,** 103044 (2010).
31. Sela, E., Punk, M. & Garst, M. Dislocation-mediated melting of one-dimensional Rydberg crystals. *Phys. Rev. B* **84,** 085434 (2011).
32. Lesanovsky, I. Many-Body Spin Interactions and the Ground State of a Dense Rydberg Lattice Gas. *Phys. Rev. Lett.* **106,** 025301 (2011).
33. Richerme, P. *et al.* Non-local propagation of correlations in quantum systems with long-range interactions. *Nature* **511,** 198–201 (2014).
34. Jurcevic, P. *et al.* Quasiparticle engineering and entanglement propagation in a quantum many-body system. *Nature* **511,** 202–205 (2014).

35. Yan, B. *et al.* Observation of dipolar spin-exchange interactions with lattice-confined polar molecules. *Nature* **501,** 521–5 (2013).

36. Pohl, T., Demler, E. & Lukin, M. D. Dynamical Crystallization in the Dipole Blockade of Ultracold Atoms. *Phys. Rev. Lett.* **104,** 043002 (2010).

37. Van Bijnen, R. M. W., Smit, S., van Leeuwen, K. a. H., Vredenbregt, E. J. D. & Kokkelmans, S. J. J. M. F. Adiabatic formation of Rydberg crystals with chirped laser pulses. *J. Phys. B At. Mol. Opt. Phys.* **44,** 184008 (2011).

38. Endres, M. *et al.* Single-site- and single-atom-resolved measurement of correlation functions. *Appl. Phys. B* **113,** 27–39 (2013).

39. Fisher, M. P. A., Grinstein, G. & Fisher, D. S. Boson localization and the superfluid-insulator transition. *Phys. Rev. B* **40,** 546–570 (1989).

40. Campbell, G. K. *et al.* Imaging the Mott insulator shells by using atomic clock shifts. *Science* **313,** 649–52 (2006).

41. Widera, A. *et al.* Precision measurement of spin-dependent interaction strengths for spin-1 and spin-2 87 Rb atoms. *New J. Phys.* **8,** 152–152 (2006).

42. Will, S. *et al.* Time-resolved observation of coherent multi-body interactions in quantum phase revivals. *Nature* **465,** 197–201 (2010).

43. Bakr, W. S. *et al.* Orbital excitation blockade and algorithmic cooling in quantum gases. *Nature* **480,** 500–503 (2011).

44. Preiss, P. M. *et al.* Strongly correlated quantum walks in optical lattices. *Science* **347,** 1229–1233 (2015).

45. Oitmaa, J., Hamer, C. & Zheng, W. *Series Expansion Methods for strongly interacting lattice models* (Cambridge University Press, Cambridge, 2006).

46. DePue, M., McCormick, C., Winoto, S., Oliver, S. & Weiss, D. Unity Occupation of Sites in a 3D Optical Lattice. *Phys. Rev. Lett.* **82,** 2262–2265 (1999).

47. Schlosser, N., Reymond, G., Protsenko, I. & Grangier, P. Sub-poissonian loading of single atoms in a microscopic dipole trap. *Nature* **411,** 1024–7 (2001).

48. Weitenberg, C. Single-Atom Resolved Imaging and Manipulation in an Atomic Mott Insulator. PhD thesis (Ludwig-Maximilians-Universität München, 2011).

49. Endres, M. Probing correlated quantum many-body systems at the single-particle level. PhD thesis (Ludwig-Maximilians-Universität München, 2012).

50. Fukuhara, T. *et al.* Quantum dynamics of a mobile spin impurity. *Nat. Phys.* **9,** 235–241 (2013).

51. Fukuhara, T. *et al.* Microscopic observation of magnon bound states and their dynamics. *Nature* **502,** 76–79 (2013).

52. Mazza, L., Rossini, D., Fazio, R. & Endres, M. Detecting two-site spin-entanglement in many-body systems with local particle-number fluctuations. *New J. Phys.* **17,** 013015 (2015).

53. Gallagher, T. F. *Rydberg Atoms* doi:`10.1017/CBO9780511524530` (Cambridge University Press, Cambridge, 1994).

54. Kazimierczuk, T., Fröhlich, D., Scheel, S., Stolz, H. & Bayer, M. Giant Rydberg excitons in the copper oxide Cu_2O. *Nature* **514,** 343–347 (2014).

55. Langer, R. A Generalization of the Rydberg Formula. *Phys. Rev.* **35,** 649–650 (1930).

56. Rydberg, J. R. Recherches sur la constitution des spectres d'émission des éléments chimiques. *K. Sven. vetenskapsakademiens Handl.* **n.f., bd.2,** 1–155 (1890).

57. Rydberg, J. R. XXXIV. On the structure of the line-spectra of the chemical elements. *Philos. Mag. Ser. 5* **29,** 331–337 (1890).

58. Rydberg, J. R. Über den Bau der Linienspektren der chemischen Grundstoffe. *Z. Phys. Chem.* **5,** 227 (1890).

59. Saßmannshausen, H., Merkt, F. & Deiglmayr, J. High-resolution spectroscopy of Rydberg states in an ultracold cesium gas. *Phys. Rev. A* **87,** 032519 (2013).

60. Balewski, J. B. *et al.* Coupling a single electron to a Bose-Einstein condensate. *Nature* **502,** 664–7 (2013).

61. Messiah, A. *Quantum Mechanics* 4th ed. (North-Holland Publishing Company, Amsterdam, 1967).

62. Landau, L. D. & Lifshitz, E. M. *Quantum mechanics - Non-relativistic theory* 3rd ed. (Pergamom Press Ltd., 1991).

63. Gounand, F. Calculation of radial matrix elements and radiative lifetimes for highly excited states of alkali atoms using the Coulomb approximation. *J. Phys.* **40,** 457–460 (1979).

64. Beterov, I., Ryabtsev, I., Tretyakov, D. & Entin, V. Quasiclassical calculations of blackbody-radiation-induced depopulation rates and effective lifetimes of Rydberg nS, nP, and nD alkali-metal atoms with $n \leq 80$. *Phys. Rev. A* **79,** 052504 (2009).

65. Boisseau, C., Simbotin, I. & Côté, R. Macrodimers: Ultralong Range Rydberg Molecules. *Phys. Rev. Lett.* **88,** 20–23 (2002).

66. Gallagher, T. F. Rydberg atoms. *Reports Prog. Phys.* **51,** 143–188 (1988).

67. Butscher, B. A Rydberg Interferometer. PhD thesis (Universität Stuttgart, 2011).

68. Flannery, M. R., Vrinceanu, D. & Ostrovsky, V. N. Long-range interaction between polar Rydberg atoms. *J. Phys. B At. Mol. Opt. Phys.* **38,** S279–S293 (2005).

69. Henkel, N. Rydberg-dressed Bose-Einstein condensates. PhD thesis (Technische Universität Dresden, 2013).

70. Johnson, T. *et al.* Rabi Oscillations between Ground and Rydberg States with Dipole-Dipole Atomic Interactions. *Phys. Rev. Lett.* **100,** 113003 (2008).

71. Miroshnychenko, Y. *et al.* Coherent excitation of a single atom to a Rydberg state. *Phys. Rev. A* **82,** 013405 (2010).

72. Hankin, A. M. *et al.* Two-atom Rydberg blockade using direct 6S to nP excitation. *Phys. Rev. A* **89,** 033416 (2014).

73. Lukin, M. D., Fleischhauer, M. & Cote, R. Dipole Blockade and Quantum Information Processing in Mesoscopic Atomic Ensembles. *Phys. Rev. Lett.* **87,** 037901 (2001).

74. Gaëtan, A. *et al.* Observation of collective excitation of two individual atoms in the Rydberg blockade regime. *Nat. Phys.* **5,** 115–118 (2009).

75. Dudin, Y. O., Li, L., Bariani, F. & Kuzmich, A. Observation of coherent many-body Rabi oscillations. *Nat. Phys.* **8,** 790–794 (2012).

76. Ebert, M. *et al.* Atomic Fock State Preparation Using Rydberg Blockade. *Phys. Rev. Lett.* **112,** 043602 (2014).

77. Hernández, J. V. & Robicheaux, F. Simulation of a strong van der Waals blockade in a dense ultracold gas. *J. Phys. B At. Mol. Opt. Phys.* **41,** 045301 (2008).

78. Heidemann, R. Rydberg Excitation of Bose-Einstein Condensates : Coherent Collective Dynamics. PhD thesis (Universität Stuttgart, 2008).

79. Krohn, U. Universal scaling and coherence properties of an ultracold Rydberg gas. PhD thesis (Universität Stuttgart, 2008).

80. Huillery, P. Few and Many-body Physics in cold Rydberg gases. PhD thesis (Université Paris-Sud XI, 2013).

81. Metcalf, H. J. Highly excited atoms. *Nature* **284,** 127–131 (1980).

82. Amaldi, E. & Segrè, E. Effect of Pressure on High Terms of Alkaline Spectra. *Nature* **133,** 141–141 (1934).

83. Amaldi, E. & Segrè, E. Effetto della Pressione Sui Termini Elevati Degli Alcalini. *Nuovo Cim.* **11,** 145–156 (1934).

84. Bradley, D. J., Ewart, P., Nicholas, J. V. & Shaw, J. R. D. Excited state absorption spectroscopy of alkaline earths selectively pumped by tunable dye lasers. I. Barium arc spectra. *J. Phys. B At. Mol. Phys.* **6,** 1594–1602 (1973).

85. Mohapatra, A. K., Jackson, T. R. & Adams, C. S. Coherent Optical Detection of Highly Excited Rydberg States Using Electromagnetically Induced Transparency. *Phys. Rev. Lett.* **98,** 113003 (2007).

86. Mack, M. *et al.* Measurement of absolute transition frequencies of ^{87}Rb to nS and nD Rydberg states by means of electromagnetically induced transparency. *Phys. Rev. A* **83,** 052515 (2011).

87. Tauschinsky, A., Newell, R., van Linden van den Heuvell, H. B. & Spreeuw, R. J. C. Measurement of ^{87}Rb Rydberg-state hyperfine splitting in a room-temperature vapor cell. *Phys. Rev. A* **87,** 042522 (2013).

88. Abel, R. P., Carr, C., Krohn, U. & Adams, C. S. Electrometry near a dielectric surface using Rydberg electromagnetically induced transparency. *Phys. Rev. A* **84,** 023408 (2011).
89. Huber, B. *et al.* GHz Rabi Flopping to Rydberg States in Hot Atomic Vapor Cells. *Phys. Rev. Lett.* **107,** 243001 (2011).
90. Baluktsian, T., Huber, B., Löw, R. & Pfau, T. Evidence for Strong van der Waals Type Rydberg-Rydberg Interaction in a Thermal Vapor. *Phys. Rev. Lett.* **110,** 123001 (2013).
91. Brune, M., Haroche, S., Lefevre, V., Raimond, J. & Zagury, N. Quantum nondemolition measurement of small photon numbers by Rydberg-atom phase-sensitive detection. *Phys. Rev. Lett.* **65,** 976–979 (1990).
92. Gleyzes, S. *et al.* Quantum jumps of light recording the birth and death of a photon in a cavity. *Nature* **446,** 297–300 (2007).
93. Haroche, S. Nobel Lecture: Controlling photons in a box and exploring the quantum to classical boundary. *Rev. Mod. Phys.* **85,** 1083–1102 (2013).
94. Sedlacek, J. a. *et al.* Microwave electrometry with Rydberg atoms in a vapour cell using bright atomic resonances. *Nat. Phys.* **8,** 819–824 (2012).
95. Jaksch, D., Cirac, J. I., Zoller, P., Côté, R. & Lukin, M. D. Fast Quantum Gates for Neutral Atoms. *Phys. Rev. Lett.* **85,** 2208–2211 (2000).
96. Tong, D. *et al.* Local Blockade of Rydberg Excitation in an Ultracold Gas. *Phys. Rev. Lett.* **93,** 063001 (2004).
97. Singer, K., Reetz-Lamour, M., Amthor, T., Marcassa, L. G. & Weidemüller, M. Suppression of Excitation and Spectral Broadening Induced by Interactions in a Cold Gas of Rydberg Atoms. *Phys. Rev. Lett.* **93,** 163001 (2004).
98. Reinhard, A. *et al.* Double-Resonance Spectroscopy of Interacting Rydberg-Atom Systems. *Phys. Rev. Lett.* **100,** 233201 (2008).
99. Reinhard, A. W. Cold Rydberg-Atom Interactions. PhD thesis (The University of Michigan, 2008).
100. Urban, E. *et al.* Observation of Rydberg blockade between two atoms. *Nat. Phys.* **5,** 110–114 (2009).
101. Isenhower, L. *et al.* Demonstration of a Neutral Atom Controlled-NOT Quantum Gate. *Phys. Rev. Lett.* **104,** 010503 (2010).
102. Wilk, T. *et al.* Entanglement of Two Individual Neutral Atoms Using Rydberg Blockade. *Phys. Rev. Lett.* **104,** 010502 (2010).
103. Béguin, L., Vernier, A., Chicireanu, R., Lahaye, T. & Browaeys, A. Direct Measurement of the van der Waals Interaction between Two Rydberg Atoms. *Phys. Rev. Lett.* **110,** 263201 (2013).
104. Béguin, L. Measurement of the van der Waals interaction between two Rydberg atoms. PhD thesis (Institut d'optique graduate school, 2013).

105. Barredo, D. *et al.* Demonstration of a Strong Rydberg Blockade in Three-Atom Systems with Anisotropic Interactions. *Phys. Rev. Lett.* **112,** 183002 (2014).

106. Abate, J., Kimble, H. & Mandel, L. Photon statistics of a dye laser. *Phys. Rev. A* **14,** 788–795 (1976).

107. Mandel, L. Sub-Poissonian photon statistics in resonance fluorescence. *Opt. Lett.* **4,** 205–207 (1979).

108. Liebisch, T., Reinhard, A., Berman, P. & Raithel, G. Atom Counting Statistics in Ensembles of Interacting Rydberg Atoms. *Phys. Rev. Lett.* **95,** 253002 (2005).

109. Liebisch, T., Reinhard, A., Berman, P. & Raithel, G. Erratum: Atom Counting Statistics in Ensembles of Interacting Rydberg Atoms [Phys. Rev. Lett. 95, 253002 (2005)]. *Phys. Rev. Lett.* **98,** 109903 (2007).

110. Viteau, M. *et al.* Rydberg Excitations in Bose-Einstein Condensates in Quasi-One-Dimensional Potentials and Optical Lattices. *Phys. Rev. Lett.* **107,** 060402 (2011).

111. Viteau, M. *et al.* Rydberg excitation of a Bose-Einstein condensate. *Laser Phys.* **23,** 015502 (2013).

112. Hofmann, C. S. *et al.* Sub-Poissonian Statistics of Rydberg-Interacting Dark-State Polaritons. *Phys. Rev. Lett.* **110,** 203601 (2013).

113. Viteau, M. *et al.* Cooperative Excitation and Many-Body Interactions in a Cold Rydberg Gas. *Phys. Rev. Lett.* **109,** 053002 (2012).

114. Malossi, N. *et al.* Full Counting Statistics and Phase Diagram of a Dissipative Rydberg Gas. *Phys. Rev. Lett.* **113,** 023006 (2014).

115. Schempp, H. *et al.* Full Counting Statistics of Laser Excited Rydberg Aggregates in a One-Dimensional Geometry. *Phys. Rev. Lett.* **112,** 013002 (2014).

116. Fabre, C., Haroche, S. & Goy, P. Millimeter spectroscopy in sodium Rydberg states: Quantum-defect, fine-structure, and polarizability measurements. *Phys. Rev. A* **18,** 229–237 (1978).

117. Meschede, D. Centimeter-wave spectroscopy of highly excited rubidium atoms. *J. Opt. Soc. Am. B* **4,** 413 (1987).

118. Goy, P., Raimond, J., Vitrant, G. & Haroche, S. Millimeter-wave spectroscopy in cesium Rydberg states. Quantum defects, fine- and hyperfine-structure measurements. *Phys. Rev. A* **26,** 2733–2742 (1982).

119. Li, W., Mourachko, I., Noel, M. & Gallagher, T. Millimeter-wave spectroscopy of cold Rb Rydberg atoms in a magneto-optical trap: Quantum defects of the ns, np, and nd series. *Phys. Rev. A* **67,** 052502 (2003).

120. Mudrich, M., Zahzam, N., Vogt, T., Comparat, D. & Pillet, P. Back and Forth Transfer and Coherent Coupling in a Cold Rydberg Dipole Gas. *Phys. Rev. Lett.* **95,** 233002 (2005).

121. Afrousheh, K., Bohlouli-Zanjani, P., Petrus, J. & Martin, J. Determination of the ^{85}Rb ng-series quantum defect by electric-field-induced resonant energy transfer between cold Rydberg atoms. *Phys. Rev. A* **74,** 062712 (2006).

122. Afrousheh, K., Bohlouli-Zanjani, P., Carter, J., Mugford, A. & Martin, J. Resonant electric dipole-dipole interactions between cold Rydberg atoms in a magnetic field. *Phys. Rev. A* **73,** 063403 (2006).

123. Han, J., Jamil, Y., Norum, D., Tanner, P. & Gallagher, T. Rb nf quantum defects from millimeter-wave spectroscopy of cold ^{85}Rb Rydberg atoms. *Phys. Rev. A* **74,** 054502 (2006).

124. Park, H., Tanner, P. J., Claessens, B. J., Shuman, E. S. & Gallagher, T. F. Dipole-dipole broadening of Rb ns-np microwave transitions. *Phys. Rev. A* **84,** 022704 (2011).

125. Prozument, K. *et al.* Chirped-Pulse Millimeter-Wave Spectroscopy of Rydberg-Rydberg Transitions. *Phys. Rev. Lett.* **107,** 143001 (2011).

126. Yu, Y., Park, H. & Gallagher, T. F. Microwave Transitions in Pairs of Rb Rydberg Atoms. *Phys. Rev. Lett.* **111,** 173001 (2013).

127. Maxwell, D. *et al.* Microwave control of the interaction between two optical photons. *Phys. Rev. A* **89,** 043827 (2014).

128. Paredes-Barato, D. & Adams, C. S. All-Optical Quantum Information Processing Using Rydberg Gates. *Phys. Rev. Lett.* **112,** 040501 (2014).

129. Bohlouli-Zanjani, P., Petrus, J. & Martin, J. Enhancement of Rydberg Atom Interactions Using ac Stark Shifts. *Phys. Rev. Lett.* **98,** 203005 (2007).

130. Petrus, J. A. Use of Microwave Dressing Fields to Enhance Rydberg Atom Interactions. PhD thesis (University of Waterloo, 2007).

131. Petrus, J. A., Bohlouli-Zanjani, P. & Martin, J. D. D. ac electric-field-induced resonant energy transfer between cold Rydberg atoms. *J. Phys. B At. Mol. Opt. Phys.* **41,** 245001 (2008).

132. Tanasittikosol, M. *et al.* Microwave dressing of Rydberg dark states. *J. Phys. B At. Mol. Opt. Phys.* **44,** 184020 (2011).

133. Tanasittikosol, M. & Potvliege, R. M. Sidebands shifts and induced sidebands in rf-dressed Rydberg systems. arXiv: `1206.5951` (2012).

134. Jones, L., Carter, J. & Martin, J. Rydberg atoms with a reduced sensitivity to dc and low-frequency electric fields. *Phys. Rev. A* **87,** 023423 (2013).

135. Förster, T. Energiewanderung und Fluoreszenz. *Naturwissenschaften* **33,** 166–175 (1946).

136. Förster, T. Zwischenmolekulare Energiewanderung und Fluoreszenz. *Ann. Phys.* **437,** 55–75 (1948).

137. Vogt, T. *et al.* Dipole Blockade at Förster Resonances in High Resolution Laser Excitation of Rydberg States of Cesium Atoms. *Phys. Rev. Lett.* **97,** 083003 (2006).

138. Reinhard, A., Younge, K. & Raithel, G. Effect of Förster resonances on the excitation statistics of many-body Rydberg systems. *Phys. Rev. A* **78,** 060702 (2008).

139. Ryabtsev, I. I., Tretyakov, D. B., Beterov, I. I. & Entin, V. M. Observation of the Stark-Tuned Förster Resonance between Two Rydberg Atoms. *Phys. Rev. Lett.* **104,** 073003 (2010).

140. Nipper, J. *et al.* Atomic Pair-State Interferometer: Controlling and Measuring an Interaction-Induced Phase Shift in Rydberg-Atom Pairs. *Phys. Rev. X* **2,** 031011 (2012).

141. Nipper, J. M. Interacting Rydberg atoms: Coherent control at Förster resonances and polar homonuclear molecules. PhD thesis (Universität Stuttgart, 2012).

142. Safinya, K., Delpech, J., Gounand, F., Sandner, W. & Gallagher, T. Resonant Rydberg-Atom-Rydberg-Atom Collisions. *Phys. Rev. Lett.* **47,** 405–408 (1981).

143. Van Ditzhuijzen, C. *et al.* Spatially Resolved Observation of Dipole-Dipole Interaction between Rydberg Atoms. *Phys. Rev. Lett.* **100,** 243201 (2008).

144. Ravets, S. *et al.* Coherent dipole-dipole coupling between two single Rydberg atoms at an electrically-tuned Förster resonance. *Nat. Phys.* **10,** 914–917 (2014).

145. Günter, G. *et al.* Observing the dynamics of dipole-mediated energy transport by interaction-enhanced imaging. *Science* **342,** 954–956 (2013).

146. Gurian, J. H. *et al.* Observation of a Resonant Four-Body Interaction in Cold Cesium Rydberg Atoms. *Phys. Rev. Lett.* **108,** 023005 (2012).

147. Dutta, S., Guest, J., Feldbaum, D., Walz-Flannigan, A. & Raithel, G. Ponderomotive Optical Lattice for Rydberg Atoms. *Phys. Rev. Lett.* **85,** 5551–5554 (2000).

148. Hyafil, P. *et al.* Coherence-Preserving Trap Architecture for Long-Term Control of Giant Ryberg Atoms. *Phys. Rev. Lett.* **93,** 103001 (2004).

149. Saffman, M. & Walker, T. Analysis of a quantum logic device based on dipole-dipole interactions of optically trapped Rydberg atoms. *Phys. Rev. A* **72,** 022347 (2005).

150. Zhang, S., Robicheaux, F. & Saffman, M. Magic-wavelength optical traps for Rydberg atoms. *Phys. Rev. A* **84,** 043408 (2011).

151. Morrison, M. J. & Derevianko, A. Possibility of magic trapping of a three-level system for Rydberg blockade implementation. *Phys. Rev. A* **85,** 033414 (2012).

152. Topcu, T. & Derevianko, A. Tune-out wavelengths and landscape-modulated polarizabilities of alkali-metal Rydberg atoms in infrared optical lattices. *Phys. Rev. A* **88,** 053406 (2013).

153. Carr, A. W. & Saffman, M. Doubly magic trapping for Cs atom hyperfine clock transitions. arXiv: `1406.3560` (2014).

154. Choi, J.-H., Guest, J., Povilus, A., Hansis, E. & Raithel, G. Magnetic Trapping of Long-Lived Cold Rydberg Atoms. *Phys. Rev. Lett.* **95,** 243001 (2005).

155. Hogan, S. & Merkt, F. Demonstration of Three-Dimensional Electrostatic Trapping of State-Selected Rydberg Atoms. *Phys. Rev. Lett.* **100,** 043001 (2008).

156. Younge, K. C., Knuffman, B., Anderson, S. E. & Raithel, G. State-Dependent Energy Shifts of Rydberg Atoms in a Ponderomotive Optical Lattice. *Phys. Rev. Lett.* **104,** 173001 (2010).

157. Anderson, S., Younge, K. & Raithel, G. Trapping Rydberg Atoms in an Optical Lattice. *Phys. Rev. Lett.* **107,** 263001 (2011).

158. Zhang, S. Trapping and Rydberg Excitation of a Single Atom Qubit in a Blue Detuned Bottle. PhD thesis (University of Wisconsin-Madison, 2012).

159. Markert, F. *et al.* ac-Stark shift and photoionization of Rydberg atoms in an optical dipole trap. *New J. Phys.* **12,** 113003 (2010).

160. Weber, T. M. *et al.* Continuous coupling of ultracold atoms to an ionic plasma via Rydberg excitation. *Phys. Rev. A* **86,** 020702 (2012).

161. Ryabtsev, I. I., Tretyakov, D. B. & Beterov, I. I. Stark-switching technique for fast quantum gates in Rydberg atoms. *J. Phys. B At. Mol. Opt. Phys.* **36,** 297–306 (2003).

162. Brion, E., Pedersen, L. H. & Mølmer, K. Implementing a neutral atom Rydberg gate without populating the Rydberg state. *J. Phys. B At. Mol. Opt. Phys.* **40,** S159–S166 (2007).

163. Brion, E., Mølmer, K. & Saffman, M. Quantum Computing with Collective Ensembles of Multilevel Systems. *Phys. Rev. Lett.* **99,** 260501 (2007).

164. Schlosser, M., Tichelmann, S., Kruse, J. & Birkl, G. Scalable architecture for quantum information processing with atoms in optical micro-structures. *Quantum Inf. Process.* **10,** 907–924 (2011).

165. Yavuz, D. *et al.* Fast Ground State Manipulation of Neutral Atoms in Microscopic Optical Traps. *Phys. Rev. Lett.* **96,** 063001 (2006).

166. Kaufman, A. M., Lester, B. J. & Regal, C. A. Cooling a Single Atom in an Optical Tweezer to Its Quantum Ground State. *Phys. Rev. X* **2,** 041014 (2012).

167. Thompson, J., Tiecke, T., Zibrov, A., Vuletić, V. & Lukin, M. Coherence and Raman Sideband Cooling of a Single Atom in an Optical Tweezer. *Phys. Rev. Lett.* **110,** 133001 (2013).

168. Schlosser, M. *et al.* Fast transport, atom sample splitting and single-atom qubit supply in two-dimensional arrays of optical microtraps. *New J. Phys.* **14,** 123034 (2012).

169. Grünzweig, T., Hilliard, A., McGovern, M. & Andersen, M. F. Near-deterministic preparation of a single atom in an optical microtrap. *Nat. Phys.* **6,** 951–954 (2010).

170. Anderson, W., Veale, J. & Gallagher, T. Resonant Dipole-Dipole Energy Transfer in a Nearly Frozen Rydberg Gas. *Phys. Rev. Lett.* **80,** 249–252 (1998).
171. Mourachko, I. *et al.* Many-Body Effects in a Frozen Rydberg Gas. *Phys. Rev. Lett.* **80,** 253–256 (1998).
172. Mourachko, I., Li, W. & Gallagher, T. Controlled many-body interactions in a frozen Rydberg gas. *Phys. Rev. A* **70,** 031401 (2004).
173. Carroll, T., Sunder, S. & Noel, M. Many-body interactions in a sample of ultracold Rydberg atoms with varying dimensions and densities. *Phys. Rev. A* **73,** 032725 (2006).
174. Heidemann, R. *et al.* Rydberg excitation of Bose-Einstein condensates. *Phys. Rev. Lett.* **100,** 33601 (2008).
175. Reetz-Lamour, M. Coherence and decoherence in an ultracold gas of Rydberg atoms. PhD thesis (Albert-Ludwigs-Universität Freiburg, 2006).
176. Heidemann, R. *et al.* Evidence for Coherent Collective Rydberg Excitation in the Strong Blockade Regime. *Phys. Rev. Lett.* **99,** 163601 (2007).
177. Raitzsch, U. *et al.* Echo Experiments in a Strongly Interacting Rydberg Gas. *Phys. Rev. Lett.* **100,** 013002 (2008).
178. Reetz-Lamour, M., Amthor, T., Deiglmayr, J. & Weidemüller, M. Rabi Oscillations and Excitation Trapping in the Coherent Excitation of a Mesoscopic Frozen Rydberg Gas. *Phys. Rev. Lett.* **100,** 253001 (2008).
179. Younge, K. C. & Raithel, G. Rotary echo tests of coherence in Rydberg-atom excitation. *New J. Phys.* **11,** 043006 (2009).
180. Schwarzkopf, A., Sapiro, R. E. & Raithel, G. Imaging Spatial Correlations of Rydberg Excitations in Cold Atom Clouds. *Phys. Rev. Lett.* **107,** 103001 (2011).
181. Schwarzkopf, A., Anderson, D. A., Thaicharoen, N. & Raithel, G. Spatial correlations between Rydberg atoms in an optical dipole trap. *Phys. Rev. A* **88,** 061406 (2013).
182. Urvoy, A. *et al.* Strongly correlated growth of Rydberg aggregates in a vapour cell. arXiv: `1408.0039` (2014).
183. Lochead, G. Excited state spatial distributions in a cold strontium gas. PhD thesis (Durham University, 2012).
184. McQuillen, P., Zhang, X., Strickler, T., Dunning, F. B. & Killian, T. C. Imaging the evolution of an ultracold strontium Rydberg gas. *Phys. Rev. A* **87,** 013407 (2013).
185. Greene, C., Dickinson, A. & Sadeghpour, H. Creation of Polar and Nonpolar Ultra-Long-Range Rydberg Molecules. *Phys. Rev. Lett.* **85,** 2458–2461 (2000).
186. Farooqi, S. *et al.* Long-Range Molecular Resonances in a Cold Rydberg Gas. *Phys. Rev. Lett.* **91,** 183002 (2003).
187. Bendkowsky, V. *et al.* Observation of ultralong-range Rydberg molecules. *Nature* **458,** 1005–8 (2009).

188. Bendkowsky, V. *et al.* Rydberg Trimers and Excited Dimers Bound by Internal Quantum Reflection. *Phys. Rev. Lett.* **105,** 163201 (2010).
189. Bellos, M. A. *et al.* Excitation of Weakly Bound Molecules to Trilobitelike Rydberg States. *Phys. Rev. Lett.* **111,** 053001 (2013).
190. Anderson, D. A., Miller, S. A. & Raithel, G. Photoassociation of Long-Range nD Rydberg Molecules. *Phys. Rev. Lett.* **112,** 163201 (2014).
191. Butscher, B. *et al.* Atom-molecule coherence for ultralong-range Rydberg dimers. *Nat. Phys.* **6,** 970–974 (2010).
192. Butscher, B. *et al.* Lifetimes of ultralong-range Rydberg molecules in vibrational ground and excited states. *J. Phys. B At. Mol. Opt. Phys.* **44,** 184004 (2011).
193. Li, W. *et al.* A homonuclear molecule with a permanent electric dipole moment. *Science* **334,** 1110–4 (2011).
194. Gaj, A. *et al.* From molecular spectra to a density shift in dense Rydberg gases. *Nat. Commun.* **5,** 4546 (2014).
195. Karpiuk, T. *et al.* Detecting and imaging single Rydberg electrons in a Bose-Einstein condensate. arXiv: `1402.6875` (2014).
196. Chang, D. E., Vuletić, V. & Lukin, M. D. Quantum nonlinear optics — photon by photon. *Nat. Photonics* **8,** 685–694 (2014).
197. Dudin, Y. O. & Kuzmich, A. Strongly interacting Rydberg excitations of a cold atomic gas. *Science* **336,** 887–9 (2012).
198. Peyronel, T. *et al.* Quantum nonlinear optics with single photons enabled by strongly interacting atoms. *Nature* **488,** 57–60 (2012).
199. Firstenberg, O. *et al.* Attractive photons in a quantum nonlinear medium. *Nature* **502,** 71–5 (2013).
200. Baur, S., Tiarks, D., Rempe, G. & Dürr, S. Single-Photon Switch Based on Rydberg Blockade. *Phys. Rev. Lett.* **112,** 073901 (2014).
201. Tiarks, D., Baur, S., Schneider, K., Dürr, S. & Rempe, G. Single-Photon Transistor Using a Förster Resonance. *Phys. Rev. Lett.* **113,** 053602 (2014).
202. Dudin, Y. *et al.* Entanglement of a Photon and an Optical Lattice Spin Wave. *Phys. Rev. Lett.* **103,** 020505 (2009).
203. Li, L., Dudin, Y. O. & Kuzmich, A. Entanglement between light and an optical atomic excitation. *Nature* **498,** 466–9 (2013).
204. Balewski, J. B. *et al.* Rydberg dressing: understanding of collective many-body effects and implications for experiments. *New J. Phys.* **16,** 063012 (2014).
205. Gil, L. I. R., Mukherjee, R., Bridge, E. M., Jones, M. P. A. & Pohl, T. Spin Squeezing in a Rydberg Lattice Clock. *Phys. Rev. Lett.* **112,** 103601 (2014).
206. Seaton, M. J. The Quantum Defect Method. *Mon. Not. R. Astron. Soc.* **118,** 504 (1958).

207. Freeman, R. & Kleppner, D. Core polarization and quantum defects in high-angular-momentum states of alkali atoms. *Phys. Rev. A* **14,** 1614–1619 (1976).

208. Caliebe, E. & Niemax, K. Oscillator strengths of the principal series lines of Rb. *J. Phys. B At. Mol. Phys.* **12,** L45–L51 (1979).

209. Salvat, F., Fernández-Varea, J. & Williamson, W. Accurate numerical solution of the radial Schrödinger and Dirac wave equations. *Comput. Phys. Commun.* **90,** 151–168 (1995).

210. Zilitis, V. A. Theoretical determination of oscillator strengths for the principal series of rubidium-like ions by the Dirac-Fock method. *Opt. Spectrosc.* **107,** 54–57 (2009).

211. Marinescu, M., Sadeghpour, H. & Dalgarno, A. Dispersion coefficients for alkali-metal dimers. *Phys. Rev. A* **49,** 982–988 (1994).

212. Lorenzen, C.-J. & Niemax, J. Quantum Defects of the $n^2\mathrm{P}_{1/2,3/2}$ Levels in ^{39}K I and ^{85}Rb I. *Phys. Scr.* **27,** 300–305 (1983).

213. Rau, a. R. P. The quantum defect: Early history and recent developments. *Am. J. Phys.* **65,** 221 (1997).

214. Seaton, M. J. Quantum defect theory. *Reports Prog. Phys.* **46,** 167–257 (1983).

215. *Handbook of High-resolution Spectroscopy* (eds Quack, M. & Merkt, F.) doi:`10.1002/9780470749593` (John Wiley & Sons, Ltd, Chichester, UK, 2011).

216. Lee, S. A., Helmcke, J., Hall, J. L. & Stoicheff, B. P. Doppler-free two-photon transitions to Rydberg levels: convenient, useful, and precise reference wavelengths for dye lasers. *Opt. Lett.* **3,** 141 (1978).

217. Stoicheff, B. P. & Weinberger, E. Doppler-free two-photon absorption spectrum of rubidium. *Can. J. Phys.* **57,** 2143–2154 (1979).

218. Sanguinetti, B., Majeed, H. O., Jones, M. L. & Varcoe, B. T. H. Precision measurements of quantum defects in the $\mathrm{nP}_{3/2}$ Rydberg states of ^{85}Rb. *J. Phys. B At. Mol. Opt. Phys.* **42,** 165004 (2009).

219. Lindgård, A. & Nielsen, S. E. Transition probabilities for the alkali isoelectronic sequences Li I, Na I, K I, Rb I, Cs I, Fr I. *At. Data Nucl. Data Tables* **19,** 533–633 (1977).

220. Robicheaux, F. & Shaw, J. Calculated Electron Dynamics in a Strong Electric Field. *Phys. Rev. Lett.* **77,** 4154–4157 (1996).

221. Theodosiou, C. Lifetimes of alkali-metal-atom Rydberg states. *Phys. Rev. A* **30,** 2881–2909 (1984).

222. Numerov, B. Note on the numerical integration of $d^2x/dt^2 = f(x,t)$. *Astron. Nachrichten* **230,** 359–364 (1927).

223. Blatt, J. M. Practical points concerning the solution of the Schrödinger equation. *J. Comput. Phys.* **1,** 382–396 (1967).

224. Zimmerman, M. L., Littman, M. G., Kash, M. M. & Kleppner, D. Stark structure of the Rydberg states of alkali-metal atoms. *Phys. Rev. A* **20,** 2251–2275 (1979).

225. Bhatti, S., Cromer, C. & Cooke, W. Analysis of the Rydberg character of the $5d7d^1D_2$ state of barium. *Phys. Rev. A* **24,** 161–165 (1981).

226. Singer, K. T. T. Interactions in an ultracold gas of Rydberg atoms. PhD thesis (Albert-Ludwigs-Universität Freiburg, 2004).

227. Deiglmayr, J. *et al.* Coherent excitation of Rydberg atoms in an ultracold gas. *Opt. Commun.* **264,** 293–298 (2006).

228. Grabowski, A. Aufbau einer Messapparatur zur Laserkühlung und hochauflösende Rydberg-Spektroskopie an Rb-Atomen. PhD thesis (Universität Stuttgart, 2006).

229. Mayle, M. Ultracold Rydberg Atoms in a Ioffe-Pritchard Trap * * * Creating One-Dimensional Rydberg Gases and Exploiting their Composite Character. PhD thesis (Ruperto-Carola-University of Heidelberg, 2009).

230. Pritchard, J. D. Cooperative Optical Non-linearity in a blockaded Rydberg Ensemble. PhD thesis (Durham University, 2011).

231. Enciso-Aguilar, M., López-Bonilla, J. & Sánchez-Meraz, M. Radial Matrix Elements for the Hydrogen Atom. *Electron. J. Theor. Phys.* **3,** 117–120 (2006).

232. Goltz, D. V. D., Hansen, W. & Richter, J. Experimental and Theoretical Oscillator Strengths of RbI. *Phys. Scr.* **30,** 244–248 (1984).

233. Nadeem, A. & Haq, S. U. Photoionization from the $5p^2P_{3/2}$ state of rubidium. *Phys. Rev. A* **83,** 063404 (2011).

234. Piotrowicz, M. J. *et al.* Measurement of the electric dipole moments for transitions to rubidium Rydberg states via Autler-Townes splitting. *New J. Phys.* **13,** 093012 (2011).

235. *NIST Atomic Spectra Database (ver. 5.0) - formulas* http://physics.nist.gov/Pubs/AtSpec/node17.html.

236. Friedrich, H. S. *Theoretical Atomic Physics* 3rd ed. (Springer, 2006).

237. O'Sullivan, M. & Stoicheff, B. Scalar polarizabilities and avoided crossings of high Rydberg states in Rb. *Phys. Rev. A* **31,** 2718–2720 (1985).

238. O'Brian, T., Kim, J., Lan, G., McIlrath, T. & Lucatorto, T. Verification of the ponderomotive approximation for the ac Stark shift in Xe Rydberg levels. *Phys. Rev. A* **49,** R649–R652 (1994).

239. Knuffman, B. J. Rydberg Atoms in Ponderomotive Potentials. PhD thesis (The University of Michigan, 2009).

240. Farrell, P. M. & MacGillivray, W. R. On the consistency of Rabi frequency calculations. *J. Phys. A. Math. Gen.* **28,** 209–221 (1995).

241. King, B. E. Angular Momentum Coupling and Rabi Frequencies for Simple Atomic Transitions. arXiv: `0804.4528` (2008).

242. Löw, R. *et al.* Apparatus for excitation and detection of Rydberg atoms in quantum gases. arXiv: `0706.2639` (2007).

243. Beterov, I., Ryabtsev, I., Tretyakov, D. & Entin, V. Erratum: Quasiclassical calculations of blackbody-radiation-induced depopulation rates and effective lifetimes of Rydberg nS, nP, and nD alkali-metal atoms with $n \leq 80$ [Phys. Rev. A 79, 052504 (2009)]. *Phys. Rev. A* **80,** 059902 (2009).

244. Oliveira, A., Mancini, M., Bagnato, V. & Marcassa, L. Measurement of Rydberg-state lifetimes using cold trapped atoms. *Phys. Rev. A* **65,** 031401 (2002).

245. Branden, D. B. *et al.* Radiative lifetime measurements of rubidium Rydberg states. *J. Phys. B At. Mol. Opt. Phys.* **43,** 015002 (2010).

246. Van Putten, T. Lifetime of Rubidium Rydberg Atoms in a Magneto-Optical Trap. Bachelor thesis (Amsterdam, 2009).

247. Gallagher, T. F. in (eds Stebbings, R. F. & Dunning, F. B.) chap. 5 (Cambridge University Press, 1983).

248. Middelmann, T. *et al.* Tackling the Blackbody Shift in a Strontium Optical Lattice Clock. *IEEE Trans. Instrum. Meas.* **60,** 2550–2557 (2011).

249. Bloom, B. J. *et al.* An optical lattice clock with accuracy and stability at the 10^{-18} level. *Nature* **506,** 71–5 (2014).

250. Gribakin, G. & Flambaum, V. Calculation of the scattering length in atomic collisions using the semiclassical approximation. *Phys. Rev. A* **48,** 546–553 (1993).

251. Calle Cordón, A. & Ruiz Arriola, E. Low-energy universality and scaling of van der Waals forces. *Phys. Rev. A* **81,** 044701 (2010).

252. Robicheaux, F., Hernández, J., Topçu, T. & Noordam, L. Simulation of coherent interactions between Rydberg atoms. *Phys. Rev. A* **70,** 042703 (2004).

253. Singer, K., Stanojevic, J., Weidemüller, M. & Côté, R. Long-range interactions between alkali Rydberg atom pairs correlated to the ns-ns, np-np and nd-nd asymptotes. *J. Phys. B At. Mol. Opt. Phys.* **38,** S295–S307 (2005).

254. Reinhard, A., Liebisch, T., Knuffman, B. & Raithel, G. Level shifts of rubidium Rydberg states due to binary interactions. *Phys. Rev. A* **75,** 032712 (2007).

255. Walker, T. & Saffman, M. Consequences of Zeeman degeneracy for the van der Waals blockade between Rydberg atoms. *Phys. Rev. A* **77,** 032723 (2008).

256. Glaetzle, A. W. *et al.* Quantum Spin-Ice and Dimer Models with Rydberg Atoms. *Phys. Rev. X* **4,** 041037 (2014).

257. Potvliege, R. M. & Adams, C. S. Photo-ionization in far-off-resonance optical lattices. *New J. Phys.* **8,** 163–163 (2006).

258. Anderson, S. E. & Raithel, G. Ionization of Rydberg atoms by standing-wave light fields. *Nat. Commun.* **4,** 2967 (2013).

259. Tallant, J., Booth, D. & Shaffer, J. P. Photoionization rates of Cs Rydberg atoms in a 1064-nm far-off-resonance trap. *Phys. Rev. A* **82,** 063406 (2010).

260. Farley, J., Tsekeris, P. & Gupta, R. Hyperfine-structure measurements in the Rydberg S and P states of rubidium and cesium. *Phys. Rev. A* **15,** 1530–1536 (1977).

261. Walker, T. G. & Saffman, M. Zeros of Rydberg-Rydberg Föster interactions. *J. Phys. B At. Mol. Opt. Phys.* **38,** S309–S319 (2005).

262. Radzig, A. A. & Smirnov, B. M. *Reference Data on Atoms, Molecules and Ions* (Springer, 1985).

263. Steck, D. A. *Rubidium 87 D Line Data* http://steck.us/alkalidata. 2009.

264. Johnson, J. & Rolston, S. Interactions between Rydberg-dressed atoms. *Phys. Rev. A* **82,** 5 (2010).

265. Isenhower, L., Saffman, M. & Mølmer, K. Multibit C_kNOT quantum gates via Rydberg blockade. *Quantum Inf. Process.* **10,** 755–770 (2011).

266. Gericke, T., Würtz, P., Reitz, D., Langen, T. & Ott, H. High-resolution scanning electron microscopy of an ultracold quantum gas. *Nat. Phys.* **4,** 949–953 (2008).

267. Manthey, T. *et al.* Scanning electron microscopy of Rydberg-excited Bose–Einstein condensates. *New J. Phys.* **16,** 083034 (2014).

268. Olmos, B., Li, W., Hofferberth, S. & Lesanovsky, I. Amplifying single impurities immersed in a gas of ultracold atoms. *Phys. Rev. A* **84,** 041607 (2011).

269. Günter, G. *et al.* Interaction Enhanced Imaging of Individual Rydberg Atoms in Dense Gases. *Phys. Rev. Lett.* **108,** 013002 (2012).

270. Dudin, Y. O., Bariani, F. & Kuzmich, A. Emergence of Spatial Spin-Wave Correlations in a Cold Atomic Gas. *Phys. Rev. Lett.* **109,** 133602 (2012).

271. Thoumany, P., Hänsch, T., Stania, G., Urbonas, L. & Becker, T. Optical spectroscopy of rubidium Rydberg atoms with a 297 nm frequency-doubled dye laser. *Opt. Lett.* **34,** 1621 (2009).

272. Langer, P. Aufbau eines Lasersystems bei 297 nm zur Einphotonenanregung von Rydbergzuständen in Rubidium. Diploma thesis (Technische Universität Kaiserslautern, 2012).

273. Cagnac, B., Grynberg, G. & Biraben, F. Spectroscopie d'absorption multiphotonique sans effet Doppler. *J. Phys.* **34,** 845–858 (1973).

274. Ryabtsev, I. I., Beterov, I. I., Tretyakov, D. B., Entin, V. M. & Yakshina, E. A. Doppler- and recoil-free laser excitation of Rydberg states via three-photon transitions. *Phys. Rev. A* **84,** 053409 (2011).

275. Schmid, T. High precision excitation, manipulation and detection of Rydberg atoms. Master thesis (Universität Stuttgart, 2014).

276. Cubel, T. *et al.* Coherent population transfer of ground-state atoms into Rydberg states. *Phys. Rev. A* **72,** 023405 (2005).

277. Grabowski, A., Heidemann, R., Löw, R., Stuhler, J. & Pfau, T. High resolution Rydberg spectroscopy of ultracold rubidium atoms. *Fortschritte der Phys.* **54,** 765–775 (2006).

278. Viteau, M. *et al.* Ion detection in the photoionization of a Rb Bose-Einstein condensate. *J. Phys. B At. Mol. Opt. Phys.* **44,** 079802 (2011).

279. Ryabtsev, I., Tretyakov, D., Beterov, I. & Entin, V. Effect of finite detection efficiency on the observation of the dipole-dipole interaction of a few Rydberg atoms. *Phys. Rev. A* **76,** 012722 (2007).

280. Ryabtsev, I., Tretyakov, D., Beterov, I. & Entin, V. Erratum: Effect of finite detection efficiency on the observation of the dipole-dipole interaction of a few Rydberg atoms [Phys. Rev. A 76, 012722 (2007)]. *Phys. Rev. A* **76,** 049902 (2007).

281. Stibor, A. *et al.* Calibration of a single-atom detector for atomic microchips. *Phys. Rev. A* **76,** 033614 (2007).

282. Van Bijnen, R. M. W. Quantum Engineering with Ultracold Atoms. PhD thesis (Universiteit Eindhoven, 2013).

283. Omran, A. Excitation of Ultracold Rydberg Atoms in Optical Lattices. Master thesis (Technische Universität München, 2011).

284. Alnis, J., Matveev, A., Kolachevsky, N., Udem, T. & Hänsch, T. W. Sub-hertz linewidth diode lasers by stabilization to vibrationally and thermally compensated ultralow-expansion glass Fabry-Pérot cavities. *Phys. Rev. A* **77,** 053809 (2008).

285. Vogt, S. *et al.* Demonstration of a transportable 1 Hz-linewidth laser. *Appl. Phys. B* **104,** 741–745 (2011).

286. Weatherill, K. J. *et al.* Electromagnetically induced transparency of an interacting cold Rydberg ensemble. *J. Phys. B At. Mol. Opt. Phys.* **41,** 201002 (2008).

287. Fleischhauer, M., Imamoglu, A. & Marangos, J. Electromagnetically induced transparency: Optics in coherent media. *Rev. Mod. Phys.* **77,** 633–673 (2005).

288. Abi-Salloum, T. Y. Electromagnetically induced transparency and Autler-Townes splitting: Two similar but distinct phenomena in two categories of three-level atomic systems. *Phys. Rev. A* **81,** 053836 (2010).

289. Baum, J., Tycko, R. & Pines, A. Broadband and adiabatic inversion of a two-level system by phase-modulated pulses. *Phys. Rev. A* **32,** 3435–3447 (1985).

290. Garwood, M. & DelaBarre, L. The return of the frequency sweep: designing adiabatic pulses for contemporary NMR. *J. Magn. Reson.* **153,** 155–77 (2001).

291. Schauß, P. *et al.* Observation of spatially ordered structures in a two-dimensional Rydberg gas. *Nature* **491,** 87–91 (2012).

292. Zeiher, J. *et al.* *Microscopy of a scalable superatom, in preparation* 2015.

293. Bissbort, U. Dynamical Effects and Disorder in Ultracold Bosonic Matter. PhD thesis (Johann Wolfgang Goethe-Universität Frankfurt, 2012).

294. Schauß, P. *et al.* Crystallization in Ising quantum magnets. *Science* **347,** 1455–1458 (2015).

295. Hernández, J. V. & Robicheaux, F. Coherence conditions for groups of Rydberg atoms. *J. Phys. B At. Mol. Opt. Phys.* **39,** 4883–4893 (2006).

296. Ates, C., Pohl, T., Pattard, T. & Rost, J. Many-body theory of excitation dynamics in an ultracold Rydberg gas. *Phys. Rev. A* **76,** 013413 (2007).

297. Olmos, B., González-Férez, R. & Lesanovsky, I. Collective Rydberg excitations of an atomic gas confined in a ring lattice. *Phys. Rev. A* **79,** 043419 (2009).

298. Stanojevic, J. & Côté, R. Many-body dynamics of Rydberg excitation using the Ω expansion. *Phys. Rev. A* **81,** 053406 (2010).

299. Petrosyan, D., Höning, M. & Fleischhauer, M. Spatial correlations of Rydberg excitations in optically driven atomic ensembles. *Phys. Rev. A* **87,** 053414 (2013).

300. Gärttner, M., Heeg, K. P., Gasenzer, T. & Evers, J. Dynamic formation of Rydberg aggregates at off-resonant excitation. *Phys. Rev. A* **88,** 043410 (2013).

301. Höning, M., Muth, D., Petrosyan, D. & Fleischhauer, M. Steady-state crystallization of Rydberg excitations in an optically driven lattice gas. *Phys. Rev. A* **87,** 023401 (2013).

302. Petrosyan, D. Two-dimensional crystals of Rydberg excitations in a resonantly driven lattice gas. *Phys. Rev. A* **88,** 043431 (2013).

303. Hoening, M., Abdussalam, W., Fleischhauer, M. & Pohl, T. Antiferromagnetic long-range order in dissipative Rydberg lattices. *Phys. Rev. A* **90,** 021603 (2014).

304. Schönleber, D. W., Gärttner, M. & Evers, J. Coherent versus incoherent excitation dynamics in dissipative many-body Rydberg systems. *Phys. Rev. A* **89,** 033421 (2014).

305. Breyel, D., Schmidt, T. L. & Komnik, A. Rydberg crystallization detection by statistical means. *Phys. Rev. A* **86,** 023405 (2012).

306. Schwarzkopf, A. D. Imaging Spatial Correlations of Rydberg Excitations in Cold Atom Clouds. PhD thesis (The University of Michigan, 2013).

307. Li, W., Tanner, P. & Gallagher, T. Dipole-Dipole Excitation and Ionization in an Ultracold Gas of Rydberg Atoms. *Phys. Rev. Lett.* **94,** 173001 (2005).

308. Heeg, K. P., Gärttner, M. & Evers, J. Hybrid model for Rydberg gases including exact two-body correlations. *Phys. Rev. A* **86,** 063421 (2012).

309. Bailey, L. E. & Sesé, L. M. The decay of pair correlations in quantum hard-sphere fluids. *J. Chem. Phys.* **121,** 10076–87 (2004).

310. Stanojevic, J. & Côté, R. Many-body Rabi oscillations of Rydberg excitation in small mesoscopic samples. *Phys. Rev. A* **80,** 033418 (2009).

311. *Fast Methods for Long-Range Interactions in Complex Systems* (eds Sutmann, G., Gibbon, P. & Lippert, T.) (Forschungszentrum Jülich, Jülich, 2010).

312. Baker, G. Ising Model with a Long-Range Interaction in the Presence of Residual Short-Range Interactions. *Phys. Rev.* **130,** 1406–1411 (1963).

313. Wragg, M. J. & Gehring, G. A. The Ising model with long-range ferromagnetic interactions. *J. Phys. A. Math. Gen.* **23,** 2157–2164 (1990).

314. Monroe, J. L. One-dimensional Ising models with long-range interactions. *J. Phys. A. Math. Gen.* **31,** 9809–9817 (1998).

315. Giuliani, A. & Lieb, E. H. Ising models with long-range antiferromagnetic and short-range ferromagnetic interactions. *Phys. Rev. B* **74,** 064420 (2006).

316. Blanchard, T., Picco, M. & Rajabpour, M. A. Influence of long-range interactions on the critical behavior of the Ising model. *Europhys. Lett.* **101,** 56003 (2013).

317. Schachenmayer, J., Lanyon, B. P., Roos, C. F. & Daley, A. J. Entanglement Growth in Quench Dynamics with Variable Range Interactions. *Phys. Rev. X* **3,** 031015 (2013).

318. Weimer, H. & Büchler, H. P. Two-Stage Melting in Systems of Strongly Interacting Rydberg Atoms. *Phys. Rev. Lett.* **105,** 230403 (2010).

319. Richerme, P. *et al.* Quantum Catalysis of Magnetic Phase Transitions in a Quantum Simulator. *Phys. Rev. Lett.* **111,** 100506 (2013).

320. Bak, P. & Bruinsma, R. One-Dimensional Ising Model and the Complete Devil's Staircase. *Phys. Rev. Lett.* **49,** 249–251 (1982).

321. Lesanovsky, I. Many-Body Spin Interactions and the Ground State of a Dense Rydberg Lattice Gas. *Phys. Rev. Lett.* **106,** 025301 (2011).

322. Zener, C. Non-Adiabatic Crossing of Energy Levels. *Proc. R. Soc. A Math. Phys. Eng. Sci.* **137,** 696–702 (1932).

323. Brierley, R. T., Creatore, C., Littlewood, P. B. & Eastham, P. R. Adiabatic State Preparation of Interacting Two-Level Systems. *Phys. Rev. Lett.* **109,** 043002 (2012).

324. Bellem, D. Generation of Spatially and Temporally Varying Light Potentials in Optical Lattices. Diploma thesis (Ludwig-Maximilians-Universität München, 2011).

325. Lesanovsky, I., Olmos, B. & Garrahan, J. P. Thermalization in a Coherently Driven Ensemble of Two-Level Systems. *Phys. Rev. Lett.* **105,** 100603 (2010).

326. Ates, C. & Lesanovsky, I. Entropic enhancement of spatial correlations in a laser-driven Rydberg gas. *Phys. Rev. A* **86,** 013408 (2012).

327. Petrosyan, D., Höning, M. & Fleischhauer, M. Spatial correlations of Rydberg excitations in optically driven atomic ensembles. *Phys. Rev. A* **87,** 053414 (2013).

328. Vermersch, B., Punk, M., Glaetzle, A. W., Gross, C. & Zoller, P. Dynamical preparation of laser-excited anisotropic Rydberg crystals in 2D optical lattices. *New J. Phys.* **17,** 013008 (2015).

329. Ni, K.-K. *et al.* A high phase-space-density gas of polar molecules. *Science* **322,** 231–5 (2008).

330. Takekoshi, T. *et al.* Ultracold Dense Samples of Dipolar RbCs Molecules in the Rovibrational and Hyperfine Ground State. *Phys. Rev. Lett.* **113,** 205301 (2014).

331. Molony, P. K. *et al.* Creation of Ultracold ^{87}Rb^{133}Cs Molecules in the Rovibrational Ground State. *Phys. Rev. Lett.* **113,** 255301 (2014).

332. Griesmaier, A., Werner, J., Hensler, S., Stuhler, J. & Pfau, T. Bose-Einstein Condensation of Chromium. *Phys. Rev. Lett.* **94,** 160401 (2005).

333. Lu, M., Burdick, N. Q., Youn, S. H. & Lev, B. L. Strongly Dipolar Bose-Einstein Condensate of Dysprosium. *Phys. Rev. Lett.* **107,** 190401 (2011).

334. Aikawa, K. *et al.* Bose-Einstein Condensation of Erbium. *Phys. Rev. Lett.* **108,** 210401 (2012).

335. Żuchowski, P. S. & Hutson, J. M. Reactions of ultracold alkali-metal dimers. *Phys. Rev. A* **81,** 060703 (2010).

336. Ni, K.-K. *et al.* Dipolar collisions of polar molecules in the quantum regime. *Nature* **464,** 1324–8 (2010).

337. Frisch, A. *et al.* Quantum chaos in ultracold collisions of gas-phase erbium atoms. *Nature* **507,** 475–9 (2014).

338. Petrosyan, D. Dynamics and equilibration of Rydberg excitations in dissipative atomic ensembles. *J. Phys. B At. Mol. Opt. Phys.* **46,** 141001 (2013).

339. Barredo, D. *et al.* Coherent Excitation Transfer in a Spin Chain of Three Rydberg Atoms. *Phys. Rev. Lett.* **114,** 113002 (2015).

340. DiVincenzo, D. P. in *Mesoscopic Electron Transp.* (eds Sohn, L. L., Kouwenhoven, L. P. & Schön, G.) (Springer Netherlands, Dordrecht, 1997). doi:`10.1007/978-94-015-8839-3`.

341. Camargo, F. *et al.* *Abstract: K1.00027 : An Experimental Apparatus for Studying Rydberg-Rydberg Interactions in Quantum Degenerate Gases of Strontium* http://meetings.aps.org/link/BAPS.2014.DAMOP.K1.27. 2014.

342. Zeiher, J. Work in progress. PhD thesis (Ludwig-Maximilians-Universität München).

343. Thoumany, P. Optical Spectroscopy and Cavity QED Experiments with Rydberg Atoms. PhD thesis (Ludwig-Maximilians-Universität München, 2011).

344. Weber, T. M. *et al.* Mesoscopic Rydberg-blockaded ensembles in the superatom regime and beyond. *Nat. Phys.* **11,** 157–161 (2015).

345. Bouchoule, I. & Mølmer, K. Spin squeezing of atoms by the dipole interaction in virtually excited Rydberg states. *Phys. Rev. A* **65,** 041803 (2002).

346. Leggett, A. J. Can a Solid Be "Superfluid"? *Phys. Rev. Lett.* **25,** 1543–1546 (1970).

347. Balibar, S. The enigma of supersolidity. *Nature* **464,** 176–82 (2010).

348. Boninsegni, M. & Prokof'ev, N. V. Colloquium: Supersolids: What and where are they? *Rev. Mod. Phys.* **84,** 759–776 (2012).

349. Kim, E. & Chan, M. H. W. Probable observation of a supersolid helium phase. *Nature* **427,** 225–7 (2004).

350. Day, J. & Beamish, J. Low-temperature shear modulus changes in solid ^{4}He and connection to supersolidity. *Nature* **450,** 853–6 (2007).

351. Kim, D. Y. & Chan, M. H. W. Absence of Supersolidity in Solid Helium in Porous Vycor Glass. *Phys. Rev. Lett.* **109,** 155301 (2012).

352. Dalla Torre, E. G., Berg, E. & Altman, E. Hidden Order in 1D Bose Insulators. *Phys. Rev. Lett.* **97,** 260401 (2006).

353. Berg, E., Dalla Torre, E., Giamarchi, T. & Altman, E. Rise and fall of hidden string order of lattice bosons. *Phys. Rev. B* **77,** 245119 (2008).

354. Rossini, D., Gibertini, M., Giovannetti, V. & Fazio, R. Topological pumping in the one-dimensional Bose-Hubbard model. *Phys. Rev. B* **87,** 085131 (2013).

355. Rossini, D. & Fazio, R. Phase diagram of the extended Bose-Hubbard model. *New J. Phys.* **14,** 065012 (2012).

356. Torre, E. G. D. Dynamical probing of a topological phase of bosons in one dimension. *J. Phys. B At. Mol. Opt. Phys.* **46,** 085303 (2013).

357. Safronova, M., Williams, C. & Clark, C. Relativistic many-body calculations of electric-dipole matrix elements, lifetimes, and polarizabilities in rubidium. *Phys. Rev. A* **69,** 022509 (2004).

358. Arora, B. & Sahoo, B. K. State-insensitive trapping of Rb atoms: Linearly versus circularly polarized light. *Phys. Rev. A* **86,** 033416 (2012).

359. Piotrowicz, M. J. Ultracold Rydberg Atoms. PhD thesis (The Open University, 2010).

360. Beterov, I. I. *et al.* Cooper minima in the transitions from low-excited and Rydberg states of alkali-metal atoms. arXiv: `1207.3626` (2012).

361. Li, W., Tanner, P. J., Jamil, Y. & Gallagher, T. F. Ionization and plasma formation in high n cold Rydberg samples. *Eur. Phys. J. D* **40,** 27–35 (2006).

362. Shore, B. W. *The theory of coherent atomic excitation, Multilevel atoms and incoherence (Volume 2)* (Wiley, 1990).

363. Shore, B. W. Coherent manipulation of atoms using laser light. *Acta Phys. Slovaca* **58,** 243–486 (2008).

364. Johnson, T. A. Rabi oscillations and excitation blockade between ground and Rydberg states of single optically trapped rubidium atoms. PhD thesis (University of Wisconsin-Madison, 2008).

365. Gärttner, M. Many-Body Effects in Rydberg Gases. PhD thesis (Universität Heidelberg, 2013).

366. Steck, D. A. *Quantum and Atom Optics* http://steck.us/teaching. 2014.

367. Brion, E., Pedersen, L. H. & Mølmer, K. Adiabatic elimination in a lambda system. *J. Phys. A Math. Theor.* **40,** 1033–1043 (2007).

368. Shore, B. W. Definition of virtual levels. *Am. J. Phys.* **47,** 262 (1979).

369. Torosov, B. T. & Vitanov, N. V. Adiabatic elimination of a nearly resonant quantum state. *J. Phys. B At. Mol. Opt. Phys.* **45,** 135502 (2012).

370. Paulisch, V., Rui, H., Ng, H. K. & Englert, B.-G. Beyond adiabatic elimination: A hierarchy of approximations for multi-photon processes. *Eur. Phys. J. Plus* **129,** 12 (2014).

371. Schwabl, F. *Statistische Mechanik* (Springer, 2006).

372. Raj, R., Bloch, D., Snyder, J., Camy, G. & Ducloy, M. High-Frequency Optically Heterodyned Saturation Spectroscopy Via Resonant Degenerate Four-Wave Mixing. *Phys. Rev. Lett.* **44,** 1251–1254 (1980).

373. Camy, G., Bordé, C. & Ducloy, M. Heterodyne saturation spectroscopy through frequency modulation of the saturating beam. *Opt. Commun.* **41,** 325–330 (1982).

374. Shirley, J. H. Modulation transfer processes in optical heterodyne saturation spectroscopy. *Opt. Lett.* **7,** 537 (1982).

375. Long-sheng, M., Hollberg, L., Shirley, J. & Hall, J. *Modulation transfer spectroscopy for stabilizing lasers* http://www.google.com/patents/US4590597. 1986.

376. Jaatinen, E. Theoretical determination of maximum signal levels obtainable with modulation transfer spectroscopy. *Opt. Commun.* **120,** 91–97 (1995).

377. Deiglmayr, J. Coherent excitation of an ultracold gas of Rydberg atoms. Diploma thesis (Albert-Ludwigs-Universität Freiburg, 2006).

378. Eble, J. & Schmidt-Kaler, F. Optimization of frequency modulation transfer spectroscopy on the calcium 4^1S_0 to 4^1P_1 transition. *Appl. Phys. B* **88,** 563–568 (2007).

379. McCarron, D. J., King, S. a. & Cornish, S. L. Modulation transfer spectroscopy in atomic rubidium. *Meas. Sci. Technol.* **19,** 105601 (2008).

380. Hopper, D. J. Investigation of Laser Frequency Stabilisation Using Modulation Transfer Spectroscopy. PhD thesis (Queensland University of Technology, 2008).

381. Jaatinen, E. & Hopper, D. J. Compensating for frequency shifts in modulation transfer spectroscopy caused by residual amplitude modulation. *Opt. Lasers Eng.* **46,** 69–74 (2008).

382. Xiang-Hui, Q. *et al.* Ultra-Stable Rubidium-Stabilized External-Cavity Diode Laser Based on the Modulation Transfer Spectroscopy Technique. *Chinese Phys. Lett.* **26,** 044205 (2009).

383. Zhou, Z.-C., Wei, R., Shi, C.-Y. & Wang, Y.-Z. Observation of Modulation Transfer Spectroscopy in the Deep Modulation Regime. *Chinese Phys. Lett.* **27,** 124211 (2010).

384. Zhe Li, L., Eon Park, S., Noh, H.-R., Park, J.-D. & Cho, C.-H. Modulation Transfer Spectroscopy for a Two-Level Atomic System with a Non-Cycling Transition. *J. Phys. Soc. Japan* **80,** 074301 (2011).

385. Ye, J., Swartz, S., Jungner, P. & Hall, J. L. Hyperfine structure and absolute frequency of the ^{87}Rb $5P_{3/2}$ state. *Opt. Lett.* **21,** 1280 (1996).
386. Fornberg, B. Generation of finite difference formulas on arbitrarily spaced grids. *Math. Comput.* **51,** 699–706 (1988).
387. Grimm, R., Ovchinnikov, Y., Sidorov, A. & Letokhov, V. Observation of a strong rectified dipole force in a bichromatic standing light wave. *Phys. Rev. Lett.* **65,** 1415–1418 (1990).
388. Grimm, R., Ovchinnikov, Y., Sidorov, A. & Letokhov, V. Observation of a Strong Rectified Dipole Force in a Bichromatic Standing Light Wave. *Phys. Rev. Lett.* **65,** 3210–3210 (1990).
389. Söding, J. Atomstrahlabbresmung mit der stimuleirten bichromatischen Lichtkraft. PhD thesis (Ruprecht-Karls-Universität Heidelberg, 1996).
390. Söding, J., Grimm, R., Ovchinnikov, Y., Bouyer, P. & Salomon, C. Short-Distance Atomic Beam Deceleration with a Stimulated Light Force. *Phys. Rev. Lett.* **78,** 1420–1423 (1997).
391. Williams, M., Chi, F., Cashen, M. & Metcalf, H. Measurement of the bichromatic optical force on Rb atoms. *Phys. Rev. A* **60,** R1763–R1766 (1999).
392. Williams, M., Chi, F., Cashen, M. & Metcalf, H. Bichromatic force measurements using atomic beam deflections. *Phys. Rev. A* **61,** 023408 (2000).
393. Cashen, M. & Metcalf, H. Optical forces on atoms in nonmonochromatic light. *J. Opt. Soc. Am. B* **20,** 915 (2003).
394. Malinovsky, V. & Berman, P. Momentum transfer using chirped standing-wave fields: Bragg scattering. *Phys. Rev. A* **68,** 023610 (2003).
395. Yatsenko, L. & Metcalf, H. Dressed-atom description of the bichromatic force. *Phys. Rev. A* **70,** 063402 (2004).
396. Chieda, M. A. & Eyler, E. E. Bichromatic slowing of metastable helium. *Phys. Rev. A* **86,** 053415 (2012).
397. Eichmann, U., Nubbemeyer, T., Rottke, H. & Sandner, W. Acceleration of neutral atoms in strong short-pulse laser fields. *Nature* **461,** 1261–4 (2009).
398. Maher-McWilliams, C., Douglas, P. & Barker, P. F. Laser-driven acceleration of neutral particles. *Nat. Photonics* **6,** 386–390 (2012).
399. Zhao, X.-G., Georgakis, G. & Niu, Q. Rabi oscillations between Bloch bands. *Phys. Rev. B* **54,** R5235–R5238 (1996).
400. Fischer, M., Madison, K., Niu, Q. & Raizen, M. Observation of Rabi oscillations between Bloch bands in an optical potential. *Phys. Rev. A* **58,** R2648–R2651 (1998).
401. Sias, C. *et al.* Observation of Photon-Assisted Tunneling in Optical Lattices. *Phys. Rev. Lett.* **100,** 040404 (2008).
402. Ivanov, V. *et al.* Coherent Delocalization of Atomic Wave Packets in Driven Lattice Potentials. *Phys. Rev. Lett.* **100,** 043602 (2008).

403. Ma, R. *et al.* Photon-Assisted Tunneling in a Biased Strongly Correlated Bose Gas. *Phys. Rev. Lett.* **107,** 095301 (2011).

404. Blakie, P. B. & Clark, C. W. Wannier states and Bose–Hubbard parameters for 2D optical lattices. *J. Phys. B At. Mol. Opt. Phys.* **37,** 1391–1404 (2004).

405. Wannier, G. The Structure of Electronic Excitation Levels in Insulating Crystals. *Phys. Rev.* **52,** 191–197 (1937).

406. Hung, C.-L. In situ probing of two-dimensional quantum gases. PhD thesis (The University of Chicago, 2011).

407. Wüster, S. *et al.* Correlations of Rydberg excitations in an ultracold gas after an echo sequence. *Phys. Rev. A* **81,** 023406 (2010).

408. Fölling, S. *et al.* Spatial quantum noise interferometry in expanding ultracold atom clouds. *Nature* **434,** 481–4 (2005).

409. Hild, S. *et al.* Far-from-Equilibrium Spin Transport in Heisenberg Quantum Magnets. *Phys. Rev. Lett.* **113,** 147205 (2014).

410. Metcalf, H. J. & van Der Straten, P. *Laser cooling and trapping* 2nd ed. (Springer, 1999).

411. Urban, E. Coherent manipulation of single atom qubits using Rydberg states. PhD thesis (University of Wisconsin-Madison, 2009).

412. Gaetan, A. Intrication de deux atomes en utilisant le blocage de Rydberg. PhD thesis (Université Paris XI Orsay, 2009).

413. Johnson, L. A. M., Majeed, H. O., Sanguinetti, B., Becker, T. & Varcoe, B. T. H. Absolute frequency measurements of ^{85}Rb nF$_{7/2}$ Rydberg states using purely optical detection. *New J. Phys.* **12,** 063028 (2010).

414. Miller, K., Krause, D. & Hunter, L. Precise measurement of the Stark shift of the rubidium and potassium D$_1$ lines. *Phys. Rev. A* **49,** 5128–5130 (1994).

415. Zu Putlitz, G. & Schenck, A. Zur Hyperfeinstruktur des $6^2P_{3/2}$-Terms von Rb^{87}. *Zeitschrift für Phys.* **183,** 428–430 (1965).

416. Thibault, C. *et al.* Hyperfine structure and isotope shift of the D$_2$ line of $^{76-98}$Rb and some of their isomers. *Phys. Rev. C* **23,** 2720–2729 (1981).

417. Maric, M., McFerran, J. & Luiten, A. Frequency-comb spectroscopy of the D$_1$ line in laser-cooled rubidium. *Phys. Rev. A* **77,** 032502 (2008).

418. Liberman, S. & Pinard, J. Experimental studies of high-lying Rydberg states in atomic rubidium. *Phys. Rev. A* **20,** 507–518 (1979).

419. Bernard, J. *et al.* Absolute frequency measurement of a laser at 1556 nm locked to the 5S$_{1/2}$-5D$_{5/2}$ two-photon transition in ^{87}Rb. *Opt. Commun.* **173,** 357–364 (2000).

420. Snigirev, S. *et al.* Measurement of the 5D-level polarizability in laser-cooled Rb atoms. *Phys. Rev. A* **89,** 012510 (2014).

421. Arora, B., Safronova, M. & Clark, C. Determination of electric-dipole matrix elements in K and Rb from Stark shift measurements. *Phys. Rev. A* **76,** 052516 (2007).

422. Lee, W.-K., Seb Moon, H. & Suhng Suh, H. Measurement of the absolute energy level and hyperfine structure of the ^{87}Rb $4D_{5/2}$ state. *Opt. Lett.* **32,** 2810 (2007).

423. Moon, H., Lee, W.-K. & Suh, H. Hyperfine-structure-constant determination and absolute-frequency measurement of the Rb $4D_{3/2}$ state. *Phys. Rev. A* **79,** 062503 (2009).

424. Ko, M.-S. & Liu, Y.-W. Observation of rubidium $5S_{1/2} \rightarrow 7S_{1/2}$ two-photon transitions with a diode laser. *Opt. Lett.* **29,** 1799 (2004).

425. Pandey, K. & Natarajan, V. Splitting of electromagnetically induced transparency under strong-probe conditions due to Doppler averaging. *J. Phys. B At. Mol. Opt. Phys.* **41,** 185504 (2008).

426. Seltzer, S. J. *et al.* Investigation of antirelaxation coatings for alkali-metal vapor cells using surface science techniques. *J. Chem. Phys.* **133,** 144703 (2010).

427. Arimondo, E., Inguscio, M. & Violino, P. Experimental determinations of the hyperfine structure in the alkali atoms. *Rev. Mod. Phys.* **49,** 31–75 (1977).

428. Luna, F. A compilation of wavelengths and energy levels for the spectrum of neutral rubidium (RbI). *J. Quant. Spectrosc. Radiat. Transf.* **75,** 559–587 (2002).

429. Sansonetti, J. E. Wavelengths, Transition Probabilities, and Energy Levels for the Spectra of Rubidium (Rb I through Rb XXXVII). *J. Phys. Chem. Ref. Data* **35,** 301 (2006).

430. Sternheimer, R. & Peierls, R. Quadrupole Antishielding Factors, and the Nuclear Quadrupole Moments of Several Alkali Isotopes. *Phys. Rev. A* **3,** 837–848 (1971).

431. Mendelsohn, A., Barty, C., Sher, M., Young, J. & Harris, A. Emission spectra of quasimetastable levels of alkali-metal atoms. *Phys. Rev. A* **35,** 2095–2101 (1987).

List of Figures

List of Tables

Acknowledgements/Danksagung

An dieser Stelle möchte ich mich bei allen bedanken, die zum Gelingen dieser Arbeit beigetragen haben.

Zunächst danke ich Prof. Immanuel Bloch und Prof. Stefan Kuhr für die freundliche Aufnahme in der Arbeitsgruppe an meinem Wunschexperiment. Die Arbeitsbedingungen in der Gruppe sind einzigartig, nicht nur die gute Arbeitsatmosphäre und exzellente Ausstattung, sondern auch die effektive Planung zukünftiger Projekte. Dankbar bin ich auch dafür, dass ich an einer Vielzahl von Konferenzen teilnehmen konnte, was insbesondere für den Überblick über das Gebiet der Rydberg-Physik und die Planung der Rydberg Experimente von entscheidender Bedeutung war.

Zu besonderem Dank bin ich den erfahrenen Mitgliedern des Single Atoms Teams (Christof Weitenberg, Manuel Endres, Jacob Sherson, Marc Cheneau, Stefan Kuhr) verpflichtet, die in langwieriger Arbeit vor meiner Zeit ein grundsolides Experiment aufgebaut haben, welches ohne große Reparaturen immer zuverlässig lief und spektakuläre Resultate hervorbrachte. Den beiden Doktoranden der ersten Generation Christof und Manuel, von denen ich viel über das Experiment und seine Eigenheiten gelernt habe. Stefan Kuhr für die initiale Planung des Rydberg Projekts und die Einführungs-Sessions in die Experimentsteuerungssoftware und die Rekonstruktionsskripte, die einen wesentlichen Anteil am Erfolg des Experiments haben. Außerdem für seinen Einsatz bei der Beschleunigung der Lieferung von diversen Firmen, der uns lange Wartezeiten erspart hat. In meine Zeit fiel auch die reibungslose Übergabe des Experiments an Christian Groß. Bei ihm möchte ich mich für die vielen Diskussionen, die effektive Unterstützung bei den Veröffentlichungen und die großen Freiheiten am Experiment bedanken.

Für die Hilfe im Labor danke ich insbesondere Ahmed Omran, Marc Cheneau und Johannes Zeiher, die das Rydberg Projekt über die verschiedenen Phasen, vom Aufbau über das erste und zweite große Projekt, begleitet haben. Takeshi Fukuhara und David Bellem für die gute Zusammenarbeit bei der Single-site-Adressierung, die es ermöglicht hat, dass diese Technik auch in Rydberg Experimenten zum Einsatz kommen konnte. An dieser Stelle danke ich auch Thomas Pohl und Tommaso Macrì für die gute Zusammenarbeit auf der Theorie-Seite und die vielen Diskussionen über Rydberg-Systeme, die wesentlich zum Verständnis beigetragen haben. Besonderer Dank gilt Tommaso für einige Berechnungen speziell für diese Arbeit. Zum einem für die Berechnung von Resonanzkurven in dichten Systemen (Fig. 5.13), zum anderen für die Rechnung zur Dynamik während der adiabatischen Präparation zwei Dimen-

sionen (Fig. 7.15). Bei Robert Löw möchte ich mich für eine Diskussion bedanken, die mich darin bestärkt hat, das Schema zur Stimulation der Rydberg-Atome zurück in der Grundzustand zu implementieren.

Für das Korrekturlesen dieser Arbeit oder Teilen davon danke ich Johannes Zeiher, Sebastian Hild, Christian Groß, Marc Cheneau, Ahmed Omran.

Den Mitarbeitern der anderen beiden Experimente am MPQ, dem Lithium und Molekül-Experiment (Ahmed Omran, Timon Hilker, Martin Boll, Michael Lohse, Thomas Gantner, Katharin Kleinlein, Christian Groß; Nikolaus Buchheim, Zhenkai Lu, Frauke Seeßelberg, Diana Amaro, Tobias Schneider, Christoph Gohle) für die gute Zusammenarbeit, auch wenn sie hin- und wieder unsere Laborvorräte geplündert haben. Danke auch an den Teil der Bloch-Gruppe an der LMU für zahlreiche Diskussionen, trotz der auf Grund der verschiedenen Standorte teils eingeschränkten Kommunikation.

Der Betriebssportgruppe "Keller-aufräumen" für Abwechslung und Erheiterung in der Mittagspause, nach der wir stets mit neuer Motivation in den Nachmittag gestartet sind.

Ich erinnere mich gern an diverse Sport-Aktivitäten mit Kollegen, die dazu beigetragen haben, das Aufschreiben der Arbeit fit und ohne Rückenprobleme zu überstehen.

Dem Dekan Prof. Schenzle danke ich für seine Unterstützung der Verlängerungen meiner Einschreibung als Promotionsstudent.

Allen nicht-wissenschaftlichen Mitarbeitern, die das Team engagiert unterstützt haben, danke ich für die gute Zusammenarbeit: Marianne Kargl, Kristina Schuldt, Karsten Förster, Markus Böhm und Michael Pruscha, die uns beide zu Gunsten der freien Wirtschaft leider verlassen haben, Anton Mayer, Oliver Mödl.

Dem Team der Haustechnik unter Leitung von Andreas Widhopf, das uns insbesondere beim Debugging der Klimaanlage geholfen hat.

Besonderer Dank gilt meinen Eltern und meiner Schwester für die Unterstützung in allen Lebenslagen und kulinarische Experimente mit (fast) selbstorganisierter Ordnung.